POLITECNICO DI MILANO
MECHANICAL ENGINEERING DEPARTMENT
DOCTORAL PROGRAMME IN MECHANICAL ENGINEERING

An investigation in Mechanical Constitutive Theories for non-metal brittle material

Doctoral Dissertation of:
Aria Mardalizad

Supervisor:
Prof. Marco Giglio

Co-supervisor:
Prof. Andrea Manes

Tutor:
Prof. Nora Lecis

The Chair of the Doctoral Program:
Prof. Daniele Rocchi

Year 2018 – Cycle XXXI

Abstract

The numerical simulation of penetration into rock is an important tool to gain insights into rock drilling mechanisms, since it can be exploited as an alternative to the expensive field testing in the pertinent fields of engineering. Developing a reliable numerical modelling technique able to deal with the dynamic bit-rock interaction process, is considered as an important challenge for fracture assessment of the geological materials. This research aims to present an innovative computer simulation of rock penetration process on the basis of a finite element method (FEM) coupled to smooth particle hydrodynamics (SPH).

The mechanical behavior of a quasi-brittle material, namely Pietra Serena sandstone, are investigated both numerically (Finite Element Method) and experimentally in order to build a reliable numerical modelling environment aimed to be transferred to more complex cases. Karagozian and Case Concrete (KCC) model is exploited as material constitutive law. A method which demonstrates the utilization of this model to simulate quasi-brittle materials with efficiency and accuracy is discussed in this thesis. The capability of this model is critically evaluated by comparing the results of numerical simulations and the corresponding experimental results and a critical assessment of the method is reported.

Several experimental tests are exploited within this research work on a medium range sandstone for material parameter identification and validating the numerical method. The comparison of the numerical and experimental results obtained led to the conclusion that the FEM-coupled to-SPH method in conjunction with the fully calibrated KCC material model is a reliable method for the study of rock penetration under extreme condition due to its ability to deal with large deformations and its realistic constitutive modelling.

The modelling approach was then applied to estimate the required force to penetrate a given (offshore) reservoir rock block under the in-situ confining pressure with a double conical tool up to a certain depth. Finally, a percussive drilling problem was simulated with a triple button-bit on a rock specimen at different drilling depth below seabed. The effect of several design parameters was investigated, which can be used further in the research and development sectors of the petroleum industries.

Contents

List of figures

List of tables

List of acronyms

ASTM	American society for testing and materials
BD	Brazilian disk
BTS	Brazilian tensile strength
DDM	displacement discontinuity method
DIC	digital image correlation
DIF	dynamic increase factor
DP	Drucker-Prager
EFFEPS	effective strain
EOS	equation-of-state
FEM	finite element method
KCC	Karagozian and Case concrete
LDP	linear Drucker-Prager
LVDT	linear variable differential transformer
MC	Mohr-Coulomb
PPT	punch penetration test
RDI	rock drillability index
SHPB	split Hopkinson pressure bar
SPH	smooth particle hydrodynamics
TXC	triaxial compression
UC	unconfined compression
UCS	unconfined compression strength
UCT	unconfined compression test
UTS	uniaxial (ultimate) tensile strength

Part I

Introduction

Chapter 1

Background and motivation

Extensive knowledge of the mechanical behaviour of quasi-brittle material is crucial in many scientific and industrial industries, e.g. deep well drilling (Hu and Randolph, 1998; Pepper, 1954), underground mining (Lacy and Lacy, 1992), etc. Although this knowledge has been boosted by the fast development of numerical analyses and computer resources, the analysis of these materials' failure modes is still a crucial problem (Chen and Egger, 1999; Santarelli and Brown, 1989). The term quasi-brittle is dedicated to the material such as rock (Labuz et al., 1985), concrete (Cornelissen et al., 1986) and most ceramics, since they express moderate strain hardening (before reaching their ultimate strength) comparable with metallic material, and sharp softening responses reminiscent of brittle material (Huang and Karihaloo, 1993). Among these quasi-brittle materials, investigation of the mechanical behaviour of rock materials in sub-aqueously deep well drilling applications is the mandatory task of the petroleum science (Brady and Brown, 2013).

The mechanical behaviour of rock at a material scale is generally controlled by the geometric arrangements of the mineral particles and voids together with the microcracks structures. However, also the micro flaws often significantly influence the mechanical behaviour (Åkesson et al., 2004; Basu et al., 2009; Szwedzicki, 2007). The failure modes of brittle crystalline rock materials are complex and difficult to predict (Santarelli and Brown, 1989). The complexity comes from various analytical procedures represented in the general field of applied mechanics, such as sensitivity to confining pressure, associativity flow, strength and post failure deformations, localization, etc. (Brady and Brown, 2013; Jaeger et al., 2007; Li et al., 2003; Malvar and Crawford, 1998; Martin, 1993). Therefore, the investigation of the mechanical properties of a rock material is aimed to promote the understanding and the future design demands of this domain.

Numerical modelling is considered as an alternative to expensive field testing, especially in the petroleum industry. Several constitutive equations have been proposed to analyse the nonlinear response of rock material (Bai et al., 1999; Jing and Hudson, 2002). The common frameworks for geological constitutive modelling is based on the theoretical concepts of continuum mechanics, i.e. elasticity, plasticity (Huang and

Karihaloo, 1993), damage (Rots and De Borst, 1987), visco-plasticity (Winnicki et al., 2001) and different combinations of these (Brannon and Leelavanichkul, 2009; Fossum and Brannon, 2004; Jiang and Zhao, 2015; Malvar et al., 2000b; Saksala, 2010a).

The Lagrangian Finite Element Method (FEM) is still one of the foremost numerical techniques to solve problems in solid mechanics. High accuracy and acceptable computing time are two noteworthy features of this method. However, as a mesh-based method, one of its main drawbacks is the low performance in dealing with large deformations and highly distorted solid elements, which is often unavoidable in the continuum mechanics based numerical modelling of fractured rock. The Smooth Particles Hydrodynamics (SPH) introduced by Monaghan (Monaghan, 1988), on the other hand, is a mesh-less method which discretizes a system into several grid-points at which the field variables are evaluated (Liu and Liu, 2010). The capability and performance of the SPH in dealing with large deformation problems, stems mainly from the fact that the nodal connectivity is not fixed in this method, as demonstrated e.g. in (Anghileri et al., 2011; Bresciani et al., 2016; Olleak and El-Hofy, 2015). However, the performance of SPH in terms of accuracy and computation time is often lower in comparison to the FEM. Therefore, looking for a scientific path to overcome these drawbacks is a challenging task.

The penetration of a tool into rock by indentation is the basic process in various excavation machines, such as roller disc cutters and percussive drills (Chen and Labuz, 2006; Kahraman et al., 2012; Kalyan et al., 2015). Depending on the rock strength, there are two basic procedures for rock excavation: shearing for soft to medium strength rocks, and indentation for medium to hard rocks (Fowell, 1993). The oil and gas reservoir rocks, e.g. Berea sandstone, are classified as medium strength rocks (UCS ranges from 40 to 80 MPa). Therefore, exploiting numerical modelling to investigate the indentation process is an interesting case of study in petroleum industries.

The conceptual model for percussive rock drilling by a drill bit with multiple button bits is illustrated in Figure 1 (Saksala et al., 2014). Drilling deep holes in bedrock poses challenges to the efficiency of rock excavation methods due to severe stress conditions prevailing in the bedrock induced by gravity (overburden stress) and tectonic activity (Zang and Stephansson, 2009). High pressure conditions are faced also in seafloor drilling (Bar-Cohen and Zacny, 2009). In-situ confining stresses lead to substantial drops in the rate of penetration of percussive drilling (Cunningham and Eenink, 1959). Therefore, it is instructive to study numerically the penetration of a bit into the rock

specimen under confining pressures conditions similar to those in deep hole drilling under the seabed.

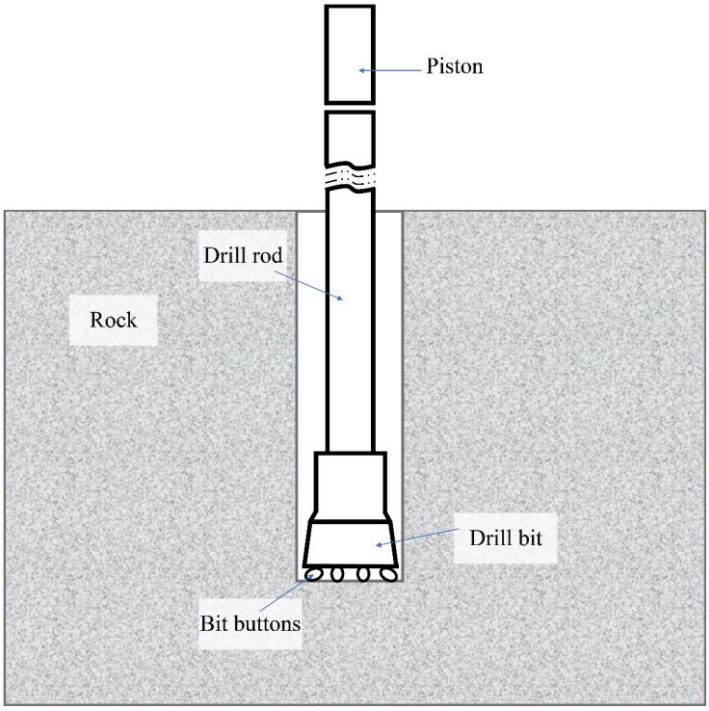

Figure 1. Schematic representation of the principle of percussive drilling.

Percussive drilling is one of the most widely used rock drilling technique in the petroleum industries. In this type of drilling, an impact which is induced by the stress wave forces the high strength multiple button-bits metal to penetrate into the rock. Increasing demands for higher quality and efficiency with lower costs have been always an inevitable fact, hence, the fracture, fragmentation and penetration prediction of rock materials are the problems required persistent investigations. The coalescence of the side cracks or the lateral chipping plays the most significant role in the fracture mechanism related to the percussive drilling.

Several numerical investigations of the rock penetration problem are limited to account for some details related to the fracture systems. The simulation of subsurface fractures are reported in (Tan et al., 1997) by applying a tensile splitting failure model in the rock indentation. The same author proposed a fracture mechanism based on displacement discontinuity method (DDM) in another study (Tan et al., 1998) to simulate the side crack formation. Liu et al. (Liu, 2004; Liu et al., 2008; Liu et al., 2002) developed a more general method to study the rock fragmentation mechanism based on a continuum scalar damage model. In all of the beforementioned studies, the indentation was considered by quasi-static loading conditions.

The interaction of drill bit-rock in the percussive drilling is a transient (and dynamic) problem, that deals with high local strain rate enhancement and propagation of the stress wave. In this regard, the impact indentation into rock material is investigated by Saksala in (Saksala, 2006) by implementing a pure scalar damage model. The same author studied a rate-independent damage plasticity model in (Saksala, 2008), and a damage-viscoplastic consistency model with a parabolic cap in (Saksala, 2010a). In a study of (Camacho and Ortiz, 1996), cohesive elements are used to investigate the impact fracture of brittle material. An orthotropic damage model in conjunction with an statistical approach for material parameters are proposed by (Denoual and Hild, 2000). Beside the previous research studies, which are developed by Finite Element Method (FEM), there are also studies of rock fracture in percussive drilling action by developing particle-based numerical methods, e.g. (Thuro and Schormair, 2008). However, all these studies were performed based on 2D numerical methods (the plain strain conditions).

An example of 3D simulation of percussive drilling action is provided in (Han et al., 2005) by implementing a modified Mohr-Coulomb strain softening model in the FLAC3D code. The unrealistic impact rates (0.2 m/impact) in the former study can be observed as the result of limitation of computational power for 3D modelling, and accordingly using coarse meshes. Another 3D simulation has been studied in (Rossmanith et al., 1996) by developing an elastic-brittle damage model implemented in a 3D finite difference method. The discrete blocks which are forming the computational grid of the latter study may have different elastic properties, hence, rigid indenters are modelled as boundary conditions for displacements with time dependent prescribed contact area (Saksala, 2010b). Therefore, the presence of some simplifying assumptions concerning the complexity of percussive rock drilling problem can be observed in these studies (Saksala, 2010b).

In view of the above discussion, it is concluded that providing a numerical method to be highly capable to deal with the complex nature of the rock material, and to accommodate all the essential phenomena involved in rock-drill bit dynamic interaction process, is an instructive task. This numerical method can be further exploited to predict the effectiveness of deep hole drilling projects and consequently as a design tool for the research and development sectors of the petroleum industries.

Chapter 2

Goals and outline of the thesis

This PhD thesis presents experimental and numerical investigations in the rock mechanics domain with the focus on the oil and gas requirements. The first objective of this PhD project is to develop a numerical method that is able to predict precisely all the failure types occurring in the dynamic drill bit-rock interaction problems involved mostly in the field of petroleum engineering.

The outline of this thesis is as follows: The *part II* of this thesis, called "state-of-the-art", considers the rock strength and failure criteria. A full description regarding the geotechnical constitutive modelling which are implemented in the numerical simulations of this research work is then provided in the second chapter of *part II*. An introduction about different numerical modelling technique, i.e. FEM and SPH is then presented in the last chapter of this part.

Berea sandstone is widely recognized by the petroleum industry as a standard rock type in oil & gas reservoir engineering (Busetti et al., 2012; Cheon et al., 2016; Hart and Wang, 1995; Menéndez et al., 1996). This rock is a highly porous and permeable sedimentary rock which is deposited sub-aqueously as an offshore bed in many well drilling applications (Hamilton, 1979; Khodja et al., 2010; Pepper, 1954). However, it is not a highly accessible material resulting in a relatively high expense for testing purposes. An extensive literature review (Coli et al., 2002; Coli et al., 2003; Coli et al., 2006) revealed the presence of another rock material, called Pietra Serena sandstone, with mechanical properties similar to Berea sandstone. These properties lead the authors to carry out extensive studies of the geotechnical investigations to obtain the mechanical response of Pietra Serena under: the uniaxial compression test (Mardalizad et al., 2018b), the Brazilian (quasi-static) tensile splitting test (Mardalizad et al., 2017a), the Flexural test (Mardalizad et al., 2017c), the triaxial compression test, the punch penetration test and the dynamic Brazilian disk test. These experimental tests are exploited either for the material parameter identification or validation of the numerical results. The experimental procedures are explained in detail in *part III* of this PhD thesis, so that they may also provide a useful validation problem for scientists and engineers who are developing a numerical model in this field.

The material model chosen for the numerical simulation of this study is the Karagozian & Case Concrete (KCC) model which is originally developed by Malvar et al. (Malvar et al., 1996; Malvar et al., 2000b; Malvar et al., 1994; Malvar et al., 1997). The KCC is an advance material model, which is implemented in LS-DYNA software. It consists of three-fixed strength surfaces and an experimental-tabular damage function in conjunction with an equation of state.

A recent feature provided in the third release of this material model which is the automatic input parameter generation capability based solely on the unconfined compression strength (Malvar et al., 2000b). This makes the use of the KCC model easier and accessible to most users, since there is no need to carry out extensive material characterization tests. This automatic method was used initially within this PhD project and the results are published in (Mardalizad et al., 2016; Mardalizad et al., 2017a; Mardalizad et al., 2017b), however, the numerical results related to these studies are not reported in this PhD thesis. The KCC model was originally developed to analyse the mechanical behaviour of concrete, and although the response of sandstone is expected to be similar to concrete, the results of the automatic input generation mode are only a rough estimation for sandstones.

A mixed experimental-numerical approach for the calibration of this material model for other types of quasi-brittle material, i.e. sandstone is proposed in the first chapter of *part IV* of this PhD thesis. For this purpose, two experimental tests, i.e. triaxial compression and Brazilian disk tests, were performed. Inspired by the studies of (Wu et al., 2017), a modification resulting in tabular damage function of the KCC model is also presented in this chapter. Although the suggested tabular damage function is provided for Pietra Serena, the suggested method can be used to find these tabular damage data for the other materials. The proposed formulation by (Malvar and Crawford, 1998) is considered in this PhD research to determine the effect of strain rate enhancement. To find the parameters of this model, the Curve Fitting Toolbox of MATLAB software is implemented to the corresponding experimental results of the dynamic Brazilian disk test (which is described in *Part III*).

Several numerical models developed in the second chapter of the *part IV* by considering the fully calibrated-modified KCC material model. The numerical results are then critically discussed by compared with other numerical models, i.e. Mohr-Coulomb plasticity model and extended (linear) Drucker-Prager model, and also with the experimental results. These critical comparisons prove that this material modelling technique provide a precise framework to describe constitutive behavior of rock material under several loading conditions (triaxial load, failure, dynamic indentation, etc). The

capability of a constitutive model to deal with a wide range of loading condition is an important aspect for the transferability of the methods in numerical analyses; this aspect is also addressed in the present part.

In the last chapter of *part IV*, inspired by the study of (Bresciani et al., 2016), an innovative approach was implemented which is called here the FEM-coupled to-SPH method. This method, which takes advantages of both the FEM and the SPH methods, erodes the elements who meet a certain failure criterion and subsequently replaces them with a specific number of SPH particles. Three different numerical techniques were applied to simulate the rock material during the penetration test: (a) constant stress FEM, (b) fully integrated FEM, and (c) coupled FEM-SPH method. The investigation provided in this chapter prove that the FEM-SPH method can clearly be considered the most realistic one among the tested methods. Hence, it can be considered as an adequate numerical technique to study the rock-bit interaction problems.

The *part V* is dedicated to the numerical studies which focus on practical issues in designing offshore deep hole drilling of real projects in the field of oil and gas industries. In the first chapter of *part V* a double button-bit penetration problem into a rock specimen at a certain depth below the seabed is investigated. The effect of two design parameters are studied in these simulations, which are: the effect of two button distances, and the effect of different in-situ pressures. Then, the percussive rock drilling at a certain depth below the seabed is investigated numerically in the last chapter, with focus on three different designing parameters, i.e. impact velocity, drilling in different depth and effect of in-situ pressures.

The *part IV* contains the last chapter of this PhD thesis and provides a conclusion by summing up the contents of this research work and debating the major achievements. Some possible future research topics are also proposed in this chapter. Finally, the full experimental results of the dynamic Brazilian disk test are presented in *Appendix A*.

Part II

State of the art

Chapter 3

Rock strength and failure criteria

The general mechanical response of a rock under a compression loading test is indicated in Figure 2. As can be seen the stress-strain diagram is divided into five sections. The first inelastic (concave-upward) section corresponds to the pores and fissures closing phase after applying the initial deviatoric stress. This section is followed in most of rocks by a linear trend related to the elastic behavior of the material. By further loading, at point B, the initiation of new cracks at high stressed areas (usually close to the middle section of the specimen) as well as the extension of the old cracks (parallel to the loading direction) cause the increase of Poisson's ratio. In the third section of Figure 2 (between points B and C) the crack propagation is stable which means the crack length increases after each stress increment to a certain level and then stops. Eventually after point C, which is called the yield strength, the density of microcracks is increased and a semi-continuous rupture surface is developed due to the unstable crack propagation, which is the reason of non-linear (convex-upward) behavior in fourth section.

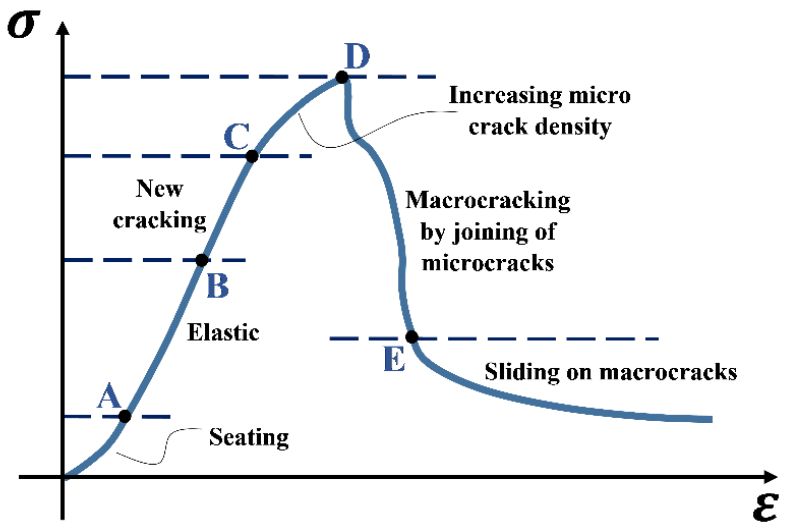

Figure 2. Typical stress-strain curve of unconfined compression test (Goodman, 1989)

The point D is considered as the ultimate strength of rocks which is usually studied by most of the failure criterions (Goodman, 1989). The post-peak behavior of brittle

rock under unconfined compression test is often observed to stop after a sudden rupture due to creation of macrocracks by joining the microcracks. However, in case of using a very stiff testing machine, the test may proceed to point E or beyond (Hudson and Harrison, 2000).

The geological materials reveal a very complex mechanical behaviour due to several issues; i.e. pressure (first invariant) dependency, hardening (and/or softening), yield failure, different tension-compression behaviour, complex volumetric strain, high dependency on environment condition (i.e. confining pressure), etc.

The Figure 3 indicates the failure surface of a typical geological material in the compressive meridional. As can be seen, the curve of failure surface behaves significantly different in tension and compression regimes, so that the compressive strength is often one order of magnitude higher than the tensile strength.

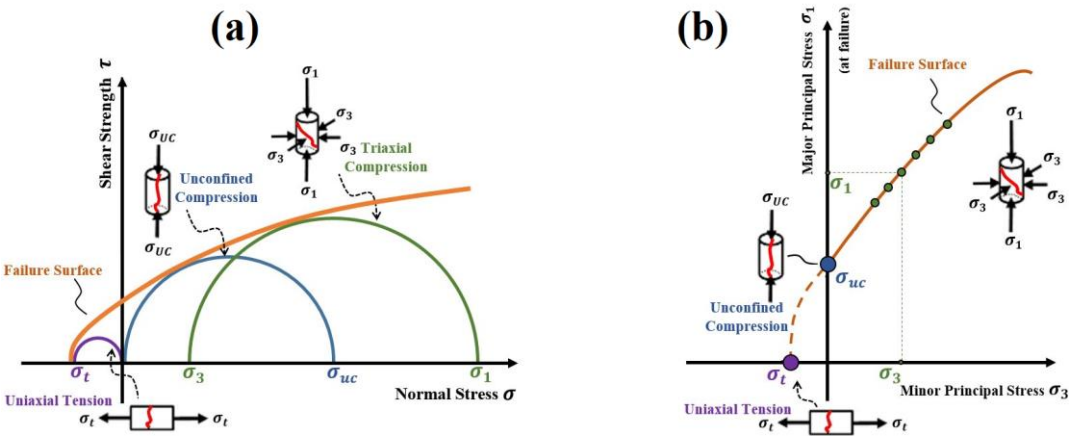

Figure 3. the failure surface for different state of stress of geomaterials; (a) $\tau - \sigma$ plane and (b) $\sigma_1 - \sigma_3$ plane.

The variations of load arrangements are such than it is difficult to find a single mode of rock failure predominates. However, in order to investigate the mixed failure modes, it is essential to study single failure modes separately. The different failure modes are also represented in the Figure 3, where the flexure, compressive and shear failure mode are related to the tension, unconfined compression and triaxial compression loadings, respectively. The following represents three common failure mode of geomaterials (Goodman, 1989).

- **Flexural (or tensile splitting) failure mode:** This mode refers to bending failure with tensile cracks propagation. It can also occur in rock slopes with steeply dipping layers as the layers' overturn toward the free space. This mode is predominant in Brazilian and Flexural test (see Figure 4).

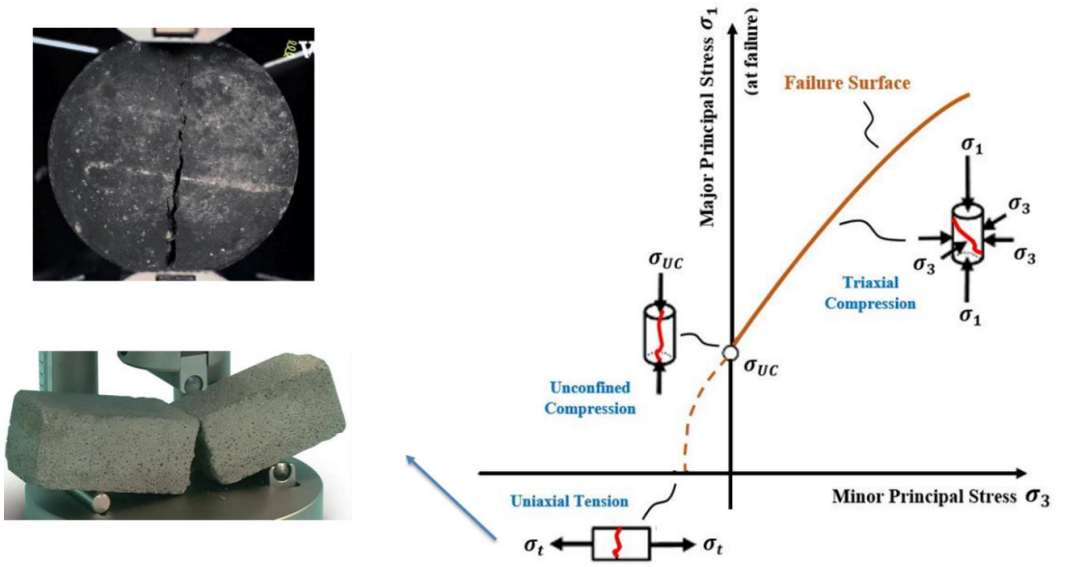

Figure 4. flexure failure mode in rock mechanics.

- **Shear:** It refers to formation of a surface of rupture where the shear stresses have become critical, followed by release of the shear stress as the rock suffers a displacement along the rupture surface. This mode is predominant in triaxial compression test (see Figure 5).

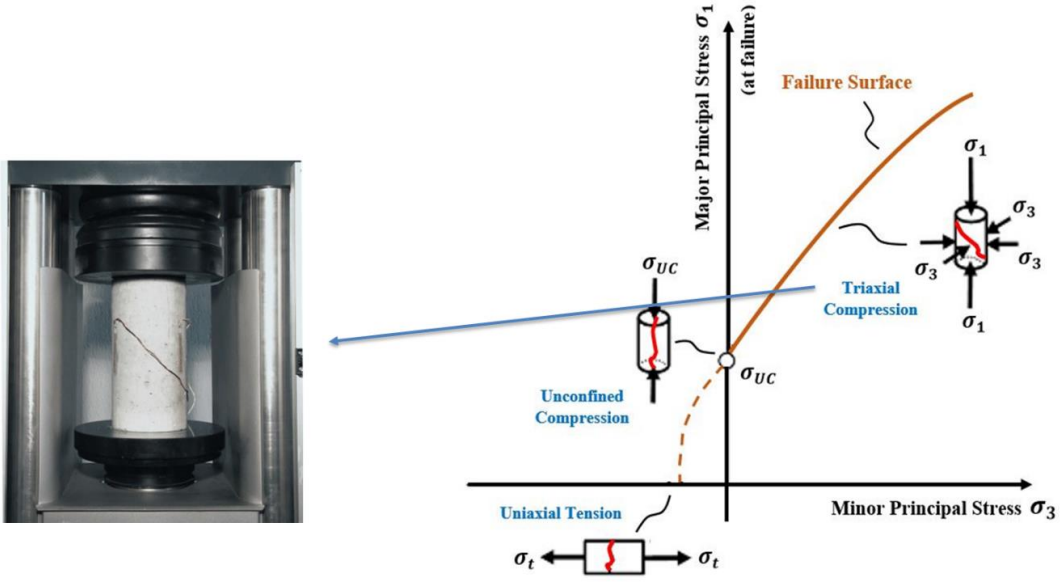

Figure 5. shear failure mode in rock mechanics.

- **Crushing or compression failure mode:** This type of failure occurs in intensely shortened volumes or rock penetrated by a stiff punch. However,

examination of processes of crushing shows it to be a highly complex mode, including formation of tensile cracks and their growth and interaction through flexure and shear. This mode is predominant in uniaxial compression test (see Figure 6)

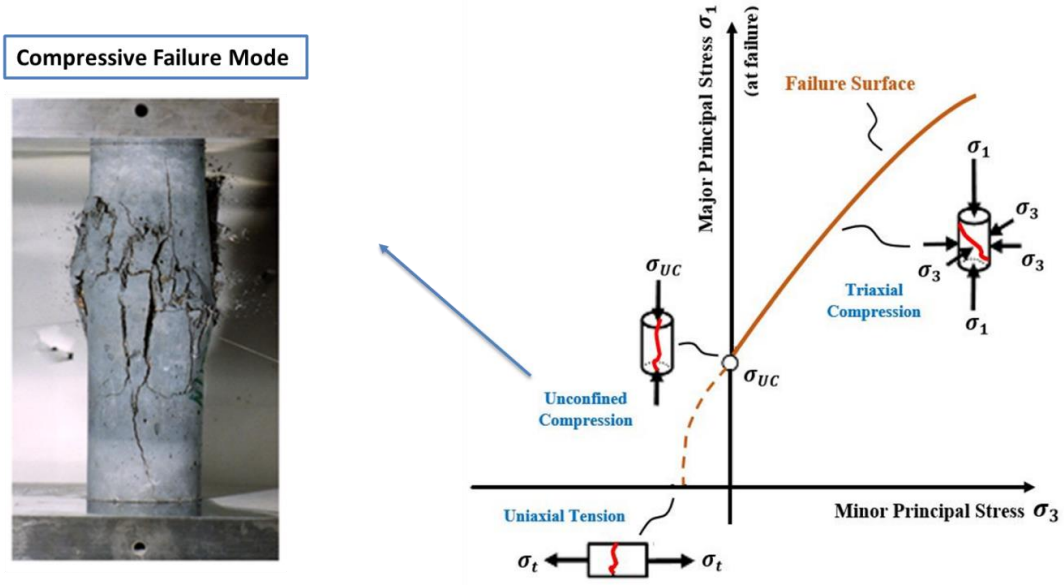

Figure 6. compression failure mode in rock mechanics.

Chapter 4

Constitutive modelling of geomaterials

The constitutive models in geomaterial plasticity are often based on an initial yield surface which is coupled with a hardening rule. The subsequent yield surfaces will expand as the loading increases, so that finally match with the failure surface. There are many research studies to investigate and define the failure function, which accordingly leads to describe the failure surface of the geomaterial. The key feature of yielding of cohesive-frictional soil and rock materials is their mean pressure dependence. The experimental studies show that the failure surfaces of rock materials are curved and have smooth meridians. It is more convenient to define the failure surfaces in the Haigh-Westergaard 3D stress space due to its cylindrical coordinate system. It is possible to use the equation (1) to transform the cartesian coordinate system of principal stress into the Haigh-Westergaard system.

$$\begin{bmatrix}\sigma_1\\ \sigma_2\\ \sigma_3\end{bmatrix}=\frac{1}{\sqrt{3}}\begin{bmatrix}\xi\\ \xi\\ \xi\end{bmatrix}+\sqrt{\frac{2}{3}}\,\rho\begin{bmatrix}\cos\theta\\ \cos(\theta-2\pi/3)\\ \cos(\theta+2\pi/3)\end{bmatrix} \tag{1}$$

Where, the ξ, ρ and θ are the Haigh-Westergaard coordinates defined as equation (2).

$$\begin{cases}\xi=\dfrac{1}{\sqrt{3}}I_1=\sqrt{3}\,p\\ \rho=\sqrt{2J_2}=\sqrt{\dfrac{2}{3}}\,\sigma_{eq} & \left[\sigma_{eq}=q\right]\\ \cos(3\theta)=\left(\dfrac{r}{q}\right)^3=\dfrac{3\sqrt{3}}{2}\dfrac{J_3}{J_2^{3/2}} & \left[r=3\left(\dfrac{1}{2}J_3\right)^{1/3}\right]\end{cases} \tag{2}$$

Where, I_1 is the first principal invariant of the Cauchy stress, J_2 and J_3 are the second and third principal invariants of the deviatoric part of the Cauchy stress, respectively.

4.1 Mohr-Coulomb Plasticity model

The yield function of this material model is based on the conventional Mohr-Coulomb (MC) which is one of the most widely used constitutive laws to deal with brittle materials, and in particular rock mechanics (see Figure 7). The implementation of Mohr-Coulomb material model was investigated by ABAQUS/Explicit software within this study. The conventional yield criterion which is proposed by (Coulomb, 1773) is in terms of shear stress τ and normal stress σ_n acting on a plane. This model suggests that the yielding begins if the shear stress and the normal stress satisfy the equation (3).

$$|\tau| = c + \sigma_n \tan\varphi \tag{3}$$

Where, c and φ are the cohesion and internal friction angle of geomaterials, respectively. Equation (4) expresses the MC's yield criterion in terms of the principal stresses, when $\sigma_1 \geq \sigma_2 \geq \sigma_3$.

$$|\tau| = c + \sigma_n \tan\varphi \tag{4}$$

It is possible to use the matrices of equation (1) to transform the equation (4) from principal coordinate system into Haigh-Westergaard one, according to equation (5).

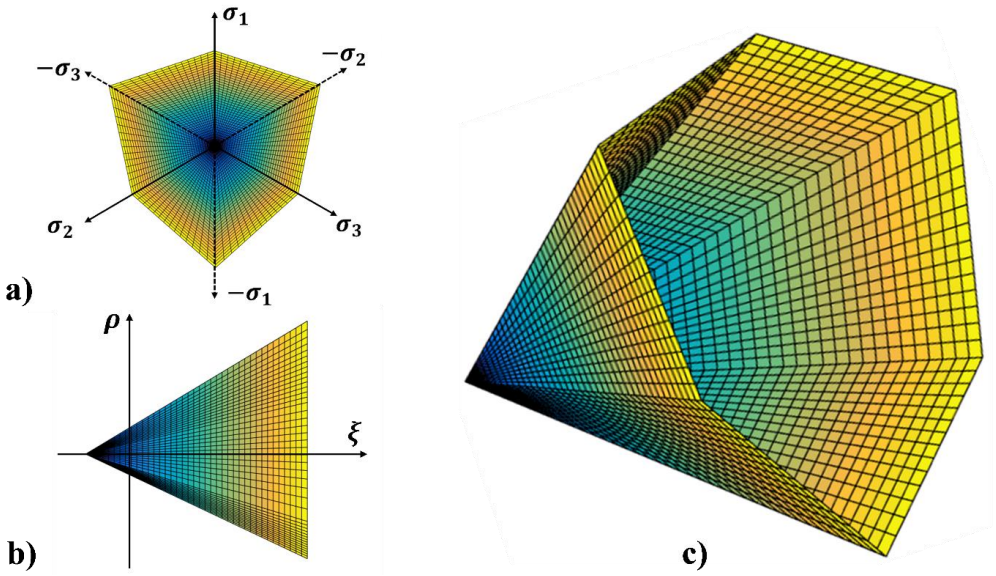

Figure 7. The Mohr-Coulomb failure surface; (a) deviatoric plane, (b) Rendulic plane, and (c) 3D stress space.

$$f(\rho,\theta,\xi)=\left[\sqrt{3}\sin(\theta+\pi/3)-\sin\varphi\cos(\theta+\pi/3)\right]\rho-\left(\sqrt{2}\sin\varphi\right)\xi-\sqrt{6}\,c(\epsilon_p)\cos\varphi=0 \quad (5)$$

The Mohr-Coulomb plasticity implemented in ABAQUS takes advantage of an isotropic cohesion hardening model. It is possible to define the unconfined compressive stress σ_{uc} as a function of the absolute plastic strain ε_p by the tabular data from the compression post-yield stress-strain diagram. Accordingly, the cohesion yield stress $c(\varepsilon_p)$ values can be computed by equation (6).

$$c(\epsilon_p)=\left(\frac{1-\sin\varphi}{2\cos\varphi}\right)\gamma\,\sigma_{uc}(\epsilon_p) \quad (6)$$

Where, γ is a parameter to adjust the value of the cohesion for improving the accuracy of the numerical models. The projection of Mohr-Coulomb model on the Rendulic plane $(\rho-\xi)$ and the deviatoric plane $(\rho-\theta)$ are indicated in Figure 8a and Figure 8b, respectively. Because of Lode effect, this model has an irregular hexagonal surface in the deviatoric plane. This surface can be defined by ρ_{c_0} and ρ_{t_0}, which are the maximum magnitude (at yield) of the deviatoric stresses in uniaxial compression and tension, respectively. These two values are given by equations (7) and (8).

$$\rho_{c_0}=f_c'\left(\sqrt{6}\,\frac{1-\sin\varphi}{3-\cos\varphi}\right) \quad (7)$$

$$\rho_{t_0}=f_c'\left(\sqrt{6}\,\frac{1-\sin\varphi}{3+\cos\varphi}\right) \quad (8)$$

Where, f_c' is the unconfined compression strength. As can be seen in Figure 8, the internal friction angle φ can vary from 0° to 90°. These two limiting cases correspond to Tresca and Rankine yield functions, respectively. The experimental tests show that the results obtained by Mohr-Coulomb criterion are usually overestimated than the experimental data in the tensile regime. Therefore, ABAQUS provides the opportunity to optionally define a Rankine yield function f_t as the tension cut-off criterion according to equation (9).

$$f_t(\rho,\theta,\xi)=\left(\sqrt{2}\cos\theta\right)\rho-\xi-\sqrt{3}\,t_c\left(\bar{\epsilon}_p^{\,t}\right)=0 \quad (9)$$

Where, t_c is the value of tension cut-off, which is equal to the value of the yield stress in the uniaxial tension. ABAQUS allows to define an optional softening (or

hardening) of Rankine yield surface by providing the values of tension cut-off t_c as a function of tensile equivalent plastic strain $\bar{\epsilon}_p^{\,t}$ (in the form of tabular data).

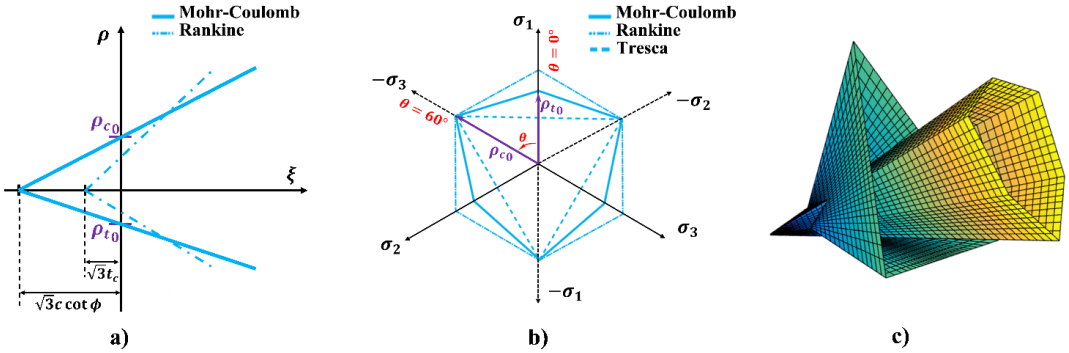

Figure 8. Comparison of MC and Rankine criteria; (a) Rendulic plane, (b) deviatoric plane, and (c) 3D stress space.

Both Mohr-Coulomb yield surface and Rankine tension cut-off have corners in the stress space that causes numerical complications. Two smooth elliptic functions are implemented in ABAQUS as the flow potential rules of these models. The plastic flow of Mohr-Coulomb is constructed by means of a continuous flow potential function G_{mw} proposed in (Menetrey and Willam, 1995), which is characterised as a hyperbolic and smooth elliptic function in the Rendulic and deviatoric planes, respectively (see Figure 9). The Menétrey and Willam's flow, which ensures the direction of the plastic strain flow can be always uniquely defined, is given by equation (10).

$$G_{mw} = \sqrt{\left(\in c_0 \tan\psi\right)^2 + \left(R_{mw}\, q\right)^2} - p\tan\psi \qquad (10)$$

Where, ψ is the friction angle, c_0 is the initial cohesion yield stress and the parameter $\in$, called meridional eccentricity, expresses how much the hyperbolic function of this flow potential tends to the asymptote. The ABAQUS default value ($\in$=0.1) was used in all the models of this research study. The parameter $R_{mw}q$, termed as Menétrey and Willam's equivalent stress, can be described as equation (11).

$$R_{mw}(\theta,e)\, q = \left[\frac{4\left(1-e^2\right)\cos^2\theta + \left(2e-1\right)^2}{2\left(1-e^2\right)\cos\theta + \left(2e-1\right)\sqrt{4\left(1-e^2\right)\cos^2\theta + 5e^2 - 4e}}\right]\left(\frac{3-\sin\theta}{6\cos\theta}\right)q \qquad (11)$$

The parameter e, known as deviatoric eccentricity, indicates how much the elliptic function is out of roundness. Indeed, this parameter considers the ratio between the

shear stress along the extension and compression meridians and can be calculated according to the equation (12).

$$e = \frac{3 - \sin\varphi}{3 + \sin\varphi} \tag{12}$$

It is also possible to define "*e*" as an independent material parameter by directly providing its value into ABAQUS. To keep the Menétrey and Willam elliptic function in the deviatoric plane, the value of "*e*" is required to be limited between 0.5 and 1. It is worth to mention that these two values refer to two extreme cases of Rankine triangle (φ = 90°) and Mises circle (φ = 0°) in the deviatoric plane. However, in this study, the deviatoric eccentricity doesn't consider as an input parameter and it is determined automatically by ABAQUS.

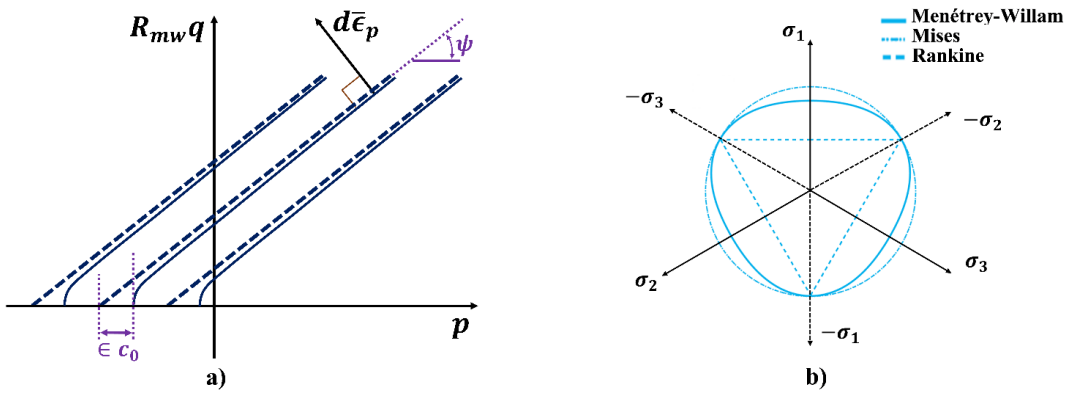

Figure 9. The Menétrey-Willam flow potential; (a) $R_{mw}q - p$ plane, (b) deviatoric plane (Menetrey and Willam, 1995).

The plastic flow provided by this model is always non-associative in the deviatoric plane. Although the plastic flow in the meridional is generally non-associative, it is possible to obtain the associativity by setting $\psi = \beta$ and very small meridional eccentricity. A nearly associative plastic flow is considered in ABAQUS for the Rankine surface by means of a modified Menétrey and Willam flow potential function G_t according to the equation (13).

$$G_t = \sqrt{\left(\epsilon_t\, \sigma_{t_0}\right)^2 + \left(R_t\, q\right)^2} - p \tag{13}$$

The parameter ϵ_t has similar definition to ϵ (with the same default value ϵ=0.1, which is used in all the models of this study). The parameter R_t is calculated by equation (14).

$$R_t(\theta, e_t) = \frac{1}{3}\left[\frac{4\left(1-e_t^{\,2}\right)\cos^2\theta + \left(2e_t - 1\right)^2}{2\left(1-e_t^{\,2}\right)\cos\theta + \left(2e_t - 1\right)\sqrt{4\left(1-e_t^{\,2}\right)\cos^2\theta + 5e_t^{\,2} - 4e_t}}\right] \tag{14}$$

Where, e_t has the same meaning as *e*, while the default values of ABAQUS for these parameter ($e_t = 0.6$) are different. In this study, both the Mohr-Coulomb plasticity and the Linear Drucker-Prager failure criteria are intended as a yield surface, i.e. the plastic flow occurs when equations (5) and (18) are satisfied. Hardening (intended as hardening followed by softening) of the yield function is described by the equation proposed by (Lubliner et al., 1989) for concrete as defined in equation (15).

$$\sigma_{uc}\left(\epsilon_p\right) = \sigma_y\left[(1+a)\cdot\exp(-b\cdot\epsilon_p) - a\cdot\exp(-2b\cdot\epsilon_p)\right] \tag{15}$$

Equation (15) expresses the unconfined compressive stress σ_{uc} as a function of the axial plastic strain ε_p. The parameter σ_y is the yield strength and the parameters *a* and *b* can be defined according to the equations (16) and (17), respectively.

$$a = \left(\frac{f_c'}{\sigma_y}\right) - 1 + 2\sqrt{\left(\frac{f_c'}{\sigma_y}\right)^2 - \left(\frac{f_c'}{\sigma_y}\right)} \tag{16}$$

$$b = -\left(\overline{\epsilon_p} \Big/ \ln\frac{1+a}{a}\right) \tag{17}$$

The plastic strain at equation (17), $\overline{\epsilon_p}$ (to define the parameter *b*) is determined when the derivative of equation (15) is equal to zero. This plastic strain corresponds to the experimental data at which the maximum stress is reached.

4.2 Drucker-Prager extended model

This is an advanced material model implemented by ABAQUS, which is based on the conventional Drucker-Prager constitutive law. There are three forms of the extended Drucker-Prager material model developed in ABAQUS which are the linear, the hyperbolic and the general exponential forms (Manual, 2009). Within this research work, the linear form of this model was investigated. The linear Drucker-Prager (LDP) model consists of a pressure-dependent three-invariant failure surface which provides the opportunity of having the non-circular yield surface (unlike the conventional

Drucker-Prager) in the deviatoric plane (see Figure 10). This model also takes advantage of the associated inelastic flow and hardening (or softening) rules, and different dilation and friction angles. The general form of the failure surface in the Haigh-Westergaard coordinate system is given by equation (18).

$$f = f(\xi,\rho,\theta) = t(\rho,\theta) - \frac{\tan\beta}{\sqrt{3}}\xi - d(\epsilon_p) \tag{18}$$

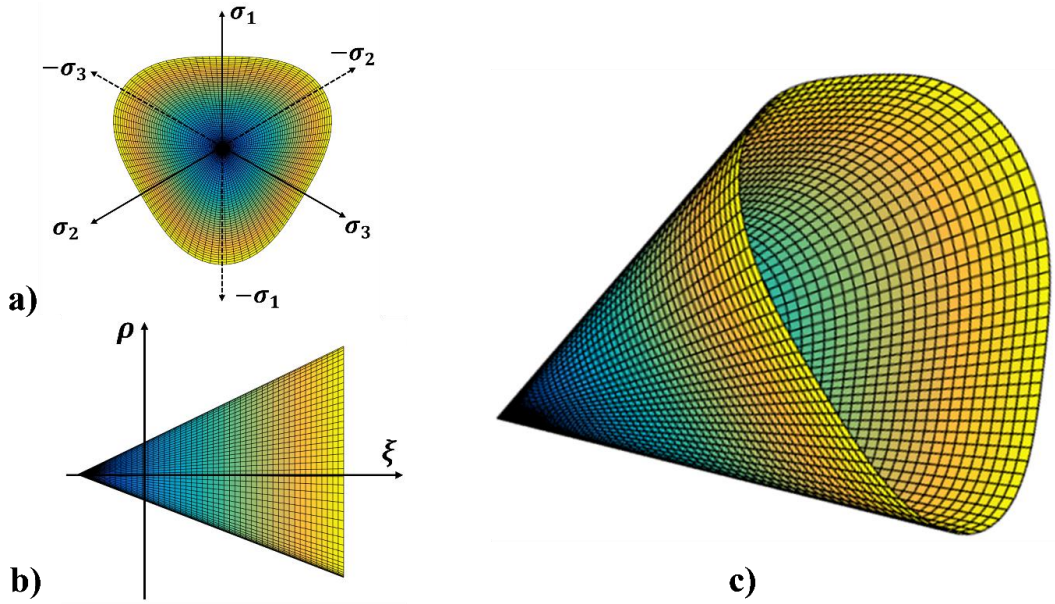

Figure 10. The Linear Drucker-Prager failure surface; (a) deviatoric plane, (b) Rendulic plane, and (c) 3D stress space.

The effect of the Lode angle θ is considered by $t(\rho,\theta)$ according to the equation (19).

$$t(\rho,\theta) = \sqrt{\frac{3}{8}}\left[\left(1+\frac{1}{K}\right) - \left(1-\frac{1}{K}\right)\cos 3\theta\right]\rho \tag{19}$$

Where, the material parameter K is defined as the ratio of yield stresses at triaxial tension to triaxial compression, which means it controls the shape of the linear Drucker-Prager yield function at the deviatoric plane. As can be seen in Figure 11b, a circular failure function presents in the deviatoric plane when *K=1.0*, which is the same as the conventional Drucker-Prager. It is proved that to verify the convexity of the yield function, the value of parameter K should be in the range of 0.778 to 1.0. By means of an approach to match the parameters of the Mohr-Coulomb and linear Drucker-Prager (for materials with low friction angles), K can be defined according to equation (20).

$$K = \frac{3 - \sin\varphi}{3 + \sin\varphi} \tag{20}$$

where, φ is the internal friction angle used in the Mohr-Coulomb model. The parameter β is commonly termed as the friction angle (in case of dealing with the Drucker-Prager theory), which can be computed as the slope of the yield function in the t – p meridian plane (see Figure 11a). By a similar computing approach for K, it is possible to derive the parameter β according to equation (21).

$$\beta = \arctan\left(\frac{6\sin\varphi}{3 - \sin\varphi}\right) \tag{21}$$

It is worth mentioning that both these parameters can be defined in ABAQUS as a function of temperature and other field variables (e.g. temperature, etc.). However, they are considered as constant variables in this study because of the negligible effect of the other fields.

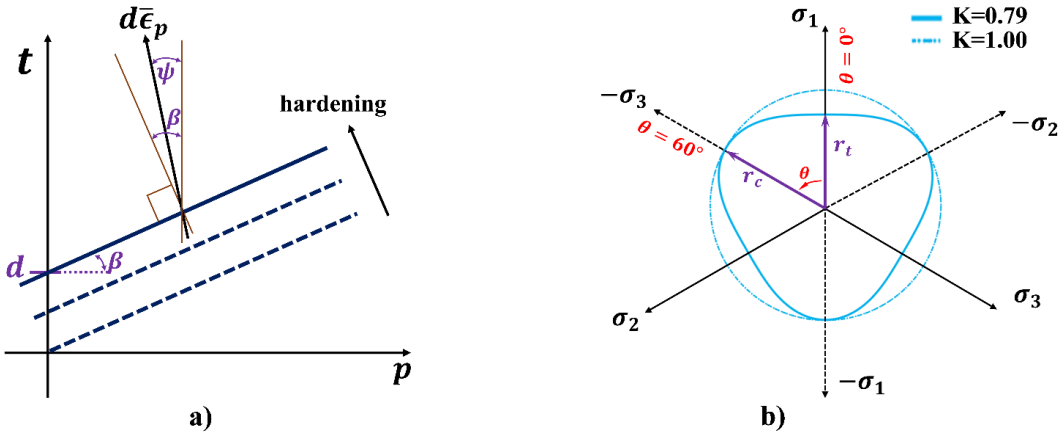

Figure 11. The linear Drucker-Prager criterion; (a) t – p plane, (b) deviatoric plane.

The parameters r_c and r_t in Figure 11a are the distances of Drucker-Prager failure surface from the hydrostatic pressure axis at compressive and tensile meridians, respectively. The parameter d, called the cohesion of the material (in case of dealing with the Drucker-Prager model), is defined automatically by ABAQUS according to equation (22).

$$d\left(\epsilon_p\right) = \left(1 - \frac{1}{3}\tan\beta\right)\sigma_{uc}\left(\epsilon_p\right) \tag{22}$$

Where, σ_{uc} is the unconfined (uniaxial) compression stress. An isotropic hardening is implemented for this model in ABAQUS by a *sub-option* called "Drucker-Prager Hardening" at the property module. Therefore, the tabular data from the compression post-yield stress-strain diagram can be used to define σ_{uc} (and accordingly *d*) as a function of the absolute plastic strain ε_p. The plastic flow of the linear Drucker-Prager is considered by means of a flow potential function G_{LDP} given by equation (23).

$$G_{LDP} = t - p\tan\psi \tag{23}$$

The parameter ψ, called dilation angle, specifies the direction of the plastic strain flow. As can be seen in Figure 11a, the plastic flow is associative if $\psi = \beta$, otherwise it is non-associative. The same hardening function, equation (15), described in Mohr-Coulomb material model is developed for the Linear Drucker-Prager model as well.

4.3 Karagozian and Case Concrete model

This material model, also known as the "Karagozian and Case Concrete (KCC or K&C)" model, was developed by Malvar et al. from 1994 to 2000 (Malvar et al., 2000a; Malvar et al., 1996; Malvar et al., 1994; Malvar et al., 1997). The failure function of the KCC material model, implemented in LS-DYNA, is characterized by a pressure-dependent yield surface $\Phi(\rho,\theta,\xi,\lambda)$ formulated as equation (24) in terms of the Haigh-Westergaard stress invariants.

$$\Phi(\rho,\theta,\xi,\lambda) = \sqrt{3/2}\ \rho - \varphi(\theta,\xi,\lambda) \tag{24}$$

Where, the λ is the KCC – damage parameter. Based on the equation (24), it is possible to categorize the KCC material model as the constitutive models with hybrid formulation $\Phi(\rho,\theta,\xi) = \Phi(\rho) - \Phi(\xi)\Phi(\theta,\xi)$, since the deviatoric function is decoupled (and discussed below, the shape of the Lode function is changed in a different range of the hydrostatic pressure).

The failure surface of the KCC model $\varphi(\theta,\xi,\lambda)$ is a dynamic function of the current values computed for a specific set of state variables that specify the strength of the material. The term *dynamic* means the failure surface is computed by means of the linear interpolation functions that uses a pair of fixed- and independent- strength

surfaces which are defined by the user. These interpolation functions are different for hardening and softening. The pair for hardening and softening is denoted as the yield-maximum and maximum-residual strength surfaces, respectively. Therefore, the $\varphi(\theta,\xi,\lambda)$ function can be described by the equation (25).

$$\varphi(\theta,\xi,\lambda)=\begin{cases} if\ \ \lambda\le\lambda_0; & r_f\hat{r}[\Psi(p),\theta]\left[\hat{\sigma}_y(p)\right] \\ if\ \ \lambda_0\le\lambda\le\lambda_m; & r_f\hat{r}[\Psi(p),\theta]\left[\eta(\lambda)\left[\hat{\sigma}_m(p)-\hat{\sigma}_y(p)\right]+\hat{\sigma}_y(p)\right] \\ if\ \ \lambda_m\le\lambda; & r_f\hat{r}[\Psi(p),\theta]\left[\eta(\lambda)\left[\hat{\sigma}_m(p)-\hat{\sigma}_r(p)\right]+\hat{\sigma}_r(p)\right] \end{cases} \quad (25)$$

The parameters λ_0 and λ_m corresponds to the points at which the hardening and softening regime are started, respectively. The parameter r_f considers the strain rate enhancement. The parameters $\hat{\sigma}_y(p)$, $\hat{\sigma}_m(p)$ and $\hat{\sigma}_r(p)$ correspond with the three fixed strength surfaces in the triaxial compression state of stress, when the Lode angle θ is equal to 60° (see Figure 12). The $\eta(\lambda)$ is the interpolation damage function, and the non-dimensional function $\hat{r}[\Psi(p),\theta]$ is the ratio between the current radius of the failure surface $r(\theta)$ (see Figure 13b) and the compressive meridian.

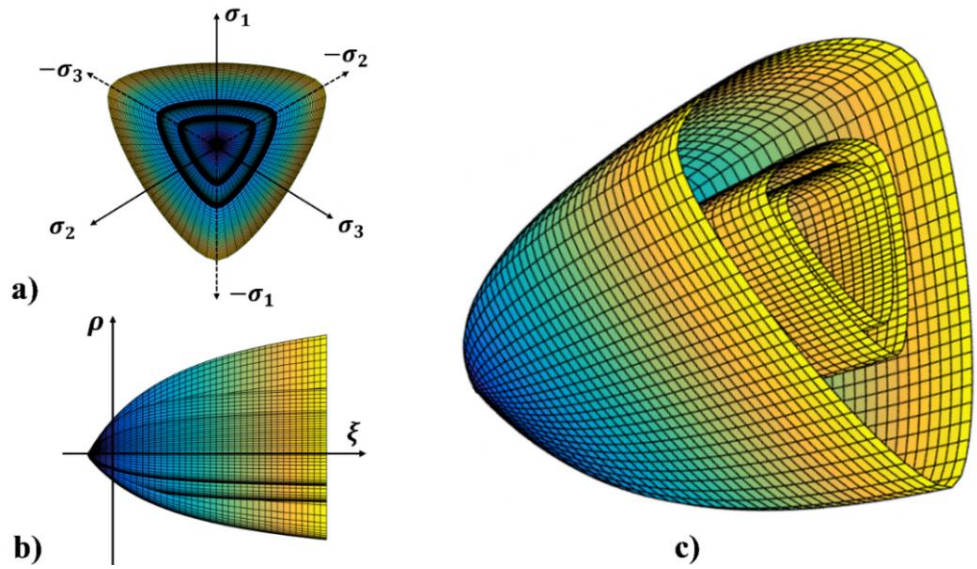

Figure 12. The KCC fixed – strength surfaces; (a) deviatoric plane, (b) Rendulic plane, and (c) 3D stress space.

As written in equation (25), the KCC material model considers the effect of the third invariant, i.e. the Lode angle θ, by means of the function $\hat{r}[\Psi(p),\theta]$. This function was

originally derived from equation (26), which is the shape of the failure criterion in the deviatoric plane, proposed by (Willam and Warnke, 1975).

$$r(\theta)=\frac{2r_c(r_c^{\,2}-r_t^{\,2})\cos\theta+r_c(2r_t-r_c)\sqrt{4(r_c^{\,2}-r_t^{\,2})\cos^2\theta+5r_t^{\,2}-4r_tr_c}}{4(r_c^{\,2}-r_t^{\,2})\cos^2\theta+(2r_t-r_c)^2} \tag{26}$$

Where, $r(\theta)$ determines the distance of the failure surface at the deviatoric section by considering the effect of the Lode angle θ. The parameters r_c and r_t express the distances of the failure surfaces from the hydrostatic axis at the compressive and tensile meridian, respectively. The deviatoric plane of a Willam-Warnke failure model is indicated in Figure 13b.

The $\hat{r}[\Psi(p),\theta]$, which is the ratio between the current radius of the failure surface $r(\theta)$ and the distance of the failure surfaces from the hydrostatic axis at the compressive meridian r_c, is computed by means of the equation (27). This equation was obtained by dividing both sides of equation (26) by r_c. In order to present the term $\Psi(p)$, which is a strength index of the brittle material related to the confining pressure that a material is subjected to it (and equal to $\Delta\sigma_t/\Delta\sigma_c$ - in the KCC model also equal to r_t/r_c), both the numerator and the denominator of the right-hand side of equation are divided by $r_c^{\,2}$.

$$\hat{r}[\Psi(p),\theta]=\frac{r(\theta)}{r_c}=\frac{2(1-\Psi^2)\cos\theta+(2\Psi-1)\sqrt{4(1-\Psi^2)\cos^2\theta+5\Psi^2-4\Psi}}{4(1-\Psi^2)\cos^2\theta+(1-2\Psi)^2} \tag{27}$$

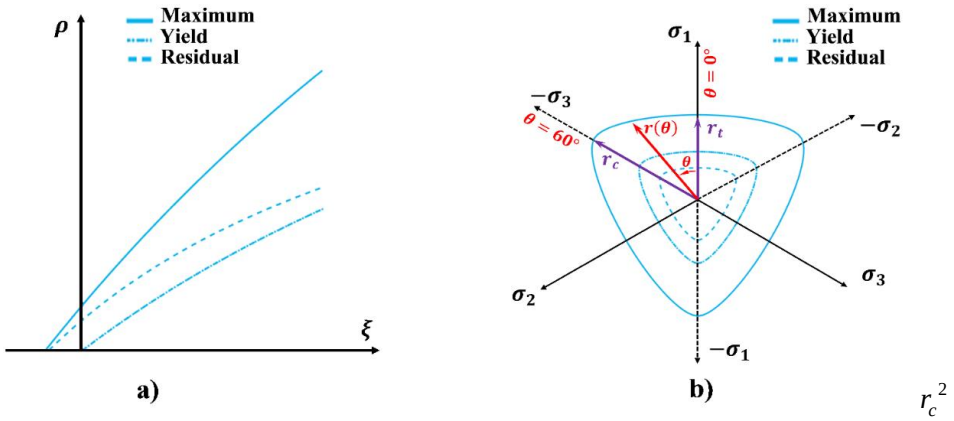

Figure 13. (a) KCC failure surfaces in a compressive meridian, (b) deviatoric section proposed by the Willam-Warnke model.

The fact that $\hat{r}$ is just a function of $\Psi(p)$ and θ, and that the lode angle can be determined based on the loading conditions, implies the role of $\Psi(p)$ for computational purposes. It means that the implementation of the failure surface is completed by means of this parameter $\Psi(p)$. This parameter generally depends on the hydrostatic stress and can be obtained empirically. Malvar et al. in (Malvar et al., 1997) defined this parameter as a linear piecewise function on the full range of pressure according to equation (28).

$$\Psi(p)=\begin{cases}\dfrac{1}{2}, & -f_t \le p \le 0\\ 1/2+3f_t/2\,f_c', & p=f_c'/3\\ \dfrac{\alpha f_c'}{a_0+\dfrac{2\alpha f_c'/3}{a_1+2a_2\alpha\, f_c'/3}}, & p=2\alpha f_c'/3\\ 0.753, & p=3f_c'\\ 1, & p\ge 8.45 f_c'\end{cases} \tag{28}$$

Where, f_c' is the unconfined compression strength, f_t is the principal tensile strength and α is an experimental parameter related to the biaxial compression test. According to equation (28), $\Psi(p)$ varies from 1⁄2 to 1, which is in accordance with the experimental data previously obtained. It also indicates that $p=8.45 f_c'$ is the transition point in which the compression meridian is equal to tension one, and accordingly from this point onwards, there is a circular failure surface on the deviatoric plan section. Moreover, it considers a value equal to 1⁄2 for the negative range of pressures. It is worth mentioning that this function was implemented in LS-DYNA and no input is required of the users.

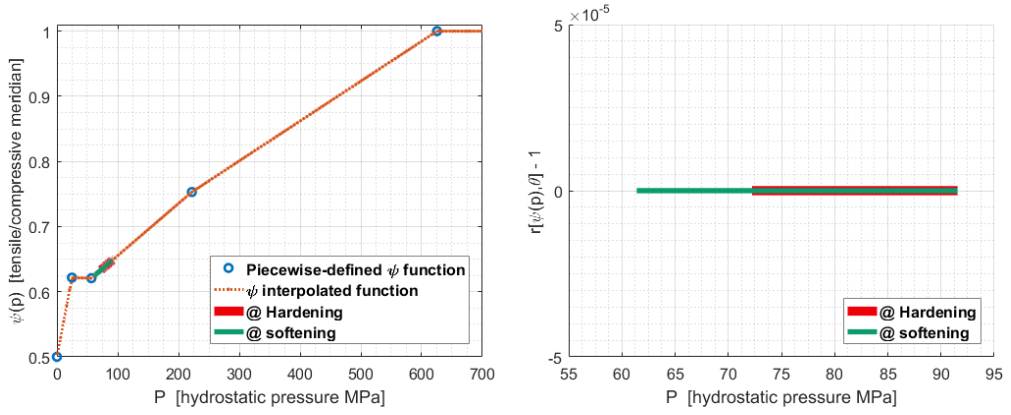

Figure 14. Investigation of the experimental data on; (a) $\Psi(p)-p$, and (b) $\hat{r}[\Psi(p),\theta]-p$ diagrams.

As a simple investigation, the experimental data of one of the triaxial compression tests (second test of 28 MPa confining pressure) is first calculated by equation (28) (see Figure 14a). Based on the corresponding value of $\Psi(p)$, the $\hat{r}[\Psi(p),\theta]$ function was calculated and it reached to unity for the whole hardening and softening regime, as expected ($\theta = 60°$) (see Figure 14b).

The Karagozian and Case concrete model takes advantage of the three-fixed independent failure surfaces in the compressive meridian ($\xi - \rho$ plane), which correspond to the yield, the ultimate and the residual strength of the material. The $\hat{\sigma}_y(p)$, $\hat{\sigma}_m(p)$ and $\hat{\sigma}_r(p)$ pressure-sensitive strength surfaces are defined as equations (29), (30) and (31), respectively (Mardalizad et al., 2018b).

$$\hat{\sigma}_y(p) = a_{0_y} + \frac{p}{a_{1_y} + a_{2_y} p} \quad \left[or \quad (\rho)_y = \sqrt{2/3}\, a_{0_y} + \frac{\sqrt{2}\,\xi}{3a_{1_y} + \sqrt{3}\, a_{2_y}\xi} \right] \tag{29}$$

$$\hat{\sigma}_m(p) = a_0 + \frac{p}{a_1 + a_2 p} \quad \left[or \quad (\rho)_m = \sqrt{2/3}\, a_0 + \frac{\sqrt{2}\,\xi}{3a_1 + \sqrt{3}\, a_2\xi} \right] \tag{30}$$

$$\hat{\sigma}_r(p) = \frac{p}{a_{1_f} + a_{2_f} p} \quad \left[or \quad (\rho)_r = \frac{\sqrt{2}\,\xi}{3a_{1_f} + \sqrt{3}\, a_{2_f}\xi} \right] \tag{31}$$

Where, the a_i – parameters are the user-defined input parameters to define the failure surfaces in the compressive meridian. The ξ in equation (24) is related to the pressure p which is calculated by the equation of state (EOS) to represent the volumetric responses. The damage evolution imparted by the KCC model to the material is depicted in the damage parameter λ, which reflects the magnitude of the plastic flow. In general, the plastic flow can be described as equation (32).

$$\dot{\varepsilon}^p = \dot{\mu} \frac{\partial g(\rho,\theta,\xi,\lambda)}{\partial \sigma} \tag{32}$$

The comprehensive expression of the parameter $\dot{\mu}$, which is the plasticity consistency parameter, can be found in detail in (Wu and Crawford, 2015). The partial-associative plastic potential of the KCC model $g(\rho,\theta,\xi,\lambda)$ can be expressed by equation (33).

$$g(\rho,\theta,\xi,\lambda) = \sqrt{3/2}\ \rho - \omega\varphi(\theta,\xi,\lambda) \tag{33}$$

The parameter ω in equation (33) is the associativity parameter that serves a significant role in identifying the proportionality between the deviatoric and volumetric

components of the plastic strain. This parameter is limited between the critical values of 0 and 1, which provides associative (normal to the failure surface) and Prandtl-Reuss (plastic volume strain is precluded) forms of plasticity, respectively.

Chapter 5

Numerical modelling techniques

The numerical modelling problems involved in the petroleum industries are mainly investigated by The Lagrangian Finite Element Method (FEM) due to its accuracy, maturity and computational efficiency. However, because of the mesh-based nature of this method, the performance of FEM in dealing with problems involving large deformation, and severe element distortion and fragmentation, are limited (Salagame and Belegundu, 1994). The fragmentation of quasi-brittle material and large deformations are widely existing phenomena in rock mechanics applications, such as rock cutting and blasting. Therefore, it is expected that particle-based methods can offer better performance in such applications.

One of these particle-based methods is the Smooth Particle Hydrodynamics (SPH) method (Monaghan, 1992), which has an inherent ability to deal with large deformation problems and complex physical phenomena. A significant feature of meshless methods is that they can be exploited to represent highly distortions in a Lagrangian framework, since a discrete set of disordered points is implemented to approximate the state variables and material properties (Limido et al., 2007).

Although the implementation of SPH particle method seems to be an adequate way to solve the problems of rock mechanics domain, its accuracy and computation time efficiency is significantly lower than the FEM. In the followings, the basics of both the FEM and the SPH methods are presented briefly. Then an innovative numerical technique is introduced which can take advantageous of both methods and, in the same time, is able to highly avoid their drawbacks.

5.1 Finite Element Method (FEM)

The equation of motion of a system can be described with an ordinary differential equation. Since there are no analytical methods to deal with nonlinear ordinary differential equations, a numerical technique should be implemented. The Finite Element Method is almost the most common numerical technique implemented in research fields as well as industrial applications. The implementation of Finite Element Method

(FEM) for solving the solid mechanics problems which are analysed in continuum domain, is still one of the most accurate numerical simulation techniques.

The approximate solutions of differential equations can be provided by FE method in order to cope with boundary value problems. Within this method, first the problem should be discretised with respect to time. For this purpose, there are generally two mathematical methods were developed, which are explicit and implicit direct integration. An explicit technique, namely the central difference method, is executed in this research program, which means that the velocity and acceleration vectors are assumed to be approximated as equations (34) and (35), respectively.

$$\dot{u}_t = \frac{u_{t+\Delta t} - u_{t-\Delta t}}{2\Delta t} \tag{34}$$

$$\ddot{u}_t = \frac{u_{t+\Delta t} - 2u_t + u_{t-\Delta t}}{\Delta t^2} \tag{35}$$

The domain of the problem is divided into simple-geometry and smaller sub-domains by means of mesh generation. The differential equations are then considered for each one of these finite elements and solved approximately by an interpolation function. These local approximations are assembled into global matrices for the whole domain later.

5.2 Smooth Particle Hydrodynamics (SPH)

The Smooth Particles Hydrodynamics method was originally developed to cope with the astrophysics problems. After observing the similar movements of particles in astrophysics and fluid flows, this method is modified to be implemented in fluid mechanics (Monaghan, 1988). The SPH has been improved significantly within last decay, and nowadays, it can be applied to most of the continuum mechanics problems, i.e. solid mechanics.

The SPH is a mesh-less Lagrangian method which discretises a system as a number of particles (or “mesh-points”) carrying the field variables. These particles move and interact with each other. The SPH particles (in a 2D domain) are represented in Figure 15 as a series of red spheres. Let’s consider any given particle in the problem domain Ω (i.e. the green sphere located in the center of the grid in Figure 15); this particle interacts with all the other neighbour particles within a given distance which is determined by the smoothing length “h”. The area of the smoothing function at the problem domain, also called support domain, is controlled by a smoothing or kernel function

"*W*" (the blue surface). The interaction of the particles is weighted by means of this smoothing kernel. This function which is based on random distributing interpolation points, is implemented to calculate the spatial derivatives equations of the system. The SPH simulations are carried out by solving the three fundamental conservation laws, i.e. conservation of mass, momentum and energy, in conjunction with the material constitutive rule (and equation of state).

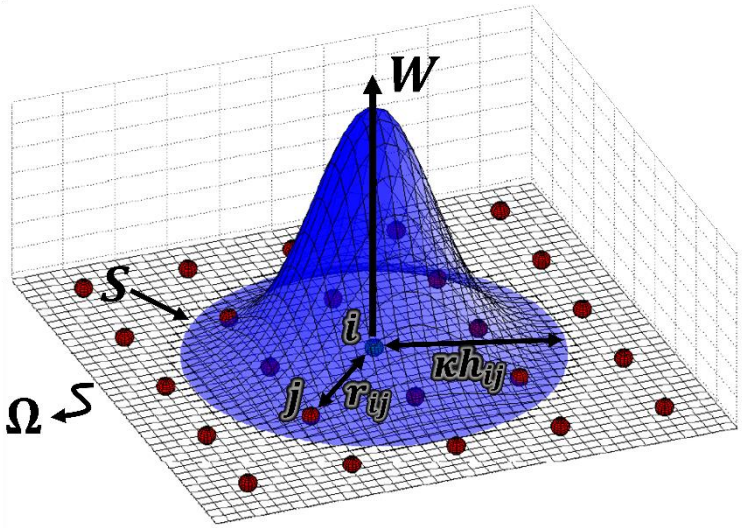

Figure 15. SPH particles in a 2D problem domain

SPH method is formulated by two fundamental steps. The first step, called kernel approximation, is the integral representation of a function f (and its derivatives) in the continuous form. This step is followed by discretisation of the continuous form of this kernel approximation into a finite number of particles. The kernel approximation (Monaghan, 1992) for any two given particles, i and j, is determined by equation (36).

$$f\left(x_i\right)=\int_{\Omega} f\left(x_j\right) W\left(x_i-x_j, h\right) dx_j \tag{36}$$

Where, the smooth function W is given by equation (37).

$$W\left(x_i-x_j, h\right)=\frac{1}{h\left(x_i-x_j\right)^d}\theta\left(x_i-x_j\right) \tag{37}$$

Where, "*d*" is number of space dimension and "θ" is an auxiliary function. Generally speaking, the higher order of the kernel function brings greater accuracy for the SPH scheme. However, due to time computation cost, it is not convenient to use very high

order kernel functions. Therefore, the most widely used kernel function is called cubic spline which can be defined by means of an auxiliary function θ according to the equation (38).

$$\theta\left(u=\frac{r_{ij}}{h}\right)=\kappa\begin{cases}1-\frac{3}{2}u^2+\frac{3}{4}u^3, & |u|\le 1\\ \frac{1}{4}(2-u)^3, & 1\le|u|\le 2\\ 0, & |u|\ge 2\end{cases} \tag{38}$$

The parameter "κ" in equation (38) is a normalization constant, relies upon the number of space dimensions, so that the effective regime (and accordingly, the computation time) is increased by means of higher values of this parameter. The equation (36), which is written in discrete notation, then should be transformed into a continuous form as equation (39).

$$f\left(x_i\right)=\sum_{j=1}^{N}\frac{m_j}{\rho_j}f\left(x_j\right)W\left(x_i-x_j,h\right) \tag{39}$$

The equation (39) is called the "particle approximation" and its summation is over all the finite number of particles "*N*". In this equation, m_j and ρ_j are the mass and density of any given particles inside the problem domain, respectively.

5.3 FEM-coupled to-SPH

Although the SPH method is generally more suitable, efficient and robust for problems involving severe distortions, its accuracy and efficiency is not as good as that of the FEM for problems with mild distortions (Johnson et al., 2002). Therefore, the idea of combining the advantages of these two numerical methods by using the FEM for the mildly distorted regions and the SPH for the highly distorted regions arises. The concept of linking particle elements with a standard grid was originally represented by (Johnson et al., 1986). The same author proposed in (Johnson, 1994) an algorithm that demonstrates how the SPH particles interact with Lagrangian finite elements on a sliding interface. A similar contact-like algorithm aiming to couple SPH elements to the quadrilateral finite elements was developed by (Attaway et al., 1994). Finally, an

algorithm able to automatically convert distorted finite elements into SPH particles was proposed in (Johnson et al., 2002).

In the present study, the commercial software LS-DYNA was employed. The (automatic) node-to-surface contact algorithm in LS-DYNA can govern the normal interaction between finite elements and SPH particles, since both methods are based on the Lagrangian formulation (Xu and Wang, 2014). Inspired by the study presented in (Bresciani et al., 2016), in which a ceramic tile was modelled with an adaptive conversion of solid elements to SPH particles technique, a similar approach was chosen to simulate the rock specimen in the present study. The keyword *Define_ADAPTIVE_SOLID_TO_SPH was implemented in LS-DYNA to adaptively transform a Lagrangian solid element into a certain number (1, 8 or 27 – see Figure 16) of SPH particles (Mardalizad et al., 2018b).

The newly generated SPH particle(s) inherit all the mechanical properties of the eroded solid element, i.e. the mass, kinematic and constitutive properties. Therefore, the constitutive relationship of the damaged material (expressed by SPH particles) is the same as the initial material model specified for the intact meshed part.

There are two user-input parameters related to this LS-DYNA keyword that defines the coupling approach (ICPL and IOPT). When both of these parameters are set equal to 1, the SPH particles are bonded with the solid elements as a single part (Xu and Wang, 2014). Finally, it is noted that either an automatic or an external eroding algorithm (i.e. MAT_ADD_EROSION in LS-DYNA) should be used to define the element erosion criteria (e.g. effective plastic strain, etc.).

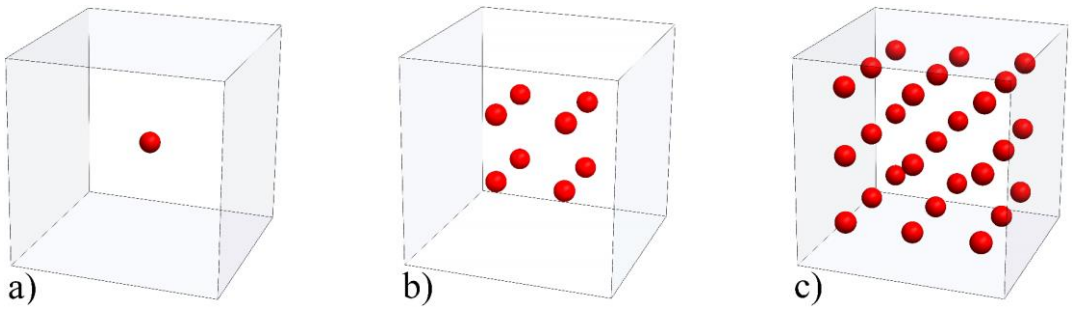

Figure 16. the SPH particles which are converted from a hexahedral 3D solid element.

Part III

Experimental tests

Chapter 6
Unconfined Compression Test

The boreability, strength and deformability of rocks all have a great influence on deep hole drillings. The unconfined compressive strength (UCS) is one of the most significant parameters to characterize the rock materials. It plays an important role to predict the boreability of the material (Ceryan et al., 2013; Kahraman, 2001). Boreability is used widely in the design and classification of rocks. It is expressed by the maximum principal stress that the material can sustain under a uniaxial compression test. Since the UCS is a fundamental property of rock materials, a precise approach for its measurement is a necessary tool. A cylindrical specimen loaded by two compressive platens in parallel to its main axis is considered conventionally as the configuration of UC test. This conventional test, which is also suggested by the ASTM (ASTM, 2004), presents a drawback. This negative feature is mainly due to the radial shearing forces generated at the contact interface after applying the load. These undesired radial forces are appeared because of the different elastic properties of the rock specimen and the steel of the testing apparatus. Another arrangement is suggested by Mogi (Mogi, 1966; Mogi, 2007) to design a specimen in order to reduce these drawbacks. The experimental and numerical analyses presented in this PhD project demonstrate that the Mogi's suggested method, which is not tough and effortful to be prepared, lead to measure the unconfined compression strength more precisely. The experimental tests express that the variability of the results obtained by the Mogi's method are significantly lower than the ones of ASTM configuration. The assessments exploited based on numerical simulations justifies this issue when the existence of stress concentration will be considered at the rock-steel interface of conventional configuration. In this chapter, the methods and the results obtained during the experimental tests are reported. Both the ASTM and the Mogi configurations were implemented to perform these tests, and the results are discussed to highlight the differences.

The unconfined compression test is conventionally performed by applying axial load to a cylindrical specimen with a specific length to diameter ratio. Different configurations which have been studied to perform the unconfined compression test are expressed in Figure 17. The short and right cylindrical specimen represented as type 1 is the configuration suggested by the ASTM standard. This configuration is in direct contact with the compressive platens of the apparatus. The different mechanical

behaviour of the rock specimen and the steel of compressive platens results in producing radial shear forces at their interfaces. The two arrangements which are expressed as type 2 and type 3 in Figure 17 were developed to overcome the shortcomings of the type 1.

Several lubricants have been applied at the interfaces to eliminate the friction forces presents in the type 2 arrangement. Initially it may seem that this type 2 configuration is the preferred one because of the frictionless boundaries. Since the end conditions are principal planes, the deformation is homogeneous, and the state of stress doesn't vary throughout the specimen. However, several vertical cracks propagate, starting from the outer surfaces of the rock, after performing the test. The reason behind this crack formation is the intrusion of soft lubricator into the specimen (Mogi, 2007). Therefore, it was concluded that the idea of type 2 configuration (using lubrication to have frictionless boundaries) is not practical.

The dog-bone specimen, which was suggested by Brace (Brace et al., 1966), is indicated in type 3. Brace designed this method to avoid extending the effect of a mismatch at the both ends of the specimen into the region of the specimen where fracture occurs. This dog-bone specimen also yields to unsuitable for performing the UC test. It is mainly because of two drawbacks: first, the rough fabrication procedure, and second, the presence of the bending stresses. Therefore, Mogi in (Mogi, 2007) suggested another configuration (which is expressed in type 4) to overcome the drawbacks of all the other configurations. Table 1 summarized the pros and cons of these configurations.

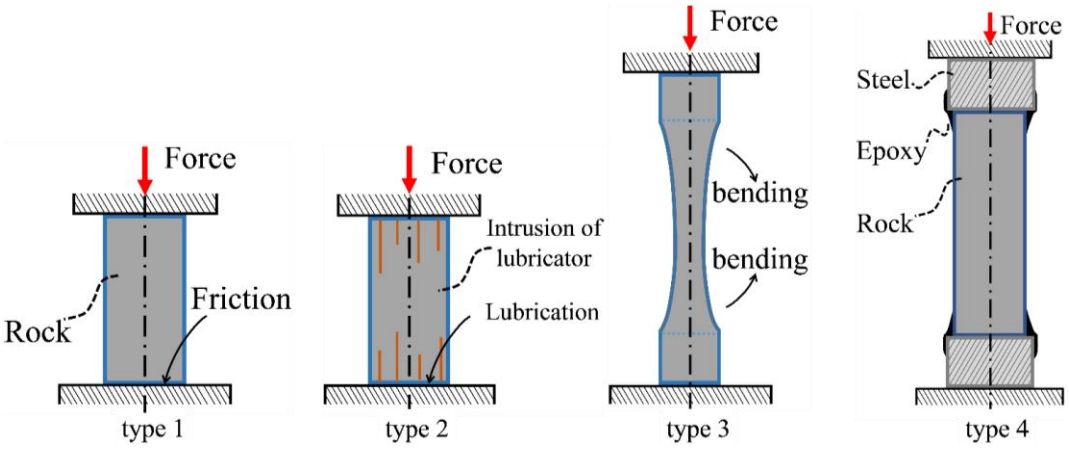

Figure 17. The configurations of rock specimens under a UC test (Mogi, 2007).

Table 1. the pros and cons of different arrangement types under an unconfined compression test (Mogi, 2007).

	Type 1	Type 2	Type 3	Type 4
Pros	-easy fabrication	-easy fabrication	-no stress concentration -low clamping effect	-No end effects -No bending -Easy fabrication
Cons	-stress concentration -clamping effect	-vertical cracking at the end surface	-bending -difficult fabrication	

Two different experimental programs are performed within this PhD project by considering the type 1 and the type 4 as the methods of testing rock samples. The Mogi's arrangement (Type 4) is aimed to counteract the major drawbacks of the conventional configuration, which is the stress intensification presents at the interface of the specimen and steel plates of apparatus. Therefore, the Mogi's configuration is expected to bring two main advantages, which are the precise determination of material strength; and the increase the re-producibility of the UC strength.

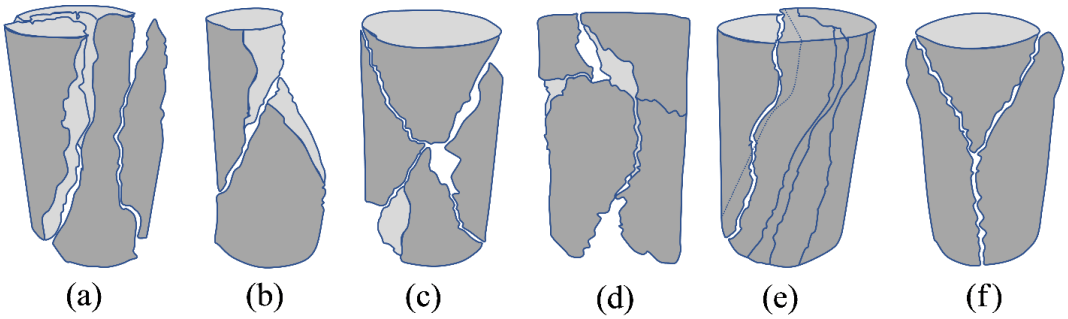

Figure 18. Schematic representation of possible failure modes under the unconfined compression test; (a) axial splitting, (b) shearing along single plane, (c) double shear, (d) multiple fracturing, (e) along foliation, (f) Y-shaped (Basu et al., 2013).

Prediction of rock failure modes is a complex and challenging task. Several research studies were carried out; however, the understanding of this phenomena is still under investigation(Basu et al., 2013). It is suggested in (Bieniawski, 1984) that investigation of the physical models of the rock materials may provide useful information, especially when the failure modes are studied at laboratory scale, since there is no straightforward mathematical or numerical analyses model that can strongly ascertain the nature of fracture development. In (Santarelli and Brown, 1989), the failed rock specimens of dolomite and sandstones under triaxial compression tests have been studied. Based on these investigations, it was concluded that failure can manifest itself

in various ways, which is depend on the microstructure of the rocks. A survey provided by (Basu et al., 2013) on granite (brittle crystalline rock), schist (anisotropic metamorphic rock), and sandstones (sedimentary rocks) claims that the failure mode under a UCT may be one of the types indicated in Figure 18.

The uniaxial loading condition imposes both tensile stresses at the specimens so that the cracks initiate and propagate from the tip of the microcracks and other defects when these stresses exceed the local tensile strength at that tip. These propagating cracks are called wing cracks. The predominant failure mode of the ASTM arrangement is expected to be axial splitting since wing cracks cannot be tolerated and eventually will be aligned parallel to the maximum principal stress (Basu et al., 2013). However, the failure mode of the Mogi's configuration is supposed to be yet another type. When the wing crack propagation is inhibited, the coalescence of adjacent wing cracks, or of wing cracks in close proximity generated from the tips of suitably oriented microcracks, takes place in order to release the strain energy in the form of a shear fracture. Therefore, it is assumed that the presence of the epoxy cap stops the propagation of the wing cracks and so, the specimen fails by the shear mode (Mogi, 2007).

6.1 ASTM configuration

The first series of the unconfined compression tests have been performed based on the protocols of the ASTM standard (ASTM, 2004). According to the specifications provided by the standard, the rock specimens should have cylindrical shape with a length to diameter ratio, L_0/D between 2 and 2.5. The dimeter of these specimens should be greater than ten times the maximum grain size. Sandstone is a medium-grained sedimentary rock which has a sand size between 0.06 to 2 mm. The geometry data of the specimens are reported in Table 2 (Mardalizad et al., 2018b).

Table 2. Dimension of the specimens - the ASTM standard (Mardalizad et al., 2018b).

Specimen	Length, L_0 [mm]	Diameter, D [mm]	$\cong L_0/D$
A1	41.3	20.4	2
A2	40.9	20.4	2
A3	40.8	20.4	2
B1	44.8	20.5	2.25
B2	44.9	20.4	2.25
C1	49.9	20.4	2.5
C2	49.8	20.4	2.5

The testing machine which is used for the ASTM standard configuration is indicated in Figure 19. The cylindrical specimen is compressed between the two platens and the upper compressive platen is spherically seated. This upper platen is displacement controlled, while the lower platen is fixed. The seating sphere has been properly lubricated and centred on the specimen faces. Its diameter should be higher or equal as the specimen's diameter and less than its double. The platens should have a diameter of at least the same as the specimen's diameter and a minimum of thickness to diameter ratio equal to 0.5. The upper platen should be displaced vertically at a constant speed of 0.1 mm/min. In this way, the failure of specimens may occur between 2÷15 min as prescribed by the standard. An axial extensometer is placed at the mid height of the specimen to measure the axial strain. Due to the presence of friction forces, the state of stress can vary throughout the specimen and the deformation is not completely homogenous. Therefore, the gauge length of the axial extensometer used for the ASTM configuration is equal to 8 mm (less than 50% of the length of shortest specimen) in order to be sure that the axial deformation at this span remains homogenous. The applied loading amounts as well as the crosshead displacement were measured automatically by the testing apparatus (Mardalizad et al., 2018b).

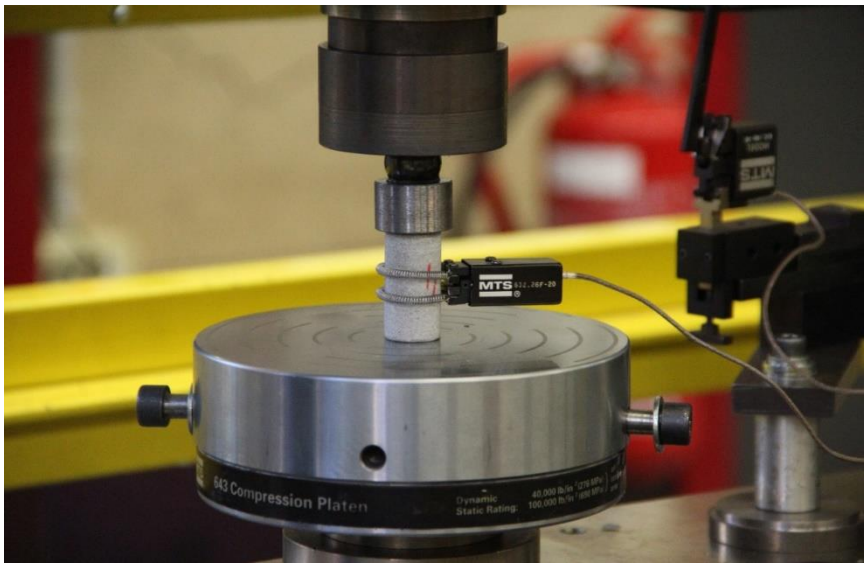

Figure 19. UC test apparatus – the ASTM configuration (Mardalizad et al., 2018b).

According to the protocols of ASTM standard (ASTM, 2004), the Young's modulus can be obtained from this experimental test by considering the stress-strain diagram according to one of the following methods:

- The tangent modulus at a percentage of the failure stress *E%*, i.e. E_{25} and E_{50}.

- The average slope of the straight line of the stress-strain curve E_{av}.
- The secant modulus from zero to the failure stress E_s.

The uniaxial compressive strength, σ_{uc} of a material can be calculated as P/A, where P is the maximum load measured by the testing machine and A is the cross-sectional area of the specimen. Each experimental result of this study is reported as an average value and a repeatability limit. The repeatability limit, r is equal to $2\sqrt{2}\cdot S_r$, where S_r is the repeatability standard deviation (the standard deviation of the values was obtained with the same testing apparatus and the same material). By definition, the probability of two identical tests which do not differ from one another by more than the repeatability limit, should be about 95%. The stress-strain diagrams for the ASTM standard configuration specimens are shown in Figure 20. As can be seen in Figure 20, the post-failure behaviour is not recorded in the stress-strain diagrams due to the limitation of testing apparatus. As discussed in (Hudson and Harrison, 2000), it may be possible to obtain the complete stress-strain curve (i.e. the post-failure behaviour) for the rock materials, if the stiffness of the apparatus is greater than the absolute value of the slope at any point on the descending portion of the stress-strain diagram. In this case, the system is continuously stable which permits reaching the post-failure area. It seems that the stiffness of testing apparatus used for this experimental campaign is not high enough to capture these data (Mardalizad et al., 2018b).

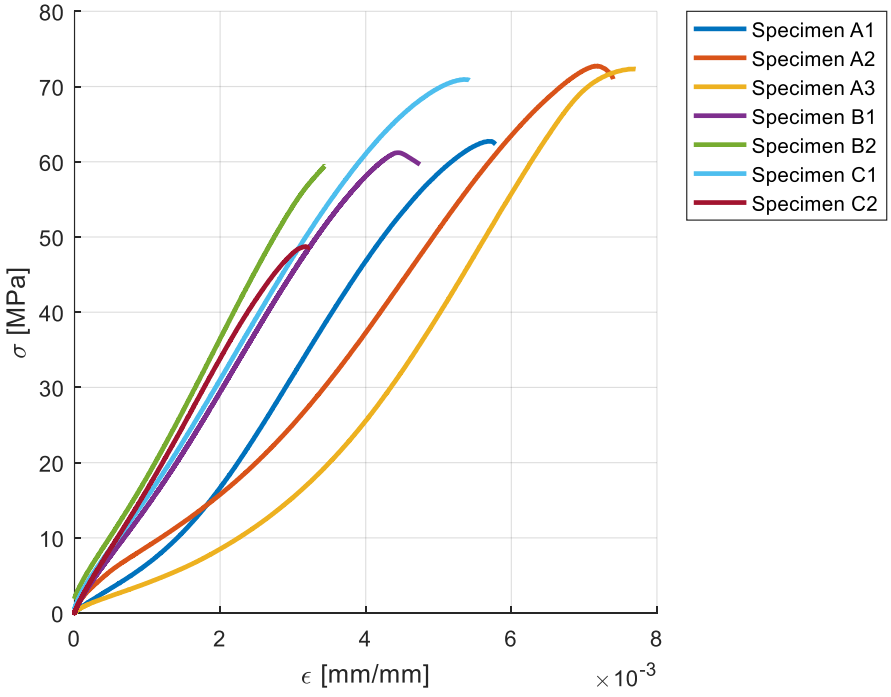

Figure 20. The stress-strain curves of an unconfined compression test; the ASTM's layout (Mardalizad et al., 2018b).

The uniaxial compressive strength and the different extrapolation of the elastic modulus for each specimen, reported in Table 3, were obtained from the experimental data expressed in Figure 20.

Table 3. Uniaxial compressive strength and the elastic modulus for the standard configuration specimen (Mardalizad et al., 2018b).

Specimen	σ_{uc} [MPa]	E_{25} [MPa]	E_{50} [MPa]	E_{av} [MPa]	E_s [MPa]
A1	62.72	12587	15679	15522	11050
A2	72.73	8663	13224	12804	10121
A3	72.34	9411	15039	14525	9400
B1	61.20	13809	16349	16046	13778
B2	59.443	15925	18766	18534	17309
C1	70.94	14664	16575	16308	13260
C2	48.73	15549	17648	17339	15351

Since the ratio between the repeatability limit and the average value of a parameter can be considered as a benchmark to measure its variability, some of the experimental data (and their corresponding *r/average* values) obtained for the Pietra Serena by both the ASTM and the Mogi configurations are expressed in Table 6.

The high amount of E_{25} variability (*r/average* = 0.38) of the Pietra Serena (which was measured in this research work) demonstrates an undesired issue. This issue can be explained by Figure 20, where a nonlinear regime is present at the beginning of almost all the stress-strain diagrams. Moreover, the results of experimental tests on different specimens at this regime are not the same and differ significantly. It is concluded that this response may have two main causes: (1) very smooth surface finishing on rock specimens is difficult to obtain and the upper compressive platen therefore needs to be adjusted automatically and aligned to the surface of the specimens at the beginning of the test; (2) the presence of the high amount of pre-existence micro-cracks in the specimens created during their fabrication process. It is worth mentioning that the density of these micro-cracks is much higher near the outer edges of the specimens than in the middle region.

It has been tried to reduce the effect of this phase (that is more related to specimen issue) by means of a post-processing step. For this purpose, first the linear elastic regime was determined. Then the E_{50} elastic modulus of each specimen was measured. The elastic regime then was expanded with the same elastic modulus up to the null stress level. Finally, the whole curve was shifted along the strain axis to be started

from the origin. The conclusive results of the post-processing procedure are expressed in Figure 21 (Mardalizad et al., 2018b).

The fractured specimens of the ASTM arrangement are shown in Figure 22 exhibiting an almost identical failure mode for all the specimens. A crack initiates at the edge of the specimen and propagates mainly in the vertical direction (parallel to the axis) demonstrating that the failure mode of the ASTM configuration test is in accordance to the definition of the axial splitting failure mode which is schematically represented in Figure 18.

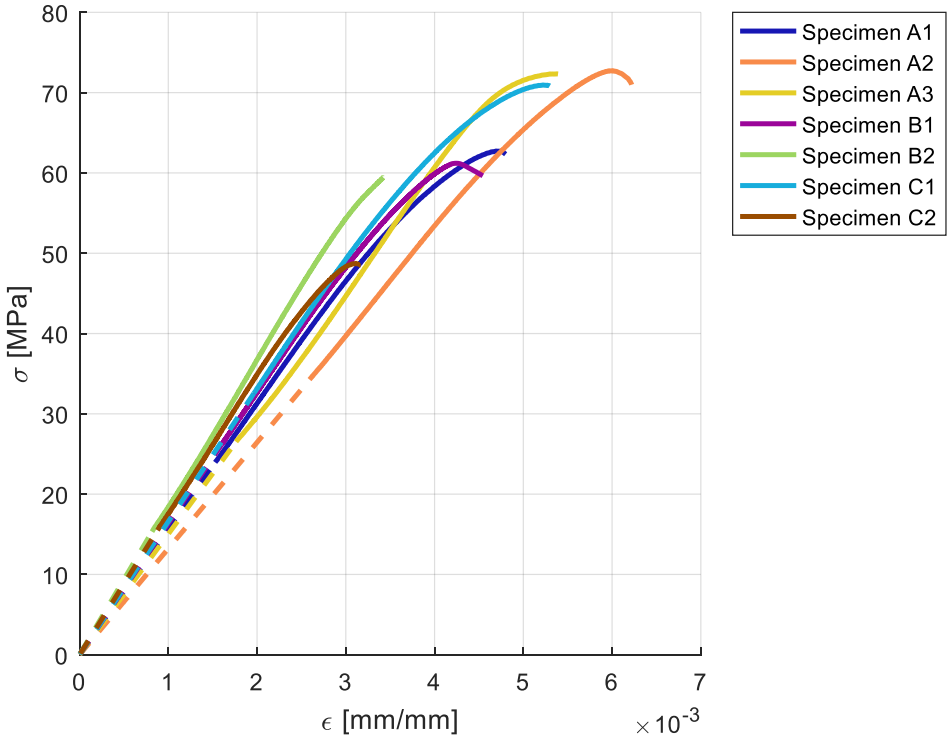

Figure 21. The standard configuration results of an unconfined compression test after post processing (Mardalizad et al., 2018b).

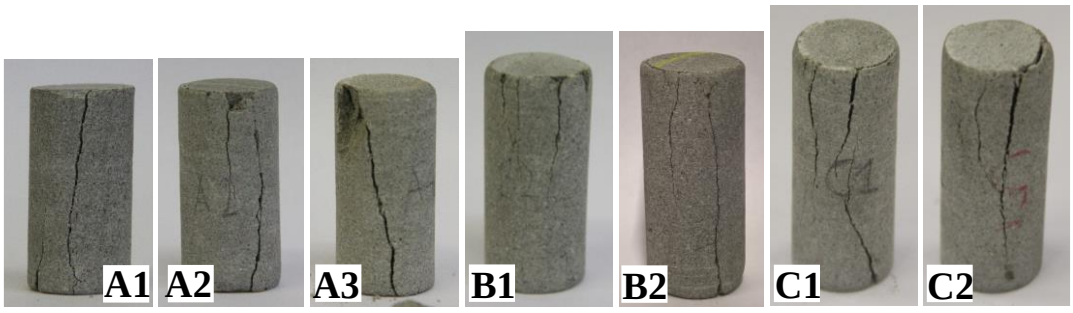

Figure 22. The broken specimens – the ASTM configuration (Mardalizad et al., 2018b).

6.2 Mogi's configuration

Due to the different elastic properties of the steel of the testing machine platen and the rock specimen, radial shearing forces are generated at the contact interface after applying the compressive load. These forces produce an undesired clamping effect at the end of specimen. This issue raises two potential problems: (a) due to the unexpected and sudden shearing stress mutation, the stress concentration occurs at the specimen outer edge near the interface, (b) if a crack propagates into this area, the corresponding fracture growth is potentially prevented. These two issues may affect the realistic strength of a rock. As the stress concentration tends to decrease the strength, the fracture growth prevention tends to increase it, however the factors almost never cancel each other's effect (Mogi, 2007).

The drawback caused by these undesirable forces can be strongly reduced by an enhanced arrangement designed by Mogi (see Type 4 in Figure 17). It consists of a cylinder connected to two aluminium end pieces by epoxy. The thickness of the epoxy is gradually decreased towards the middle of the specimens to form a smooth fillet in order to eliminate the stress concentration at the contact interface of rock and steel. However, it is not critical to obtain an exact surface of the fillet since the epoxy has an elastic property lower than most rocks.

The main disadvantage of Mogi's configuration is since the state of stress varies through the specimen. Due to this issue, the deformation is not homogenous along the entire length of the specimen. However, this non-homogeneity is more observed near the end surfaces and in a large span around the mid-height of the specimen the displacement is almost homogenous. Therefore, during this research study it was tried to overcome this drawback by using an axial extensometer (located around the mid-height) that its gauge length is much shorter than the length of specimens. In this way, it is expected that what extensometer measures will be the (almost) homogenous displacement.

An alignment cover was designed and fabricated in order to perfectly adjust the axis of the cylinders, i.e. the specimen and each of the steel end pieces assuring also that the two ending surfaces are parallel. The structural adhesive 3M Scotch Weld DP490 was used to attach the end bases to the specimens. Figure 23 indicates the procedures for preparing the specimens of the Mogi's configuration. The outer edges were smoothed initially by sandpaper and then by a fine rasp and then cleaned with acetone (see Figure 23a). The primary configuration was fixed by using the alignment cover and one drop of the acrylic glue between the end pieces and the specimen (see Figure

23b and Figure 23c). The specimens remained untouched for two days. Then the secondary gluing was performed using the structural adhesive 3M Scotch Weld (see Figure 23d). Again, the specimens remained untouched for one week, in order to reach the full curing period of Scotch Weld.

The specimen dimensions are listed as the average of the three measurements and their L_0/D in Table 4. It should be noted that the L_0 parameter for the Mogi configuration is the distance between the two-inner sides of the epoxy layers and thus differs from the ASTM parameter. The specimen of class *C* has a slightly lower L_0/D ratio and was used to investigate if any differences occur between the two tests. The minimum suggested L_0/D ratio should be greater than 2, according to (Mogi, 2007). As reported below, the experimental result of specimen *C3* was unacceptable, was therefore not considered for further investigation (Mardalizad et al., 2018b).

Table 4. Dimensions of the specimens - Mogi's layout (Mardalizad et al., 2018b).

Specimen	Length, L_0 [mm]	Diameter, D [mm]	L_0/D
C3	37.2	20.4	1.8
D1	46.8	20.4	2.3
D2	45.2	20.4	2.2
D3	49.1	20.4	2.4
E1	65.0	20.5	3.2
E2	68.7	20.3	3.4

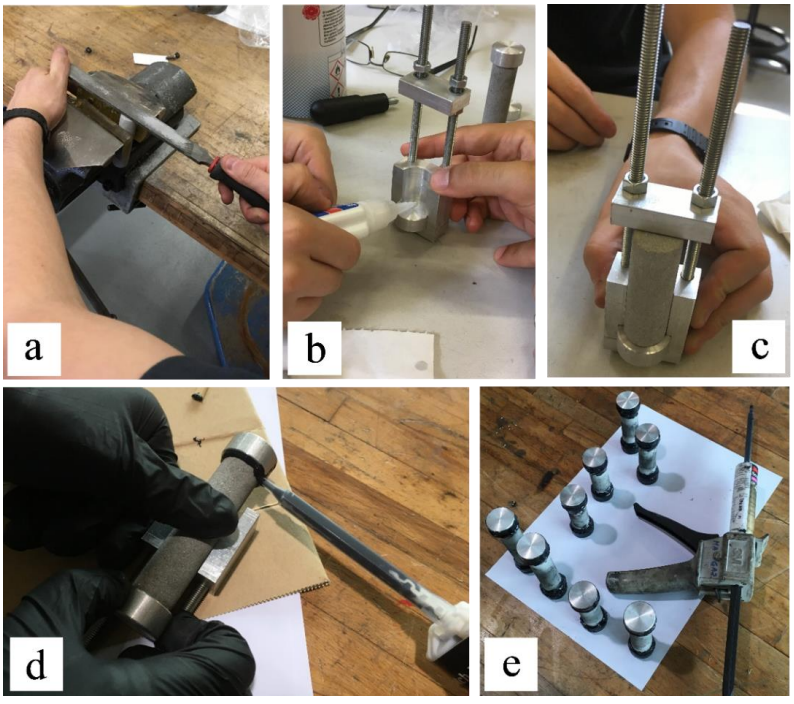

Figure 23. The pre-processing preparation of the Mogi's layout specimen; (a) the outer edges were smoothed initially by a fine rasp; (b) one drop of an acrylic glue was applied to the end piece and the specimen interface; (c) the primary configuration was fixed via an alignment cover; (d) the structural adhesive 3M Scotch Weld was applied for the secondary gluing; (e) the specimens remained untouched for one week (Mardalizad et al., 2018b).

The testing apparatus for the improved configuration is shown in Figure 24 (which is identical with the standard configuration). However, the diameter of upper platen is larger because the diameter of the steel end base of the Mogi's specimen has larger diameter than the one used in the standard configuration. An axial extensometer with a longer gauge length (20 mm) was used for specimen *E.*

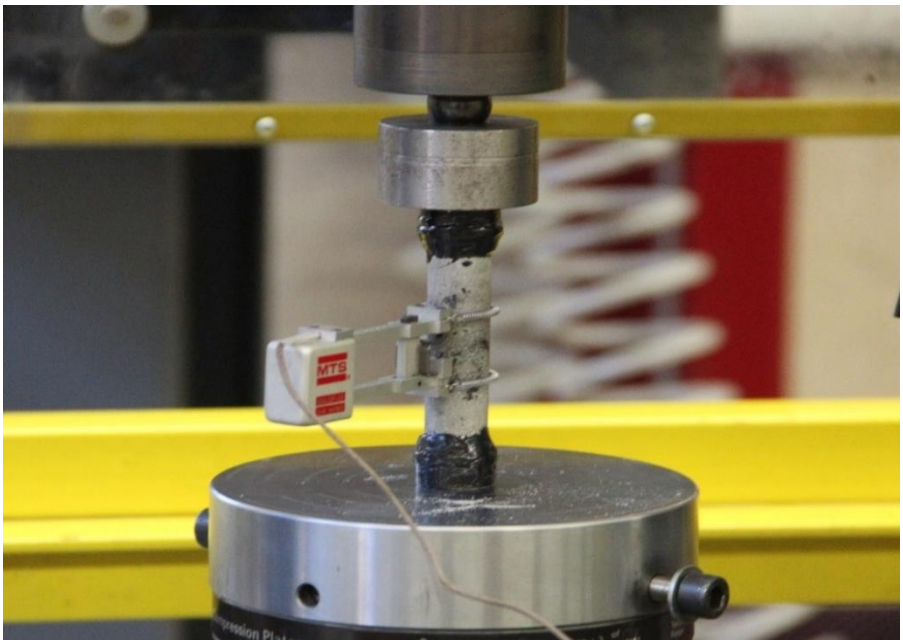

Figure 24. UC test apparatus - the Mogi's configuration (Mardalizad et al., 2018b).

The stress-strain diagrams of the Mogi's specimens are shown in Figure 25. The unconfined compressive strengths and different extrapolation of elastic modulus for each specimen are also given in Table 5. Identical mechanical properties which were provided for the ASTM configuration (reported in Table 3) can be measured for the Mogi's arrangement and are reported in Table 6. The stress strain diagram and the mechanical properties of specimen *C3*, expressed in Figure 25 and Table 5, respectively, show inappropriate responses and approve the Mogi's suggestion about the range of the L_0/D ratio (L_0/D ratio of specimen *C3* is equal to 1.8). Therefore, the

experimental data related to this specimen is not considered for computing the average values in Table 6.

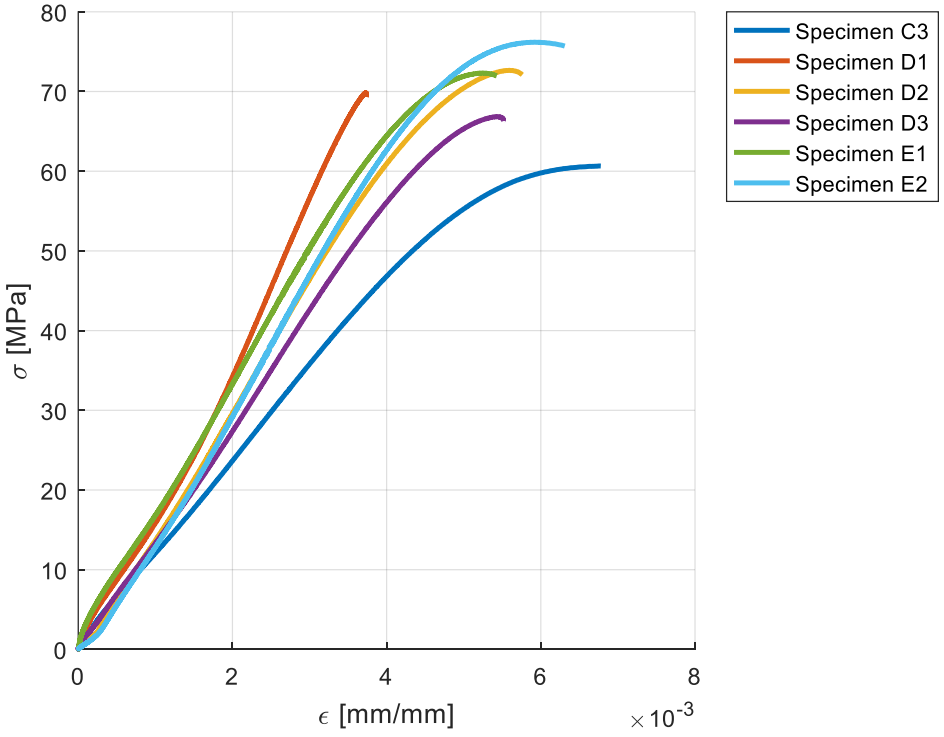

Figure 25. The stress-strain curves of an unconfined compression test; the Mogi's layout

Table 5. Uniaxial compressive strength and the elastic modulus for the Mogi's specimen (Mardalizad et al., 2018b).

Specimen	σ_{uc} [MPa]	E_{25} [MPa]	E_{50} [MPa]	E_{av} [MPa]	E_s [MPa]
C3	60.66	11303	12195	12012	8980
D1	69.83	15954	21452	21105	18721
D2	72.66	15342	17055	16798	12994
D3	66.85	13474	15355	15123	12321
E1	72.32	15022	17220	17196	13776
E2	76.19	16094	17943	17657	12873

Table 6. The mechanical response of the Mogi's layout under an unconfined compressive test (Mardalizad et al., 2018b).

		σ_{uc} [MPa]	E_{25} [MPa]	E_{50} [MPa]
	average	64.02	12944	16183
Pietra Serena	***r* [MPa]**	24.7	8191	5075
(ASTM)	***r/average***	0.38	0.63	0.31

	average	71.57	15177	17805
Pietra Serena	***r* [MPa]**	9.84	2966	6360
(Mogi)	***r/average***	0.14	0.19	0.35

The fractured specimens of the Mogi arrangement are shown in Figure 26. Unlike the specimen of the ASTM configuration, shear planes are observed, and the crack propagates through them. The fracture pattern of all the specimens are very similar and in accordance to the shearing along single (or double) plane failure mode which is schematically represented in Figure 18.

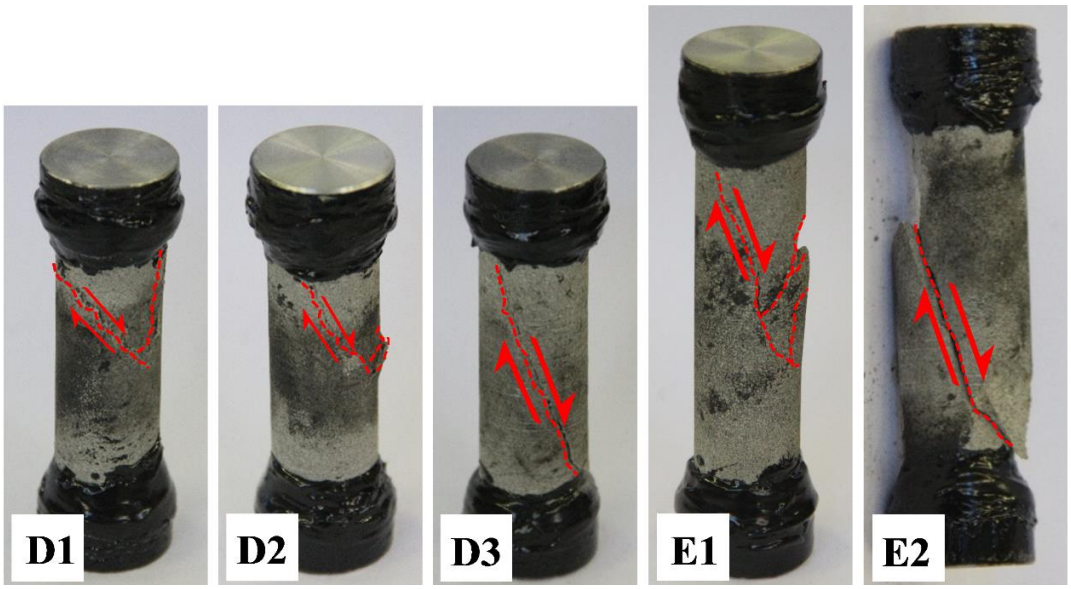

Figure 26. The broken Mogi's configuration specimens (Mardalizad et al., 2018b).

6.3 Comparison of Mogi and ASTM results

As can be seen in Table 6, the average unconfined compressive strength of the Mogi's arrangement is almost equal to (slightly higher than) the one obtained with the ASTM standard configuration. The variability of the 25% tangent modulus of the ASTM configuration, E_{25} is significantly higher than the Mogi variability, while the variability of their 50% tangent modulus, E_{50} are almost equal. The Mogi's approach, therefore prevents the undesired effects of the pre-existence micro-cracks close to the ends of the specimens. The Mogi specimens do not show the initial non-linear behaviour, mainly, due to their higher length. The Mogi's layout consists in longer specimens; therefore, the measurement of the displacement is less affected by the presence of the

micro-cracks, which are concentrated near the end bases of the specimen (where the glue fillet is also present). If the specimen is long enough, the cracks due to the machining at the bases are not present in the zone where the extensometer is applied. Therefore, the non-linear deformation due to the presence of the cracks is not recorded by the extensometer. In addition, the glue fillet covers partially the zone where these cracks are present. Indeed, also longer ASTM specimens (B and C) show lower initial non-linear phase. Moreover, due to the utilization of steel end pieces at the Mogi's layout and their significant surface finishing, the upper compressive platen is almost perfectly aligned from the beginning of the test. The effects of these features are clearly visible in the comparison of Figure 27a and Figure 27b, where the post-processed stress-strain curves of the ASTM configuration exhibit an almost identical behaviour as the Mogi's arrangement.

As previously remarked, the two types of specimens show different failure modes. The Mogi's specimens have a shear failure mode (see Figure 26), while the compressive failure mode (vertical crack propagation parallel to the loading axis) was observed for the standard arrangement (see Figure 22).

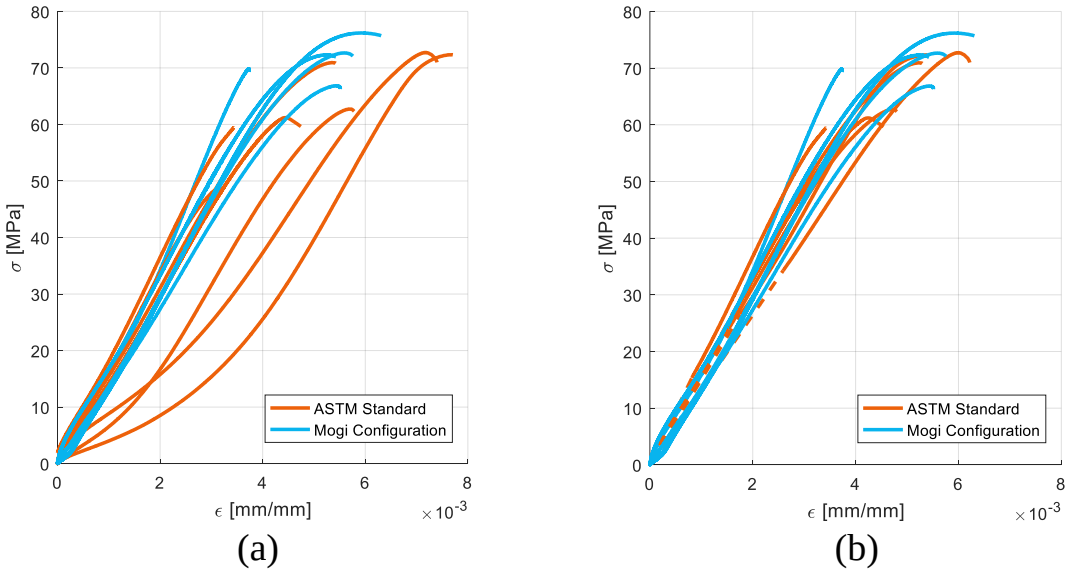

Figure 27. Comparison of the Mogi's configuration with; (a) the original results and; (b) the post-processed results of the ASTM layout (Mardalizad et al., 2018b).

Chapter 7

Quasi-static Brazilian disk test

The maximum principal tensile stress is one of the key parameters in the description of the mechanical behaviour of rocks. Due to several issues, including the poor tensile resistance of rocks, performing a conventional direct tensile test is particularly difficult. However, the tensile strength of a brittle material can be measured indirectly by means of the Brazilian test. The test consists of a compressive loading applied to a cylindrical disk periphery. This loading condition initiates a fracture along the compressive diametral direction, where the maximum principal tensile stress is dominant. Therefore, the splitting tensile strength measured by the Brazilian test is representative of the maximum principal tensile strength of a material. Different failure modes of a rock material under Brazilian disk test was studied by (Basu et al., 2013). This study suggests categorizing the failure modes by four classes: (a) fracture is located in the central part, (b) non-central fracture which are mainly curved lines, (c) layer activation that is mainly formed as a combination of central and non-central fracture modes and (d) central multiple fracture that develops to release the high amount of stored fracture energy. The investigation of the fracture pattern of sandstones, which is carried on (Basu et al., 2013), consider the first type (fracture in central part) as the often fracture pattern. It is due to the fact that the compression-induced tensile stress is not strong enough to exploit the foliations for the strain energy, so that it will be released before it can form non-central or multiple central fractures.

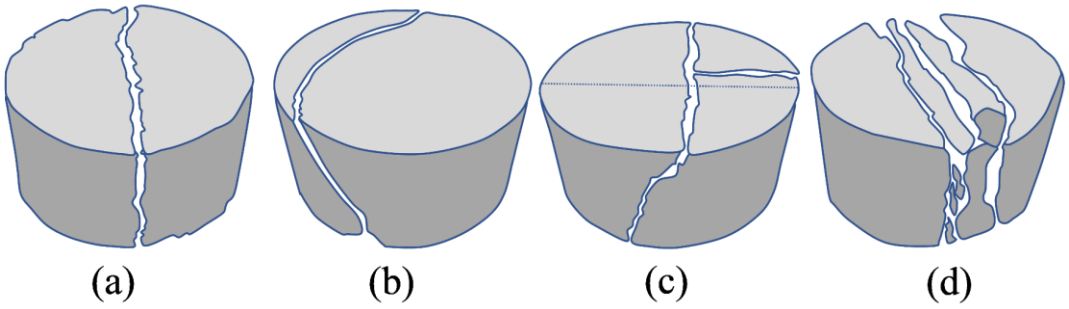

Figure 28. Schematic representation of different failure modes of rock materials under Brazilian disk test (Basu et al., 2013).

The identification of the location where the maximum tensile strain takes place is another challenging issue. It can be described by a transition failure mode between a

tensile failure mode that refers to the diametral splitting fracture, and a shear failure mode, associated to the parts close to the loading platens (Li and Wong, 2013).

Table 7. The geometrical data corresponding to different classes of Brazilian disk test samples.

	d_m [mm]	t_m [mm]		d_m [mm]	t_m [mm]
G1	39.7	16.1	**H1**	39.8	20.6
G2	39.7	15.4	**H2**	39.8	20.7
G3	39.7	16.2	**H3**	39.5	20.9
			H4	39.7	20.8
			H5	39.7	20.3

	d_m [mm]	t_m [mm]		d_m [mm]	t_m [mm]
I1	39.6	23.9	**J1**	39.6	27.6
I2	39.8	24.0	**J2**	39.6	27.7
I3	39.7	23.9	**J3**	39.7	28.3
			J4	39.6	27.7

The Brazilian disk tests were performed according to the protocols of the ASTM standard (Standard, 2008). According to the standard, the cylindrical specimens should have a thickness to diameter ratio (t_m/d_m) between 0.2 and 0.75. Also, the specimen diameter should be greater than (at least) ten times the maximum grain size. The sandstone is a medium-grained clastic sedimentary rock, with a sand size between 0.06 to 2 mm. The geometry data of the specimens are reported in Table 7.

According to Table 7, the specimens were grouped into four classes, named; G, H, I and J, based on their thickness, while their diameters were almost identical. As shown in Figure 29a, the testing apparatus consists of an upper compressive platen which is displacement controlled and a lower steel platen which is rigid. The upper platen is moved downwards to apply a compressive load. The velocity of this platen is set to 0.15 mm/min to assure that failure occurs between 1 and 10 min as prescribed by the standard.

Figure 29b indicates a steel bearing block with a curved surface that is designed and fabricated within this experimental campaign. This block is positioned in between the upper platen and the specimen to decrease the contact stresses as suggested by the standard. Since the splitting tensile strength measured by the Brazilian test is computed based on a line load, the applied load should be limited to a narrow band. However, the narrow strip loading may create extremely high contact stresses which cause premature cracking. Investigations provided in the standard indicate that if the arc of contact remains smaller than 15°, the error in deriving the principal tensile strength

is less than 2 %, while the chance of the premature cracking existence is decreased dramatically. Therefore, the curvature radius of this supplementary bearing plate was designed so that its arc of contact with the specimen does not exceed 15° and the width of contact is less than 6.5 mm (which refers to 40 / 6 ≅6.5).

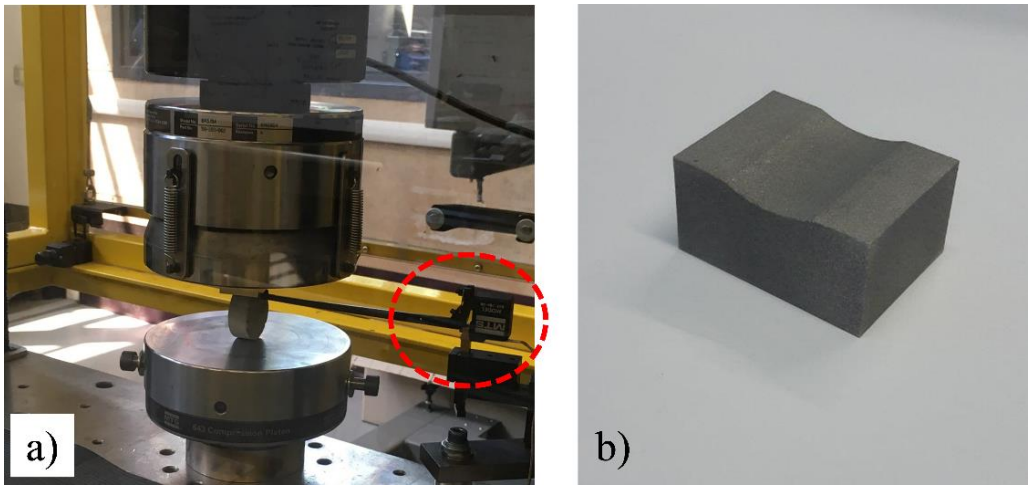

Figure 29. The Brazilian disk test; (a) apparatus, based on the ASTM configuration, (b) curved bearing block.

According to the standard, grease should be used to decrease the friction between the specimen and the testing apparatus. It can also provide a better self-adjustment of the specimens during the loading. The applied load of the compressive platen was measured automatically by the load cell of the apparatus. The measurement of the displacement of the specimen is not described in the ASTM standard. It was decided to measure the displacement of the specimen by means of a displacement gauge contacting extensometer. As can be seen in Figure 29a, the flexible tip of the extensometer is located at the center of the lower face of a curved bearing block. However, since the extensometer itself is fixed to the fixture of the testing machine, the displacements of all the components in between are measured. Therefore, in the configuration expressed in Figure 29a, the experimental data provided by the extensometer contains the displacements of both the specimen and the cylindrical steel blocks (which is placed between the specimen and the fixture of the apparatus). This set of data therefore doesn't represent the actual displacement of the specimen, but since the mechanical properties of the steel blocks are known, they can be replicated in the numerical simulations as well. This set up is thus a convenient way to record the experimental data of the Brazilian disk test in terms of displacement.

The tensile splitting strength is defined by means of equation (40).

$$\sigma_t = \frac{2F_{\max}}{\pi d_m t_m} \tag{40}$$

Where, $F_{\max}$ is the maximum load recorded during the tests, d_m and t_m are the diameter and thickness of the specimens, respectively. The standard suggests reporting the repeatability limit as well. The experimental results of the Brazilian disk test in terms of maximum force and its corresponding displacement, the average tensile splitting strength and repeatability limit are listed in Table 8. The ratio between the repeatability limit and the tensile splitting strength is also reported as a measure of the variability of the results.

The variability of the tensile splitting strength of all the four classes of specimens is acceptable and in agreement with the results provided by other experimental programs, i.e. (Standard, 2008). The force – displacement diagrams of each classes are shown in Figure 30, separately.

Figure 31 illustrates the broken specimens of the Brazilian test performed within this research work. The black lines and the dashed red lines represent the diametral loading direction and the fracture pattern, respectively. The tensile failure mode is observed for all types of specimens. The fracture pattern was independent of the thickness-to-diameter ratio and the crack initiated near the interface between the specimen and the bottom steel plate and propagated along the loading direction. The failure modes observed during the experimental tests are also in agreement with the reported results for sandstones under a Brazilian test in (Basu et al., 2013); where the specimen failed by a central crack mainly parallel to the loading direction.

Table 8. The experimental results of the Brazilian disk test for the four different samples.

	$F_{max}[kN]$	$\Delta l_{max}[mm]$	$\hat{\sigma}_{bt}[MPa]$
G1	5.835	0.198	5.80
G2	6.155	0.177	6.39
G3	5.266	0.235	5.21
Average			**5.80**
Repeatability			**1.67**
Repeatability/Average			**0.28**

	$F_{max}[kN]$	$\Delta l_{max}[mm]$	$\hat{\sigma}_{bt}[MPa]$
H1	7.153	0.191	5.55
H2	6.708	0.182	5.19
H3	6.445	0.203	5.22
H4	7.108	0.157	5.49
H5	7.294	0.182	5.48

Average	**5.39**
Repeatability	**0.48**
Repeatability/Average	**0.09**

	$F_{max}\,[kN]$	$\Delta l_{max}\,[mm]$	$\hat{\sigma}_{bt}\,[MPa]$
I1	7.889	0.220	5.28
I2	10.324	0.264	6.90
I3	9.145	0.283	6.15
Average			**6.11**
Repeatability			**2.29**
Repeatability/Average			**0.37**

	$F_{max}\,[kN]$	$\Delta l_{max}\,[mm]$	$\hat{\sigma}_{bt}\,[MPa]$
J1	8.513	0.320	4.94
J2	8.772	0.279	5.09
J3	9.762	0.294	5.527
J4	7.666	0.254	4.45
Average			**5.01**
Repeatability			**1.25**
Repeatability/Average			**0.25**

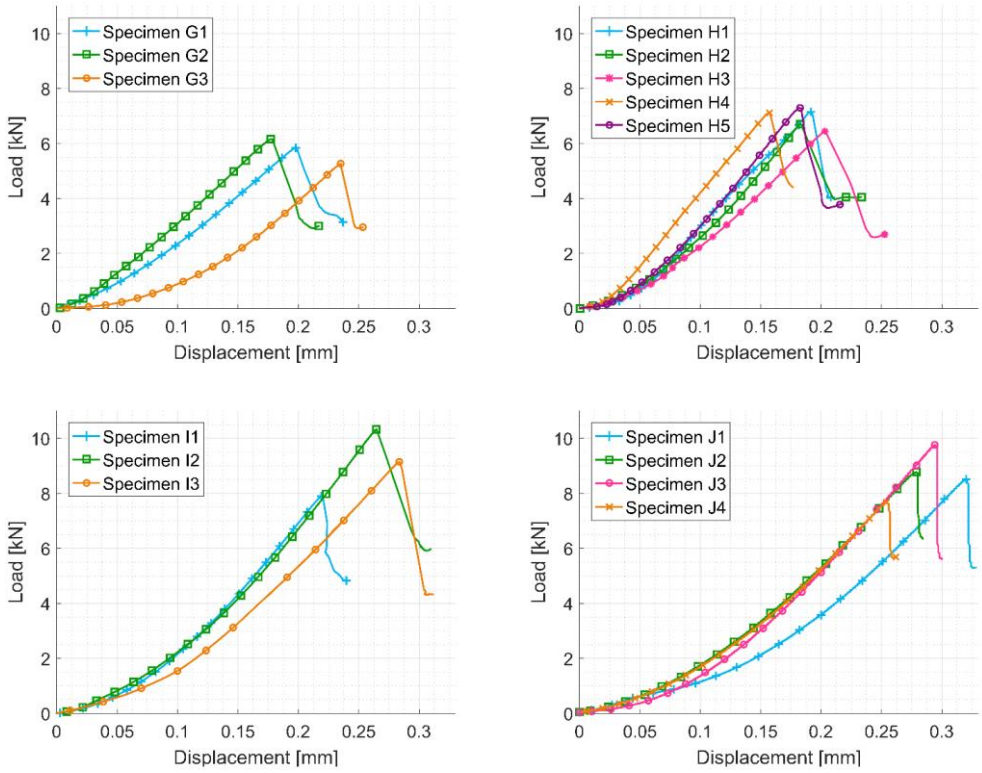

Figure 30. The force-displacement diagrams of the Brazilian disk test for the four different classes of specimens.

Figure 31. The broken specimens of the Brazilian disk test.

Chapter 8
Flexural test

Rock engineers perform the Brazilian and the Flexural (four-point bending) test to investigate the tensile behaviour of rock materials. These tests are designed to investigate indirectly a normal tensile stress state (at least) in a specific portion of the specimen. The numerical and experimental investigation of the mechanical behaviour of a middle strength rock material which is subjected to a Four-Point Bending (or Flexural) test is the aim of this research study.

The Four-Point Bending test is an indirect way to estimate the tensile strength, which consists of a beam in flexure. The strength of the beam, in this test, is expressed mainly in terms of modulus of rupture, which usually tends to overestimate the tensile strength up to one-hundred percent (Biolzi et al., 2001). This overestimation is mainly caused by the hypothesis of the test which assumes that the mechanical characteristics, i.e. the stress-strain behaviour, are linear all the way through the critical cross-sectional area of the beam (Jaeger and Cook, 1979). Due to the sensitivity of this test to the boundary conditions, it may be inaccurate in large displacement (which is similar to the direct tensile test) (Cattaneo and Rosati, 1999). In addition to these difficulties, the strength of quasi-brittle materials, e.g. rock, is considered to be dependent on their size and scale (Bažant and Kazemi, 1990; Biolzi and Labuz, 1993; Labuz and Biolzi, 1991). However, the Flexural test is considered as the simplest method to investigate the creep (time-dependent behaviour) of rock (Price, 1964), and accordingly, represents an interesting alternative for the investigation of the stress-strain relationships (Laws, 1981; Mayville and Finnie, 1982). The experimental campaign designed for this research study follows the protocols of the ASTM standard and the results can therefore be easily compared with similar studies, i.e. on other materials (Mardalizad et al., 2017c).

The experimental configuration for the Flexural test is designed based on the protocols of the ASTM standard (ASTM, 1998). This configuration consists of a rectangular cubic specimen which is supported by two fixed rollers near the end of its length span (see Figure 32a). Thus, the specimen is loaded vertically by means of two compressive rollers at a certain distance from the center of the specimen. This symmetrical configuration causes nominally zero shear forces, and accordingly constant bending moment between the two compressive rollers. The normal tensile and compressive

stresses appear at the top and bottom of this middle span, respectively. According to the beam theory, the maximum principal stress corresponding to the ultimate loading value can be determined, which is called the flexural strength and gives a rough approximation of the principal tensile strength.

The flexural strength tends to overestimate the tensile strength, because the measuring process considers a linear relationship (as the stress-strain behaviour of the material) at the beam critical cross-section. Furthermore, all the materials have a certain amount of anisotropic level in their structure (Biolzi et al., 2001). The flexural strength σ_{flex} [MPa], which is given by the equation (41), can be considered as a parameter to validate the numerical models.

$$\sigma_{flex} = \frac{3WL}{4bd^2} \tag{41}$$

Where, W was measured as the maximum applied force. The experimental tests within this study were performed on five specimens of Pietra Serena sandstone with the same geometries. The span length L, width b and height d of all the specimens were equal to 318, 102 and 32 [mm], respectively. However, the total length of the specimen was measured as 381 [mm].

Two pairs of steel rods were embedded to the testing apparatus (see Figure 32). The axes of lower rods were fixed to the bed of testing machine while the upper rods were displacement controlled by means of a compressive platen. According to (ASTM, 1998) the speed was set to 0.2 [mm/min] in order to apply the load at a uniform stress rate of 4.14 [MPa/min].

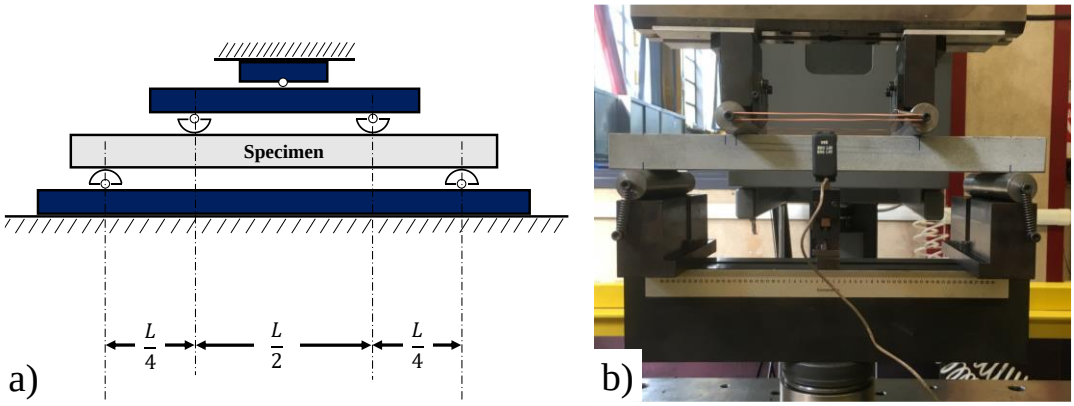

Figure 32. (a) ASTM arrangement of Flexural test (ASTM, 1998); (b) corresponding experimental layout of this research work (Mardalizad et al., 2017c).

This study is aimed to investigate the mechanical response of the rock based on both the maximum loading and the displacement. The applied load of the compressive platen was measured automatically by the load cell of the apparatus. It is not mentioned how to measure the displacement of the specimen on the ASTM standard. It was decided to measure the displacement of the specimen by means of a displacement gage contacting extensometer. As can be seen in Figure 33, the flexible tip of the extensometer is located at the center of the lower face of specimen. However, since the extensometer, itself, is fixed to the fixture of the testing machine, the displacements of all the components in between are measured. Therefore, in the configuration expressed in Figure 33, the experimental data provided by the extensometer contains the displacements of the specimen, the fixed rollers and the steel blocks between the rollers and the fixture of the apparatus. This set of data therefore doesn't represent the actual displacement of the specimen, but since the mechanical properties of the rollers and the steel blocks are known, they can be replicated in the numerical simulations as well. This set up is thus a convenient way to record the experimental data of the flexural test in terms of displacement.

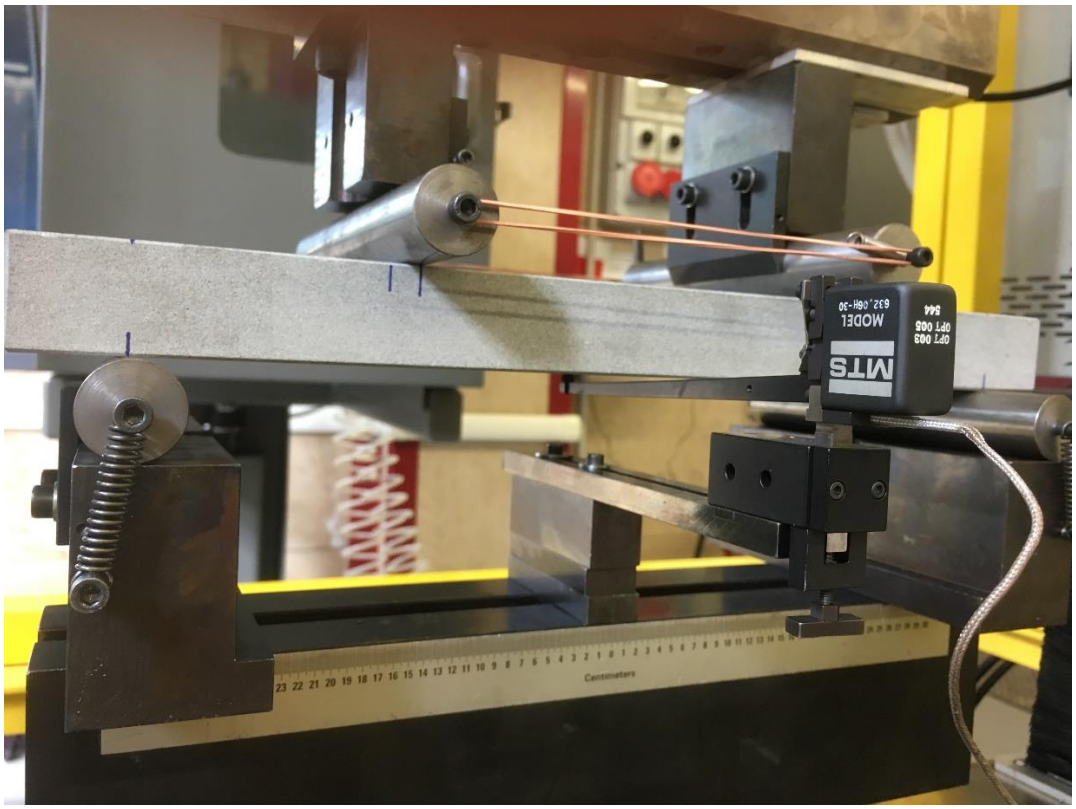

Figure 33. The extensometer set up on the flexural test configuration (Mardalizad et al., 2017c).

The broken specimens after performing the flexural test are indicated in Figure 34. In all of the specimens, cracks initiate at the lower part, which is subjected to tension stresses and then propagate in an upward manner through the depth. Also, the cracks are located under (and close to) the section of the specimens which are in contact with the moving rods.

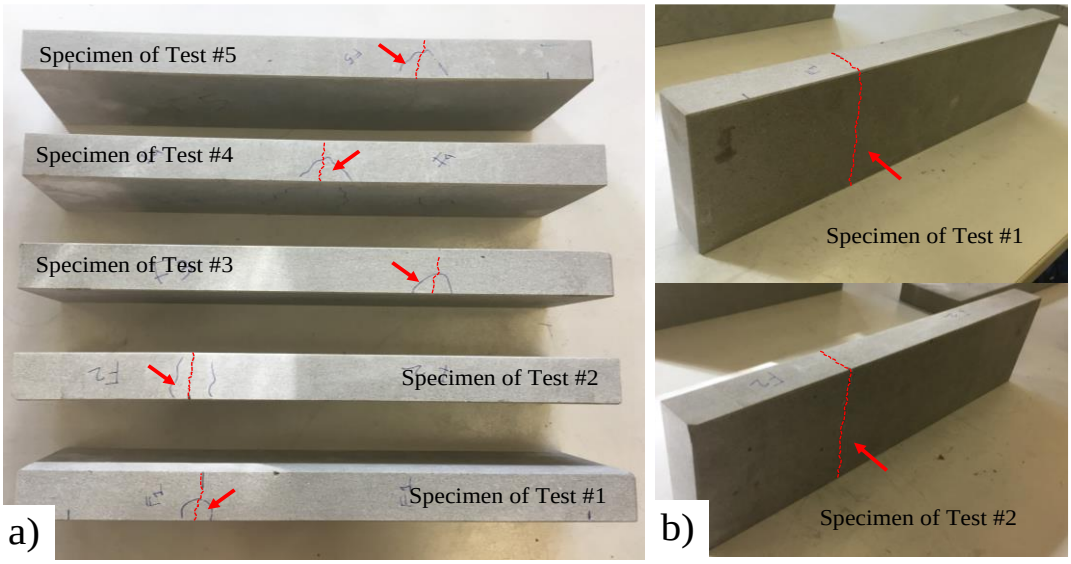

Figure 34. The broken specimens after performing the flexural test; (a) front view; (b) isometric view (Mardalizad et al., 2017c).

The maximum load, displacement and the flexural strength are reported in Table 9, separately for each specimen and then as average values, 95% Confidence Interval ("95% CI") and standard deviations. Figure 35 also expresses the load-mid span displacement diagram of the all specimens.

Table 9. the experimental results of the flexural test (Mardalizad et al., 2017c)

	Maximum Load [kN]	Maximum displacement	Flexural Strength [MPa]
Specimen K1	3.59	0.502	8.3124
Specimen K2	4.258	0.662	10.024
Specimen K3	2.963	0.313	6.831
Specimen K4	4.16	0.669	9.7927
Specimen K5	4.206	0.628	9.9576
Average value	3.8354	0.5548	8.9836
"95% CI" of average value	[3.1433; 4.5275]	[0.36737; 0.74223]	[7.2530; 10.7140]
Standard deviation	0.55736	0.15095	1.3937

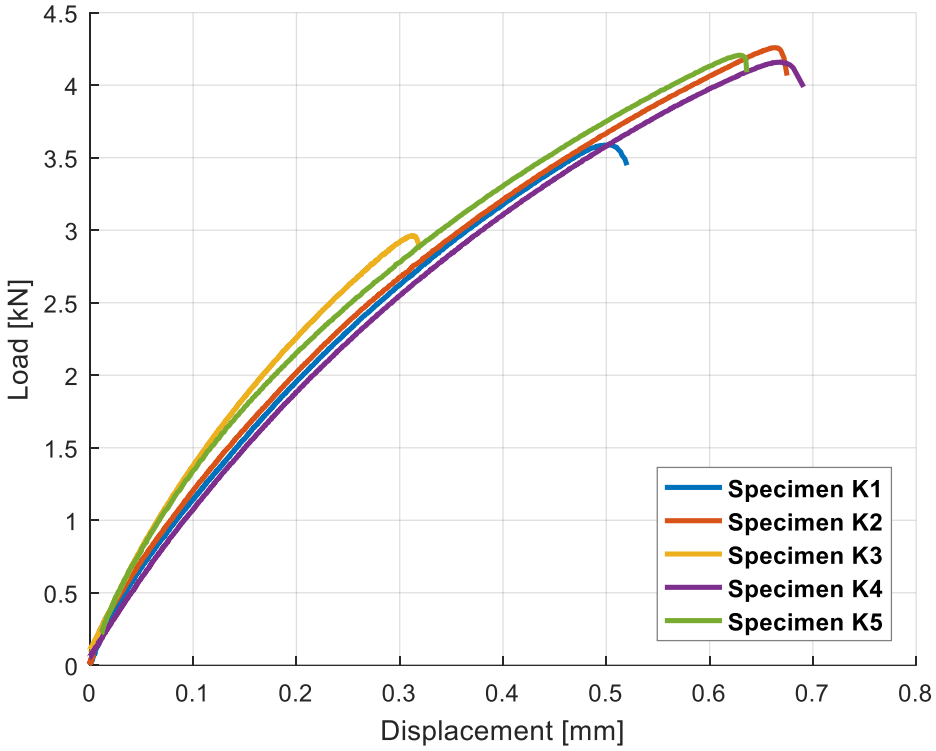

Figure 35. The load-displacement diagram of the flexural test (Mardalizad et al., 2017c).

The shape of the load-mid span displacement, represented in Figure 35, indicates a significant non-linear behaviour until the failure. The failure is denoted by a sudden drop of the loading level. A study by (Meda, 2003), investigated Pietra-Serena sandstone under a flexural test. They performed the tests on specimens with different shapes and considered a notch in the middle-span of the specimens to assure that the crack takes place at the center. The experimental data provided by Meda et al. are in a good agreement with the results obtained during this research work where the geometries are similar to each other; i.e. the flexural strength and the load-displacement diagrams of the Meda's work were reported as 9.1 MPa and 3.4 mm, respectively.

Chapter 9

Triaxial Compression test

This experimental program includes a series of triaxial tests at increasing confining pressures. These tests were carried out with a triaxial apparatus available at geotechnical division of the Material Testing Laboratory, Politecnico di Milano (Cividini et al., 1992) by employing the protocols of the ASTM standard (ASTM, 2004). This apparatus is mainly composed of a cell and a loading frame (see Figure 36). The cell is designed to perform tests on 100 mm diameter samples up to 200 mm height, and to withstand a confining pressure up to 50 MPa.

Figure 36. The triaxial testing apparatus (Cividini et al., 1992).

The cell rests on the circular bottom plate of the loading frame which moves upwards to increase the axial load. The loading frame in conjunction with the load cell it is equipped with, allow a maximum loading capacity of 2200 kN. Both the confining pressure and the load frame are driven by two independent servo-hydraulic system, with a close loop control managed by a dedicated controller. The equipment allows the performance of either pressure/load-controlled or displacement-controlled tests or a combination of the two.

The feedback control for the confining pressure includes a pressure transducer HBM - Model P3M (measuring range: 0÷50 MPa, accuracy: 0.2%), while the applied force is measured by a load cell BLH - Model CP21 (capacity 2225 kN, accuracy 0.05% RO). The axial displacements are measured by means of a system which refers the measurement on the axial distance between the upper and the lower surface of the sample. This is achieved by means of an external frame, which lies on an aluminium rod, in contact with the top surface of the specimen through a top cap hole, and which, at its bottom, holds an LVDT (NE – Model SE375 – Class A). The LVDT, in its turn, maintains the contact with the specimen bottom base (with the help of a second aluminium rod inserted into a bottom hole) thanks to its return spring. Therefore, any changes in the specimen height cause a correspondent change in the transducer rod position.

The triaxial tests of this experimental campaign was performed on 5 cylindrical specimens, with an identical nominal diameter and a height equal to 100 mm and 200 mm, respectively. Each sample was jacketed with a reinforced 3 mm thick rubber membrane. After being placed on the cell base plate, the top cap was applied to the upper base and the membrane was tightened to both the top piston and the bottom base, by mean of two worm gear hose clamps, to prevent the hydraulic oil from penetrating the rock during the test. Finally, the cell was assembled and inserted into a load frame with all hydraulic lines properly connected.

All specimens were subjected to a stress state (see Figure 37) assumed to be isotropic, which increased at an average constant rate of 0.3 MPa/s (AB) up to the required value $\bar{\sigma}$ for each test (10, 20 or 28 MPa). In fact, to accurately control the isotropic stage and prevent any test failure, each increase stress consisted of two steps: an initial increase of s_1 followed by a s_3 increase at constant s_1. The maximum difference between s_1 and s_3 was always maintained below 0.1 MPa. The samples were then sheared under displacement control settings at a constant rate of 0.001 mm/s up to failure (BC).

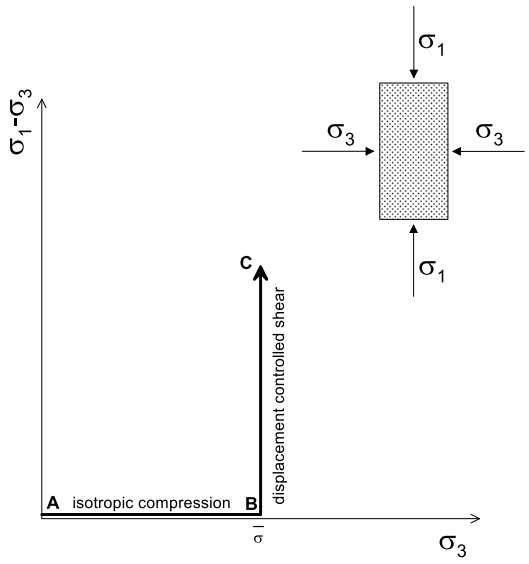

Figure 37. The diagram of the stress path for the triaxial compression test.

The test results are summarized in Figure 38 and Figure 39 for the isotropic stress and the shear stages, respectively. Figure 38a clearly shows the isotropic stress state increase procedure as previously described. Figure 38b presents the specimen deformations during this increment, showing the almost similar behaviour of all specimen except for specimen *B2* which differed slightly from the others.

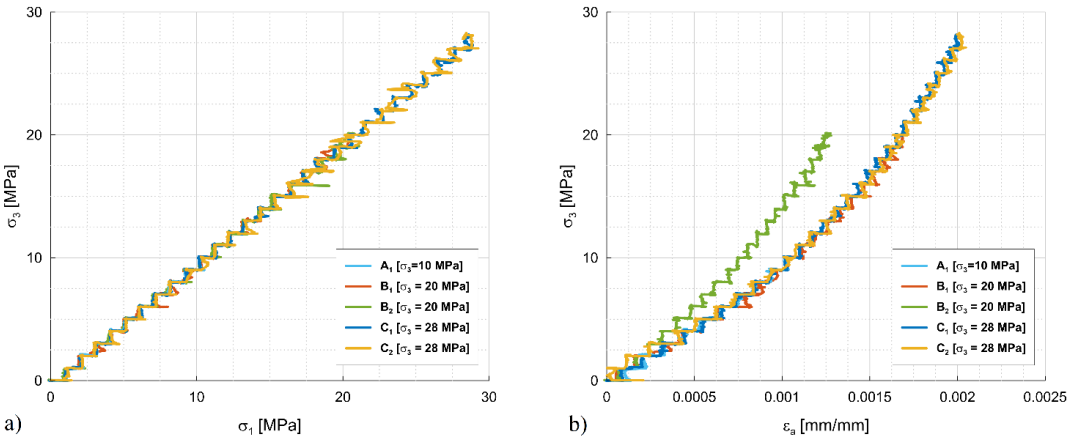

Figure 38. The confining pressure-axial strain diagrams; (a) isotropic stage, (b) deviatoric stage.

A similar difference can also be identified in Figure 39 and Figure 40, in which all the shear stages of all the performed tests are compared. The maximum deviatoric sample *B2* differs from the other test results since the maximum deviatoric load rose to a value comparable with the 28 MPa tests (see Table 10). Also, the initial stiffness

appeared to be comparable with the 28MPa tests. The reason of this undesired response of specimen *B2* (lower compressibility in the isotropic stage and a higher resistance in the shear stage) is probably due to both the specimen arrangement in the load cell and the mechanical locking along the failure surface, which also caused an immediate decrease of the deviatoric stress after failure. A comparison of the failure mode of each specimen is also presented in Figure 41.

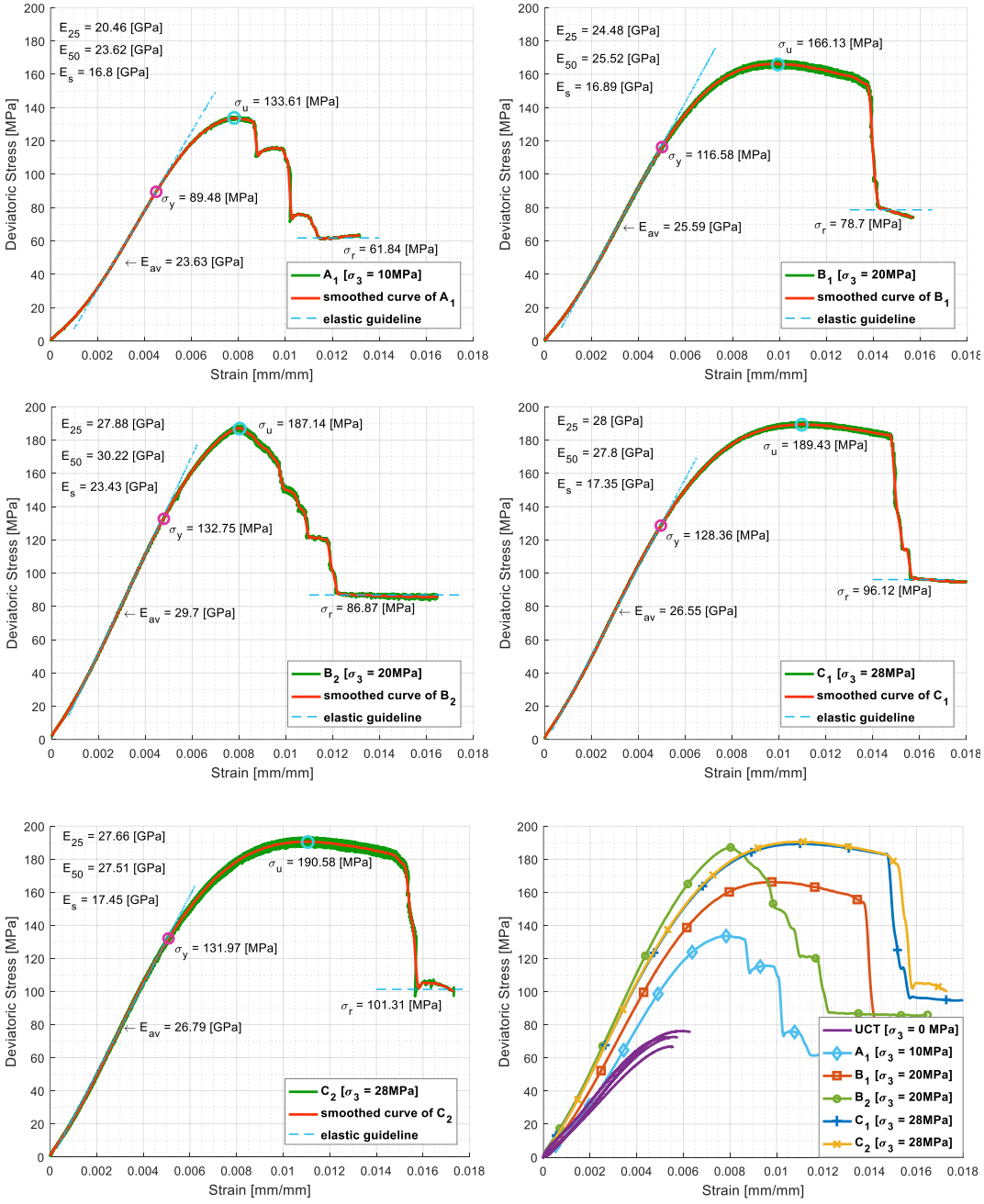

Figure 39. The experimental results of the triaxial compression tests, in terms of deviatoric stress-axial strain.

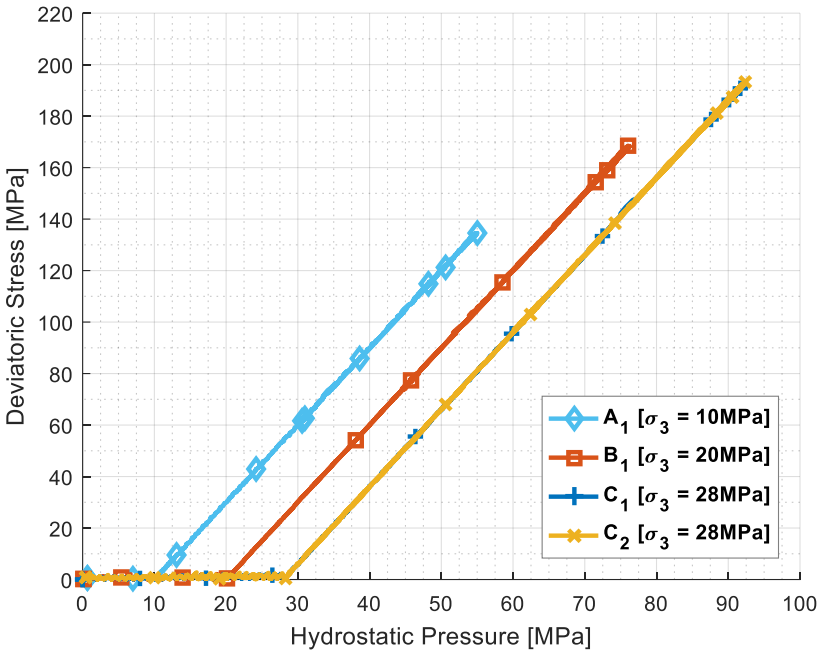

Figure 40. The experimental results of the triaxial compression tests, in terms of deviatoric stress-hydrostatic pressure.

Table 10. The experimental results of the triaxial compression test for three levels of confining pressures.

	$\sigma_y[MPa]$	$\sigma_u[MPa]$	$\sigma_r[MPa]$	$E_{25}[GPa]$	$E_{50}[GPa]$	$E_s[GPa]$	$E_{av}[GPa]$
A1	89.48	133.61	61.84	20.46	23.62	16.80	23.63
B1	116.58	266.13	78.70	24.48	25.52	16.89	25.59
B2	132.75	187.14	86.87	27.88	30.22	23.43	29.70
C1	128.36	189.43	96.12	28.01	27.83	17.35	26.55
C2	131.97	190.58	101.31	27.65	27.51	17.45	26.79

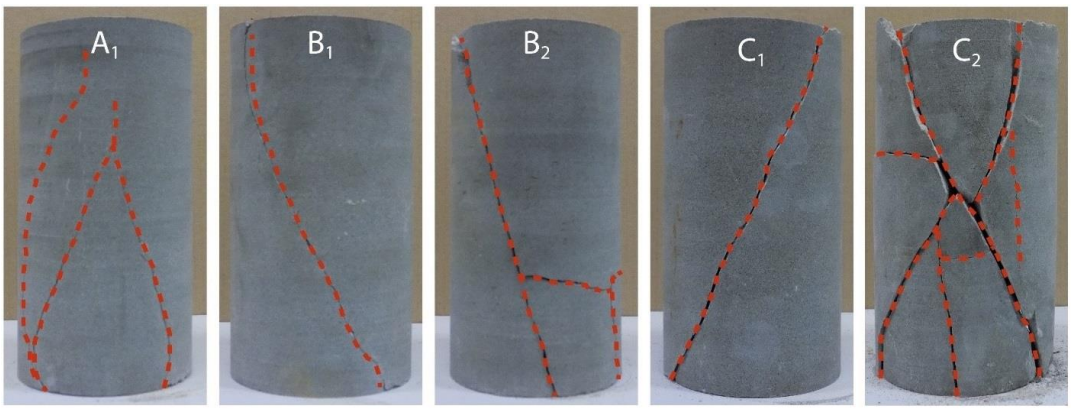

Figure 41. The broken specimen of the triaxial compression test.

Chapter 10

Punch penetration test

The penetration of a tool into rock by indentation is the basic process in various excavation machines, such as roller disc cutters and percussive drills (Chen and Labuz, 2006; Kahraman et al., 2012; Kalyan et al., 2015). Depending on the rock strength, there are two basic procedures for rock excavation: shearing for soft to medium strength rocks, and indentation for medium to hard rocks (Fowell, 1993). The oil and gas reservoir rocks, e.g. Berea sandstone, are classified as medium strength rocks (UCS ranges from 40 to 80 MPa). Therefore, exploiting numerical modelling to investigate the indentation process is an interesting case of study in petroleum industries.

Figure 42 illustrates schematically the indentation process by a conical tool (Fowell, 1993). This process can be divided into different phases: (a) creation of a rock crushed zone, (b) formation of a cracked zone, (c) crack propagation and chipping (Heiniö, 1999). When the tip of the tool initiates the penetration, the stress at the rock surface increases due to the increasing load on the tool. This progressive local deformation underneath the tool tip develops a crushed zone consisting of highly micro-fractured and irreversibly deformed rock. As the loading increased and the tool penetrates deeper, the micro-cracks in the crushed zone propagate and coalesce to form the primary cracks across the rock. The location of these cracks depends on the shape of the tool tip (Zou, 2017). The concentrated energy at the crack tip is increased because of further penetration and once it reaches a certain limit, the crack grows abruptly and, upon reaching the rock surface, forms chips or spalls. These fractures cause a sudden drop of the applied force and further penetration requires the applied force to be increased to a higher level (Anemangely et al., 2018).

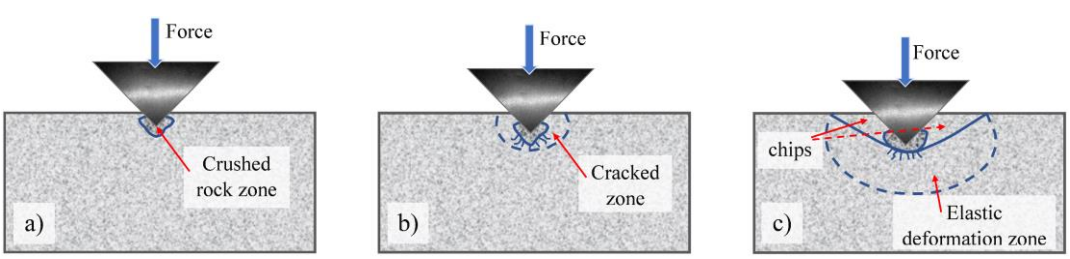

Figure 42. The phases of rock breakage; (a) creation of the crushed zone, (b) crack formation, and (c) chipping and crack propagation (Heiniö, 1999).

The indentation process illustrated in Figure 42 is well attested in the Punch Penetration test (PPT) and, hence, many studies have considered this experimental test as an adequate mean to evaluate the drillability of rock materials (Copur, 2003; Dollinger et al., 1998; Jeong et al., 2016; Yagiz, 2009; Yagiz and Rostami, 2012). The punch penetration test was originally designed by (Handewith, 1970) to investigate the brittleness behaviour of rock materials.

This is a non-standard test and different approaches were proposed for the apparatus, data analysis method and procedures of this test (Dollinger et al., 1998). Generally, the procedures of this test consist of a conical punch loaded vertically against a rock sample that is confined by a casing material into a steel ring (Yagiz, 2009). The outcome of this test can be reported as the force-penetration depth diagram. There are many research studies that tried to relate this diagram with the mechanical properties of a rock by different indices, such as brittleness index, Rock Drillability index (RDI), UCS, BTS and fracture toughness, etc. (Anemangely et al., 2018; Copur, 2001; Kahraman, 2001; Ramezanzadeh et al., 2008; Yagiz, 2009).

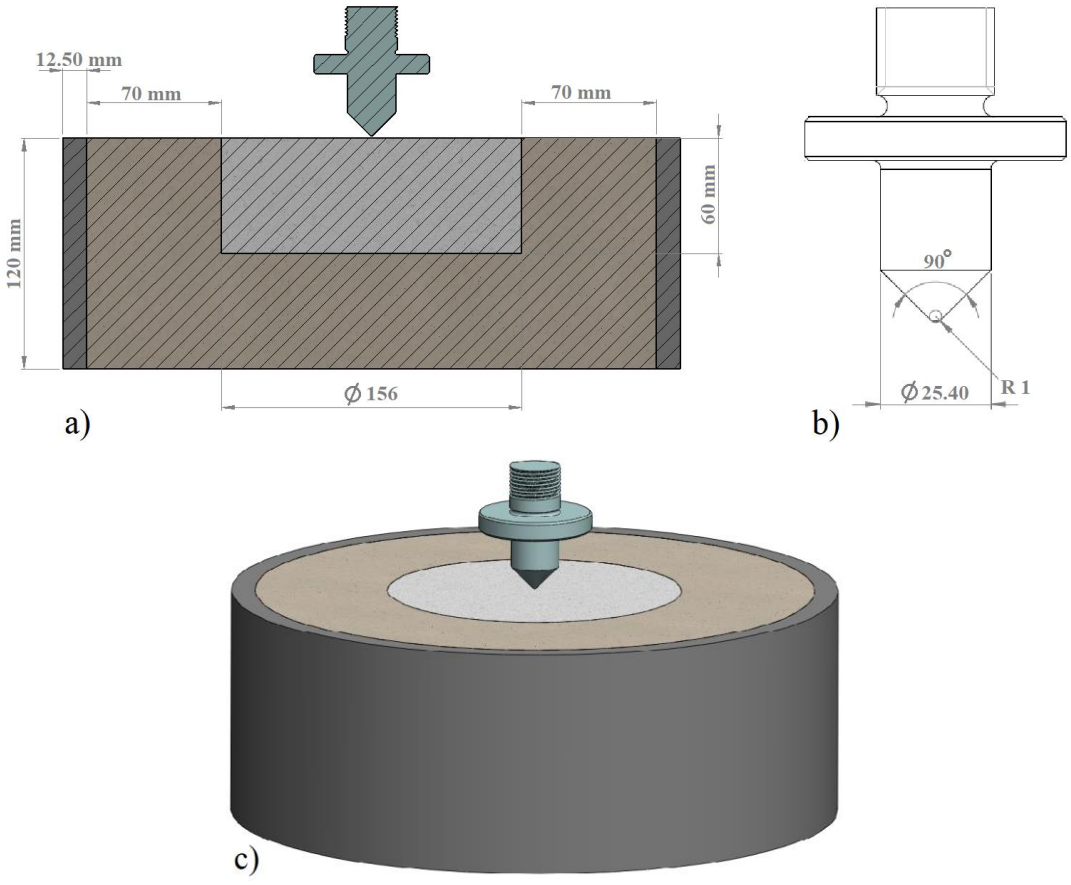

Figure 43. Schematic representation of the punch penetration test; (a) sample, (b) punch, and (c) 3D configuration.

Since the goal of this PhD project is to critically discuss the comparison between numerical simulations and experimental results, hence, it is not focused on performing various experimental tests on different rock samples. Figure 43 represents the schematic of the PPT sample investigated in this study. The corresponding dimensions of the sample and the punch were designed by considering the recommendations obtained from (Yagiz, 2009) and (Jeong et al., 2016).

The experimental sample consists of four parts: rock specimen, concrete, steel tube and punch (see Figure 43c). The rock specimen has a cylindrical shape (with a 156 mm diameter and a 60 mm length) made of Pietra-Serena sandstone. The material of the punch is 52SiCrNi5, a tempered steel with the ultimate tensile strength (UTS) in the range of 1450 to 1750 MPa. A heat treatment (quenching and tempering) was applied to the punch to increase the Rockwell toughness up to 40 Rc. The quenching of the punch was performed at a temperature close to 850°C with a polymer air cooling, while the tempering at a temperature ranging from 400°C to 450°C was exploited with air cooling. The steel tube is made of steel Fe360, with the inner diameter and the thickness equal to 296 mm and 12.5 mm, respectively. The casing material used to avoid the dislocation of rock sample against the tube, is a high-strength concrete composed of a mixture of 750 g of sand (maximum aggregate size equal to 15 mm), 250 g of R52.5 cement (UCS=52.5 MPa) and 400 cc of water. The tests were executed on two samples that underwent a seven-day ageing period (hydration) for the concrete to reach the maximum compressive strength. The penetration load was applied with a servo-control loading machine at a constant rate of about 0.02 mm/s. The normal force and penetration depth were measured automatically by the apparatus. The loading capacity of this machine is about 200 kN±10.

The indentation processes are shown in Figure 44, Figure 45 and Figure 46. The initial cracks were propagated underneath the loading spot. A dense grid of radial cracks was developed due to the generation of additional cracks between the initial ones. Afterwards, an obvious chipping process could be observed upon increasing the loading. The gradual propagation of these additional cracks produced rock chips or spalls and induced radial cracks even in the concrete. The crack propagation in the concrete means that the confinement on the rock sample decreased so that the normal load applied to the rock can reach a maximum value eventually.

It should be noted that failure of the rock under the punch is related to initiation of chipping and subsequently brittleness feature of rock. It is known that rock must absorb enough energy before chipping and broken; and then, it suddenly loss its strength with little or no plastic deformation under the punch. This behavior of rock could be

monitored from the beginning of the test to the end by observing the force–penetration data chart. On obtained chart, high brittle rock demonstrates fluctuated force–penetration relationship due to the both large forces drop and large chips (Yagiz, 2009).

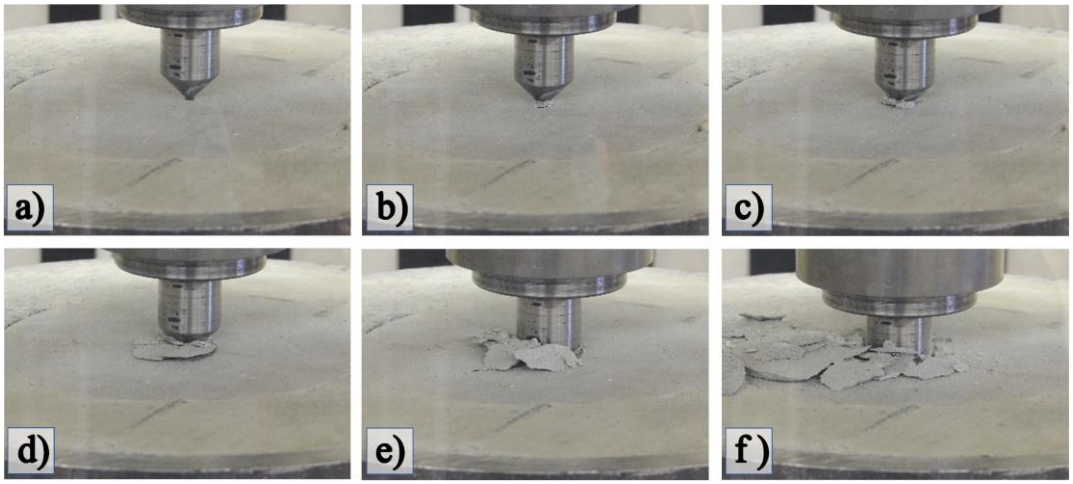

Figure 44. First punch penetration test; the figures were captured at; a) 0.2 mm, b) 1.5 mm, c) 5.3 mm, d) 9.5 mm, e) 14.6 mm, and f) 15.7 mm.

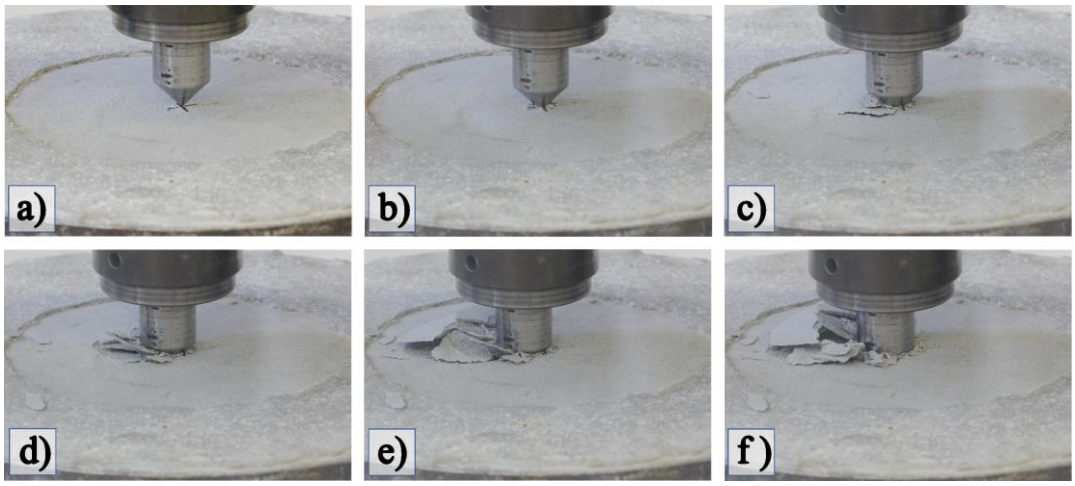

Figure 45. Second punch penetration test; the figures were captured at; a) 0.3 mm, b) 2.5 mm, c) 7.2 mm, d) 10.5 mm, e) 14.5 mm, and f) 16 mm

Figure 47 shows the normal force-penetration depth graphs measured during the experimental tests. Utilizing the punch penetration test, the obtained force-penetration graph has three distinct phases. In the first phase, there is elastic deformation and very fine crushing of rock surface. In the second phase, there is crushing of rock fabric as in the third phase chips of rock are formed. Elastic deformation and very fine

crushing are represented by a linear relation. Crushing in represented by "steps" on the profile and chipping of the rock fragments is represented by peaks (Yagiz and Rostami, 2012).

Based on the normal force-penetration depth diagram obtained from the PPT, (Yagiz, 2009) suggested an experimental rock brittleness index (in kN/mm) defined as the ratio of the maximum applied force (kN) to the corresponding penetration depth (mm). By means of the diagrams reported in Figure 47, the average experimental brittleness index for Pietra-Serena is 12.6 kN/mm. Table 11 presents the brittleness index of three rock materials with relevant mechanical properties close to those of Pietra-Serena. Yagiz concluded in (Yagiz, 2009) that these mechanical properties, which are unconfined compressive strength (UCS), uniaxial tensile strength (UTS) and density, have a significant effect on the brittleness of rock materials.

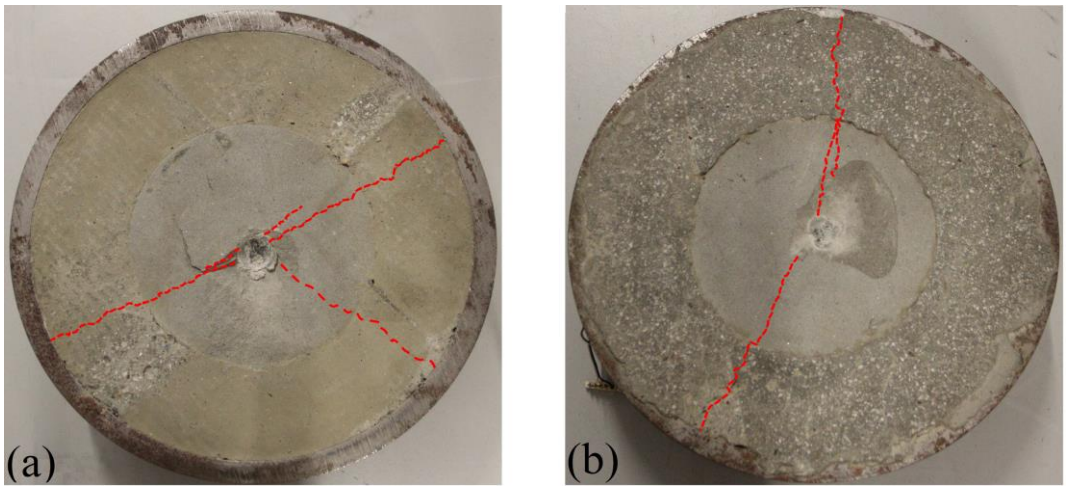

Figure 46. Fracture pattern on the surface after removing debris from the crater; (a) first and (b) second PP test.

By inserting the mechanical properties of Pietra-Serena into equation **Error! Reference source not found.**, the predicted brittleness index BI_p is 13.8 kN/mm, which has an 8% relative error in comparison to the experimentally measured brittleness index BI_m. Thus, the experimental results of the PPT on Pietra-Serena are in accordance with the Yagiz model.

Table 11. Comparison of the mechanical properties and the brittleness index of some intact rock provided by (Yagiz, 2009) vs. Pietra-Serena sandstone studied within this study.

Project name	Rock class	Rock type	$\rho_r\left(kN/m^3\right)$	$\sigma_c\left(MPa\right)$	$\sigma_t\left(MPa\right)$	$BI_m\left(kN/mm\right)$

Metrowest Water Supply, Boston, USA	Metamor-phic	Argillite	24.6	52	4.7	13.0
Plateau Creek Pipe-line, Colorado, USA	Sedimentary	Siltstone	22.1	82	8.7	13.0
Rock Saw Project, Mexico	Volcanic	Basalt-ve-sicular	22.9	73	5.9	12.7
Pietra-Serena	Sedimentary	Sandstone	20.1	71	6.8	12.6

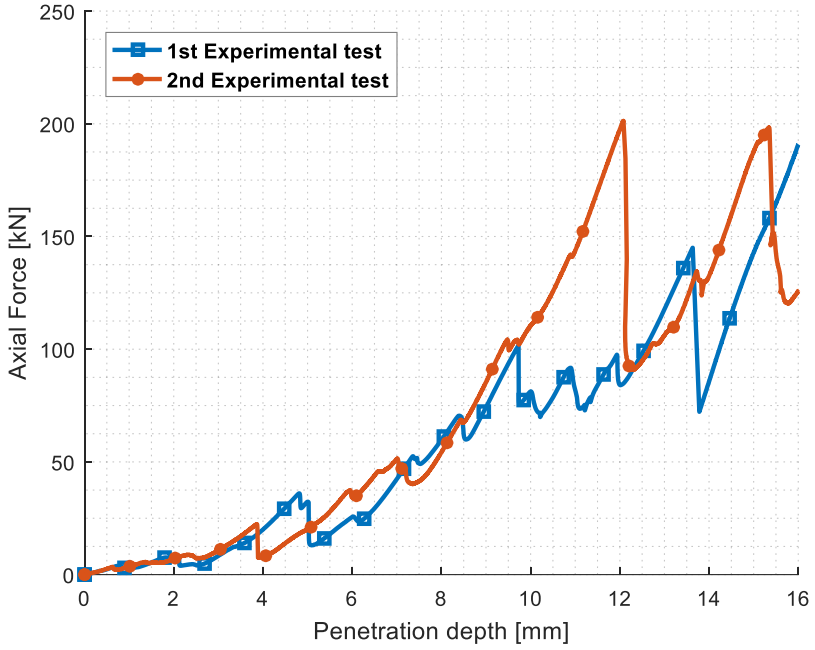

Figure 47. The load-penetration depth diagram of the punch penetration test performed on Pietra-Serena sandstone.

Chapter 11
Dynamic Brazilian disk test by SHPB

The high strain rates tests were carried out using a Split Hopkinson Pressure Bar (SHPB) device at Tampere University of Technology. Flat-ended pressure bars of AISI 4340 steel with diameter of 22 mm and the length of 1200 mm were used as well as a striker bar of the same materials with the length of 300 mm. The bars were resting on adjustable stanchions and were supported by bearings to allow the accurate alignment of the bars in z- and y-directions. As the striker bar impacts the free end of the incident bar, three optical IR sender-receiver pairs measure the velocity of the impact. Two active strain gages in the middle of the incident and transmitted bar were used to measure strains in the stress bar. The strain gage signals were amplified by a Kyowa CDV 700A series signal conditioner and recorder on a 12-bit 10MSample Yokogawa digital oscilloscope. All the functions of the device, including loading of the striker bar, pressurizing, shooting of the striker, and reading the recorded data from the oscilloscope, are controlled by a computer. For more details about the instrument, the readers are referred to (Hokka, 2008). A numerical dispersion correction based on the work of Gorham and Wu (Wu and Gorham, 1997) was used to correct any changes in the signals due to the dispersion of the stress waves as they propagate in the steel bars.

The use of a pulse shaper in the Brazilian disc test is important, especially for the materials, which have a low tension to compression strength ratio, as the stress state is two-dimensional, and the force balance does not necessarily guarantee the dynamic equilibrium all over the sample. Dai et al. (Dai et al., 2010) have proven that dynamic force balance can be achieved using a pulse shaper. In this work, a disk of soft and deformable rubber with a thickness of 1 mm was used to increase the rise of time of the incident pulse and to improve the reaching of the dynamic stress equilibrium. Each test was repeated five times at the impact speeds of 10, 15, and 20m/s, with the geometrical data reported in Table 12. The specimens are prepared by the abrasive waterjet cutting method at the water jet laboratory of the mechanical engineering department of Politecnico di Milano (see Figure 48).

Figure 49 expresses schematically the high strain rate testing equipment. Two Photron SA-X2 high-speed cameras were used to record images during the high strain rate deformation of the samples. Moreover, Digital Image Correlation (DIC) was used to study the fracture of the samples during the tests. Unfortunately, the rock surface itself

does not provide enough contrast for the correlation algorithm. Therefore, the surfaces of the samples were painted with a white base coat and black spackles were applied on the surface using a permanent marker. The images were recorded at 160 kfps with the image size of 272 x 211 pixels. The recorded images were analysed with the LaVision StrainMaster (DaVis) 3D-DIC software using a subset of 9 pixels and stepsize of 3 pixels.

Table 12. The geometrical data of dynamic Brazilian disk test.

		Thickness [mm]	Diameter [mm]
10 m/s	Test 1	15.4	29.9
	Test 2	15.3	28.9
	Test 3	15.1	30.0
	Test 4	15.2	29.9
	Test 5	15.3	29.8
15 m/s	Test 1	15.1	29.9
	Test 2	15.2	30.0
	Test 3	15.2	29.9
	Test 4	15.3	29.8
	Test 5	15.0	29.8
20 m/s	Test 1	15.1	29.9
	Test 2	15.0	29.9
	Test 3	15.0	29.8
	Test 4	15.1	30.0
	Test 5	15.0	29.9

Figure 48. The prepared specimen of Pietra serena sandstone by abrasive water jet technique for dynamic Brazilian disk test.

The experimental incident stress pulses are converted from the voltages and illustrated in Figure 50 for tests 10 m/s, 15 m/s and 20 m/s. These stress pulses are not

plotted in the real time scale and shifted to the origin. The diagrams of incident strain ε_i, reflected strain ε_r and transmitted strain ε_t, as well as the diagram of forces, both at the front and the back surfaces, of all the specimens (all as the function of time) are reported in "*Appendix A: Dynamic Brazilian disk test*". The dynamic forces which are acting on the both sides of the Brazilian dynamic test can be calculated based on the dispersion corrected strain according to equation (42).

$$P_1 = A_b E_b (\varepsilon_i + \varepsilon_r), \quad P_2 = A_b E_b \varepsilon_t \tag{42}$$

Where, P_1 and P_2 are the dynamic forces acting on the front surface and the back surface (transmitted pulse), respectively. The parameters A_b and E_b are the cross-section area and the elastic modulus of the bars.

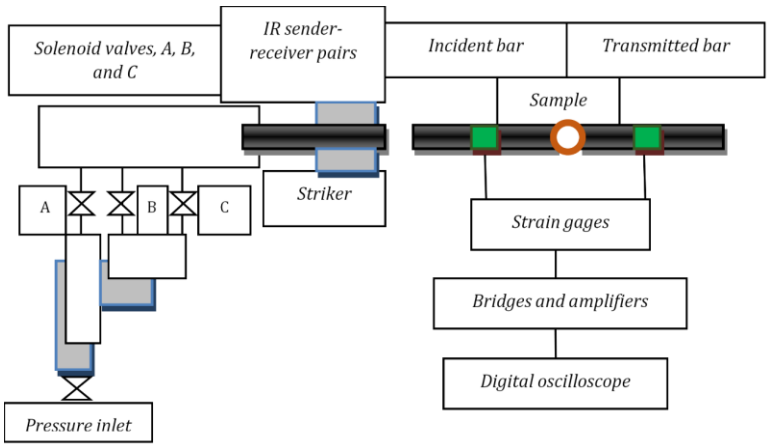

Figure 49. the schematic representation of the SHPB device.

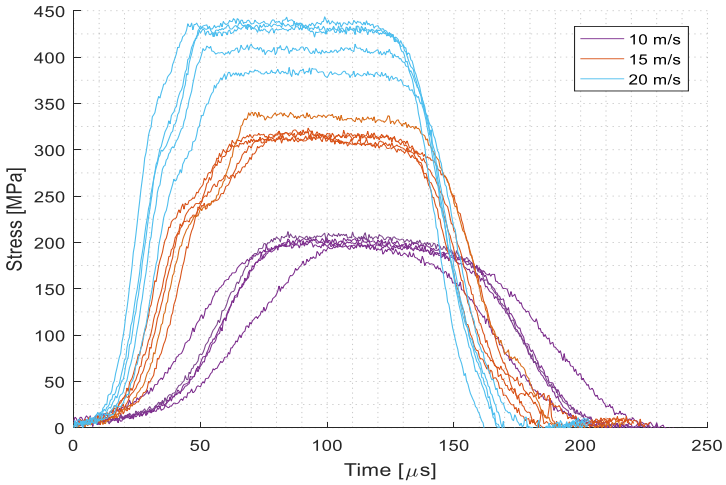

Figure 50. the incident stress pulses which are converted from the measured voltage in the experimental dynamic Brazilian disk test.

The indirect tensile strength can be calculated at the center of the disk based on the linear elastic theory of a cylindrical disk under diametral compression loading according to equation (43).

$$\sigma_t = 2P/\pi ld \tag{43}$$

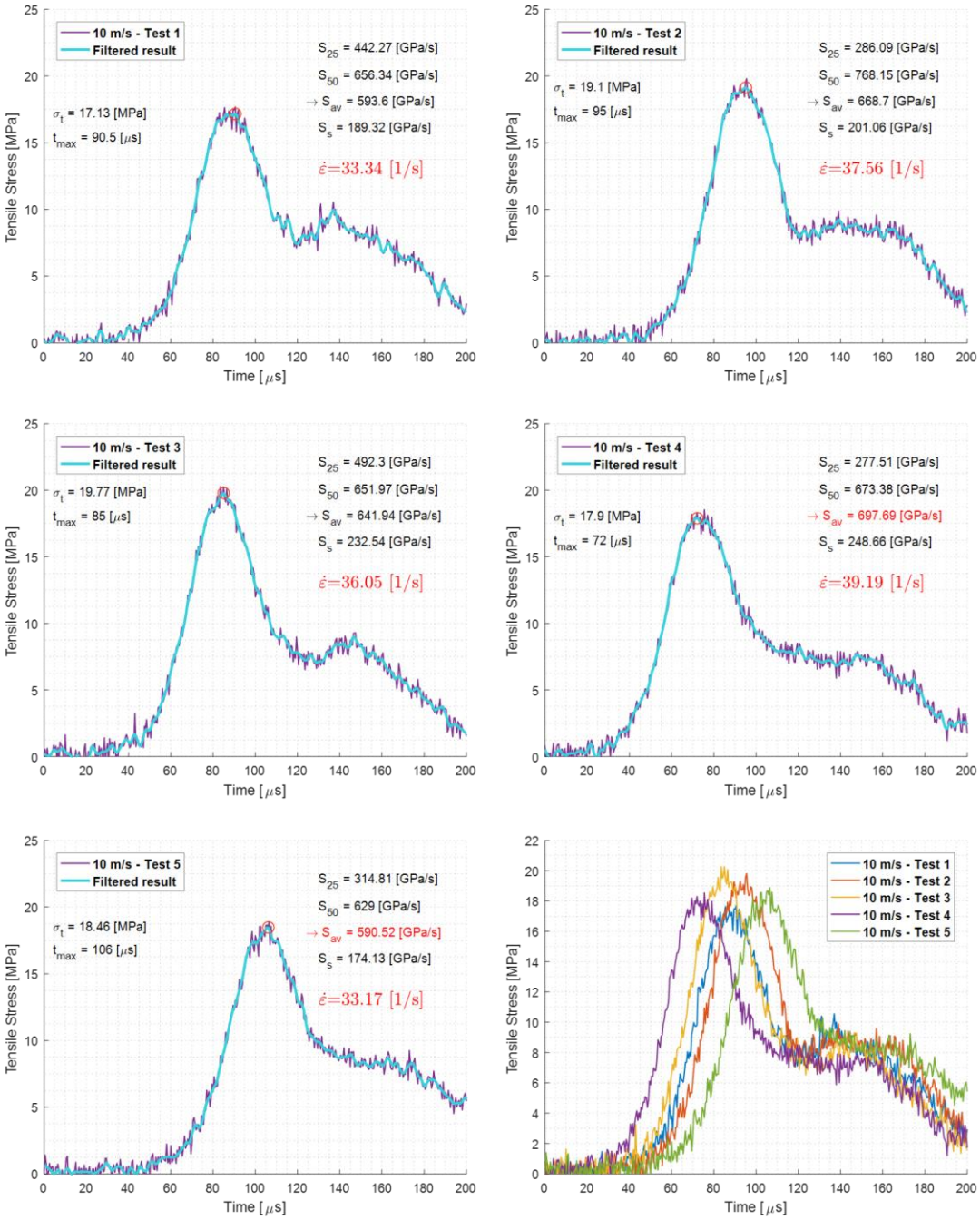

Figure 51. Experimental tensile stresses at the BD center at the striker velocity of 10m/s.

Where, the *l* and *d* are the length and the diameter of the specimens (reported in Table 12). The experimental diagrams of the indirect tensile strength-time for all the samples at 10 m/s, 15 m/s and 20 m/s striking velocities are indicated in Figure 51, Figure 52 and Figure 53, respectively, while the transmitted pulses are considered as the dynamic force *P* of the equation (43).

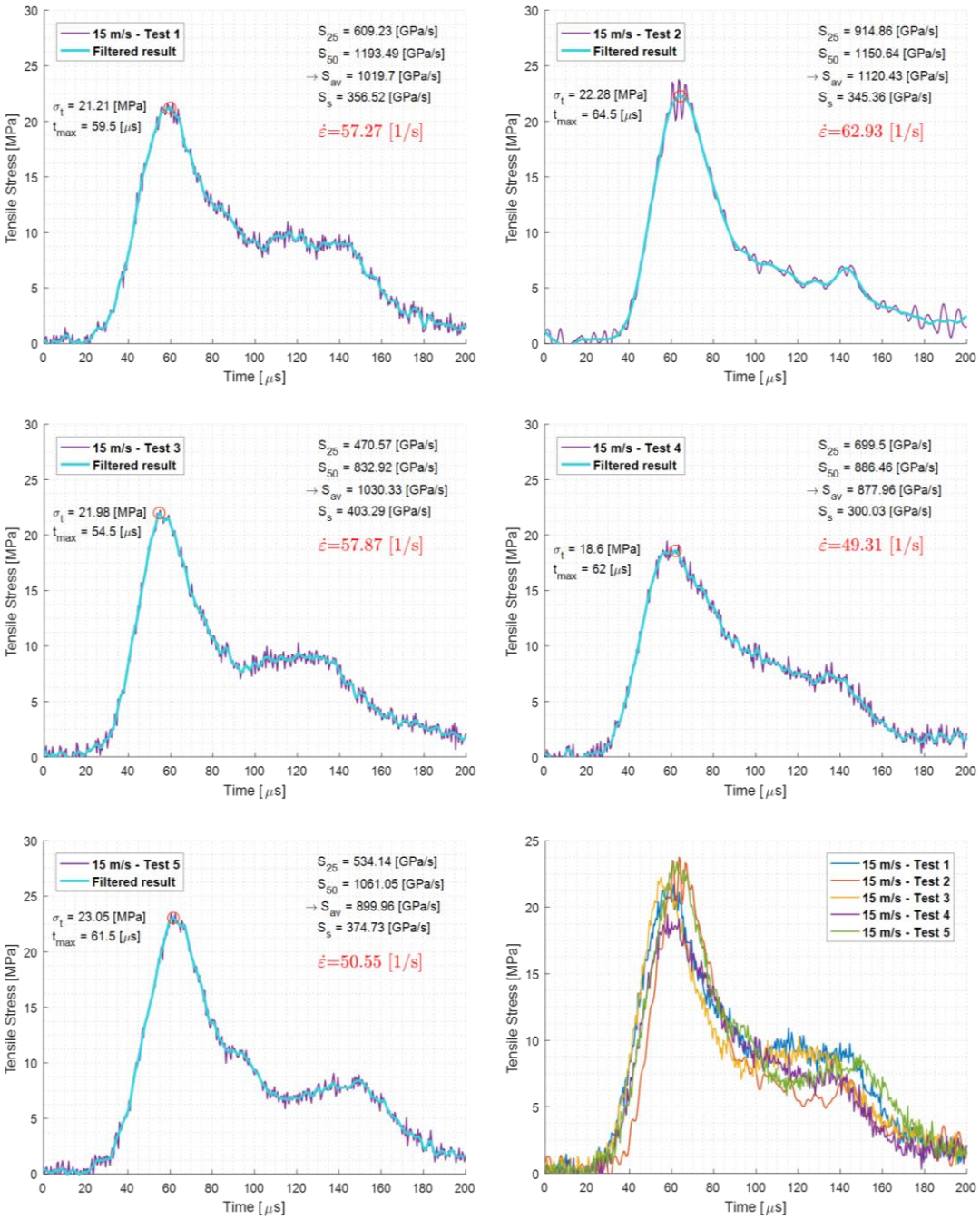

Figure 52. Experimental tensile stresses at the BD center at the striker velocity of 15m/s.

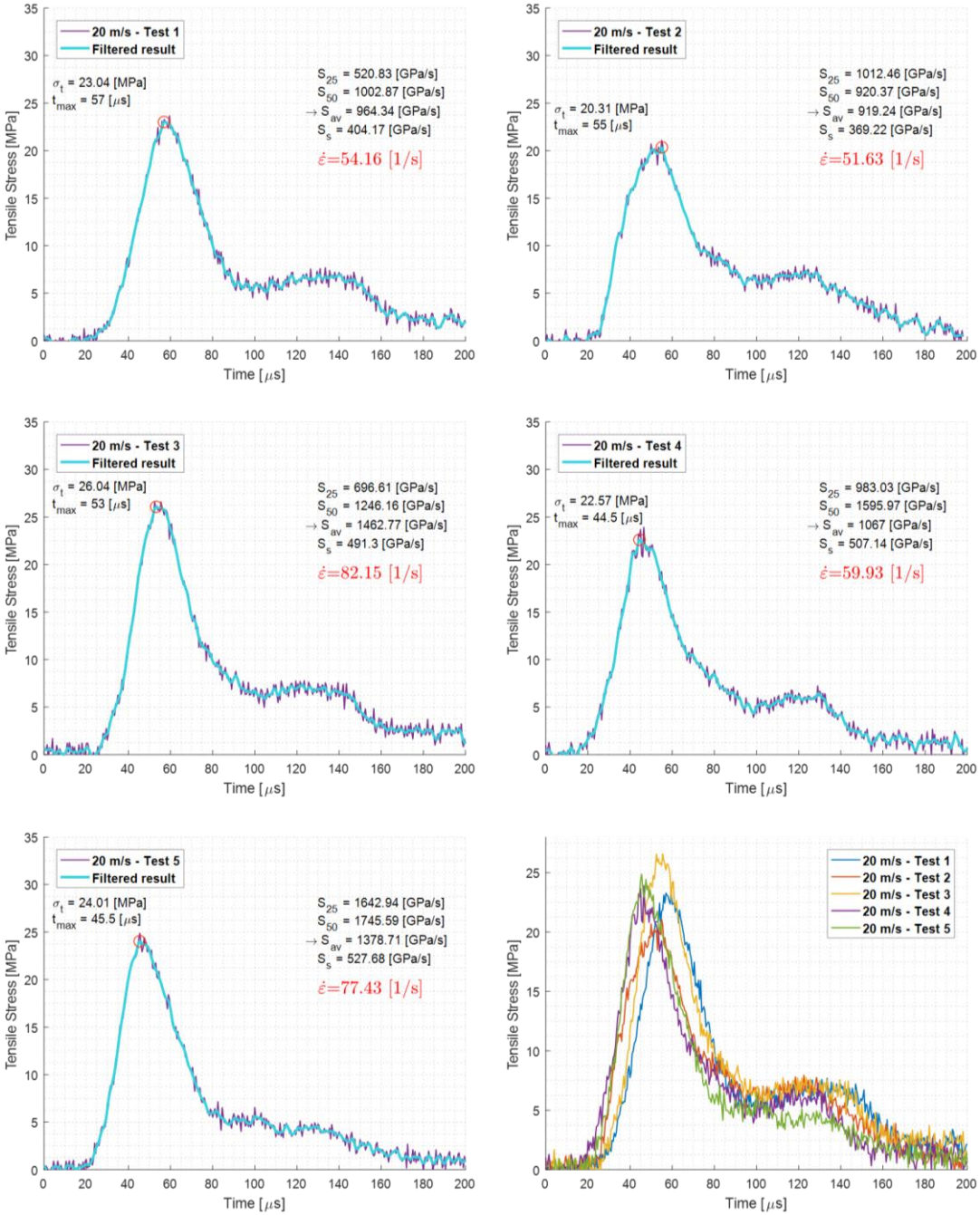

Figure 53. Experimental tensile stresses at the BD center at the striker velocity of 20m/s.

The loading rate dependency of the indirect tensile strength of the Pietra-Serena sandstone is investigated by considering the peak stresses obtained from the diagrams indicated in Figure 51, Figure 52 and Figure 53. Four different indexes are measured as the loading rate parameter, according to:

- The tangent modulus at a percentage of the tensile stress, i.e. S_{25} and S_{50}.

- The average slope of the straight line of the stress-trim curve S_{av}.
- The secant modulus from zero to the failure stress S_s.

As can be seen in Figure 51, Figure 52 and Figure 53, the parameters S_{50} and S_{av} have almost the same values and represent a more realistic value corresponding to the loading rate dependency. Therefore, the average slope of the straight line of the stress-trim curve S_{av} are considered for further analyses as the loading rate parameter [GPa/s]. The strain rates of these tests are also calculated by diving this loading rate parameter S_{av} by the elastic modulus of the specimens. The experimental mechanical characteristics obtained from these tests are reported in Table 13.

Table 13. The experimental results of the dynamic Brazilian test for three levels of striker bar velocities.

	Indirect tensile strength [MPa]	Loading rate [Gpa/s]	Strain rate [1/s]	Dynamic Increase Factor (DIF)
10m/s – test 1	17.067	612.252	34.386	2.8927
10m/s – test 2	18.943	666.298	37.422	3.2107
10m/s – test 3	19.268	682.578	38.336	3.2658
10m/s – test 4	17.821	644.337	36.188	3.0204
10m/s – test 5	17.918	574.950	32.291	3.0369
15m/s – test 1	20.711	890.854	50.034	3.5102
15m/s – test 2	22.035	1075.023	60.377	3.7347
15m/s – test 3	21.184	1012.554	56.869	3.5905
15m/s – test 4	18.329	832.732	46.769	3.1065
15m/s – test 5	22.349	907.969	50.995	3.7879
20m/s – test 1	22.350	978.112	54.934	3.7882
20m/s – test 2	19.769	981.271	55.112	3.3506
20m/s – test 3	25.481	1290.667	72.489	4.3188
20m/s – test 4	21.927	1073.474	60.291	3.7164
20m/s – test 5	23.299	1300.189	73.024	3.9490

The high-speed camera snapshots which are obtained from the experimental dynamic Brazilian disk test by a striking velocity of 20 m/s is indicated in Figure 54. The snapshots express the presence of axial splitting tensile failure mode which is followed by the secondary shear failure mode at the contact of the disc and bar ends. These secondary fractures lead to fragmentation and chipping of the rock.

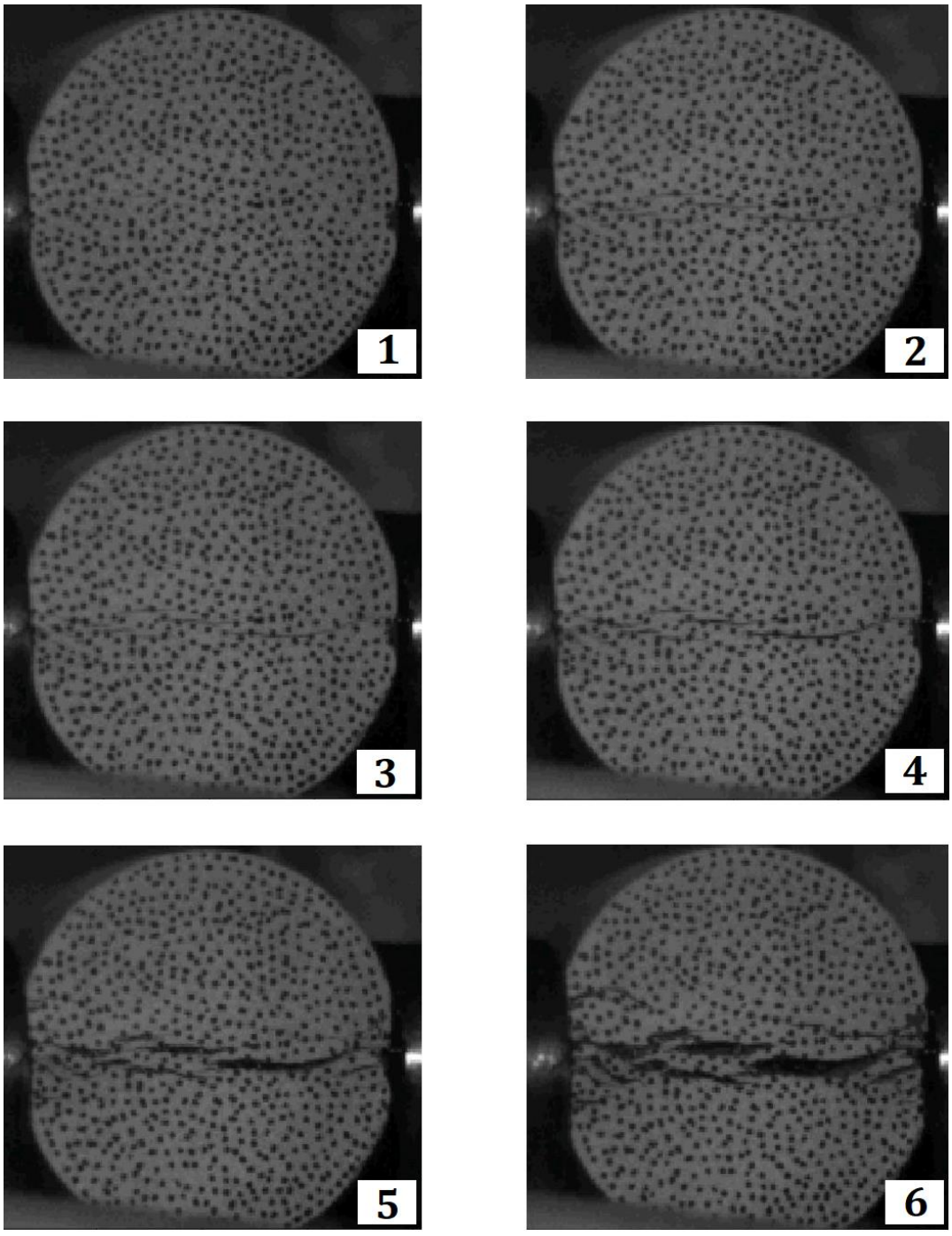

Figure 54. The snapshots of the high-speed camera expressing the failure of the dynamic Brazilian disk test by a striking velocity of 20 m/s.

Part IV

Numerical Modelling

Chapter 12

Calibration of material models

12.1 Calibration of Concrete Damage Model (Karagozian and Case Concrete – KCC or K&C)

The Karagozian and Case Concrete (KCC or K&C) model is implemented in the numerical code LS-DYNA. This material model, currently at its 3rd release, includes an option for automatic mechanical parameter generation based on the unconfined compression strength (UCS). This feature makes the model friendlier for users without laboratory data. However, since this estimation was originally designed for the concretes, using this option for other quasi-brittle materials (i.e. sandstone) may not yield precise results. An improved calibration method of the KCC material model was suggested in (Mardalizad et al., 2018a) based on triaxial compression test and static Brazilian disc test.

12.1.1 Fixed – strength surfaces of KCC

The a_i – parameters of KCC material model are the user-defined input parameters to define the failure surfaces in the compressive meridian by means of the equations (29), (30) and (31). These parameters can be calibrated based on the experimental data of the triaxial compression test by means of a curve-fitting approach. The a_i – parameters of the KCC material model for the Pietra-Serena sandstone (based on the triaxial compression test data) is reported in Table 14. These curves were obtained by the *Curve Fitting Toolbox* of *MATLAB* software, in which the Levenberg-Marquardt approach is considered as its fitting algorithm. The KCC failure surfaces and their corresponding experimental data are indicated in Figure 55.

Table 14. The calibrated KCC a_i – parameters of Pietra-Serena based on the TXC.

	$a_1[MPa]$	$a_1[-]$	$a_2\left[MPa^{-1}\right]$
Yield surface	38.771	0.55108	6.679 e-4
Maximum surface	22.645	0.50016	2.2652e-3
Residual surface	0	0.38488	3.9888e-3

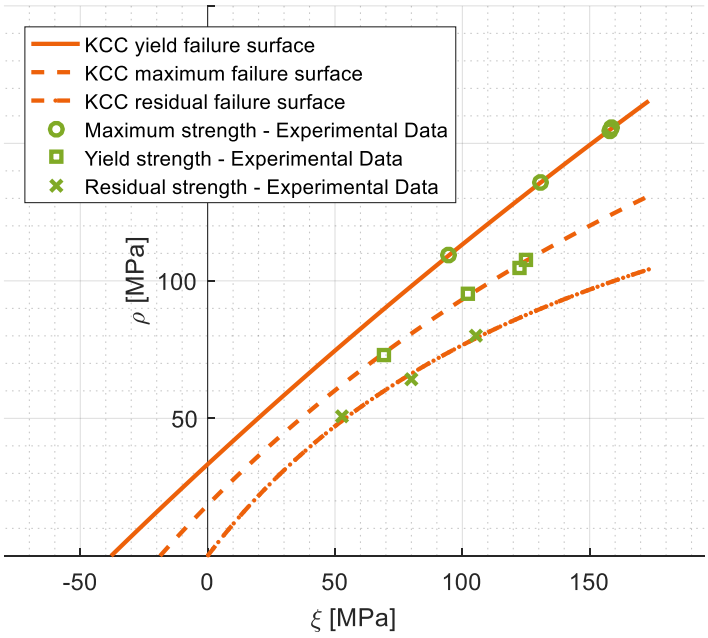

Figure 55. Calibration of the KCC a_i – parameters based on the triaxial compression tests on Pietra Serena sandstone.

12.1.2 Equation-of-State

One of the most noteworthy features of the KCC model is decoupling the shear and the compaction behaviour of the materials, which means that this model treats the deviatoric and volumetric responses separately. The deviatoric response is characterized by the migration of the current stress state between the fixed failure surfaces, while the response to pressure is defined by an equation of state as a function of the volumetric strain increments. The keyword *EOS_TABULATED_COMPACTION in LS-DYNA provides a piecewise relationship between the pressure and the volumetric strain (for loading), or the bulk modulus and the volumetric strain (for unloading) according to equation (44).

$$p = p^{EOS} + K\Delta\varepsilon_v^e \tag{44}$$

Where, p^{EOS} is the pressure from the EOS, K is the bulk modulus and $\Delta\varepsilon_v^e$ is the incremental elastic volumetric strain. Both the p^{EOS} and $\Delta\varepsilon_v^e$ can be determined by means of experimental test data, as a function of the volumetric strain. The elastic volumetric response at current step $\varepsilon_{v,n+1}^e$ in KCC is calculated according to the equation (45).

$$\varepsilon_{v,n+1}^{e} = \ln(V_{n+1}/V_0) - \varepsilon_{v,n}^{p} \tag{45}$$

Where, V_0 and V_{n+1} are the original and the current volume, respectively, and $\varepsilon_{v,n}^{p}$ is the plastic volumetric strain at the previous step. The bulk modulus in equation (44) is considered differently for loading and unloading scenarios. The unloading is beyond the scope of this study, but the loading bulk modulus is obtained based on equation (46).

$$K^{L} = \left| \frac{p_{EOS}^{\delta} - p_{EOS}^{\delta+1}}{\varepsilon_{v,EOS}^{\delta} - \varepsilon_{v,EOS}^{\delta+1}} \right| \qquad \varepsilon_{v,n+1}^{e,\min} \in \left[\varepsilon_{v,EOS}^{\delta+1} \quad \varepsilon_{v,EOS}^{\delta} \right] \tag{46}$$

The subscript EOS in equation (46) expresses that the values related to the pressure and the volumetric strain are taken from the equation of state input. The *EOS_TABULATED_COMPACTION keyword provides 10 pairs of pressure-volumetric strain data, and the superscript δ indicates the sequence on the EOS input so that $\varepsilon_{v,n+1}^{e,\min} \in \left[\varepsilon_{v,EOS}^{\delta+1} \quad \varepsilon_{v,EOS}^{\delta} \right]$. Therefore, the equation (44) can be represented for loading pressure according to equation (47).

$$p^{L} = p_{EOS}^{\delta} - K^{L}\left(\varepsilon_{v,n+1}^{e,\min} - \varepsilon_{v,EOS}^{\delta}\right) \tag{47}$$

The keyword *EOS_TABULATED_COMPACTION in LS-DYNA provides a piecewise relationship between the pressure and the volumetric strain (for loading), or the bulk modulus and the volumetric strain (for unloading) according to equation (44). Due to the lack of a radial strain gauge device during the compression test, the experimental pressure-volumetric strain data could not be measured and recorded for Pietra-Serena sandstone. The author of this PhD thesis was also unable to find any other experimental study of the EOS of Pietra-Serena. However, an extensive literature review (Coli et al., 2002; Coli et al., 2003; Coli et al., 2006) revealed the presence of another sandstone, called Berea, with similar mechanical properties to the Pietra-Serena. The blue curve in Figure 56, obtained from (Christensen and Wang, 1985), indicates the relationship between the bulk modulus and the hydrostatic pressure of Berea sandstone.

The nonlinear Least-Squares curve fitting of *MATLAB* is exploited to consider the bulk modulus as a natural logarithmic function of the hydrostatic pressure, so

$K = f(p)$. By means of this function and considering $K = -V\frac{dp}{dV}$, the volumetric strain values can be derived according to equation (48).

$$\varepsilon_{v,EOS}^{\delta+1} = -\int_{p_{EOS}^{\delta}}^{p_{EOS}^{\delta+1}} \frac{1}{f(p)} dp + \varepsilon_{v,EOS}^{\delta} \tag{48}$$

To solve the equation (48), the initial condition should be imposed as $\varepsilon_{v,EOS}^{0} = p_{EOS}^{0} = 0$. Therefore, the user input data of EOS as a series of pressure-volumetric strain are tabulated in Table 15.

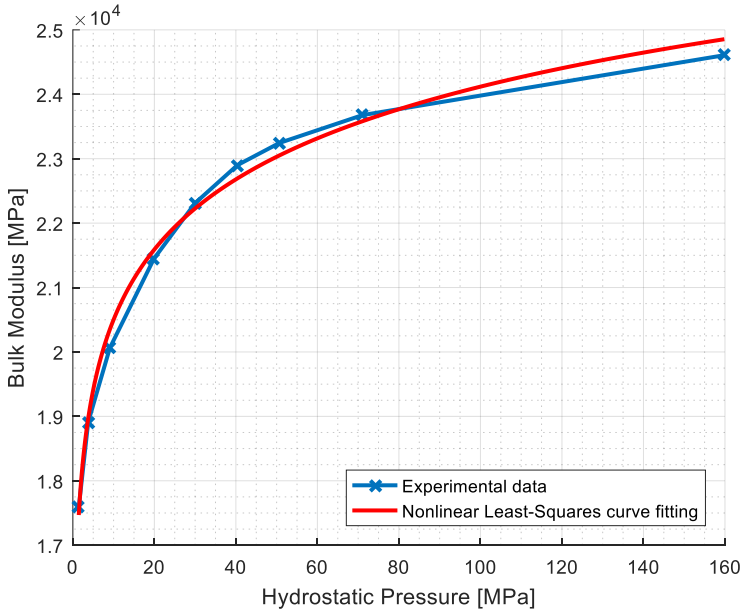

Figure 56. The bulk modulus-hydrostatic pressure diagram of Berea sandstone (Christensen and Wang, 1985).

Table 15. Equation-of-State (EOS_TABULATED_COMPACTION) for the KCC material model.

δ	ε_v	$p\,[MPa]$
1	0	0
2	-0.0001	1.4501
3	-0.0002	3.7687
4	-0.0005	9.0867
5	-0.0010	19.8859
6	-0.0015	30.0015
7	-0.0019	40.3782
8	-0.0024	50.7179
9	-0.0032	71.0554
10	-0.0069	159.8497

12.1.3 Modified Damage function

In the KCC model, the damage accumulation is imposed based on a tabular damage function, consisting of 13-pairs of $\eta - \lambda$ parameters. The original tabular function, which can be found in (Malvar et al., 2000a), and also the articles presented some modifications for this function such (Markovich et al., 2011) and (Kong et al., 2017), focused on the concrete material. (Wu et al., 2017) expressed a modified tabular function of the KCC model for asphalt concrete structures, since the corresponding strain to the peak stress of normal concretes and asphalt structures are significantly different. Inspired by the research of (Wu et al., 2017), a new modified damage accumulation function for sandstones based on the experimental results of the triaxial compression test is presented in this PhD thesis.

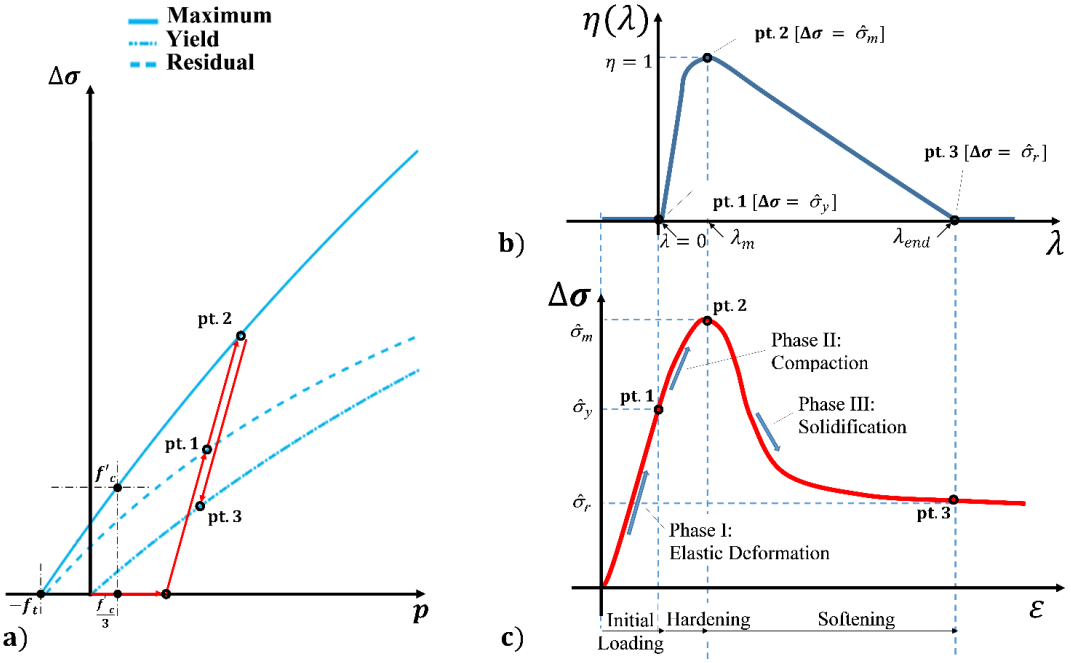

Figure 57. The schematic representation of the KCC model; (a) the linear interpolation between the failure surfaces, b) the damage function, c) a typical TXC stress-strain diagram.

The damage accumulation of the KCC model, and accordingly the current failure surfaces are expressed schematically in Figure 57. As can be seen in Figure 57a, the state of stress is determined by a linear interpolation between the three failure surfaces. The stress-strain diagram corresponding to a typical triaxial compression test is indicated in Figure 57c, which is determined by association of a damage accumulation function, shown in the Figure 57b. The response of the material to the initial loading

(phase I), is considered as a linear elastic deformation before reaching point 1. The current failure surface is therefore the same as the yield strength level $\hat{\sigma}_y$ at this range. A hardening plasticity response occurs after yielding and before reaching the maximum strength $\hat{\sigma}_m$. Based on the level of the confining pressure, a softening response occurs after reaching the maximum strength and before obtaining a residual strength $\hat{\sigma}_r$.

As can be seen in Figure 57b, the damage function is imposed so that initially and prior to the occurrence of any plasticity responses, the value of η is equal to zero. It increases up to unity at a user-defined value λ_m, corresponding to point 2 (maximum strength $\hat{\sigma}_m$). The KCC model considers the hardening plasticity by means of this linear-piecewise function of η - λ. After point 2, where the softening takes place, η decreases to zero at λ_{end} corresponding to point 3, which indicates that after this point the current failure surface is the same as the residual strength level $\hat{\sigma}_r$. Hence, as a first requirement to determine the tabulated damage function of the KCC model, the variation of η and λ should be in accordance to Table 16.

Table 16. The KCC damage evaluation parameters.

η	λ	**Current failure surface position** $\Delta\sigma$
$\mathbf{0 \le \eta < 1}$	$0 \le \lambda < \lambda_m$	$\Delta\sigma_y \le \Delta\sigma < \Delta\sigma_m$
$\boldsymbol{\eta = 1}$	$\lambda = \lambda_m$	$\Delta\sigma = \Delta\sigma_m$
$\mathbf{1 \ge \eta > 0}$	$\lambda_m \le \lambda \le \lambda_{end}$	$\Delta\sigma_m \le \Delta\sigma \le \Delta\sigma_r$

The next step to define the modification is related to determine corresponding experimental data for each one of the η and λ parameters, separately. By definition, it is possible to decompose the rate of the strain tensor $\dot{\varepsilon}$ into an elastic part $\dot{\varepsilon}^e$ and a plastic part $\dot{\varepsilon}^p$, so that $\dot{\varepsilon} = \dot{\varepsilon}^e + \dot{\varepsilon}^p$. The evolution of the damage parameter rate $\dot{\lambda}$ is computed by equation (49) as a function of the plastic strain rate tensor (Wu and Crawford, 2015).

$$\dot{\lambda} = h(p)\dot{\bar{\varepsilon}}^p \tag{49}$$

Where, $\dot{\bar{\varepsilon}}^p$ is the rate of equivalent plastic strain, and $h(p)$ is the damage evolution factor which is given by equation (50).

$$h(p)=\begin{cases} if\ \ p\geq 0 \ \ \rightarrow \ \ \dfrac{1}{r_f}\dfrac{1}{\left(1+\dfrac{p}{r_f\, f_t}\right)^{b_1}} \\ if\ \ p<0 \ \ \rightarrow \ \ \dfrac{1}{r_f}\dfrac{1}{\left(1+\dfrac{p}{r_f\, f_t}\right)^{b_2}} \end{cases} \tag{50}$$

The parameters b_1 and b_2 in equation (50) are material parameters calibrated from test data, in which the first parameter governs compression and the second affects uniaxial tension. By neglecting the effect of the strain rate ($r_f = 1$), the damage parameter λ, can be obtained just for the compressive (positive) range of the hydrostatic pressure, according to equation (51).

$$if\ \ p\geq 0 \ \ \rightarrow \ \ \lambda = \frac{1}{\left(1+\dfrac{p}{f_t}\right)^{b_1}}\,\bar{\varepsilon}^{\,p} \tag{51}$$

The experimental data of the Brazilian test is used to determine the f_t , and three triaxial compression test data (the ones that have reasonable hardening-softening behavior; 20 MPa and the two 28 MPa confining pressures) are used for the hydrostatic pressure p and the equivalent plastic strain $\bar{\varepsilon}^{\,p}$. The parameter $\bar{\varepsilon}^{\,p}$ is the one that commonly used for a Von Mises isotropic hardening model (i.e. metals) which can be expressed by equation (52).

$$\bar{\varepsilon}^{\,p} = \sqrt{\frac{2}{3}\,\varepsilon^{p} : \varepsilon^{p}} \tag{52}$$

The equation (52) for an axisymmetric loading application can be simplified as equation (53).

$$\bar{\varepsilon}^{\,p} = \sqrt{\frac{2}{3}\left[\left(\varepsilon_{axial}{}^{p}\right)^2 + 2\left(\varepsilon_{lateral}{}^{p}\right)^2\right]} \tag{53}$$

Due to the absence of a radial strain gauge device, the experimental data of lateral displacements was not measured during the triaxial compression tests, and only the test data of the axial strain was obtained. However, the lateral strain was estimated by the equation (54), proposed by (Binici, 2005) for concrete materials.

$$\begin{cases} if\ \varepsilon_{axial} \le \varepsilon_{axial}^{\ e} & \rightarrow \quad \varepsilon_{lateral} = -\upsilon\,\varepsilon_{axial} \\ if\ \varepsilon_{axial} > \varepsilon_{axial}^{\ e} & \rightarrow \quad \varepsilon_{lateral} = -\upsilon_s\,\varepsilon_{axial} \end{cases} \tag{54}$$

Where, υ is the Poisson's ratio in elastic range of 0.29 (ASTM, 2004) that was considered to be identical for Pietra Serena and Berea sandstone. The parameter υ_s is the secant Poisson's ratio that was determined by (Binici, 2005) for normal concrete according to equation (55).

$$\upsilon_s = \upsilon_l - (\upsilon_l - \upsilon)\exp\left[-\left(\frac{\varepsilon_{axial} - \varepsilon_{axial}^{\ e}}{\Delta\varsigma}\right)^2\right] \tag{55}$$

With,

$$\Delta\varsigma = \frac{\left(\varepsilon_{axial}\right)_{@\ peak\ strength} - \varepsilon_{axial}^{\ e}}{\sqrt{-\ln\beta}} \tag{56}$$

$$\beta = \frac{\upsilon_l - \upsilon_p}{\upsilon_l - \upsilon} \tag{57}$$

$$\upsilon_l = \upsilon_p + \frac{1}{\left[\left(\frac{f_r}{f_c'}\right) + 0.85\right]^4} \tag{58}$$

The parameter υ_p in the previous equations is the ratio of the lateral strain and the axial strain at the peak strain which was assumed to be 0.5.

To obtain experimental values for the parameter η, firstly equation (24) was considered; when the pressure-dependent surface $\Phi(\rho,\theta,\xi,\lambda)$ meets the yield condition, it is zero and accordingly equation (59) can be derived.

$$\Delta\sigma = \sqrt{3/2}\ \rho = \varphi(\theta,\xi,\lambda) \tag{59}$$

The modification of damage function suggested in this PhD thesis requires the experimental data of triaxial compression test, which is basically a quasi-static experimental procedure. Hence, it is possible to cancel out the effect of strain rate enhancement by setting the value of r_f parameter equal to 1. Moreover, as it is mentioned in Figure 14, the amount of function $\hat{r}[\Psi(p),\theta]$ for the triaxial compression tests (when Lode angle is $\theta = 60°$), is equal to 1. Therefore, it is possible to re-write the equation (25) as the equation (60).

$$\varphi(\theta,\xi,\lambda)=\begin{cases} \textit{for Elastic}; & \hat{r}\left[\Psi(p),\theta\right]\left[\hat{\sigma}_y(p)\right] \\ \textit{for Hardening}; & \hat{r}\left[\Psi(p),\theta\right]\left[\eta(\lambda)\left[\hat{\sigma}_m(p)-\hat{\sigma}_y(p)\right]+\hat{\sigma}_y(p)\right] \\ \textit{for Softening}; & \hat{r}\left[\Psi(p),\theta\right]\left[\eta(\lambda)\left[\hat{\sigma}_m(p)-\hat{\sigma}_r(p)\right]+\hat{\sigma}_r(p)\right] \end{cases} \quad (60)$$

By substituting the $\varphi(\theta,\xi,\lambda)$ function of equation (59) by the equation (60), the values related to the parameter η can be obtained, based on the deviatoric stress and three fixed strength surfaces according to equation (61).

$$\begin{cases} \textit{for hardening} \rightarrow & \eta(\lambda)=\dfrac{\Delta\sigma-\hat{\sigma}_y(p)}{\hat{\sigma}_m(p)-\hat{\sigma}_y(p)} \\ \textit{for softening} \rightarrow & \eta(\lambda)=\dfrac{\Delta\sigma-\hat{\sigma}_r(p)}{\hat{\sigma}_m(p)-\hat{\sigma}_r(p)} \end{cases} \quad (61)$$

Therefore, it is possible to transform the experimental data of the triaxial compression test from the $\Delta\sigma-\varepsilon$ diagram into the η – λ diagram, by means of equations (51) and (61). The parameter b_1 in equation (51) was used to adjust the tabular damage function rendering the results of the numerical simulation in accordance with the experimental ones.

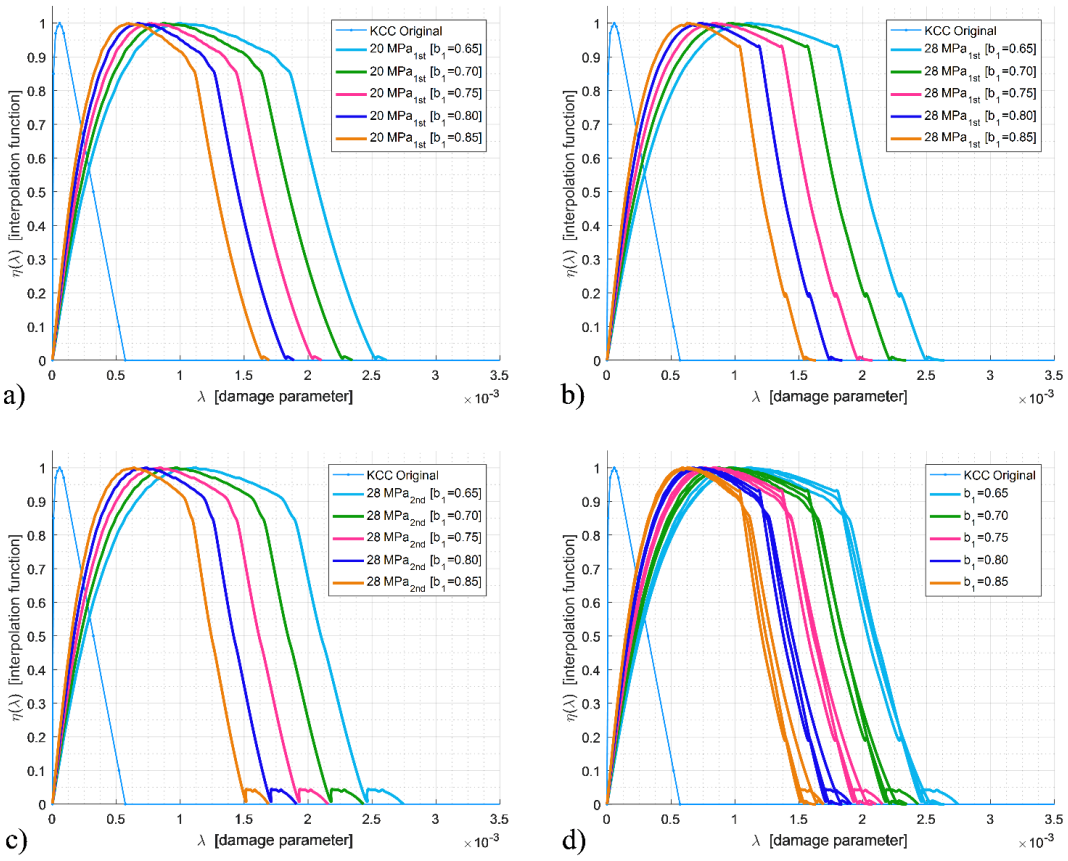

Figure 58. The experimental representation of $\eta - \lambda$ diagrams based on the b_1 parameter and; (a) 1st test with 20 MPa confining pressure; (b) 1st test with 28 MPa confining pressure; (c) 2nd test with 28 MPa confining pressure, (d) comparison of all experimental data based on the b_1 only.

It should be noted that due to some limitations, the size of the samples for the experimental tests are the same. Therefore, the sample which is used here should not be interpreted as a representative elementary volume (rev). The effect of the b_1 parameter to obtain the KCC damage function is expressed in Figure 58a, Figure 58b and Figure 58c for the triaxial compression test data of the 1st test of 20 MPa, the 1st test of 28 MPa and the 2nd test of 28 MPa confining pressure, respectively. These diagrams were merged in Figure 58d for comparison. As visible in this figure, the behaviour of all three tests (for all the b_1 parameters) are highly similar between each other indicating the validity of the proposed approach.

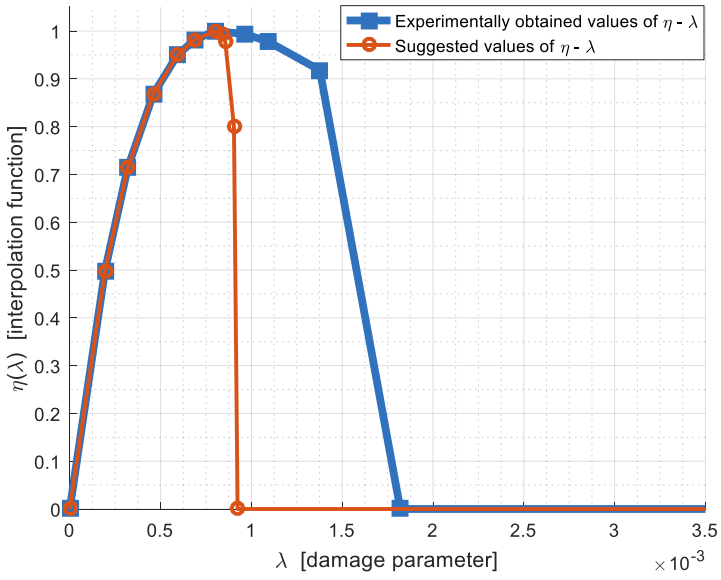

Figure 59. The comparison of experimentally evaluated and suggested KCC tabular damage functions for rock materials.

The diagram of "experimentally obtained values of $\eta - \lambda$" (by considering b_1) for Pietra-Serena sandstone is expressed in Figure 59. Although the values of this diagram yields to a very precise response in the hardening regime, the softening gradient was found to be lower compared to the empirical formula. Therefore, a new set of $\eta - \lambda$ is presented in Figure 59 as the "suggested values of $\eta - \lambda$", that consists of the same data as the "experimentally obtained values of $\eta - \lambda$" in the hardening regime, and an increased softening gradient. Further substantial proof was obtained by exploiting the present calibration in numerical simulations of the tests (virtual tests) and by

comparing the results with the experimental data. These comparisons (which are also illustrated in Figure 82) imply that the numerical results are shown to be in a reasonable agreement with the experimental data when the b_1 parameter is equal to 0.75.

It should be noted that the suggested tabular damage function was originally obtained based on equation (51) that governs only the compressive pressure. According to equation (50), the same damage evolution factor presented here, and accordingly the damage function, can be adjusted in the tensile regime by setting the b_2 (and also b_3) parameter. These b-parameters can be determined by iteration until the value of the fracture energy, G_f, converges for a specified characteristic length, which is associated with the localization width (i.e. the width of the localization path transverse to the crack advance).

The parameters *RSIZE* and *UCF* in the *MAT_072R3 keyword of LS-DYNA are unit conversion factors and the *NOUT* is called the "output selector for effective plastic strain". According to (Hallquist, 2014), when *NOUT=2*, the quantity labelled as "plastic strain" by the LS-PrePost is actually the quantity that describes the "scaled damage measure, δ" which varies from zero to two. When the amount of δ is still lower than one, the elements of the part modelled by the KCC, fail to reach the yield limit. These corresponding elements reached the yield strength at $\delta = 1$ and when $\delta = 2$ they meet their ultimate residual failure level.

12.1.4 Strain rate enhancement

The strain rate effects are realized through the parameter r_f that modified the failure surface of the KCC model $\varphi(\theta, \xi, \lambda)$ according to the equation (25). The parameter r_f of KCC material model is the same as the dynamic increase factor (DIF) which was specified as a function of strain rate $\dot{\varepsilon}$ (Malvar and Crawford, 1998). The proposed formulation by (Malvar and Crawford, 1998) is considered in this PhD research to determine the parameter r_f in the tensile regime as equation (62).

$$\begin{cases} for\ \dot{\varepsilon} \le 1\ \left[s^{-1}\right] \rightarrow \quad r_f = \left(\dfrac{\dot{\varepsilon}}{\dot{\varepsilon}_s}\right)^{\delta} \\ for\ \dot{\varepsilon} > 1\ \left[s^{-1}\right] \rightarrow \quad r_f = \beta\left(\dfrac{\dot{\varepsilon}}{\dot{\varepsilon}_s}\right)^{1/3} \end{cases} \tag{62}$$

Where, the $\dot{\varepsilon}_s$ is the static strain rate (equal to $10^{-6}[s^{-1}]$) and $\dot{\varepsilon}$ is the strain rate in the range of $10^{-6}[s^{-1}]$ up to $140[s^{-1}]$. The parameters β and δ are the Malvar-Crawford parameters that can be calibrated based on the experimental values. To find these parameters, first the average experimental values for the dynamic Brazilian disk test are calculated (see Table 17). Then, the second part of the equation (62), where the $\dot{\varepsilon} > 10^{-6}[s^{-1}]$, was fitted by means of these average values. This curve was obtained by the *Curve Fitting Toolbox* of *MATLAB* software, in which the Levenberg-Marquardt approach is considered as its fitting algorithm. Therefore, the parameter β was calculated based on this procedure to be equal to 0.009568. According to (Malvar and Crawford, 1998), the $\log\beta = 6\delta - 2$, so the parameter δ is equal to 0.016614. The calibrated tensile DIF – strain rate diagram for Pietra-Serena sandstone is indicated in Figure 60 in a semi-logarithmic scale.

Table 17. The average experimental results for the dynamic Brazilian test for three levels of striker bar velocities.

	Indirect tensile strength [MPa]	Loading rate [Gpa/s]	Strain rate [1/s]	DIF
10m/s – average	18.204	636.08	35.725	3.0854
15m/s – average	20.922	943.83	53.009	3.5460
20m/s – average	22.565	1124.7	63.17	3.8246

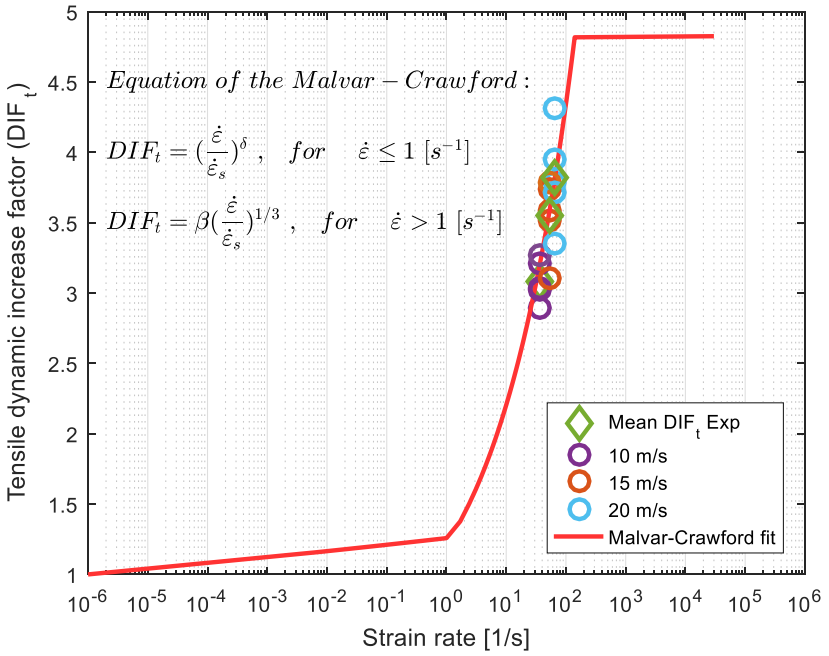

Figure 60. the tensile dynamic increase factor – strain rate diagram in the semi-logarithmic scale, calibrated for Pietra-Serena sandstone.

It is not possible to get experimental data related to compressive DIF by the dynamic Brazilian disk test. Hence, the parameter r_f in the compressive regime is obtained from (béton and précontrainte, 1991). The full set of dynamic increase factor – strain rate diagram, which is used in this study is expressed in Figure 61.

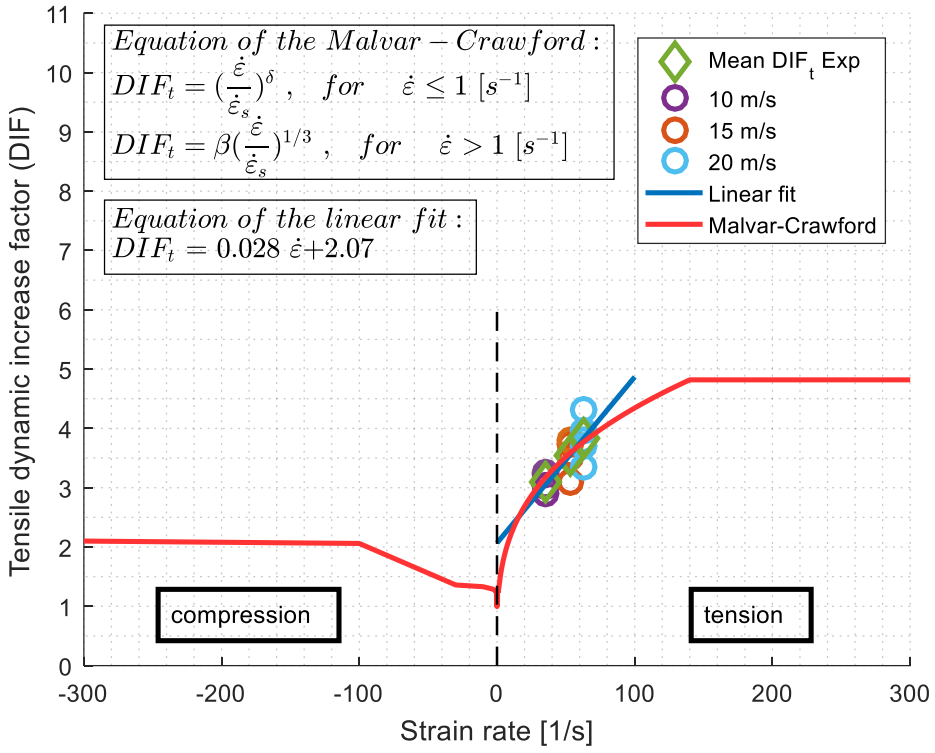

Figure 61. the full set of dynamic increase factor – strain rate diagram calibrated for Pietra-Serena sandstone.

The full user input parameters of the KCC material model are reported in Table 18.

Table 18. The full calibrated KCC material model for Pietra Serena sandstone.

MID	RO	PR					
--	2e-9	0.29					
FT	**A0**	**A1**	**A2**	**B1**	**OMEGA**	**A1F**	
5.9	40.771000	0.5511	6.680e-4	0.75	0.9	0.38488	
Slambda	**NOUT**	**EDROP**	**RSIZE**	**UCF**	**LCRATE**	**LOCWIDTH**	**NPTS**
--	2	1	0.03937	145	--	1.35	13
lambda1	**lambda2**	**lambda3**	**lambda4**	**lambda5**	**lambda6**	**lambda7**	**lambda8**
0	1.94e-4	3.19e-4	4.6e-4	5.93e-4	7.26e-4	8.37e-4	8.685e-4
lambda9	**lambda10**	**lambda11**	**lambda12**	**lambda13**	**B3**	**A0Y**	**A1Y**
9.005e-4	9.72e-4	10.83e-4	1	1000	0.5	22.645	0.50016

eta1	**eta2**	**eta3**	**eta4**	**eta5**	**eta6**	**eta7**	**eta8**
0	0.498757	0.713508	0.867684	0.949989	0.988934	1	0.993539

eta9	**eta10**	**eta11**	**eta12**	**eta13**	**B2**	**A2F**	**A2Y**
0.978281	0.917932	0	0	0	3.21	0.0039890	0.002260

12.2 Calibration of MC Plasticity and Linear DP

The procedure of material identification related to these two material models has been explained in a master thesis (which was defined in conjunction with this PhD thesis) which can be found in (SCAZZOSI and MAIOLANI, 2015-2016). However, the description is discussed briefly in the followings.

The parameters to identify these material models are reported in Table 19. The ABAQUS software automatically computes the cohesion by giving the yield stress in compression as a function of the plastic strain allowing the isotropic hardening of the yield function.

Table 19. The MC plasticity and Linear DP models' parameters.

E [MPa]	**PR**	**β [°]**	**K [-]**	**Ψ [°]**
15374	0.28	65.38	0.778	16.35

The elastic properties are taken from (Mardalizad et al., 2016). The Mohr-Coulomb friction angle is obtained through the procedure described in (Sivakugan et al., 2014) using the properties reported in Table 20. To assure convexity of the yield function, the value of the flow-stress ratio is limited by a minimum value of 0.778. Since the obtained value is lower, the minimum value allowable is used instead resulting in the criterion obtained not being equivalent to the starting Mohr-Coulomb criterion but being its best approximation (Manual, 2009).

Table 20. The experimental data of the Pietra-Serena sandstone for MC and DP.

UCS, f_c' [MPa]	**Tensile splitting strength [MPa]**	**Yield stress, σ_y [MPa]**	$\overline{\epsilon_p}$
67.99	5.66	53.79	0.00057

A good approximation of the dilation angle for rock showing brittle behavior is equal to 1/4 times the friction angle (Hoek and Brown, 1997). These failure criteria are intended as the yield surfaces, i.e. when equations (5) and (18) are satisfied, plastic flow occurs. Hardening of the yield function follows until the maximum strength is reached, afterwards failure is modelled by softening. Hardening (intended as

hardening followed by softening) of the yield function (see Figure 62) is described by the equation proposed by (Lubliner et al., 1989) for concrete as defined in equations (15).

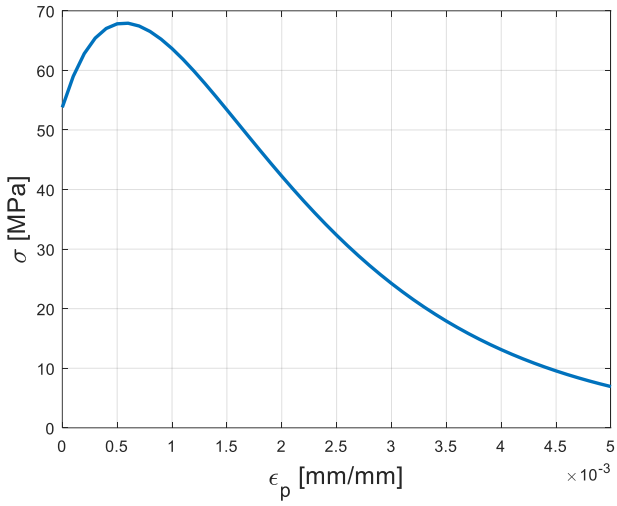

Figure 62. The post-yield stress-strain diagram used for MC and DP.

In Table 20, the parameters to define the curve of equation (15) are reported. The parameters a and b, which are obtained using equations (16) and (17), are determined equal to 2.68 and 665.32, respectively.

Chapter 13

Numerical analyses of experimental tests

13.1 Unconfined compression test

13.1.1 Material model: KCC

Two numerical models were developed in LS-DYNA to replicate the unconfined compressive test in both the ASTM and the Mogi configurations (see Figure 63). All the geometry parts were generated, assembled and meshed by ABAQUS/Explicit software and then imported in LS-PrePost to specify the required keywords. The mesh convergence studies were performed based on the elements' sizes of the specimens, and 1 mm was considered for these elements. The mesh sizes of the other components were determined by considering the requirements of the contact treatments, i.e. the element size of the slave parts was considered lower than the master ones. The numerical models of rock, replicated the ASTM and The Mogi configurations, have the same geometries as the specimens of class C and class D, respectively (Mardalizad et al., 2018b).

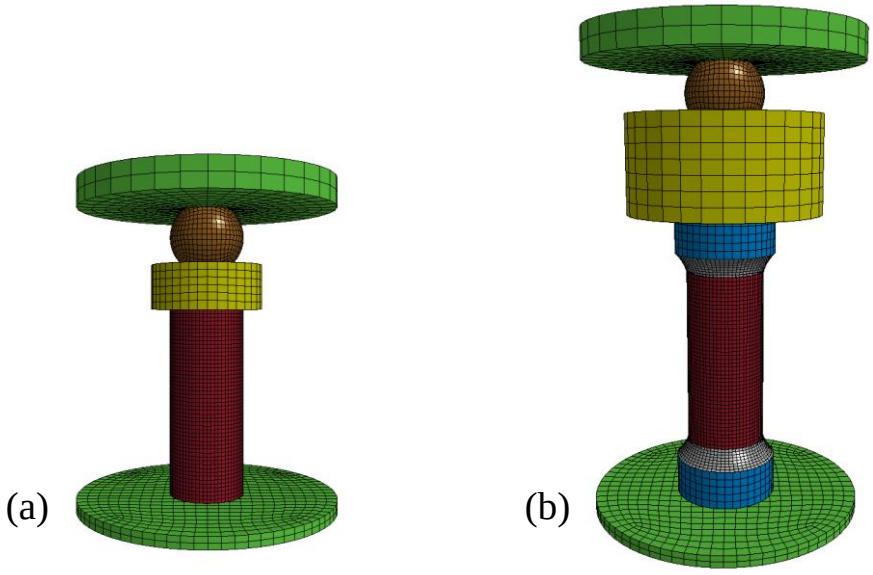

Figure 63. Numerical models developed in LS-DYNA to replicate; (a) the ASTM configuration; (b) the Mogi configuration (Mardalizad et al., 2018b)

The numerical model of the ASTM configuration consists of five parts including two rigid platens (representing the compressive platens), one elastic sphere, one elastic cylinder (representing spherical seat) and the specimen. The displacement-controlled compressive loading was imposed by the upper platen and the lower platen was fixed (zero degree of freedom). The numerical model of the Mogi configuration consists of nine parts, five of them identical with the ASTM configuration, plus further two Aluminium cylinders and two round profiles (representing the profile of the epoxy). Displacement-control loading is applied to the upper compressive platen (for both models) by a rate of 0.45 mm/ms, and the simulations are terminated after 5 ms. This loading rate (0.45 mm/ms) has been considered, since it is more convenient to reduce the computation cost in the quasi-static analyses by the time-scaling approach. However, in this case the kinetic energy should be monitored to ensure the ratio of kinetic energy to internal energy does not get too large (typically less than 10%). Figure 64 expresses the diagrams of kinetic energy-time and internal energy-time of the both ASTM and Mogi configurations. As can be seen, the amount of kinetic energy in both cases is negligible (less than 1 percent), therefore, the loading rate is acceptable (Mardalizad et al., 2018b).

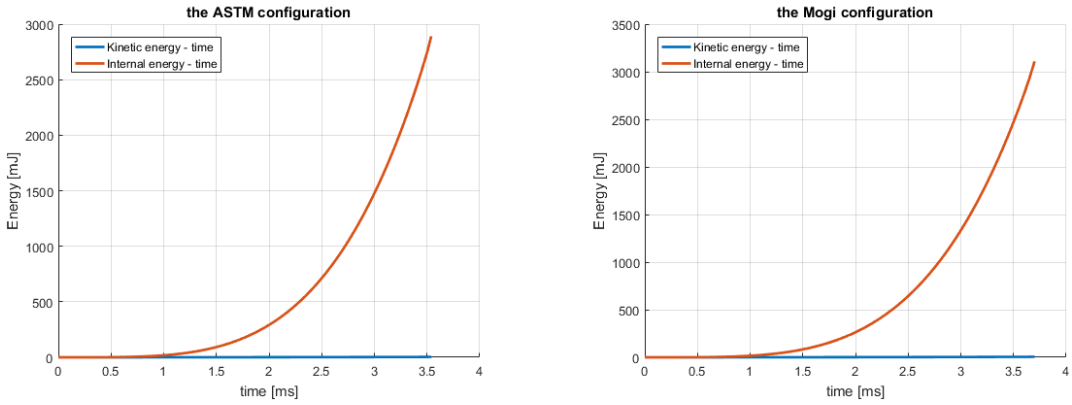

Figure 64. Comparison of the kinetic energy-time and internal energy-time diagrams of; (a) the ASTM configuration, (b) the Mogi configuration (Mardalizad et al., 2018b).

The material keywords and their corresponding mechanical properties for both models are reported in Table 21. The combination of CMO, CON1 and CON2 expressed in Table 21 determines the degree of freedom of a rigid body in LS-DYNA. The rigid body considered for the upper compressive platen has only one translational degree of freedom in z-direction, while, the lower compressive platen has no degree of freedom.

Table 21. Material keywords and their corresponding mechanical properties for both the ASTM and Mogi models (Mardalizad et al., 2018b)

	upper compressive platen (ASTM and Mogi)	Lower compressive platen (ASTM and Mogi)	sphere and the spherical seat (ASTM and Mogi)	Aluminium cylindrical end pieces (Mogi)	epoxy profile
Material keyword	MAT_RIGID	MAT_RIGID	MAT_ELASTIC	MAT_ELASTIC	MAT_ELASTIC
Density, RO [ton/mm^3]	7.85 e-9	7.85 e-9	7.85 e-9	2.4 e-9	1.4 e-9
Elastic modulus, E [MPa]	2.1 e5	2.1 e5	2.1 e5	7.0 e4	2.8 e4
Poisson ratio, PR	0.3	0.3	0.3	0.3	0.35
CMO	1.00	1.00	---	---	---
CON1	4	7	---	---	---
CON2	7	7	---	---	---

The hexagonal solid elements, with constant stress element formulation, were implemented for all the FEM's geometry parts. The SPH section was set by the default values of LS-DYNA. The automatic penalty-based contact was applied to both the solid-solid and the SPH-solid contacts. The static friction coefficient was considered equal to 0.4 for all the contact keywords contain the rock specimen (as their slave segment). The static friction coefficient of the contact between the spherical seated cylinder and the upper Aluminium end piece of the Mogi configuration was set to 0.45. Since the seating sphere was covered by grease during the experimental tests, the static friction coefficients of all the contact keywords contain this sphere were set to 0.05. However, the constraint-based contact was considered as the contact treatment between the sections related to the epoxy profile.

The adaptive conversion of meshed elements to the SPH particles was applied only to the specimens. The maximum effective strain at failure (EFFEPS), which is considered as the conversion limit should be defined as the final step for the numerical simulation. For this purpose, first the simulation should be run without the MAD_ADD_EROSION implementation to examine the presence of highly distorted elements and to identify the EFFEPS at that time step. Within this study, the EFFEPS was set to 0.03.

In order to obtain the numerical stress-strain diagram, the stress was calculated from the reaction force between platens and the specimen. The axial strain data was

computed starting from the axial displacements were measured at an 8 mm and 20 mm length spans (in the middle cross section of the specimens) for the ASTM and the Mogi configurations, respectively (similar to the gauge lengths of their extensometers). The distribution of scaled damage measure, δ of the calibrated (full input) model for both the ASTM and Mogi configurations are captured one-time step after failure and indicated in Figure 65 to express the crack propagation patterns.

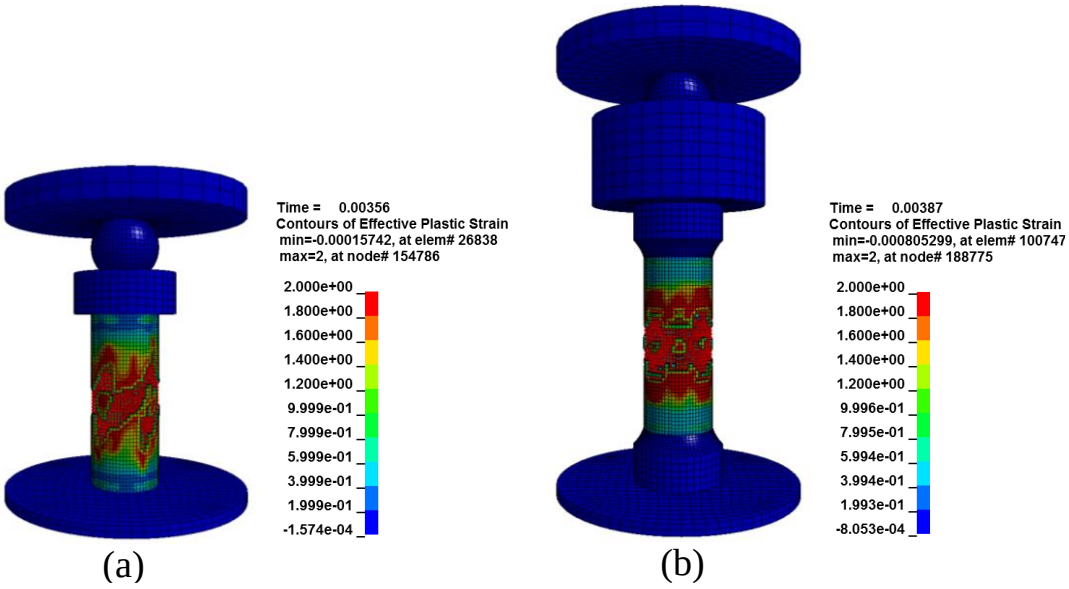

Figure 65. Distribution of the scaled damage parameter after failure; (a) the ASTM configuration; (b) the Mogi configuration (unit of time is ms) (Mardalizad et al., 2018b).

The SPH particles which are in charge of dealing with severe deformation in Figure 65 represent the crack propagation pattern. The critical parts of the specimens in Figure 65 are magnified in Figure 66 to indicate more clearly the crack pattern. As can be seen in Figure 66a, the numerical model results replicated the ASTM configuration does not demonstrate any ordered crack pattern. This failure is caused by the lack of nodes either at the top or bottom of the specimens fixed in tangential direction. This is one of the conditions that yields to disordered crack patterns in detail described in (Murray et al., 2007). However, the presence of some vertical cracks can be considered as an acceptable agreement to the crack propagation pattern obtained by the experimental tests.

As can be seen in Figure 66b, a series of X-pattern cracks follow the double diagonal damage bands which proves the presence of shear failure planes. Therefore, the failure of the Mogi configuration model represents the double shear failure mode in Figure 18. Although this is not the same as the failure mode obtained from the experimental tests (which is shearing along single plane failure mode), the divergence can be

justified based on the (ideal) symmetrical condition, e.g. loading, contact interfaces, boundary conditions, etc., exerted by numerical modelling. It has been tried to overthrow the full symmetry of the system, but it either didn't change the failure mode, or didn't reach to stable results. Therefore, the precise failure mode obtained from the experimental tests cannot be reproduced by this numerical simulation technique.

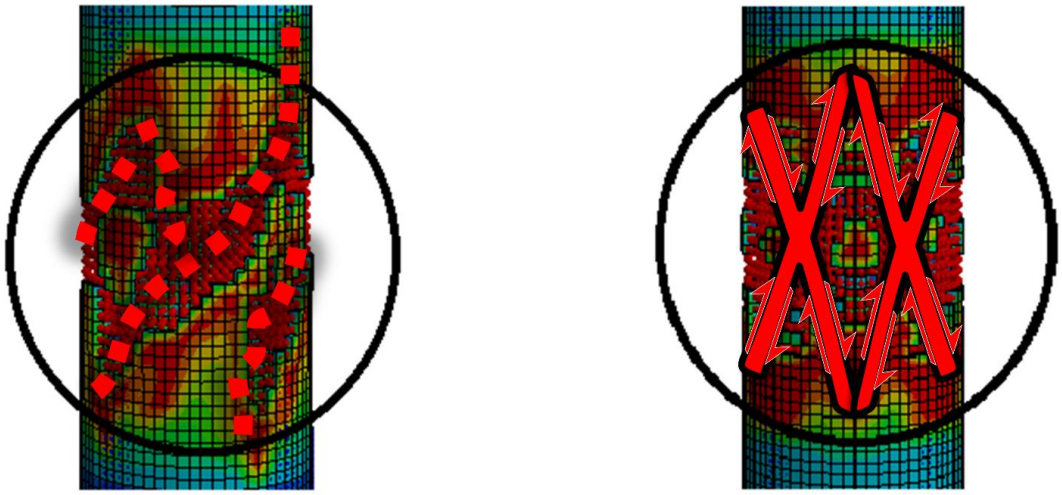

Figure 66. Magnified distribution of the scaled damage parameter after failure; (a) the ASTM configuration; (b) the Mogi configuration (Mardalizad et al., 2018b).

The stress distribution along the axial direction (compressive stress) for both the ASTM and the Mogi configuration are expressed in Figure 67. The presence of the stress concentration at the outer edge of the specimen, which was expected based on the Mogi's research in (Mogi, 2007), is visible in the ASTM model, however, the Mogi model exhibits a more uniform stress distribution.

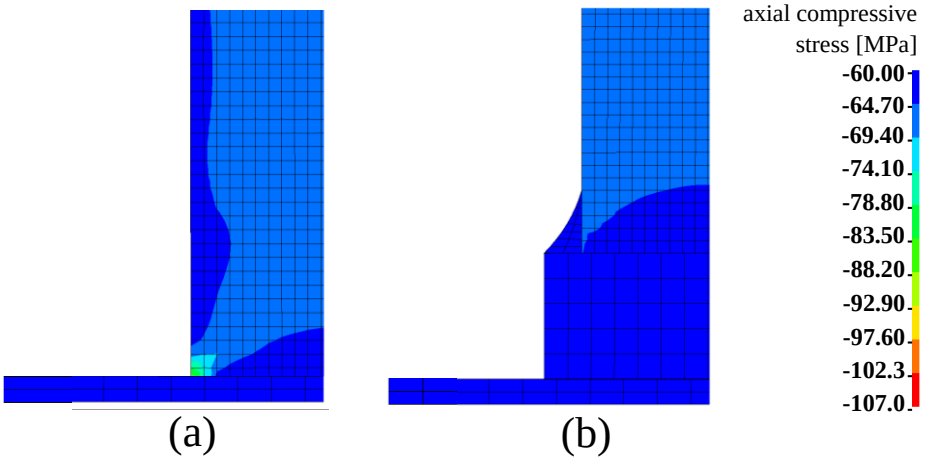

Figure 67. The distribution of the axial compressive stress of; (a) the ASTM configuration; (b) the Mogi configuration (Mardalizad et al., 2018b)

13.1.2 Material model: MC and DP

The ASTM configuration of UC test is just simulated by MC and DP material model (in the software Abaqus). All the simulations reported in this PhD thesis that are obtained by either MC or DP materials models, are explained in details in (SCAZZOSI and MAIOLANI, 2015-2016), which is a master thesis defined in conjunction to this PhD thesis. However, the results are necessary to be reported here in order to critically discuss the capability of the KCC material model.

These models consist of a specimen and two rigid platens as shown in Figure 68. The geometry of the specimen is the same as the one modelled in LS-DYNA for ASTM configuration. The material parameters are the same as the ones explained in the previous chapter related to MC and DP models. The rock specimen is discretised by 1mm meshed elements after performing the mesh sensitivity analyses. The axial displacement is measured in between points A and B in Figure 68b, which are basically located in the same position where the extensometer was set during the experimental test. The loading was applied by a smooth step function that reaches a maximum of 0.3 mm in 0.01s.

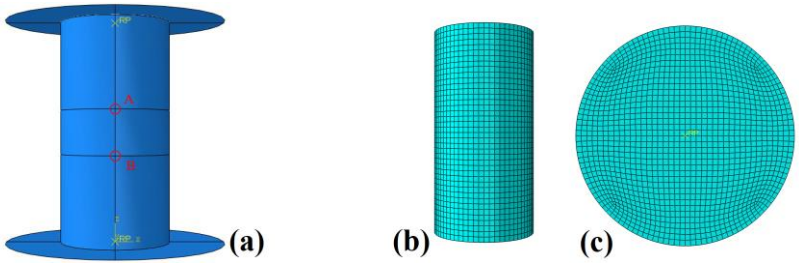

Figure 68. Numerical models developed in Abaqus to replicate the ASTM configuration; (a) model assembly, (b) 1-mm meshed specimen and (c) 1-mm meshed (rigid) platen.

The numerical results obtained by MC and DP models are indicated in Figure 69. Both of these models predict the shear failure mode similar to the failure mode of the Mogi's configuration, and not similar to the ASTM configuration.

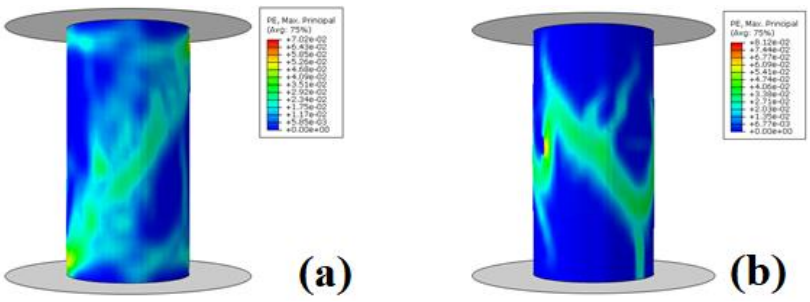

Figure 69. Distribution of the effective plastic strain after failure for the ASTM configuration; (a) the MC plasticity model and (b) the Linear DP model.

13.1.3 Comparison of the numerical and experimental results

The stress-strain diagrams of the numerical models are compared to the experimental results according to Figure 70 and Table 22. All the numerical results obtained show significant agreement with the experimental data. It should be mentioned that both the MC and DP models are calibrated mainly based on the experimental data of unconfined compression test. However, the KCC material model is calibrated based on the experimental data of triaxial compression test and Brazilian disk tests. Therefore, it can be concluded that the calibrated KCC proves to be an adequate material model to predict the unconfined compression test.

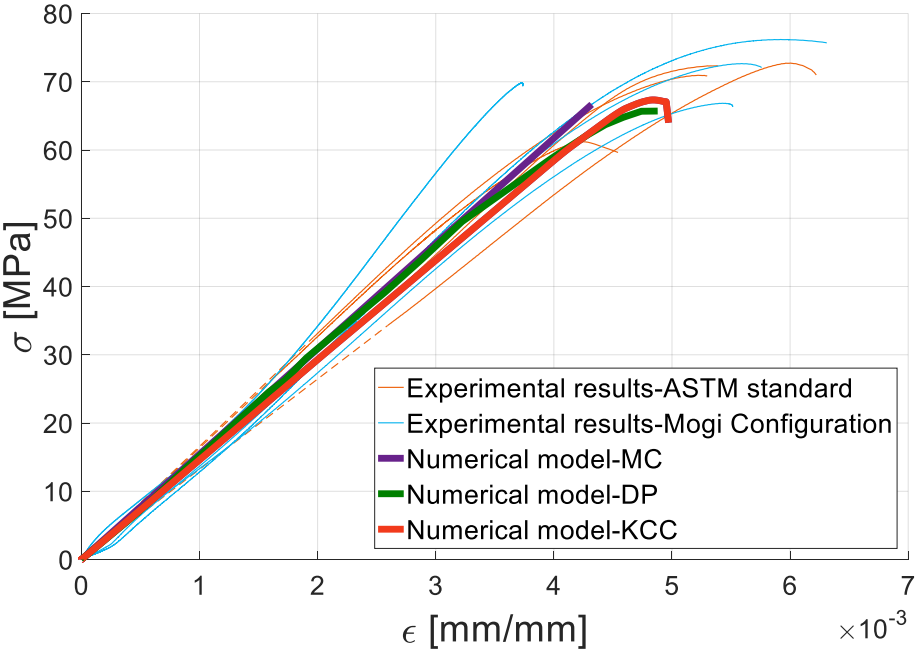

Figure 70. Comparison of experimental data and numerical results.

Table 22. comparison of the UCS values obtained by numerical simulation and the experimental tests (Mardalizad et al., 2018b)

	$(\sigma_u)_{experimental}$	$(\sigma_u)_{Numerical}$	**error**
ASTM – KCC	64.0 [MPa]	66.9 [MPa]	-1.6 %
ASTM – MC	64.0 [MPa]	65.9 [MPa]	-3.0 %
ASTM – DP	64.0 [MPa]	67.4 [MPa]	-5.3 %
Mogi – KCC	71.6 [MPa]	67.2 [MPa]	6.1 %

13.2 Quasi-Static Brazilian disk test

13.2.1 Material model: KCC

The numerical model developed to analyse the Brazilian disk test consists of four geometry parts (see Figure 71), which are: a rigid upper compressive platen, an elastic curved bearing block, the specimen and an elastic cylindrical (steel) lower platen. The simple elastic material model (*MAT_ELASTIC in LS-DYNA) was used for the bearing block and the lower platen, by considering the elastic modulus equal to 210 GPa. Since the axial deflectometer used to measure the displacement was fixed to the bed of the apparatus, this cylindrical lower platen was modelled by its real dimensions. The curved bearing block was also modelled in order to avoid excessive stress concentration within the numerical simulations (the same logic as in the experimental procedure).

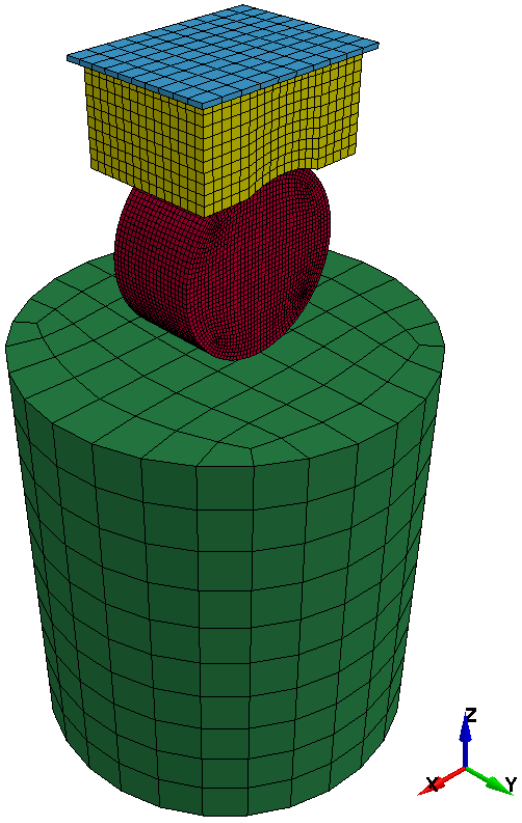

Figure 71. Numerical model developed in LS-DYNA to replicate Brazilian disk test.

The part representing the sandstone specimen has the same geometry as the specimens of class H; with a diameter of 40 mm and a thickness of 20 mm. Similar numerical analyses were performed for the specimens with other geometries, however they

are not reported here due to similar characteristics. This part is discretized by using one-integration point hexagonal solid elements. Mesh convergence analyses (similar to what was indicated for UC test) showed that solid elements with a side dimension of lower than 1.5 mm did not influence the results. Therefore, the specimen discretized with 1 mm mesh size was considered for the numerical simulations of this chapter. The displacement-control compressive loading was imposed by the upper platen and the bottom surface of the cylindrical lower platen was fixed (i.e., zero degree of freedom). Again, due to the quasi-static nature of this simulation, a time-scaling approach was exploited to save the computation time. Therefore, the upper compressive platen was pushed down by a smooth-step function at an average velocity of 0.1 mm/ms. The automatic surface to surface contact treatment was defined for all the contacts. The same method used for the UC test simulations has been considered here for adaptive conversion of distorted elements to the SPH particles. The maximum effective strain at failure (EFFEPS) is considered as the conversion. For this purpose, first the simulation should be run without the MAD_ADD_EROSION implementation to examine the presence of highly distorted elements and to identify the EFFEPS at that time step. Within this study, the EFFEPS was set to 0.03.

The fully calibrated KCC material model and the equation-of-state which are expressed in Table 18 and Table 15, respectively, were used for the numerical simulations. However, the sensitivity analyses were exploited based on the b_2 - parameter.

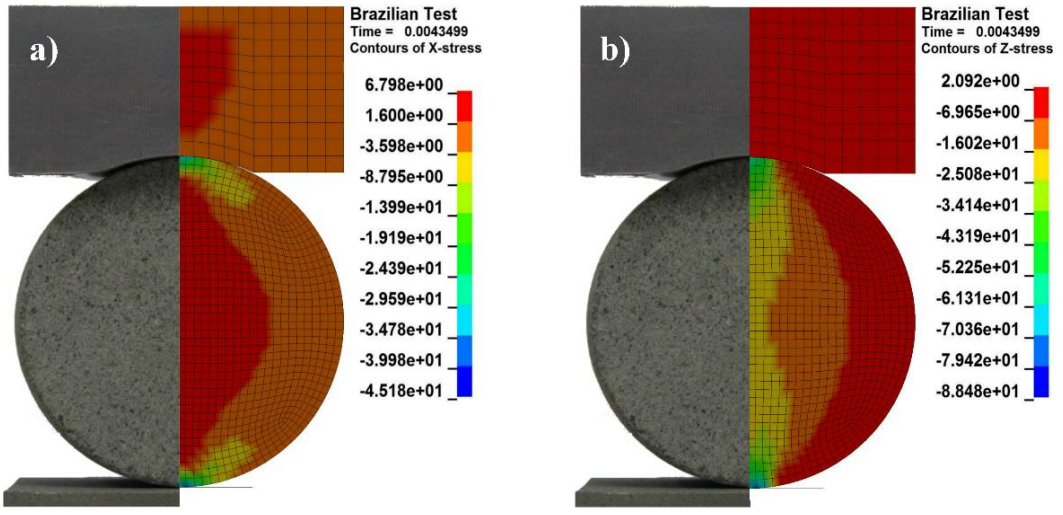

Figure 72. Distribution of the numerical stress solutions at the surface of the Brazilian disk specimen obtained by the KCC material model; (a) horizontal stresses, and (b) vertical stresses.

The stress distribution at the surface of Brazilian disk specimen in both the horizontal (perpendicular to the loading direction) and the vertical (parallel to the applied

load) directions are shown in Figure 72. The stress concentration due to local contacts are located near the upper bearing surface as well as the lower compressive platen. The contours of the horizontal stresses (see Figure 72a) are almost uniformly distributed, in particular in the diametral direction of the disk. However, the vertical stresses in this direction are increased from the center of the disk towards the loading points. The stress contours shown in this figure are in accordance to the distribution of the stress analytic solution based on the Hondros equations reported in (Jianhong et al., 2009).

The distribution of the "scaled damage parameter" (after failure) of a Brazilian disk model is indicated in Figure 73. As can be seen, the crack is propagated almost along the diametral direction, where the principle tensile stress reaches its maximum values. The same is true for the numerical results shown in Figure 73b, which is captured just one step after the failure. The shear failure mode located near the bottom contact point is shown in Figure 73c as well. This failure mode, central part fracture pattern (type a in Figure 28), is the same the one reported in (Basu et al., 2013).

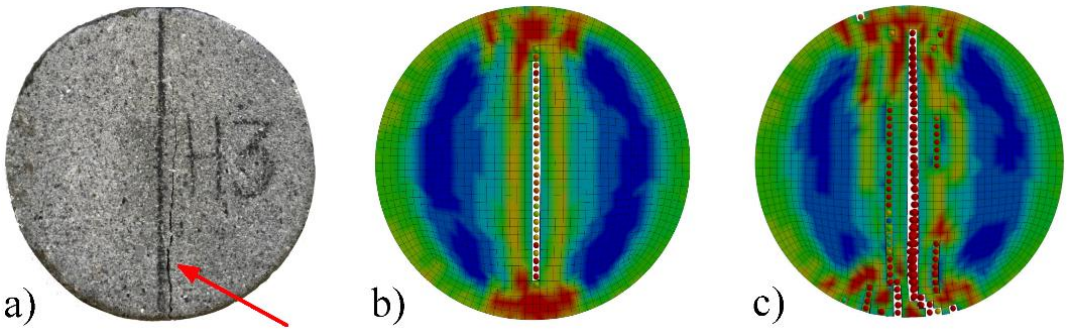

Figure 73. The crack propagation patterns; (a) after experimental test, (b) and (c) one- and two-time steps after the failure of the numerical model (KCC), respectively.

13.2.2 Material model: MC and DP

The Brazilian disk test is again simulated by MC and DP material model (in the software Abaqus) in order to critically discuss the capability of the KCC material model. These models consist of a specimen and two rigid platens as shown in Figure 74. The geometry of the specimen is the same as the one modelled in LS-DYNA. Both the upper and lower platens are rigid shell parts. However, the upper platen is modelled as a curved part with a radius of curvature equal to 30 mm. The material parameters are the same as the ones explained in the previous chapter related to MC and DP models. The lower platen is kept fixed while the axial displacement is applied by the upper

platen. The loading was applied by a smooth step function that reaches a maximum of 0.3 mm in 0.01s.

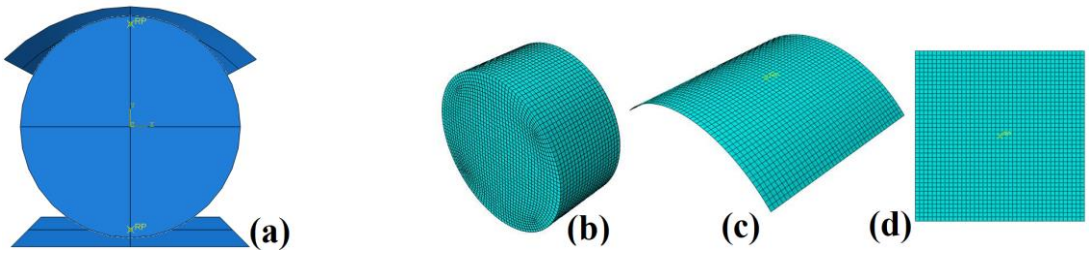

Figure 74. Numerical models developed in Abaqus to replicate the Brazilian disk test; (a) model assembly, (b) 1-mm meshed specimen, (c) curved upper platen and (d) lower platen.

The numerical results obtained by MC and DP models are indicated in Figure 75. Both of these models predict the central line fracture mode similar to experimental results.

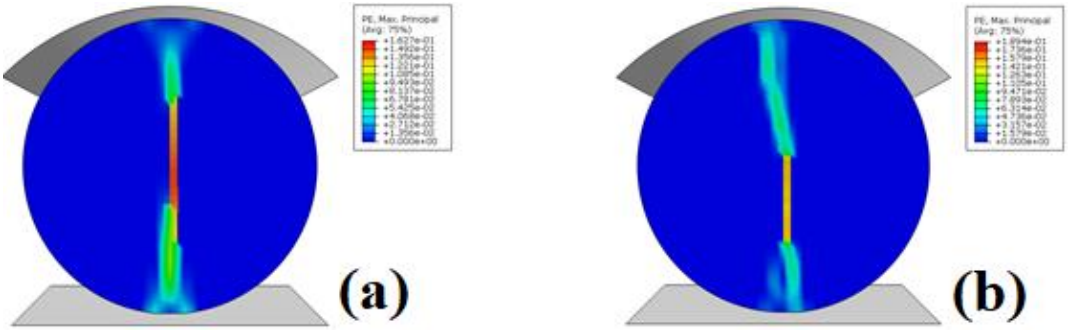

Figure 75. Distribution of the effective plastic strain after failure for Brazilian disk test; (a) the MC plasticity model and (b) the Linear DP model.

13.2.3 Comparison of Numerical results and experimental data

The numerical simulation results in terms of the load–displacement curves are compared in Figure 76 with experimental data. The last row of Table 23 represents the 95% confidential interval of the average value of each mechanical property.

In the Brazilian disk test, the principal tensile stresses were uniformly distributed along most parts of the vertical diameter (except the areas near the two contacts), therefore by considering equation (50), the b_2 - parameter was expected to have a major influence on the numerical results. By increasing the b_2 - parameter, the $h(p)$ in equation (50) is decreased causing a reduction of the area below the tabular damage

function rendering the material more brittle and accordingly decreasing the failure force. Therefore, the precise value of the b_2 - parameter for a material was determined by try and error. As can be seen in Figure 76 and Table 23, when the b_2 - parameter of KCC material model reaches a value equal to 3.21, the best fit of the numerical result with the experimental ones was obtained.

Although the level of failure load obtained by Drucker-Prager model is in the 95% confident interval of experimental results, the corresponding displacement underestimates the experimental data. The numerical results obtained by Mohr-Coulomb model, on the other hand, do not lie in the 95% of confidence interval, neither for the failure load, nor the corresponding displacement. The reason behind these less accurate results obtained by MC and DP is due to the fact that both material models are able to predict the linear dependency of the material strength with the hydrostatic pressure. While, the tensile behaviour of rocks deviates from linearity. Therefore, it is not possible to calibrate these material models so that they predict precisely both unconfined compression and tensile splitting tests in the same time.

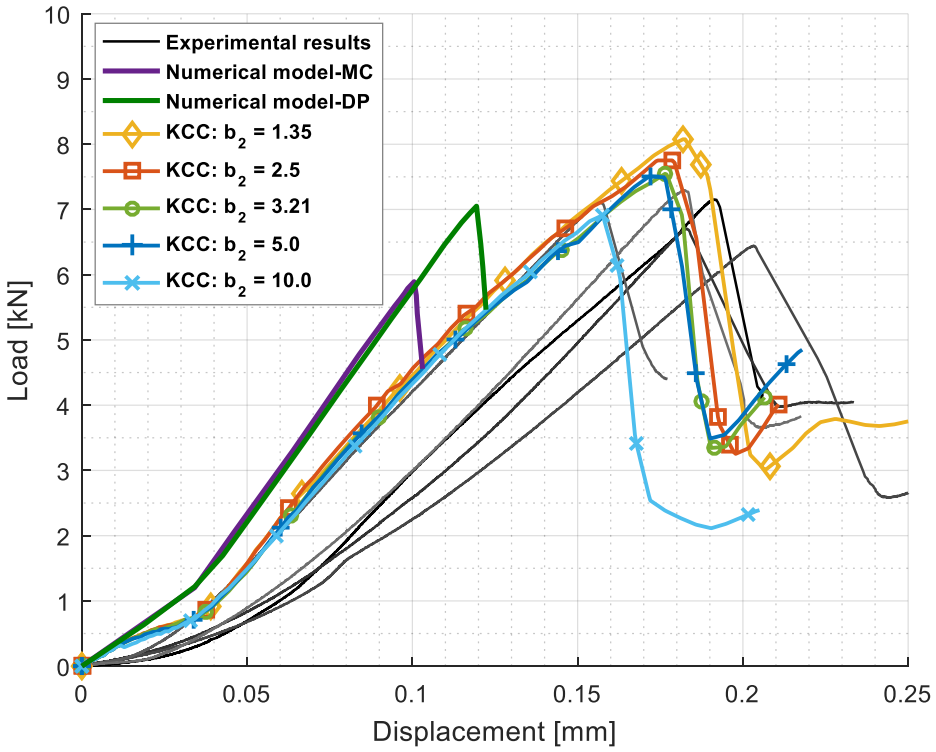

Figure 76. Comparison of the experimental and the numerical results of the Brazilian test, in terms of load-displacement.

Table 23. The numerical results of the Brazilian test and the comparison with the experimental data.

	$F_{max}\,[kN]$	$\Delta l_{max}\,[mm]$
KCC - b_2 = 1.35	8.075	0.182
KCC - b_2 = 2.50	7.752	0.178
KCC - b_2 = 3.21	7.531	0.177
KCC - b_2 = 5.0	7.503	0.172
KCC - b_2 = 10.0	6.910	0.157
MC	5.892	0.101
DP	7.050	0.119
Average of the experimental data	6.942	0.183
"95% CI" of the experimental data	[6.504-7.579]	[0.162-0.204]

13.3 Flexural test

13.3.1 Material model: KCC

The replication of the Flexural test was performed to validate the numerical investigations and the calibration procedures described within this PhD thesis. Due to the symmetrical nature of this experimental test, only one-quarter of the configuration was modelled numerically. The numerical model investigated by LS-DYNA consisted of five components, which were the upper compressive platen, two rollers, the specimen and the support steel block. The simple elastic material model (*MAT_ELASTIC in LS-DYNA) was used for both the Aluminium rollers and the support steel block, by considering their elastic modulus equal to 70 and 210 GPa, respectively. Since the axial deflectometer used to measure the displacement was fixed to the bed of the apparatus, the support block was modelled by its real dimensions.

The geometry of part representing the sandstone specimen was the same as the experimental one; with a length of 318 mm, a width of 102 mm and a height of 32 mm. This part was discretized by using one-integration point hexagonal solid elements with a side dimension of 3 mm. The displacement-control compressive loading was imposed by the upper rigid platen and the bottom surface of the steel support block was fixed (i.e., zero degree of freedom). Similar to the two previous simulations, the time-scaling approach was used to save computation cost. Therefore, the upper compressive platen was pushed down at a constant velocity of 9 mm/s. The automatic surface to surface contact treatment was defined for all the contacts. The full calibrated KCC material model and the equation-of-state which are expressed in Table 18 and Table 15, respectively were used for the numerical simulations. The sensitivity analyses were also exploited based on the b_2 -parameter.

The conversion of FEM to SPH particles is only considered for the rock specimen. In the LS-DYNA model, instead of applying single point constraints to the SPH particles, which can lead to inaccurate results and numerical instabilities, specific boundary conditions at the symmetry planes were imposed (Hallquist, 2014). The BOUNDARY_SPH_SYMMETRY_PLANE keyword creates automatically an imaginary plane which reflects the forces of a set of ghost particles to the particles in the model. Although these ghost particles have identical properties as the real ones, they do not physically exist and simply contribute to the particle approximation (Anghileri et al., 2011). The maximum principal strain is considered as the eroding criteria for FEM to SPH particles conversion for all the numerical simulations. The numerical results of

the KCC model in terms of stress distribution along length and scaled damage parameter are expressed in Figure 77.

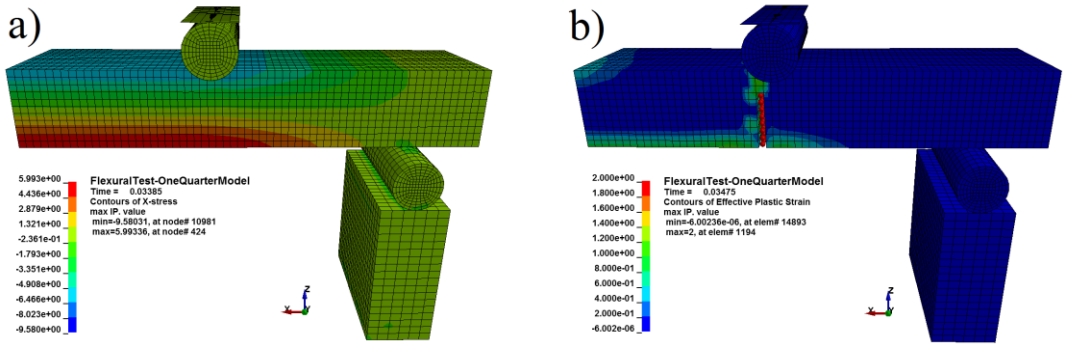

Figure 77. Distribution of (a) numerical stresses in the X direction (along the length) and (b) the scaled damage parameter by the KCC model (Mardalizad et al., 2017c).

Figure 77a represents the distribution of the X stress (along the length of specimen) one-time step before failure. The tensile and the compressive stresses at the numerical model are present in the element below and above the neutral axis, respectively. Figure 77b indicates the fracture pattern of the numerical result. The contour plot represented in Figure 77b represents the "scaled damage measure, δ". As can be seen, the SPH particles formed at the instant of failure express the crack patterns observed during the experimental test (see Figure 34).

13.3.2 Material model: MC and DP

The specimen is properly partitioned to accurately position it on the steel rods and to identify the measuring point which is exactly in the middle of the lower face as in the experimental tests. It is assumed that the specimen has got a stiffness which is negligible with respect to the one of the steel rods. This assumption allows to model the steel rods as discrete rigid shell parts. The rods are modelled as shells that reproduce part of the lateral surface of a cylinder with a diameter of 25 mm and a length of 120 mm. The movement of each rod is governed by its reference point (see RP in Figure 78). The boundary conditions are applied to the reference points of the rods which govern the motion of all the rigid part. The two bottom rods are kept fixed while a downward displacement is imposed to the two upper rods. The displacement follows the equation of the smooth step and reaches a maximum of 1 mm in 0.01 s.

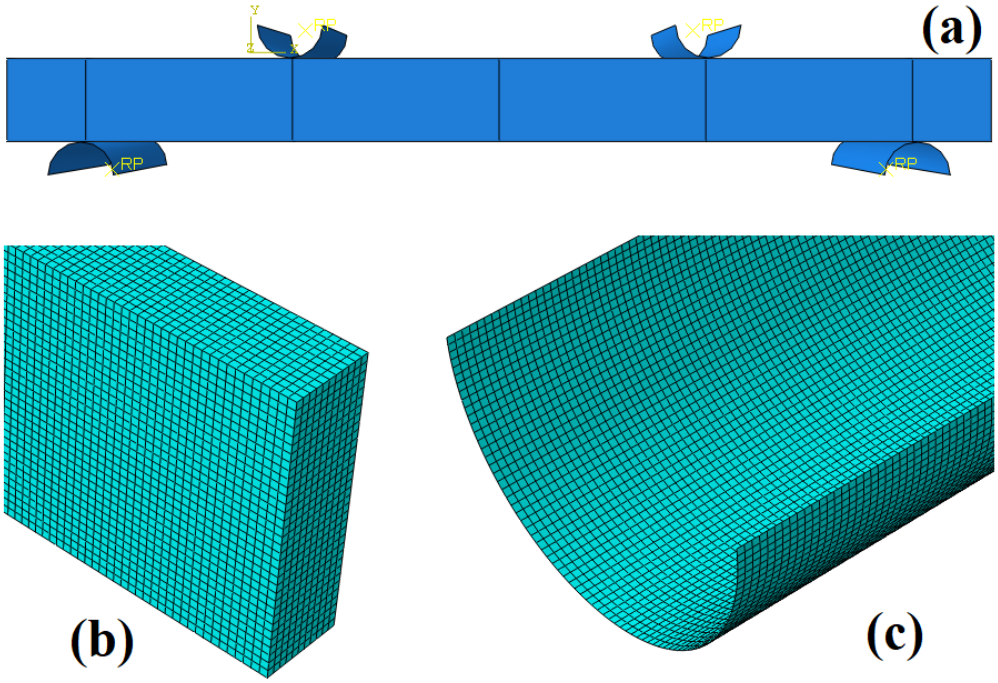

Figure 78. Numerical models developed in Abaqus to replicate the flexural test; (a) model assembly, (b) 3-mm meshed specimen, (c) curved platen.

Figure 79 represents the failure patterns. The crack propagates in the bottom face of the specimen in both models, where the state of stress is of tension, in correspondence of the moving rod. The failure pattern is the same of the experimentally observed shown in Figure 34.

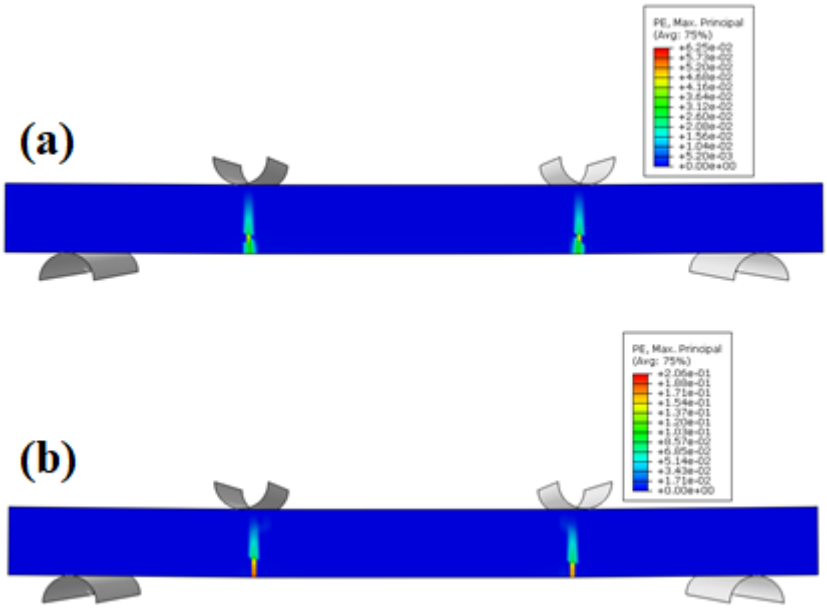

Figure 79. Distribution of the effective plastic strain after failure for Flexural test; (a) the MC plasticity model and (b) the Linear DP model.

13.3.3 Comparison of Numerical results and experimental data

The numerical results are expressed in terms of force-displacement diagrams in Figure 80 (and also Table 24) and were subsequently compared with the experimental ones. There is a row in Table 24, labelled as "*95% CI*" of experimental average value, that was also reported in Table 23. As previous described there is a probability of 95% that the average value of a set of populations lie inside this interval. Therefore, they can be considered a reasonable description of the physical phenomena thus suitable for comparing the numerical results.

Identical to the Brazilian disk test, due to the presence of the principal tensile stresses at the lower surface of the specimen, the b_2-parameter of the KCC material model was shown to greatly influence in the results. The value of the b_2-parameter determined by the Brazilian test (i.e. equal to 3.21) yielded to the best response also in the Flexural test. The numerical results, both in terms of the ultimate force and the maximum displacement, were found to lie within the 95% confidence interval of the experimental values (see Table 9). The results obtained by the MC model are also in good agreement with the experimental data and the failure force is very close to the maximum value reported as 95% Confidence Interval. However, as it was discussed in the previous section, the MC model didn't show reasonable performance to simulate the Brazilian test.

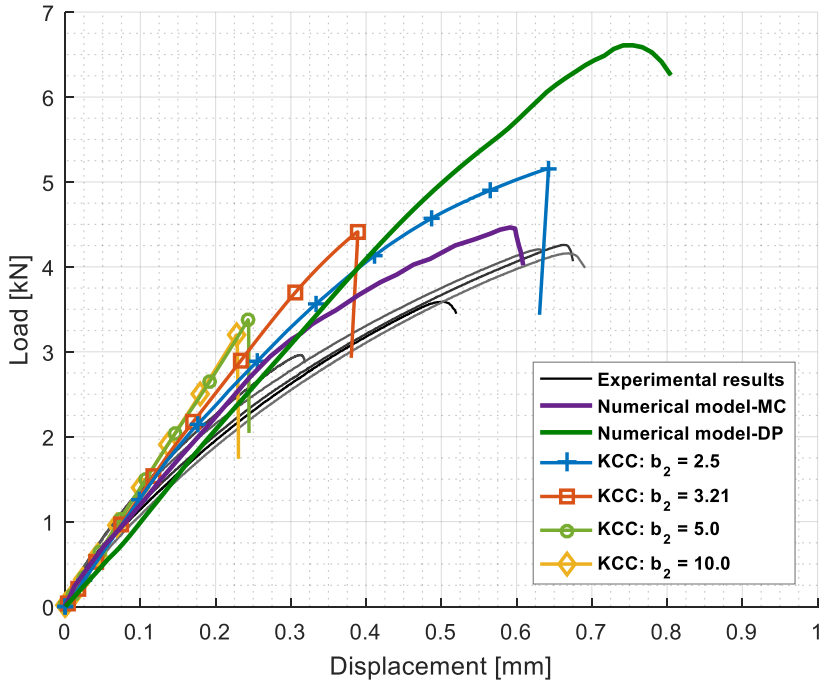

Figure 80. Comparison of the experimental and the numerical results of the Flexural test, in terms of load-displacement.

The DP model predicts the maximum load as 6.61 kN which is far from the reported 95% Confidence Interval (with an overestimation of about 80% respect to the experimental average value). Therefore, it is not reliable to model the mechanical behaviour of Pietra Serena in case of a significant tensile stress is present. Indeed, the Drucker-Prager criterion is well suitable to model the linear dependence of the material strength with p. The material behaviour of rocks, for negative values of p, deviates from linearity and the material failure points lie below the Drucker-Prager failure line leading to the overestimation of the flexural strength of the material.

Table 24. The numerical results of the Flexural test and the comparison with the experimental data.

	$F_{max}\,[kN]$	$\Delta l_{max}\,[mm]$
KCC - b_2 = 2.50	5.157	0.642
KCC - b_2 = 3.21	4.411	0.389
KCC - b_2 = 5.0	3.376	0.243
KCC - b_2 = 10.0	3.198	0.228
MC	4.451	0.598
DP	6.609	0.754
Average of the experimental data	3.835	0.554
"95% CI" of the experimental data	[3.143-4.527]	[0.367-0.742]

Therefore, by considering the numerical results obtained by the KCC, the MC and the DP models for different loading applications; i.e. unconfined compression test, Brazilian disk test and flexural test, it is proved that the KCC material model can be considered as an adequate material model to predict the complex mechanical behaviour of rock materials. The KCC material model will be implemented as the constitutive model for the next numerical simulations studied in this PhD thesis.

13.4 Triaxial Compression test

The numerical model of the triaxial compression test consists of three parts; two rigid platens (representing the compressive platens) and the specimen. The rock specimen was replicated by a cylinder with the height and diameter of 200 mm and 100 mm, respectively. The displacement-control axial loading (compressive) was imposed by the upper platen, while the lower platen was fixed (i.e., zero degree of freedom). The confinement pressure was applied by *LOAD_SEGMENT_SET keyword to the exterior lateral side of the specimen and the upper platen. This confinement was applied gradually over the first 25 ms to avoid the issue of wave propagation noise, and afterward it was kept constant. After the confinement pressure reached its constant final value, the upper compressive platen was pushed down at a constant velocity of 140 mm/s. This loading rate was utilized in these quasi-static analyses, since the reduction of the computation time by the time-scaling approach was more convenient. This approach requires the monitoring of; the ratio of the kinetic to the internal energy during the simulations to avoid a large value (typically more than 10%).

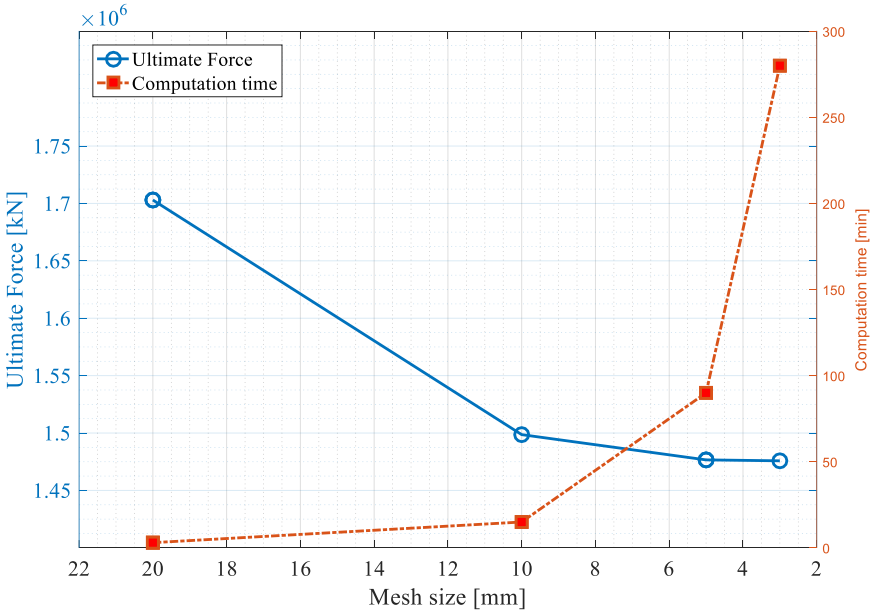

Figure 81. The effect of mesh size on the ultimate force and computation time.

The mesh convergence studies were performed, and the cylinder was discretized by four different types of meshes of a 3 mm, 5 mm, 10 mm and 20 mm size. Figure 81 indicates the numerical results of the TXC test with 20 MPa confining pressure, obtained for these different cylinders. The results are reported in terms of the ultimate

force (kN) and the computation time (minute). The blue diagram indicates that the mesh size of the numerical models doesn't influence the ultimate force when the mesh size is equal-lower than 5 mm. In order to reduce the computation time, the cylinder with a 5-mm mesh size is considered for the numerical simulations of this chapter.

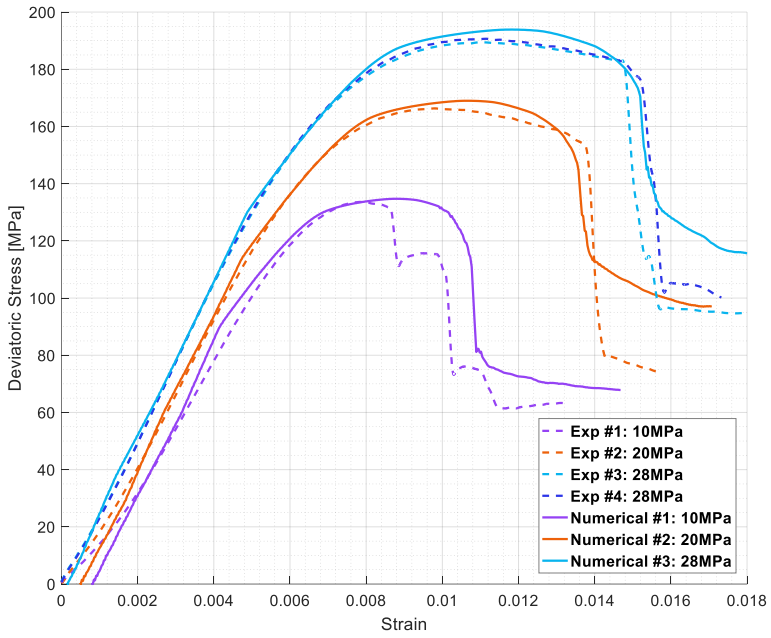

Figure 82. The comparison between the experimental results of the TXC and the corresponding numerical simulations of the fully calibrated KCC material model.

Figure 82 shows the plots of the deviatoric stress versus the axial strain computed by the full calibrated KCC material model, i.e. the $\eta - \lambda$ damage data is the "suggested values of $\eta - \lambda$" indicated in Figure 59, for confining pressures of 10 MPa, 20 MPa and 28 MPa. The deviatoric stress expressed in this figure is the difference between the engineering axial stress and the confining pressure. The solid lines of this figure represent the results of the numerical simulation, while the dashed lines express the experimental data. The solid lines were shifted to the right so that the point corresponding to the beginning of linear elastic regime was the same in both experimental and numerical diagrams. Thereby the effect of the settlement phase of the experimental tests (that occurs in the nonlinear regime at the beginning of the tests), which is not required to be replicated by the numerical simulations, could be neglected. Across all the confining pressure levels, the results of the numerical modelling revealed reasonable agreement with the experimental results, in all of the three separate phases; linear elastic, hardening and softening regimes. The most noteworthy features that was captured by this fully calibrated KCC material model is related to the

"brittle- or strain-weakening". This phenomenon is typically observed in sandstones, in which pronounce damage occurs at the softening phase and the shear plane develops so that it yields to a sudden stress drop. This phenomenon was captured due to the damage tabular function, which was obtained experimentally.

Generally, there are two different methods to control the softening behaviour of materials by the KCC material model; (a) the damage tabular function ($\eta - \lambda$ diagram that the effect of b_1 -parameter is considered in it) and (b) the *LOCWID* parameter. The result of the first method, which is also reported in Figure 82, demonstrated that the numerical simulations precisely replicate the experimental data. The damage function implemented for these simulations is the "suggested values of $\eta - \lambda$" indicated in Figure 59. However, the sensitivity analyses based on the *LOCWID* parameter is expressed in Figure 83, Figure 84 and Figure 85 for the 10 MPa, 20 MPa and 28 MPa confining pressures, respectively. The damage function implemented for these later simulations is the "experimentally obtained values of $\eta - \lambda$" reported in Figure 59, which was originally obtained based on experimental data. Although the numerical results obtained by the second approach (adjusting *LOCWID* parameter) replicate the experimental data up to an acceptable level, still the results obtained by the first approach expressed more accurate responses. This is more obvious in case of a sudden drop in the softening regime. As can be seen, the *LOCWID* parameter was able to expand the softening regime, while the gradient of the diagram could not be significantly altered.

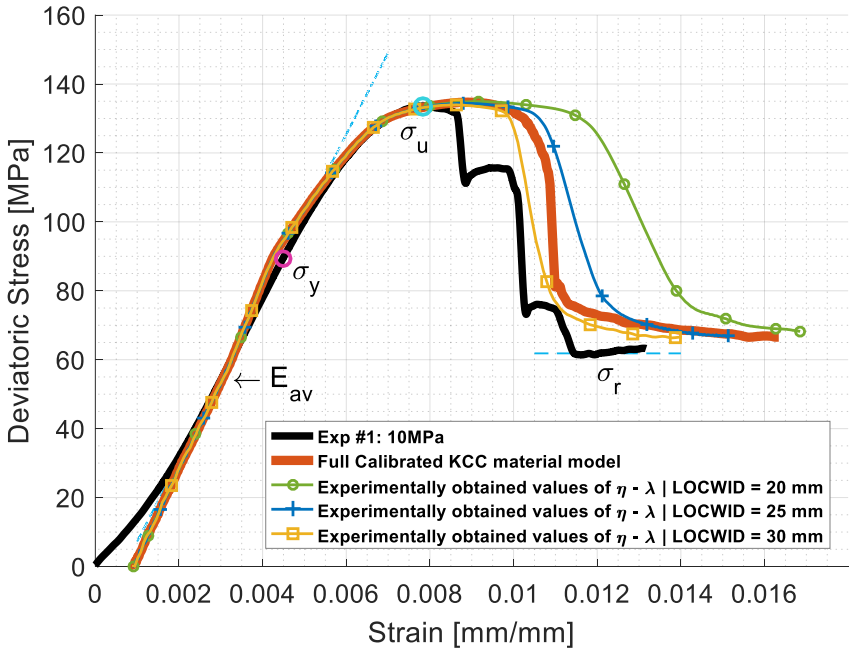

Figure 83. The effect of the LOCWID parameter on the numerical simulation results; 10 MPa confining pressure

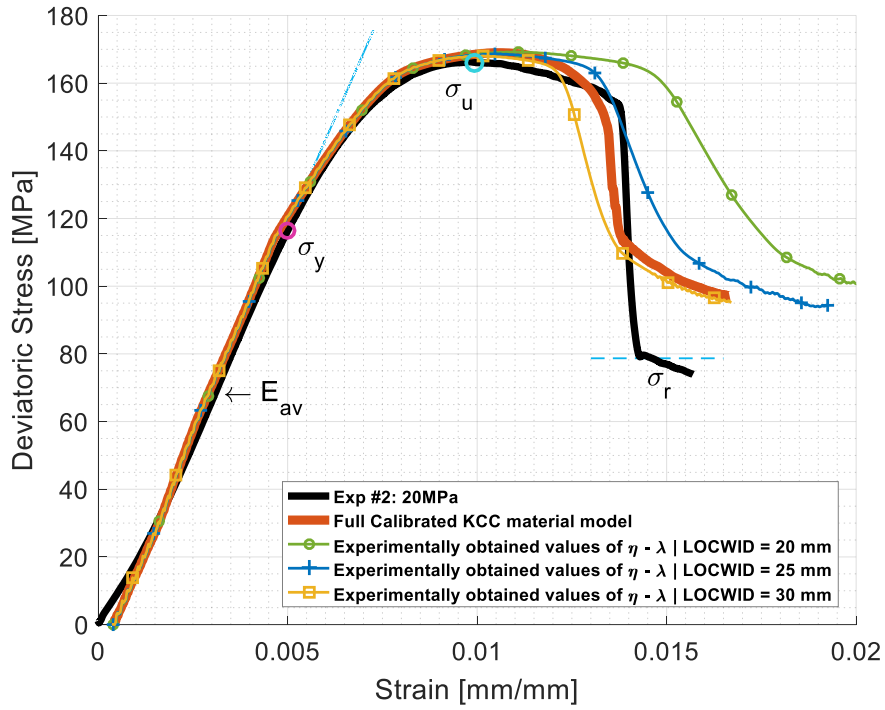

Figure 84. The effect of the LOCWID parameter on the numerical simulation results; 20 MPa confining pressure.

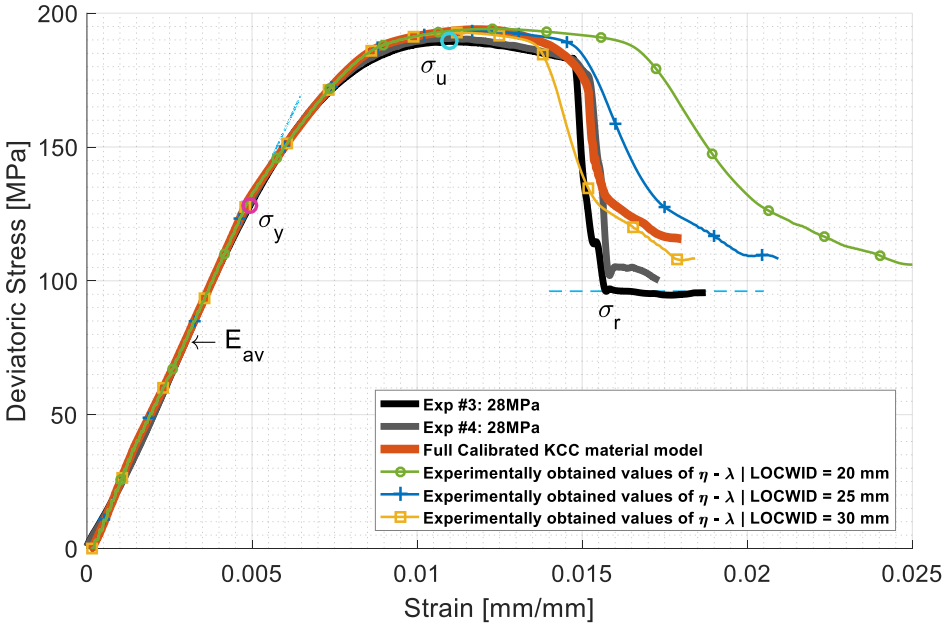

Figure 85. The effect of the LOCWID parameter on the numerical simulation results; 28 MPa confining pressure.

By definition, the b_2-parameter that governs the tensile regime, has no influence on the triaxial compression test, therefore, the sensitivity analyses are not reported for this parameter. The automatic surface to surface contact treatment was defined for all the contacts, using frictional coefficients ranging from 0.1 to 0.4. The distribution of the "scaled damage parameter" (after failure) of a triaxial compression model conducted with a 0.4 coefficient of friction is indicated in Figure 86. Additional calculations conducted with 0.1, 0.2 and 0.3 friction coefficients give similar results. The X-shaped damage bands of the failure in Figure 86 is observed as a function of non-frictionless end conditions.

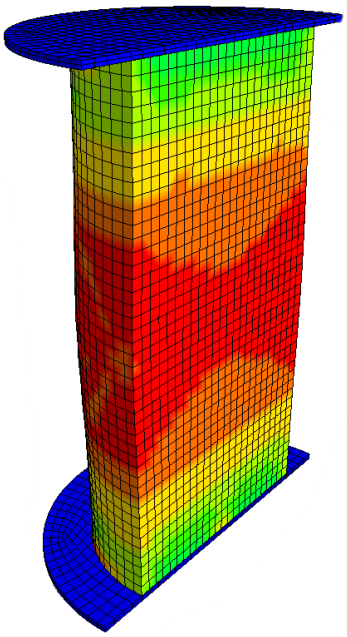

Figure 86. Distribution of the scaled damage parameter after failure for triaxial compression test.

13.5 Dynamic Brazilian disk test

The numerical model developed to analyse the dynamic Brazilian disk test consists of three geometry parts (see Figure 87), which are: the incident bar, the rock specimen and the transmission bar. The simple elastic material model (*MAT_ELASTIC in LS-DYNA) was used for both the incident and transmission bars, by considering the elastic modulus and density equal to 210 GPa and 7850 kg/m^3, respectively. All these parts have the same geometries as the experimental ones. This rock specimen is discretized by using one-integration point hexagonal solid elements. Mesh convergence analyses (similar to what was indicated for UC and quasi-static Brazilian test) showed that solid elements with a side dimension of lower than 1.5 mm did not influence the results. Therefore, the specimen discretized with 1 mm mesh size was considered for the numerical simulations of this section. The automatic surface to surface contact treatment was defined for all the contacts. The same method used for the previous numerical simulations has been considered here for adaptive conversion of distorted elements to the SPH particles. A limit value of the maximum effective strain at failure (EFFEPS) is considered as the conversion criterion. For this purpose, first the simulation should be run without the MAD_ADD_EROSION implementation to examine the presence of highly distorted elements and to identify the EFFEPS at that time step. Within this study, the EFFEPS was set to 0.1. The fully calibrated KCC material model, the equation-of-state and the strain rate enhancement diagram which are expressed in Table 18, Table 15 and Figure 61, respectively, were used for the numerical simulations.

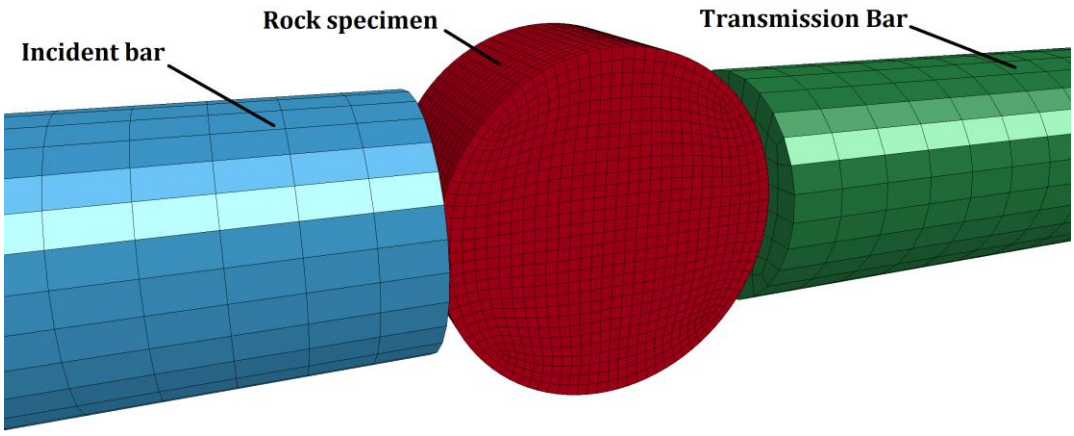

Figure 87. Numerical model developed in LS-DYNA to replicate dynamic Brazilian disk test by split Hopkinson pressure bar (SHPB).

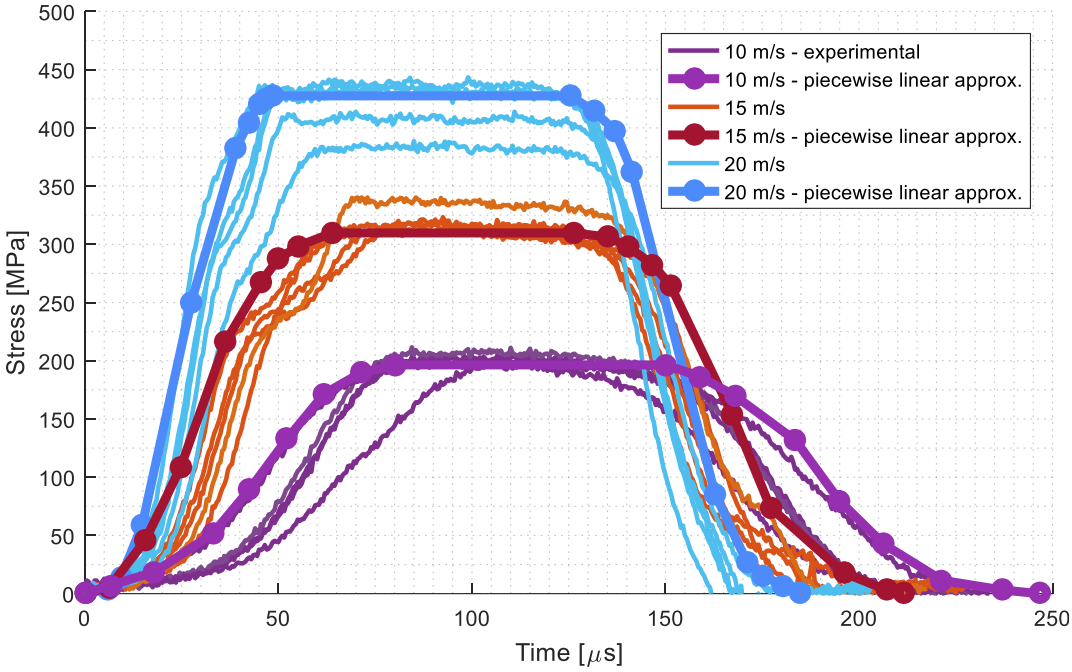

Figure 88. The experimental diagrams of the incident stress pulses and their corresponding piecewise linear approximations which are used in the numerical simulations.

Figure 88 indicates the experimental diagrams of the incident stress pulses (which are obtained from the voltages measured by SHPB) and their corresponding piecewise linear approximations. Since the purpose of this numerical modelling is to investigate the dynamic behaviour of the rock material, and not the SHPB device itself, the striker bar is not modelled. Instead, the piecewise linear approximations of the incident stress pulses are imposed by *LOAD_SEGMENT keyword of LS-DYNA at the left surface of the incident bar (corresponding to the surface that the pulse shaper is located in the experimental arrangement), according to Figure 88.

The reaction force-time diagrams of the numerical models are compared to the experimental results according to Figure 89. The P_1 and P_2 are the reaction forces corresponding to the incident and transmission bars, respectively. All the numerical results, both in terms of amplitude and the shape, show significant agreement with the experimental data.

The distribution of the KCC scaled damage parameter is expressed in Figure 90. The diametral tensile fracture patterns in the center of the disks are observed. This zone is split by the final localization zone upon reaching the dynamic tensile strength. As the loading rate increases, this zone becomes wider as well. This phenomenon representing the failure mode is observed by experimental procedures. Shear failures can be

also observed at the contact zones, particularly at the highest tested impact velocity (see Figure 90c).

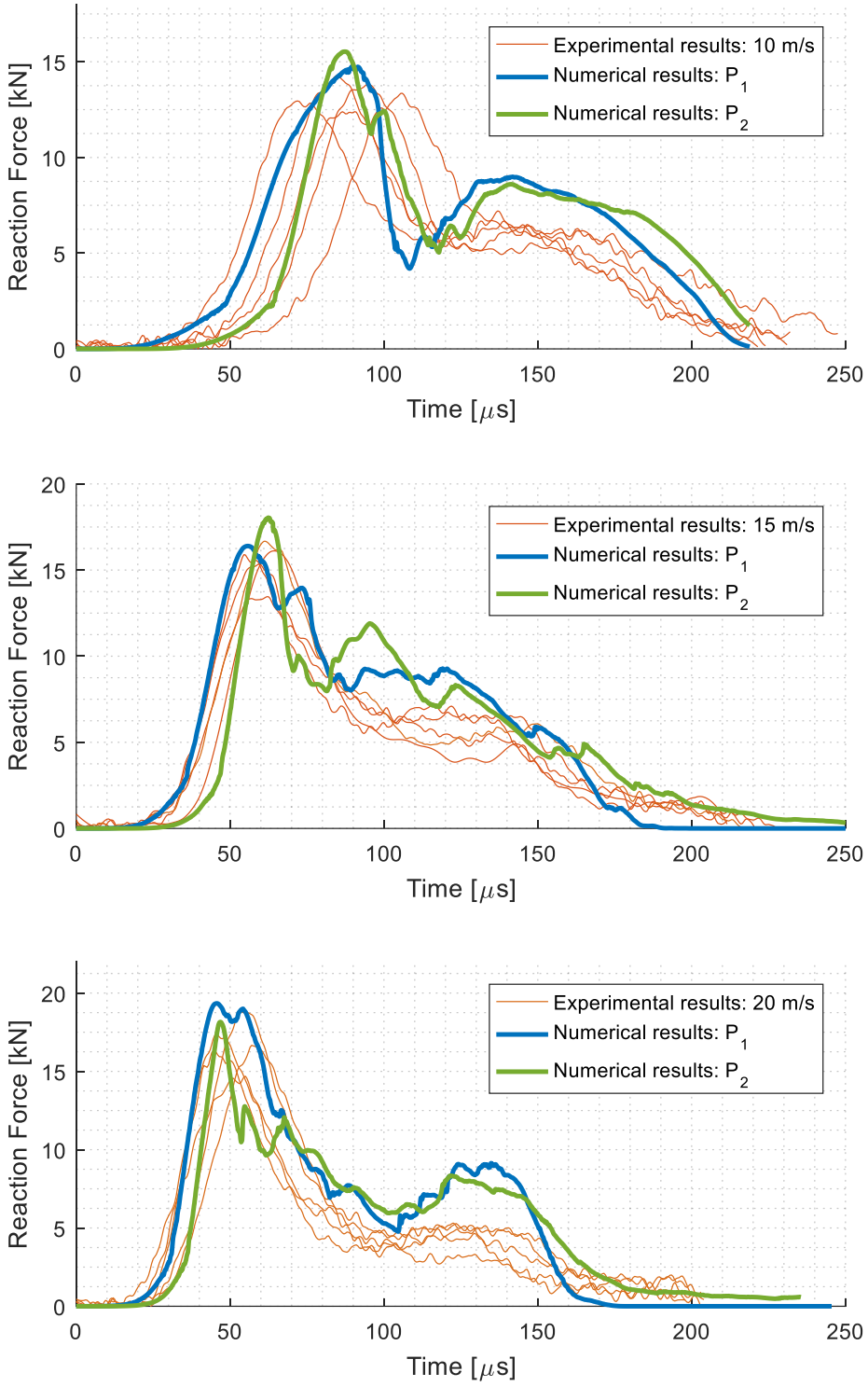

Figure 89. Comparison of the numerical results of the dynamic Brazilian disk test with the experimental values.

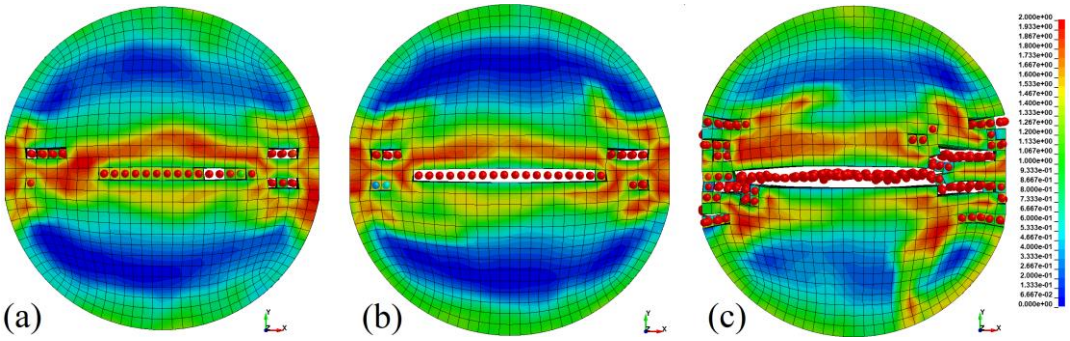

Figure 90. Distribution of the scaled damage parameter after failure for dynamic Brazilian disk test, at: (a) 10m/s, (b) 15 m/s and (c) 20 m/s.

Chapter 14

Assessment of FEM-coupled to-SPH technique

The Lagrangian Finite Element Method (FEM) is still one of the foremost numerical techniques to solve problems in solid mechanics. High accuracy and acceptable computing time are two noteworthy features of this method. However, as a mesh-based method, one of its main drawbacks is the low performance in dealing with large deformations and highly distorted solid elements, which is often unavoidable in the continuum mechanics based numerical modelling of fractured rock. The Smooth Particles Hydrodynamics (SPH) introduced by Monaghan (Monaghan, 1988), on the other hand, is a mesh-less method which discretizes a system into several grid-points at which the field variables are evaluated (Liu and Liu, 2010). The capability and performance of the SPH in dealing with large deformation problems, stems mainly from the fact that the nodal connectivity is not fixed in this method, as demonstrated e.g. in (Anghileri et al., 2011; Bresciani et al., 2016; Olleak and El-Hofy, 2015). However, the performance of SPH in terms of accuracy and computation time is often lower in comparison to the FEM. Therefore, inspired by the study of Bresciani et al., (Bresciani et al., 2016) an innovative approach was implemented in the present study which is called here the FEM-coupled to-SPH method. This method, which takes advantages of both the FEM and the SPH methods, erodes the elements who meet a certain failure criterion and subsequently replaces them with a specific number of SPH particles.

Punch Penetration test is a direct laboratory measurement deals with rock indentation. The presence of highly distorted elements (underneath the indenter tool) is inevitable in a rock indentation problem. Therefore, it has been decided to numerically study the punch penetration test with different numerical methods to assess the capability of the FEM-coupled to-SPH method.

Replication of the punch penetration test was attempted using the calibrated KCC model with the same geometry as the experimental configuration. Due to the axial symmetry of this test – an assumption strictly valid only for homogeneous materials – only one-quarter of the geometries were modelled (see Figure 91). Three different numerical techniques were applied to simulate the rock material during the penetration test: (a) constant stress FEM, (b) fully integrated FEM, and (c) coupled FEM-SPH method. The first method consists of a single-Gauss point reduced integration with an

8-node hexahedral element and an erosion algorithm to erase the elements at which the effective plastic strain reaches a certain limit (0.25). The second method is the same as the first one, while the hexahedral elements have an 8-Gauss point integration. In the last method, the constant stress solid finite elements are converted to SPH particles when the effective plastic strain reaches the same criterion (i.e. 0.25). During the course of this investigation, it was found that the response of the rock-tool simulation is sensitive to the value of the erosion criterion, therefore, the right criterion (i.e. 0.25) was selected based on a trial and error task.

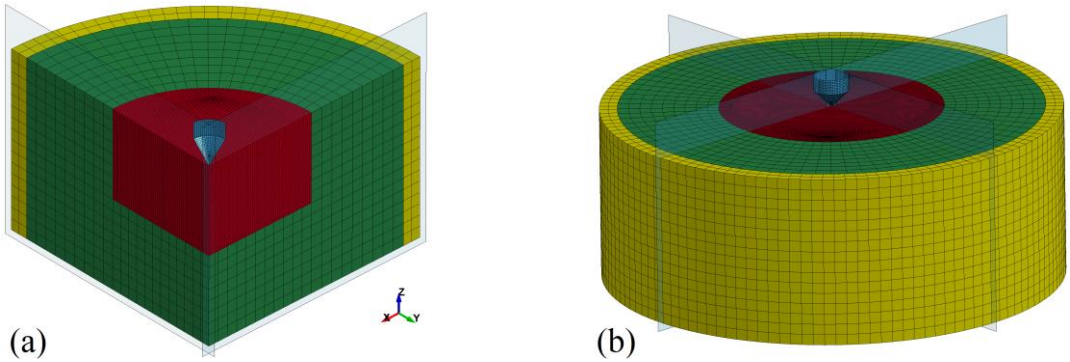

Figure 91. The numerical models of the punch penetration test; (a) ¼ symmetry, and (b) full model.

Apart from the rock specimen (the red domain in Figure 91), the hexagonal constant stress elements are used for all the other solid parts (i.e. concrete and steel tube). The linear elastic material model (*MAT_ELASTIC in LS-DYNA) with the elastic modulus of 210 GPa was assigned to the steel tube. The KCC model with the automatic calibration procedure (*MAT_072R3 in LS-DYNA) setting the UCS parameter equal to 52.5 MPa was assigned to the concrete. The compressive loading by the rigid punch was applied as a constant velocity boundary condition with a velocity of 9 mm/s and the bottom surface of the model was fixed. As the problem is solved with the explicit time marching, the mass scaling approach was used to reduce the computation time.

In the FEM-SPH model, instead of applying single point constraints to the SPH particles, which can lead to inaccurate results and numerical instabilities, specific boundary conditions at the symmetry planes were imposed (Hallquist, 2014). The recently implemented keyword in LS-DYNA, called BOUNDARY_SPH_ SYMMETRY_PLANE, creates automatically an imaginary plane, which reflects the forces of a set of ghost particles to the particles in the model. Although these ghost particles have identical properties as the real ones, they do not physically exist and simply contribute to the

particle approximation (Anghileri et al., 2011). The automatic penalty-based contact formulation was applied for all the components of the model.

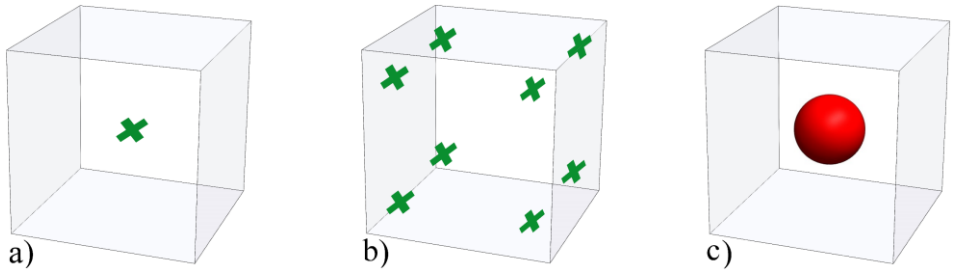

Figure 92. The schematic representation of a hexagonal solid element; (a) with 1 integration point, (b) with 8 integration points, and (c) that is converted to a SPH particle after a certain criterion.

The constant stress 8-node hexagonal element (single-integration point), see Figure 92a in combination with a suitable hourglass control scheme is usually a suitable choice for numerical modelling of solid structures due to its efficiency and sufficient accuracy (Borrvall, 2009). The domain representing the rock specimen in this study was discretized with 103320 elements (average size of 1.5 mm). The simulation results for the PPT test are shown in Figure 93, Figure 94, Figure 95 and Figure 96.

The predicted tool force-penetration curves in Figure 96 are analysed first. The reduced integration with erosion scheme exhibits an excessively too soft response with the maximum axial force being only 25 percent from the experimental ones. The overly soft response of this method might be due to the activation of the zero energy modes in the highly deformed elements just before their erosion. The full integration with the erosion method performs significantly better with the maximum axial force being 75 percent of the maximum experimental forces. However, with this method, more severe fluctuations are attested in the force-penetration curve. The fluctuations are probably caused by the element erosion events. Finally, the reduced integration with the conversion to the SPH method results, beyond 5 mm of penetration, in a stiffer response than the experimental response with the maximum force exceeding slightly the experimental ones. This change of stiffness is caused by the conversion, in contrast to the erosion in the first and second method, of the elements into SPH particles that interact with each other and with the finite elements thus conveying further loading.

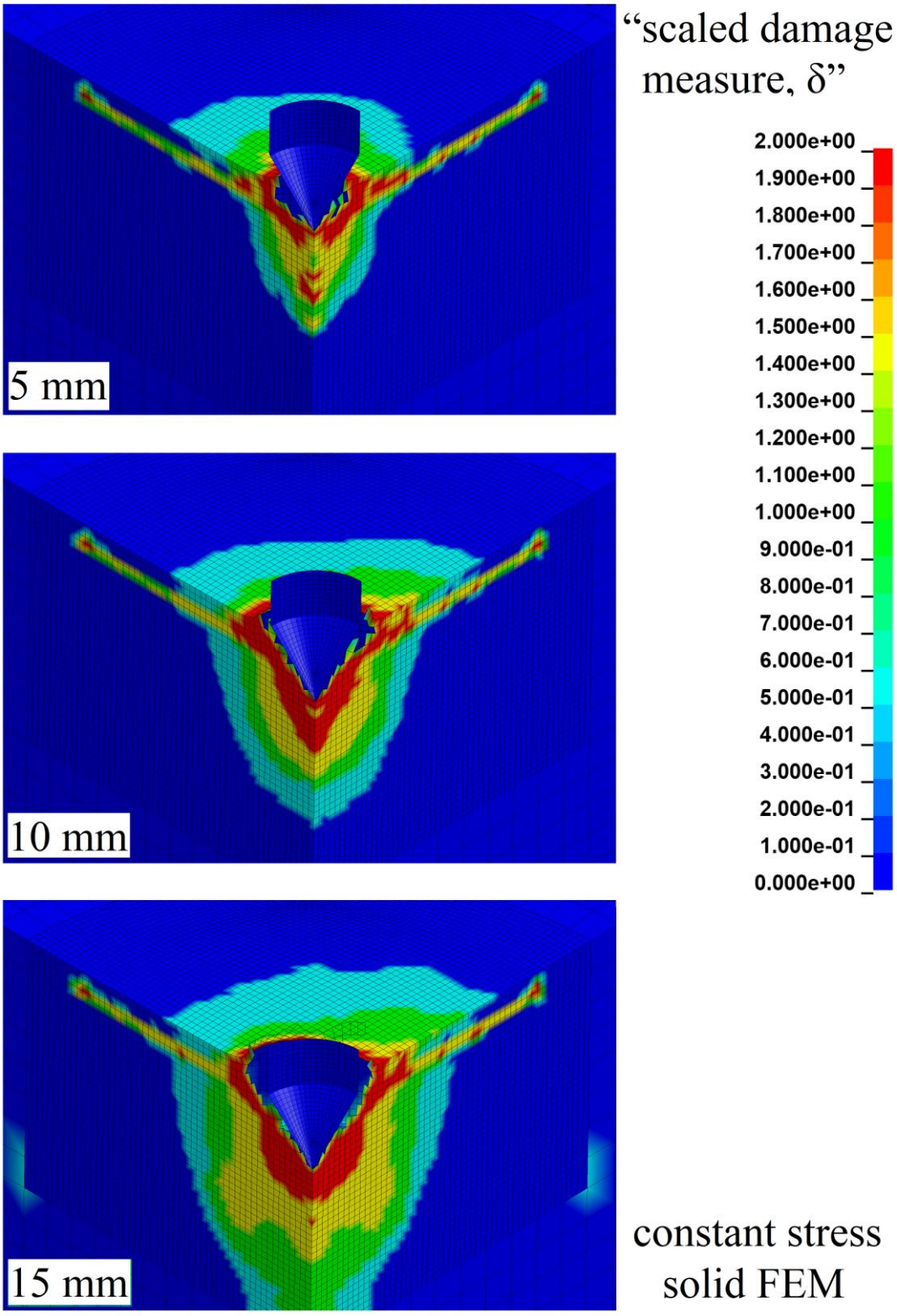

Figure 93. The results of numerical modelling at different penetration depths, made by the constant stress solid FEM.

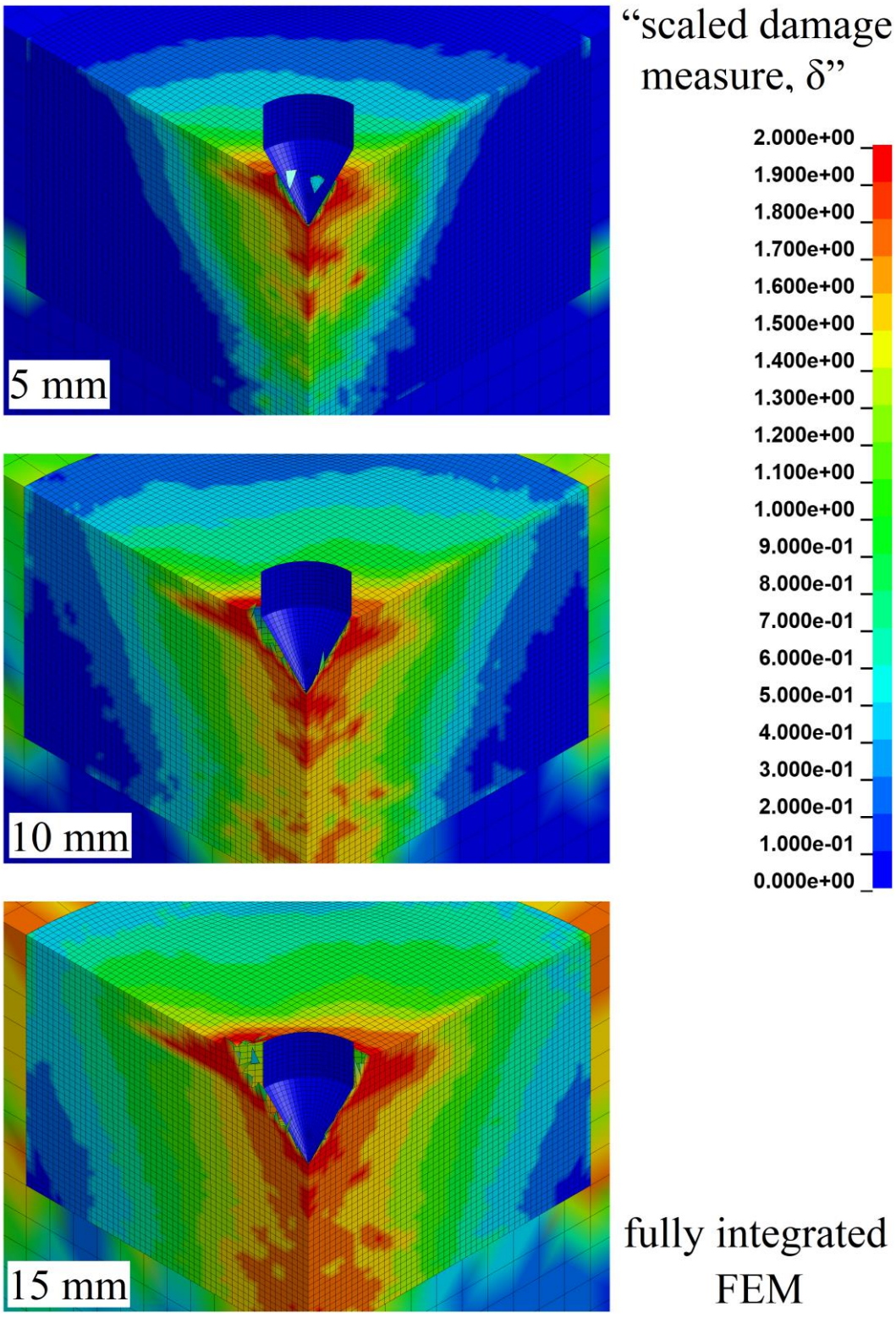

Figure 94. The results of numerical modelling at different penetration depths, made by the fully integrated FEM.

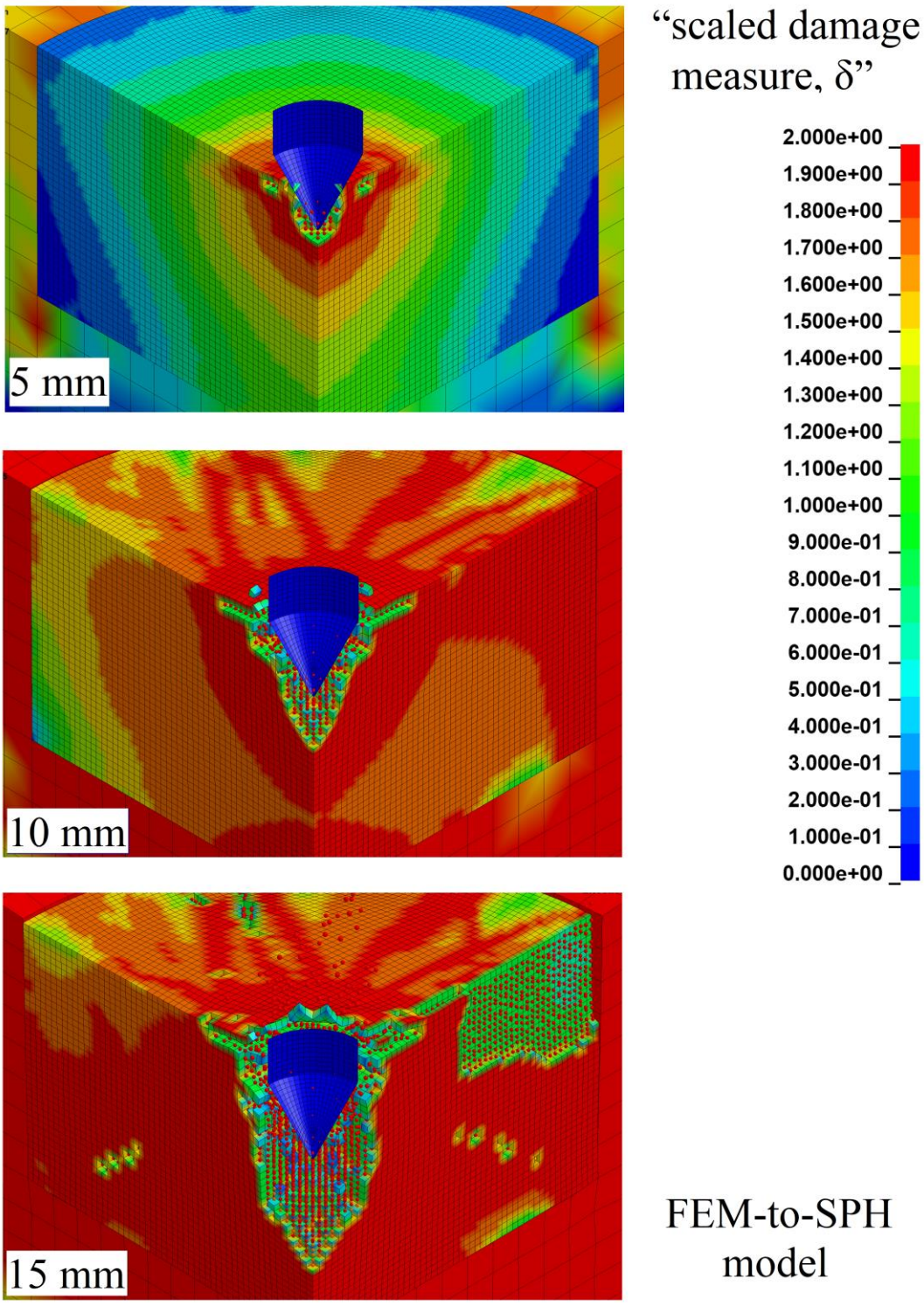

Figure 95. The results of numerical modelling at different penetration depths, made by the FEM-to-SPH model.

The characteristics of the predicted force-penetration responses correspond to the predicted damage patterns in Figure 93, Figure 94 and Figure 95 as follows. The overly

soft response of the reduced integration method is reflected in Figure 93 as an under predicted damaged zone. However, a peculiar feature of the results predicted with this method is the subsurface planar damaged area parallel to the rock surface. This feature almost disappears with the full integration method in Figure 94 but the damaged zone is substantially wider than that with the reduced integration. Because of the much stiffer response, even the concrete casing displays some yielding of the material (see Figure 94). When the highly distorted finite elements are converted to SPH particles, the interaction of the particles and finite elements results in excessive damaged zone in Figure 95. Here, the residual strength surface was reached, i.e. $\delta = 2$, in the concrete casing as well. Moreover, a large amount of SPH particles can be observed beneath the indenter where the crushed zone is located. A subsurface planar crack, formed by the SPH particles, propagating outwards from the tool can be observed as well. However, the most peculiar feature here is the radial crack plane on the symmetry plane formed by SPH particles; see Figure 95 with 15 mm of penetration. This crack type was observed in the indentation experiments on rock. Thereby, despite the slightly too stiff response, the FEM-SPH method can clearly be considered the most realistic one of the tested methods.

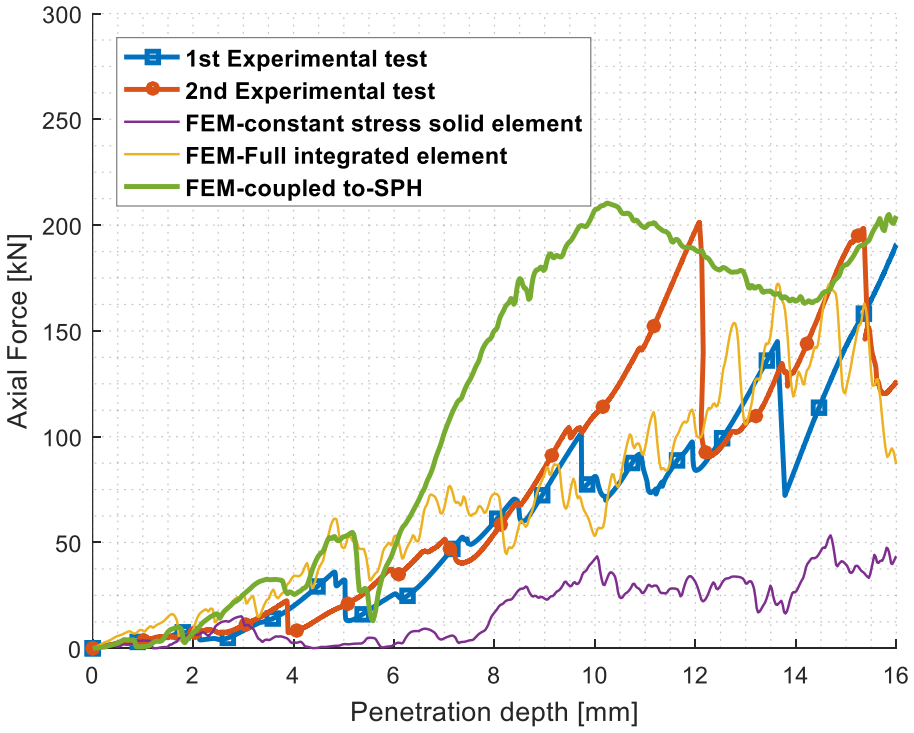

Figure 96. The axial force-penetration depth diagrams of numerical models in comparison to experimental ones.

Part V

Simulation of the offshore deep hole drilling problem in the oil and gas industry

Chapter 15

Double button-bit penetration (quasi-static) into a rock specimen under confining stresses

The conceptual model for drilling into reservoir rock by a multiple-buttons drill bit is expressed in Figure 97 (Liu et al., 2008). Drilling deep holes in bedrock poses challenges to the efficiency of rock excavation methods due to severe stress conditions prevailing in the bedrock induced by tectonic activity (Zang and Stephansson, 2009) or gravity (overburden stress). Moreover, High pressure conditions are expected in seafloor drilling (Bar-Cohen and Zacny, 2009). The penetration rate of percussive drilling is dropped significantly due to in-situ confining stresses (Cunningham and Eenink, 1959). Therefore, as a practical utilization of the numerical techniques studied within this thesis, several rock penetration problems under confining stresses are studied numerically in this chapter.

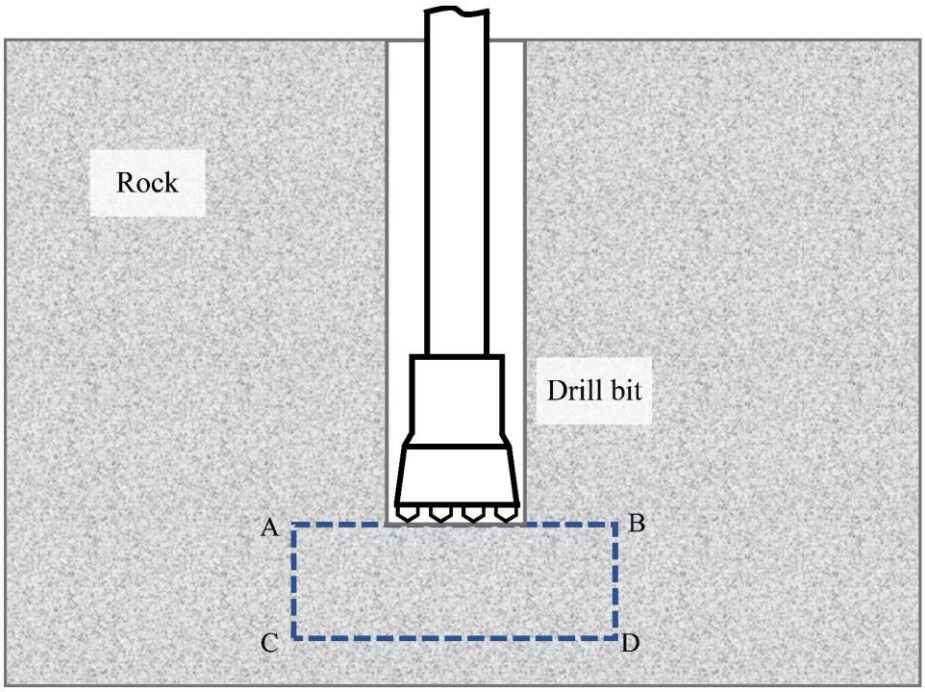

Figure 97. the model that represents schematically the rock fragmentation by a drill bit with multiple-button bits (Liu et al., 2008).

When multiple-button bits are applied on rock specimen, high stresses are induced underneath, and the stresses interact with each other between the neighbouring buttons (inserts). The area ABCD in Figure 97 (which is below the borehole bottom) is investigated numerically in this study to observe the rock failure of two neighbour buttons. The confining pressure which is considered for this area is the same as the ones at a depth of 3000 m. This representative rock cylinder has a diameter of 250 mm and a height of 120 mm (see Figure 98). These dimensions were chosen as a trade-off between the boundary effects and the computation time. Symmetry of the material and the boundary conditions were assumed so that only half of the cylinder and the punches were modelled. The rock domain was modelled with the same mesh size (1.5 mm – see Figure 98b) and the material model (KCC) as in the punch penetration simulation. In addition, the loading velocity, contact algorithms, geometry and the material model of the punches (which is rigid body) were the same as in the ones in the punch penetration simulation. The simulations were carried out with two button distances (button spacing indicated by "S" in Figure 98) equal to 20 mm and 40 mm.

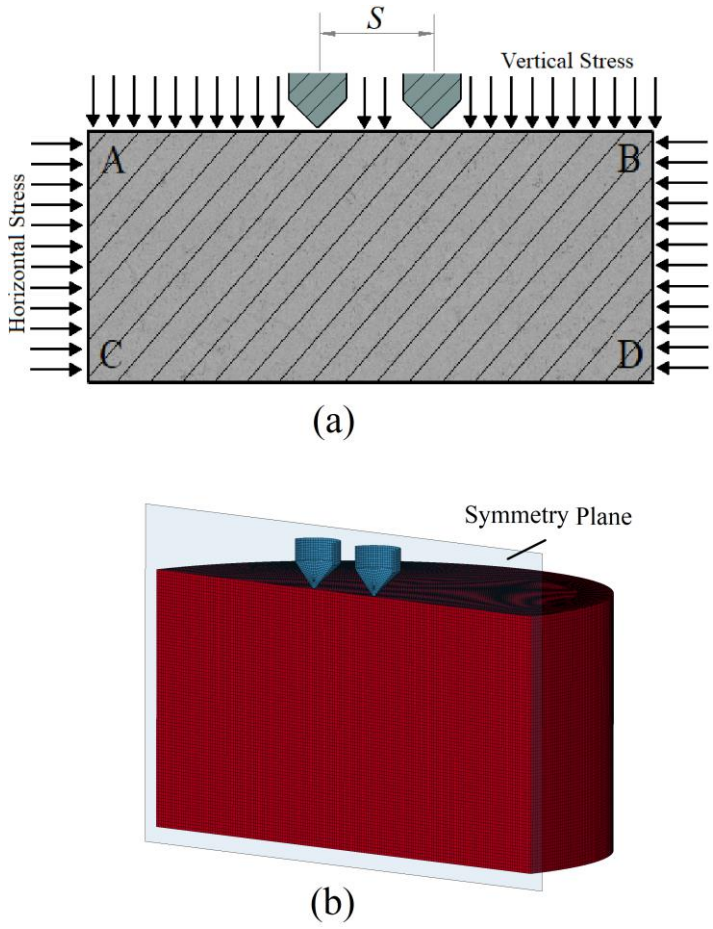

Figure 98. The numerical models of the representative cylindrical specimen at a certain depth below the seabed: (a) 2D model, and (b) ½ symmetry of the meshed 3D model.

The horizontal and vertical effective stresses at a depth of 3000 m below the seabed (in sedimentary basins of Dosso and Agosta Campus) are obtained from (Bottazzi, 2015) that estimated these values as 18.91 and 35.02 MPa, respectively. These stresses were applied as the boundary conditions for the horizontally and vertically confined cases, which was then compared to only horizontally confined and unconfined cases.

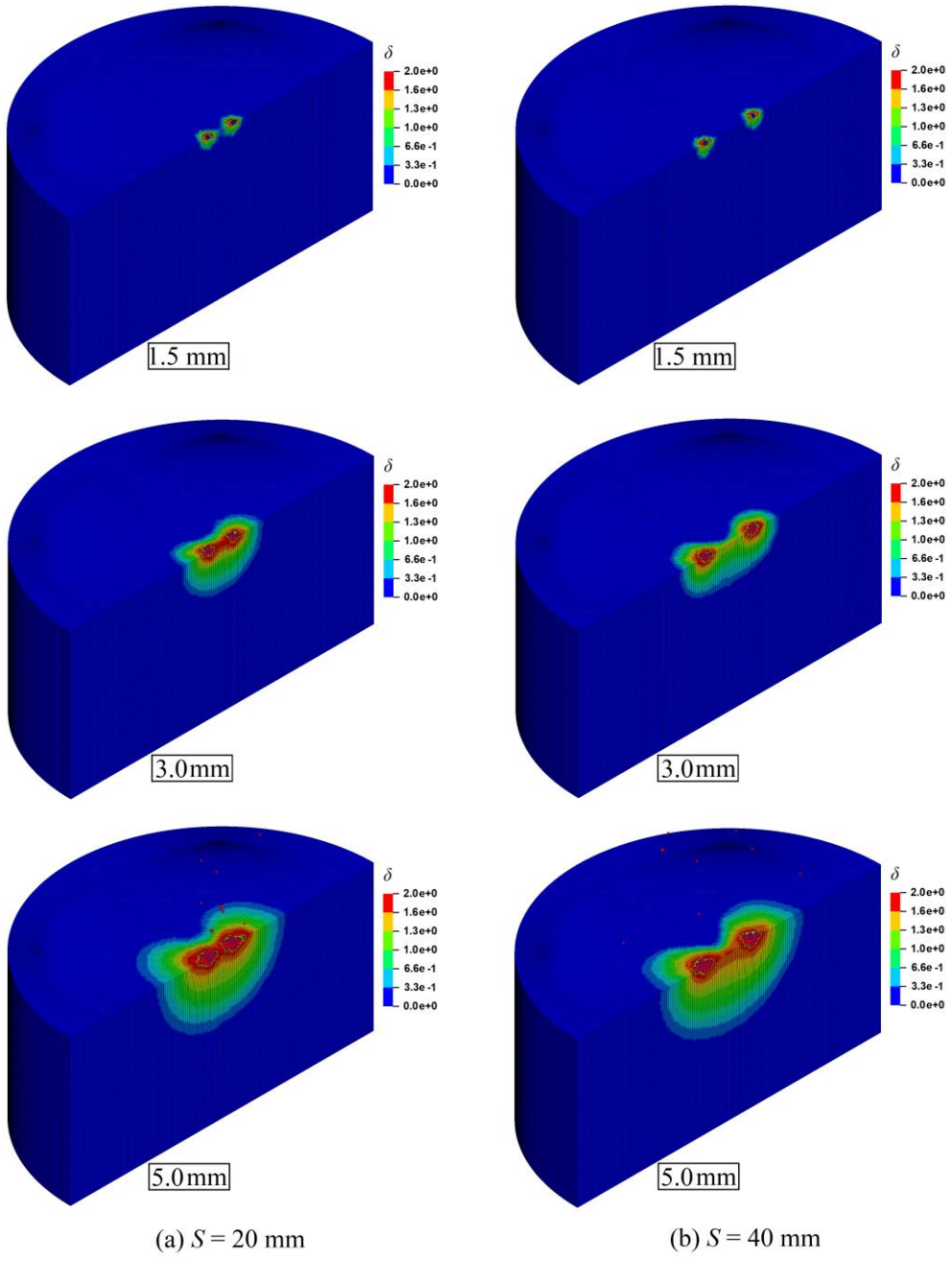

Figure 99. The "KCC scaled damage measure, δ" after 5 mm tool penetration into a rock cylinder at a depth of 3000 m below the seabed (full confinement): (a) S = 20 mm, and (b) S = 40 mm.

The "scaled damage measure, **δ**" fields for the six simulations, at three different penetration depths, are shown in Figure 99, Figure 100 and Figure 101.

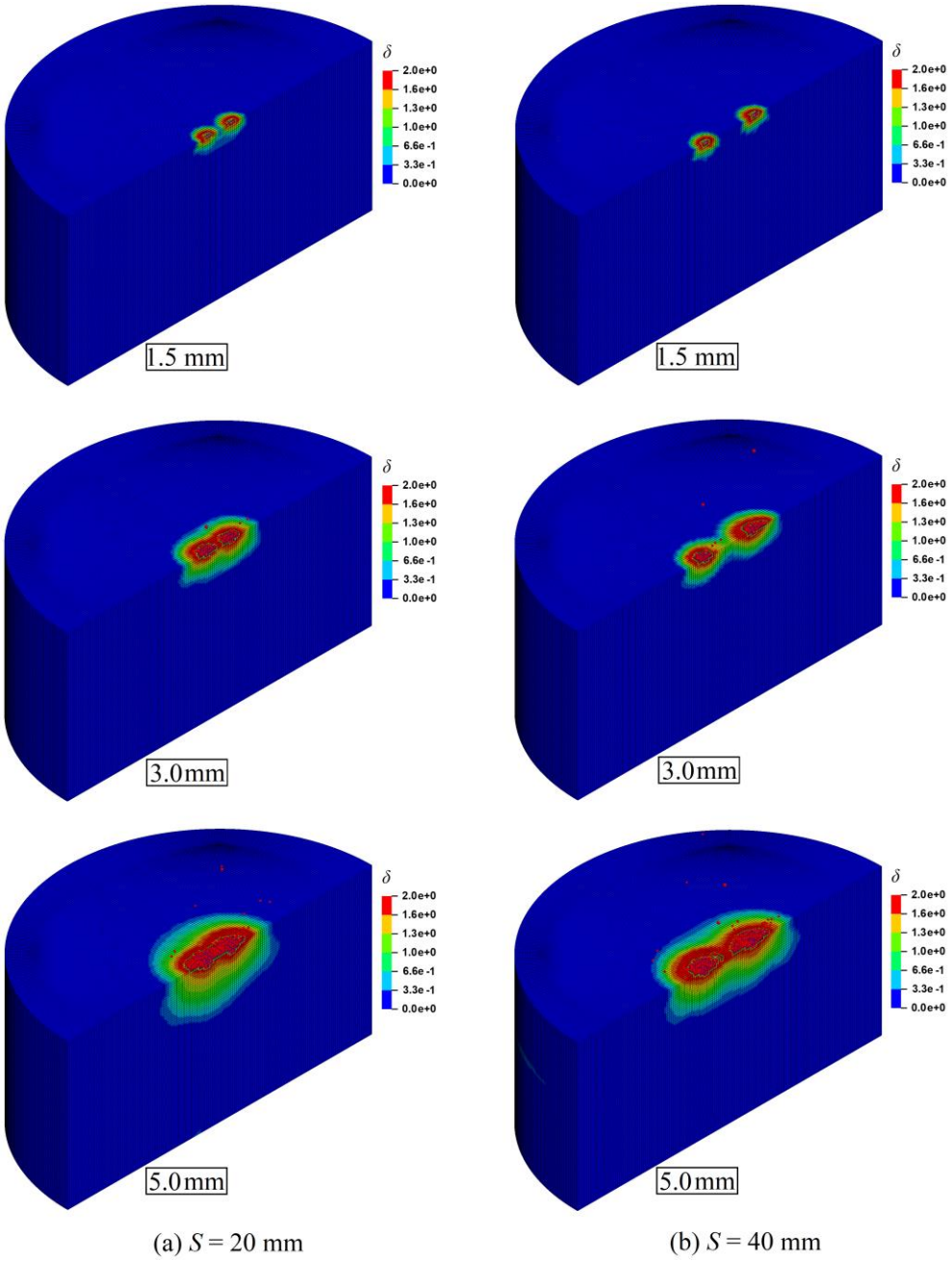

Figure 100. The "KCC scaled damage measure, δ" after 5 mm tool penetration into a rock cylinder at a depth of 3000 m below the seabed without vertical pressure (horizontal confinement only): (a) S = 20 mm, and (b) S = 40 mm.

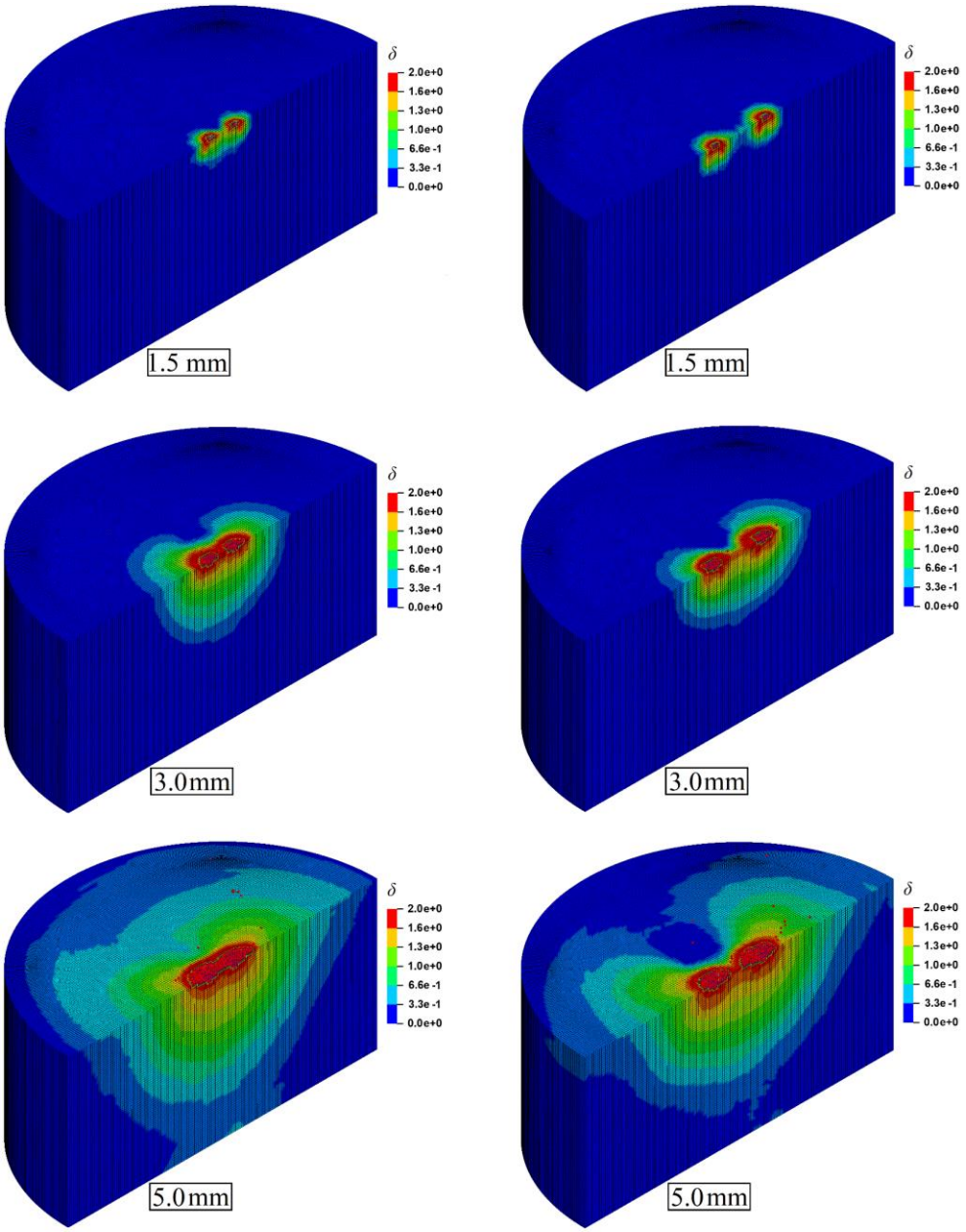

Figure 101. The "KCC scaled damage measure, δ" after 5 mm tool penetration into a rock cylinder at unconfined condition: (a) S = 20 mm, and (b) S = 40 mm.

The critical zones of the numerical results indicated in Figure 99, Figure 100 and Figure 101 are zoomed in , for better observation of the damage zone induced by the buttons.

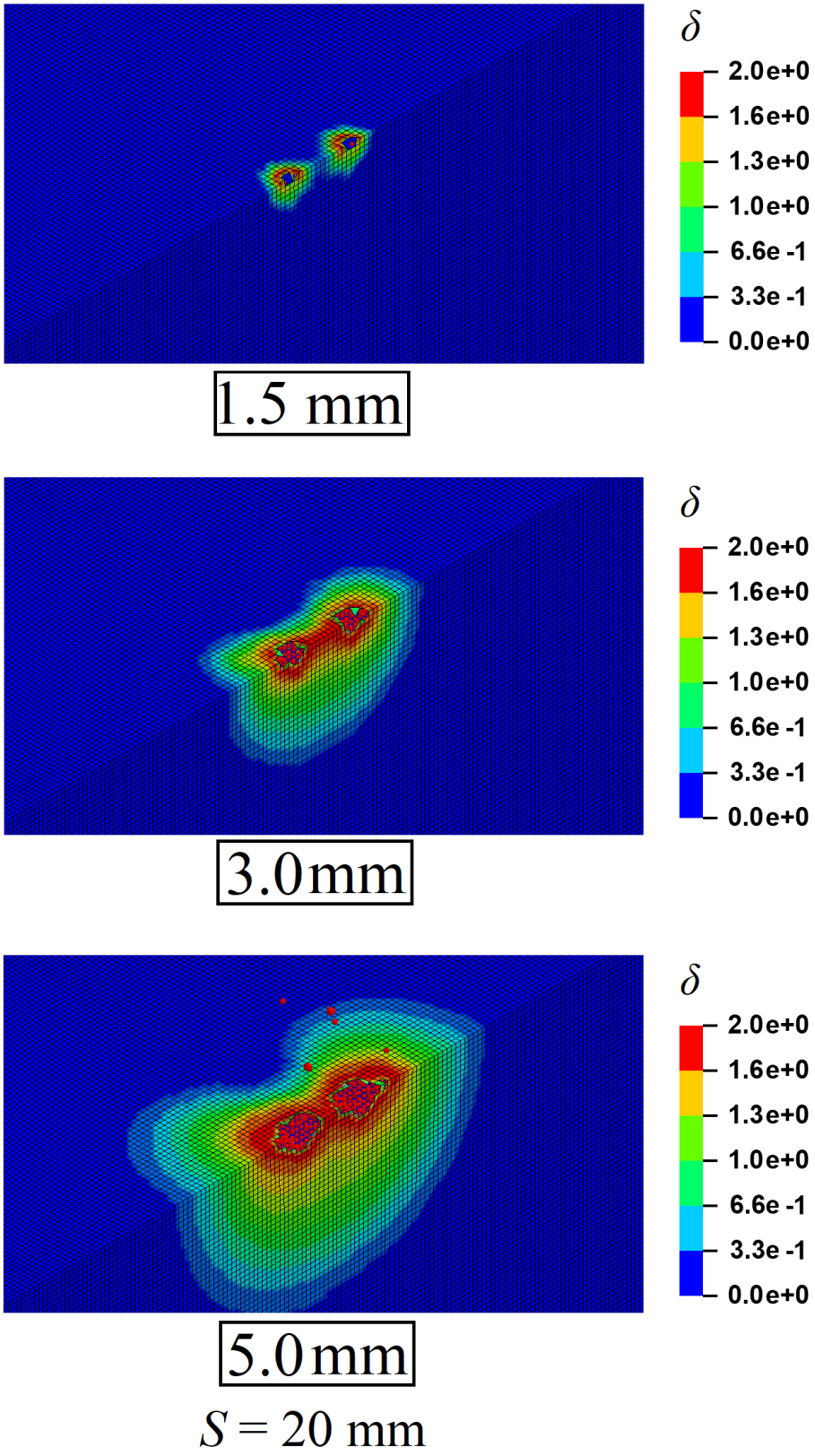

Figure 102. The "KCC scaled damage measure, δ" after 5 mm tool penetration into a rock cylinder at a depth of 3000 m below the seabed (full confinement) with S = 20 mm.

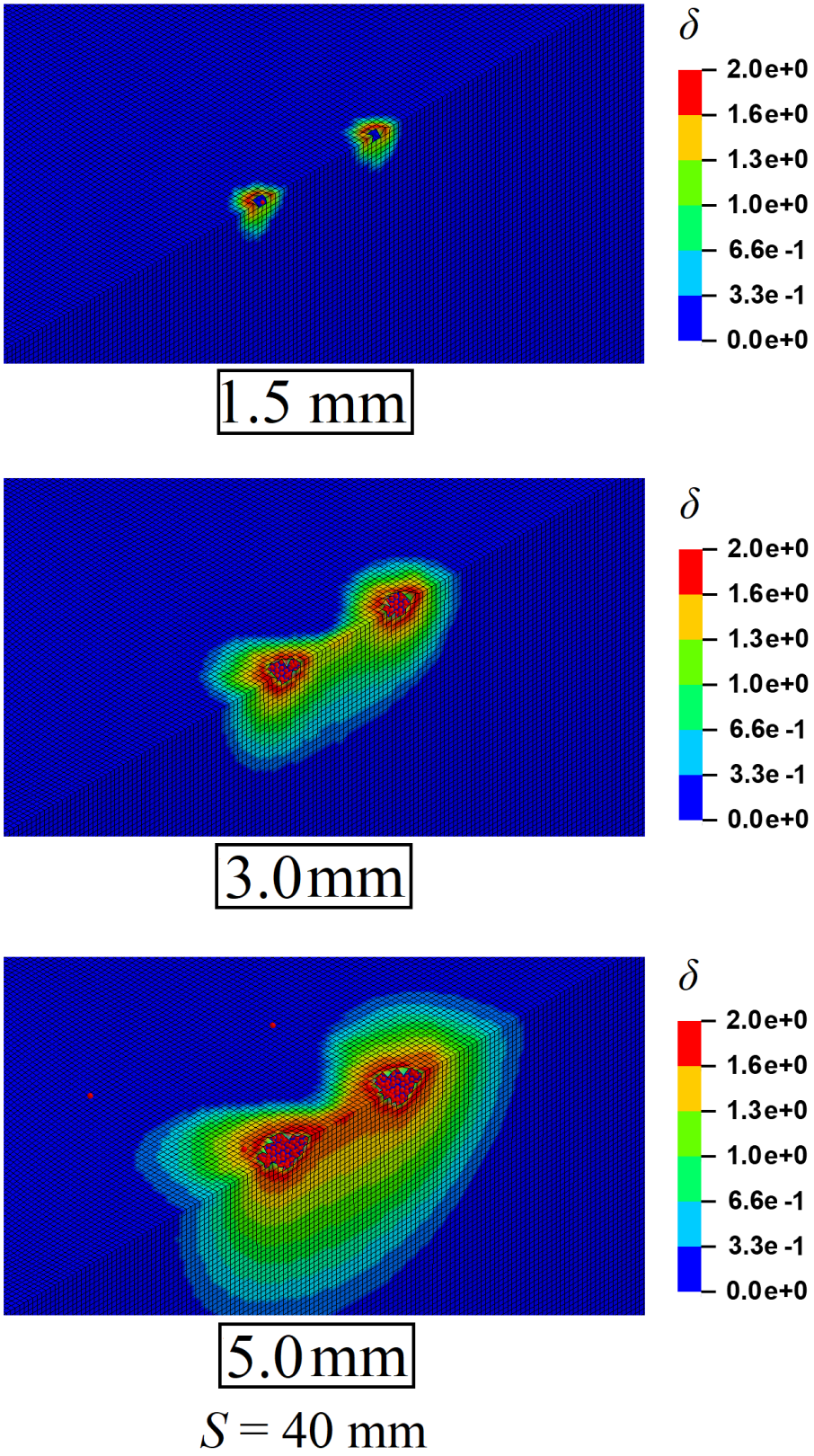

Figure 103. The "KCC scaled damage measure, δ" after 5 mm tool penetration into a rock cylinder at a depth of 3000 m below the seabed (full confinement) with S = 40 mm.

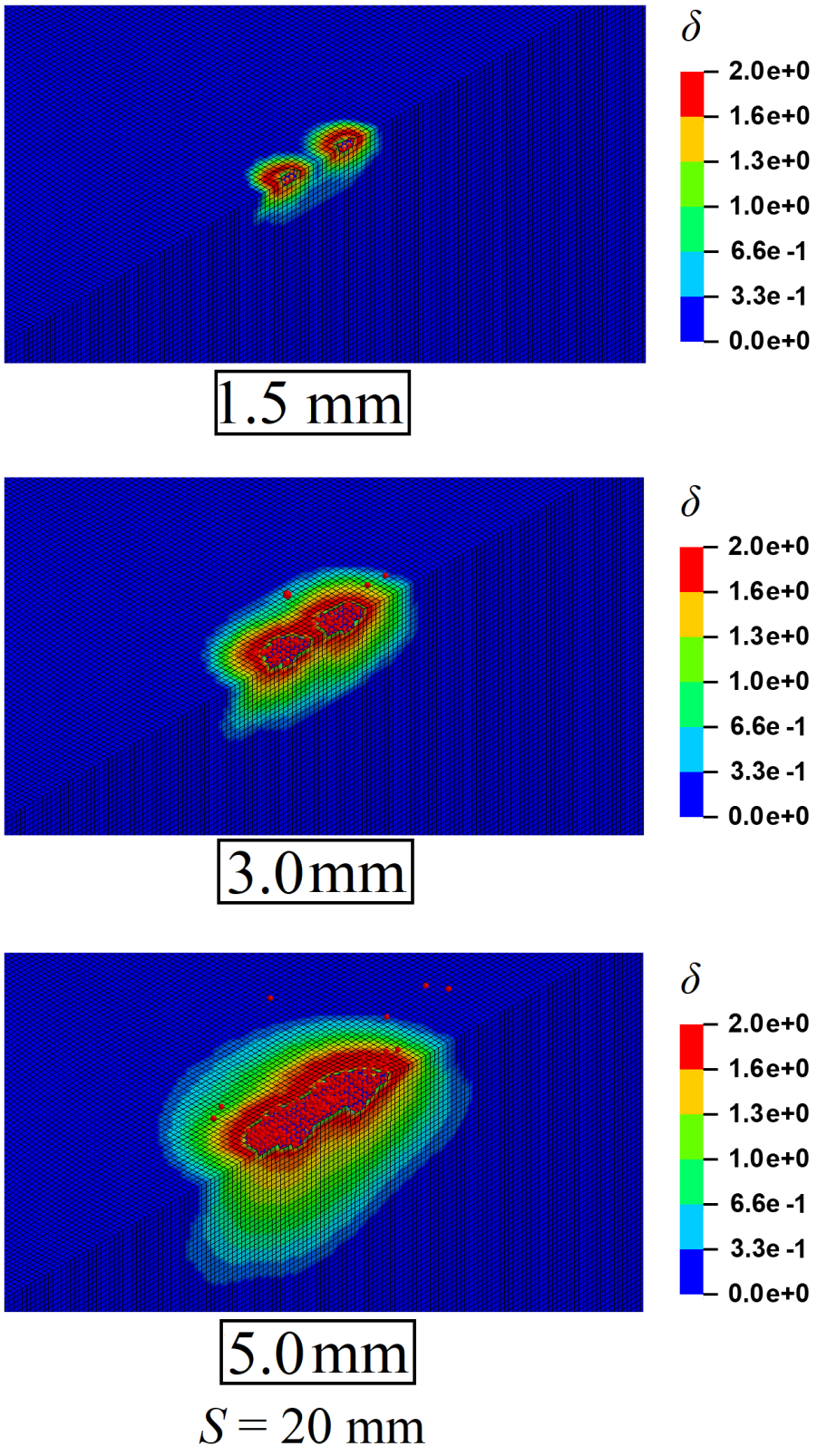

Figure 104. The "KCC scaled damage measure, δ" after 5 mm tool penetration into a rock cylinder at a depth of 3000 m below the seabed without vertical pressure (horizontal confinement only) with *S* = 20 mm.

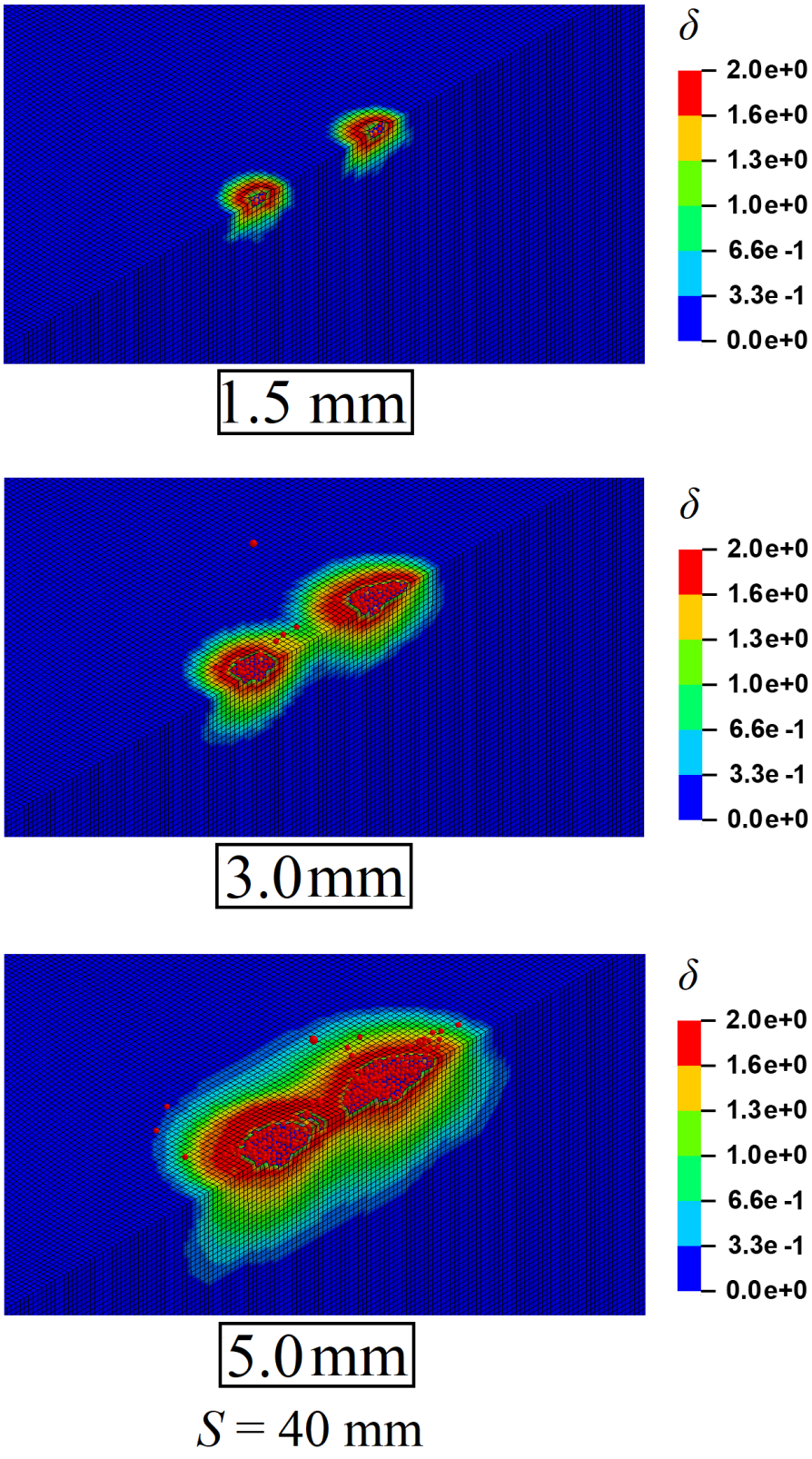

Figure 105. The "KCC scaled damage measure, δ" after 5 mm tool penetration into a rock cylinder at a depth of 3000 m below the seabed without vertical pressure (horizontal confinement only) with S = 40 mm.

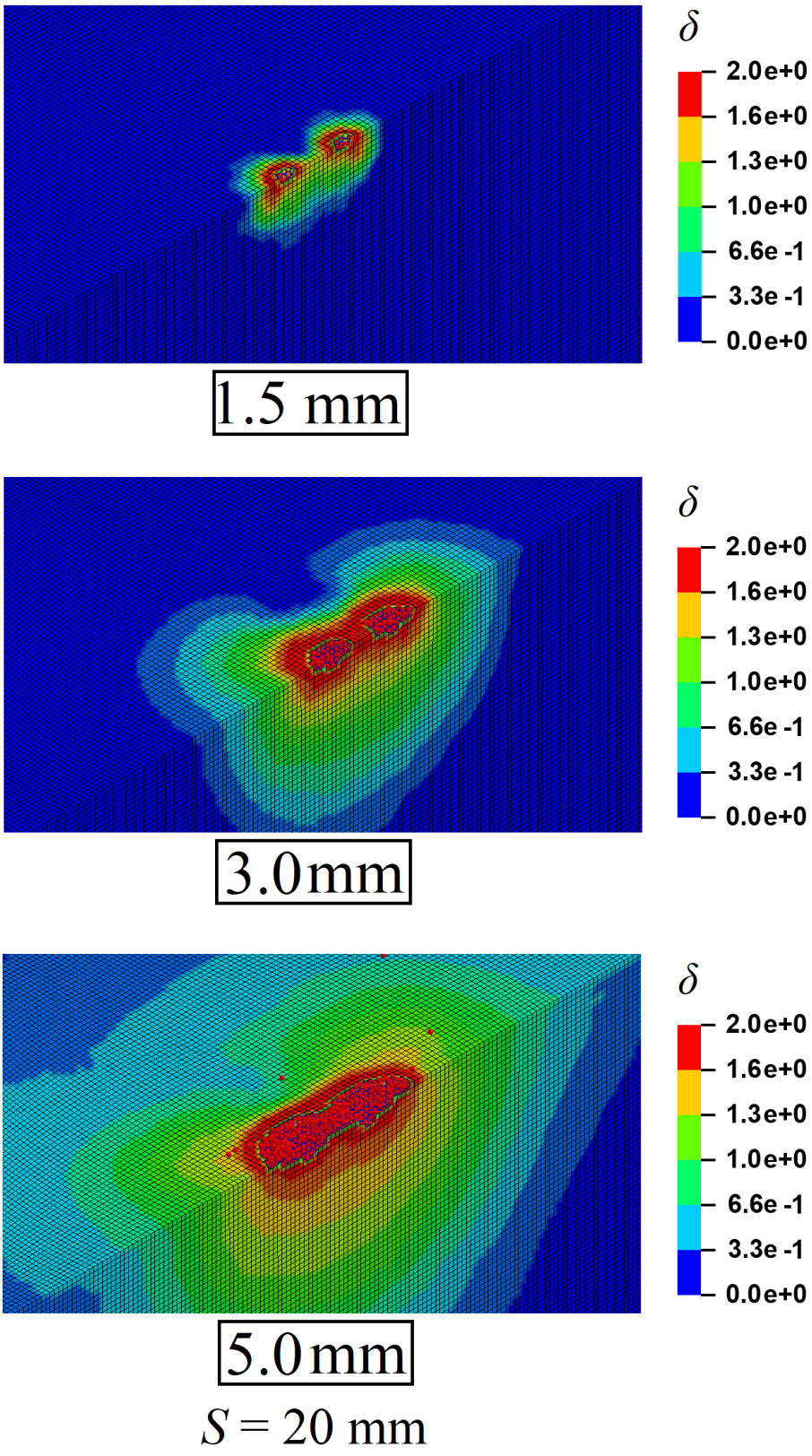

Figure 106. The "KCC scaled damage measure, δ" after 5 mm tool penetration into a rock cylinder at unconfined condition with S = 20 mm.

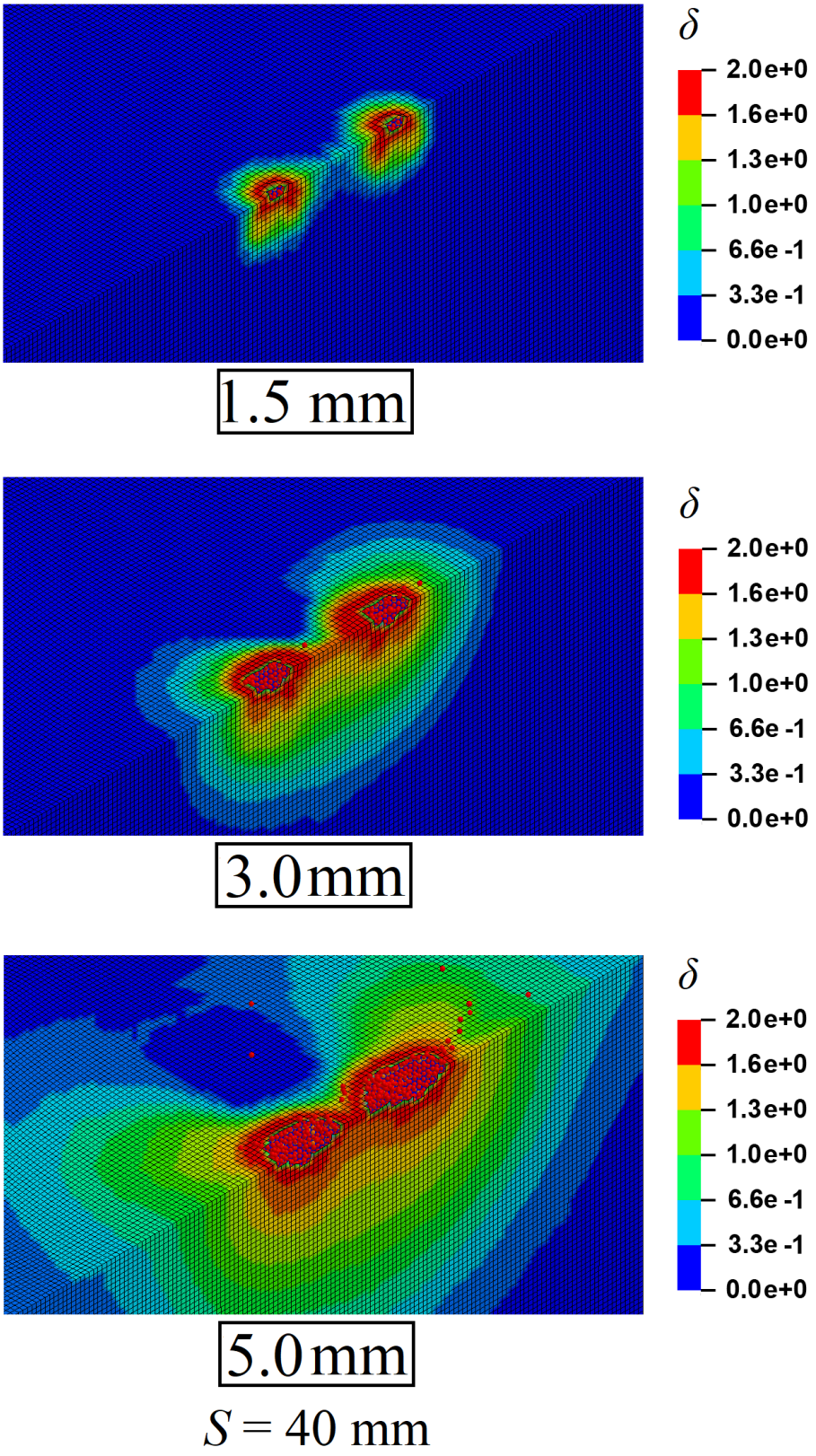

Figure 107. The "KCC scaled damage measure, δ" after 5 mm tool penetration into a rock cylinder at unconfined condition with S = 40 mm.

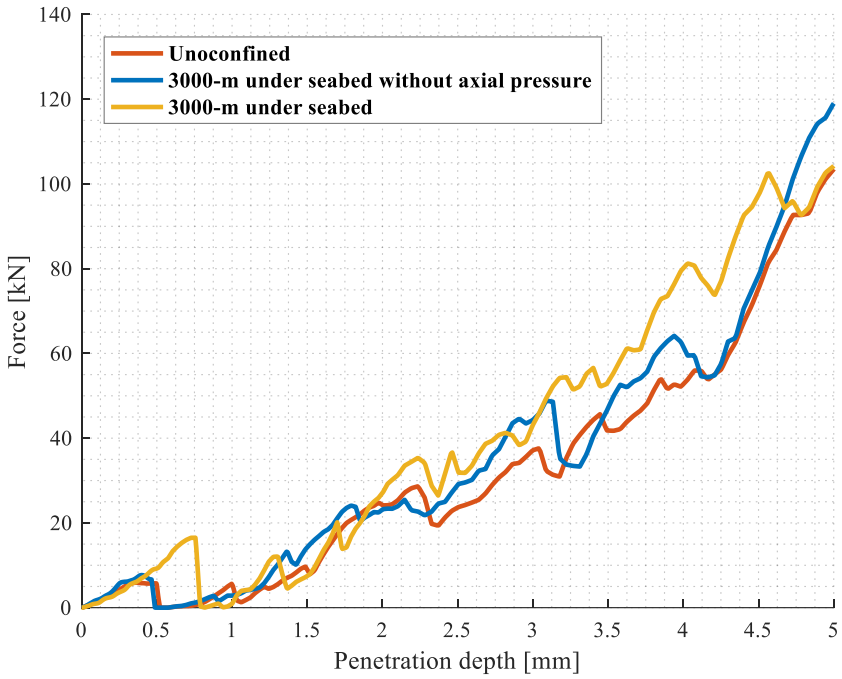

Figure 108. The axial force-penetration depth diagram of the double tool-bit penetration with 20-mm distance between the drill-bits, at different confining conditions.

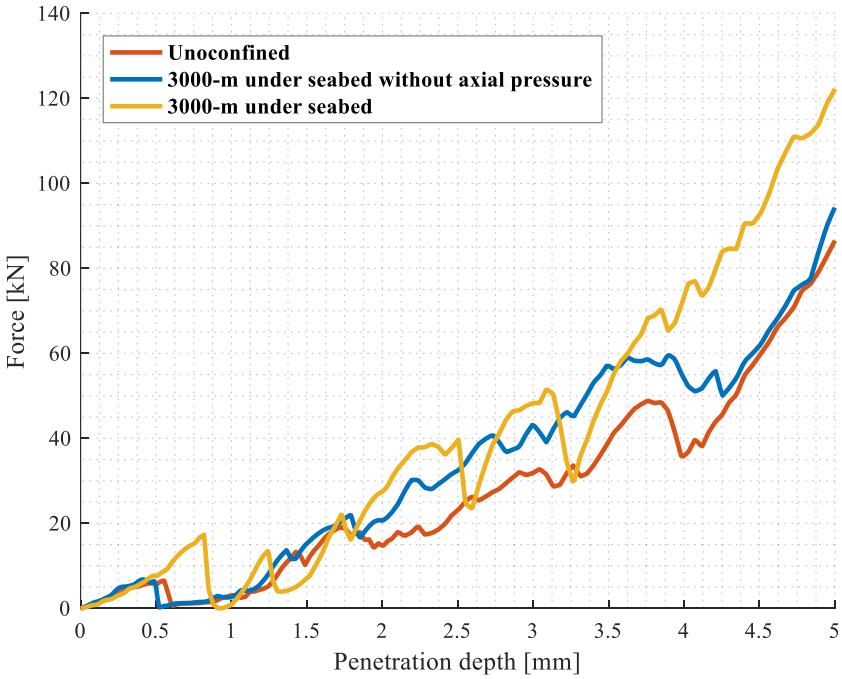

Figure 109. The axial force-penetration depth diagram of the double tool-bit penetration with 40-mm distance between the drill-bits, at different confining conditions.

The results in Figure 102 and Figure 103 show that the fully confined conditions effectively prevent the damage induced by the buttons: the condition to convert the elements between the buttons into SPH particles was not met even with the smaller spacing of 20 mm. This indicates a substantial drop in the efficiency of the drilling operation as the lateral chipping, i.e. the coalescence of the side-cracks induced by the adjacent buttons, is the most important mechanism of material removal percussive drilling as well as in disc cutting. In contrast to full confinement, the lateral only confinement scheme, while leading into a substantially smaller damaged zones than the unconfined case in Figure 106 and Figure 107, did not suppress the interaction between the buttons to prevent the lateral chipping, which can be observed in Figure 104 at 5 mm of penetration. This observation has an important practical significance for drilling at high depths: if the vertical pressure at the bottom of the borehole can somehow be released, much of the drilling efficiency reachable at the unconfined conditions with the specific drill setup can be recovered. As expected, the zone where softening, i.e. damaging as indicated by the values of δ larger than one, has begun is largest in the unconfined case (see Figure 106 and Figure 107). This naturally means more efficient drilling. Finally, the results above also demonstrate the importance of the correct drill bit design, i.e. the spacing of the tools. Indeed, if the distance between the tools is too large, the chipping effect is lost, and the drilling becomes ineffective.

Chapter 16

Numerical investigation of percussive drilling with a triple-button bit

Percussive drilling is one of the most widely used rock drilling technique in the oil and gas industries. In this type of drilling, an impact which is induced by the stress wave forces the high strength multiple button-bits to penetrate into the rock. The material removal obtained by crushing failure mode is the desired outcome of this penetration. However, the most significant fracture mechanism related to the material removal is the lateral chipping (or the coalescence of side cracks) which is induced as the result of the interaction of the adjacent button bits. The studies of (Mishnaevsky, 1995) and (Liu, 2004) express the necessity of numerical investigations of this lateral chipping fracture as the alternative of expensive field testing.

The principle for modelling the percussive drilling action (or dynamic indentation by the button bit – rock interaction) is illustrated in Figure 110 (Saksala et al., 2014). The stress wave travels through the drilling rod in the percussive drilling. In the laboratory scale, the dynamic bit-rock indentation test can be performed by modifying the split Hopkinson pressure bar (SHPB) device. An example of this type of test is illustrated in Figure 111, which is exploited in a study of (Saksala et al., 2014). The drill rod, therefore, is considered as the incident bar of the SHPB device.

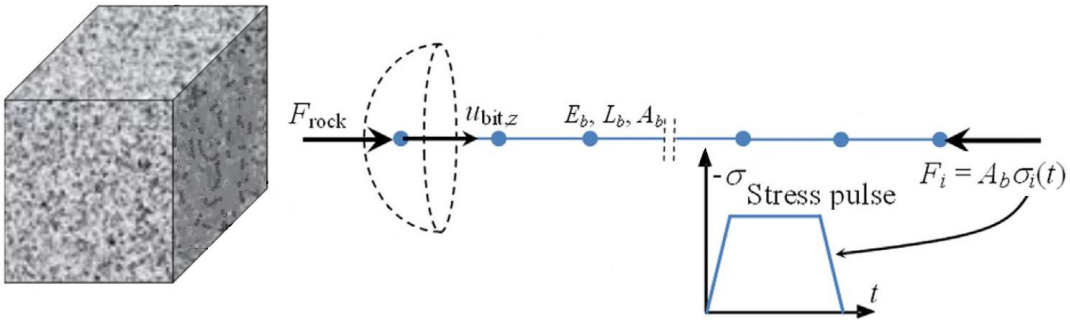

Figure 110. The principle of the bit-rock interaction model (Saksala et al., 2014).

This section is aimed to investigate numerically the effect of confining pressures below the seabed and the impact velocity on percussive drilling. Hence, the experimental arrangement suggested by (Saksala et al., 2014) is numerically modelled, while

the rock sample is considered as an representative unit at a certain depth under the seabed. The vertical and horizontal effective stresses in sedimentary basins of Agosta and Dosso Campus (Bottazzi, 2015) at a depth of 1000 m below the seabed are considered for these numerical models as 12.58 MPa and 6.79 MPa, respectively. The same analyses are performed for the stresses at a depth of 3000 m that are 35.02 MPa and 18.91 MPa, respectively. The representative rock specimen, as shown in Figure 112, is a cylinder have a diameter of 250 mm and a height of 120 mm. This dimension was chosen as a trade-off between the boundary effects and the computation time. Symmetry of the material and the boundary conditions were assumed so that only a half of the parts is modelled. The rock domain is discretised with the same mesh size (1.5 mm) as the PPT and double-punch simulations.

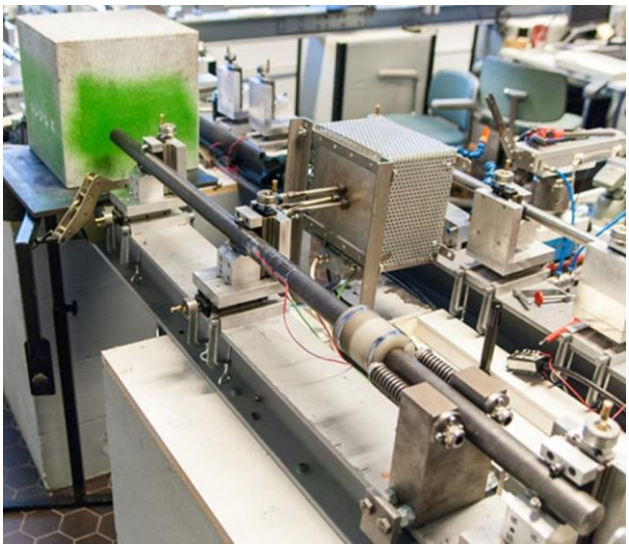

Figure 111. The experimental set of percussive drilling test by (Saksala et al., 2014).

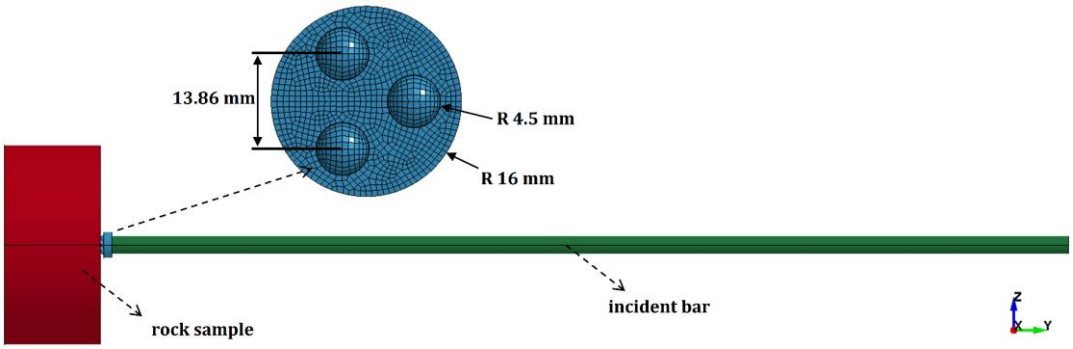

Figure 112. The numerical models of the percussive rock drilling at a certain depth below the seabed.

Four numerical simulations were carried on corresponding to depths 1000 m and 3000 m below the seabed and by two different impact velocities. The same simulation set-up, i.e. testing the effect of vertical and horizontal pressures, is taken here just by imposing the horizontal pressure to the rock, to show the effectiveness of the rock drilling by neglecting the effect of vertical pressures. The geometry, loading velocity and material model (rigid body) of punch is the same as in the PPT simulation. The triple-button dill bit with hemispherical buttons is modelled by the geometries indicated in Figure 112. The incident bar of the SPHB device was considered as an elastic 3D solid part with a length of 1200mm and a diameter of 22mm. Two piecewise linear approximations of the incident stress pulses (which was previously obtained in the dynamic Brazilian disk section) corresponding to 10m/s and 20m/s striking velocities, are imposed by *LOAD_SEGMENT keyword of LS-DYNA at the free surface of the incident bar, according to Figure 113. The maximum effective strain at failure (EFFEPS) is considered equal to 0.1 as the conversion criteria. The fully calibrated KCC material model, the equation-of-state and the strain rate enhancement diagram which are expressed in Table 18, Table 15 and Figure 61, respectively, were used for the numerical simulations.

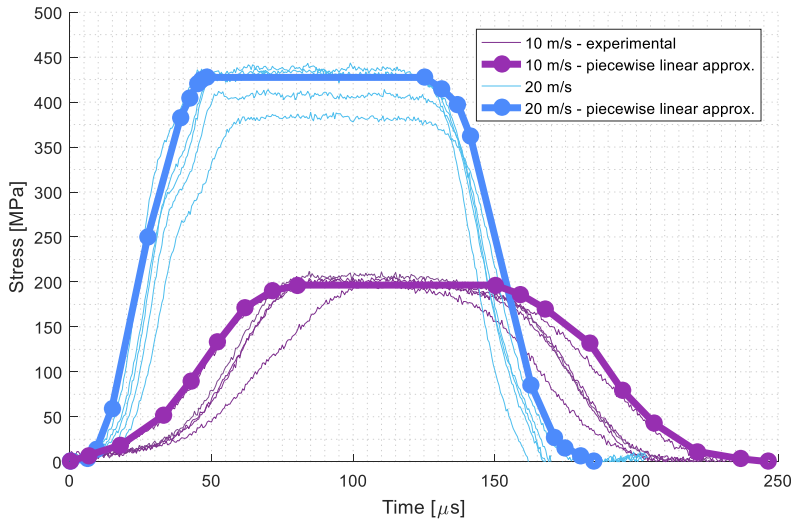

Figure 113. The experimental diagrams of the incident stress pulses obtained from dynamic Brazilian disk test by SHPB and their corresponding piecewise linear approximations.

The TIED_SURFACE_TO_SURFACE_OFFSET contact is considered for the contact treatment of incident bar and the bit. The _OFFSET keyword provides a penalty-based contact able to tie an elastic part to a rigid part. The ERODING_SURFACE_TO_SURFACE and AUTOMATIC_NODE_TO_SURFACE contacts are considered for the drill bit to solid elements, and drill bit to SPH particles, respectively.

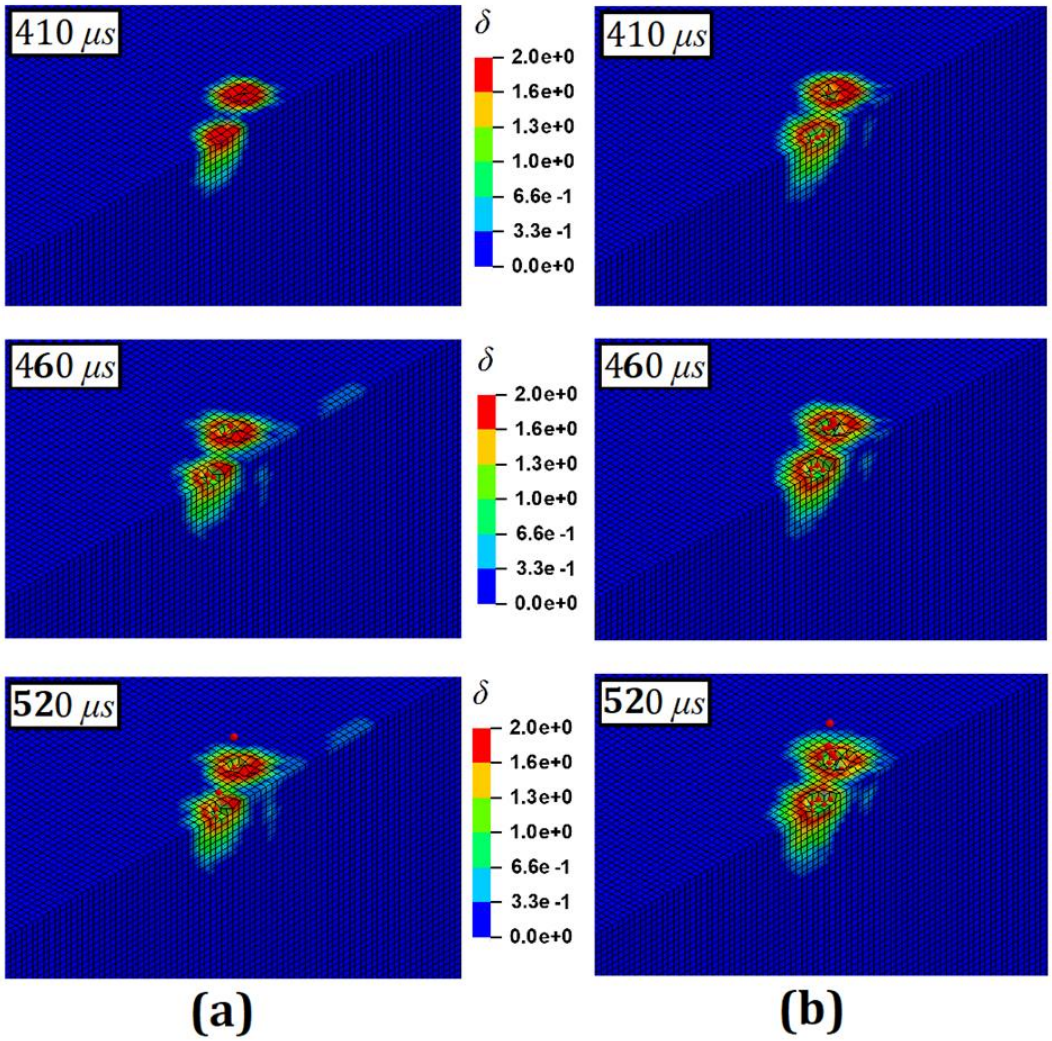

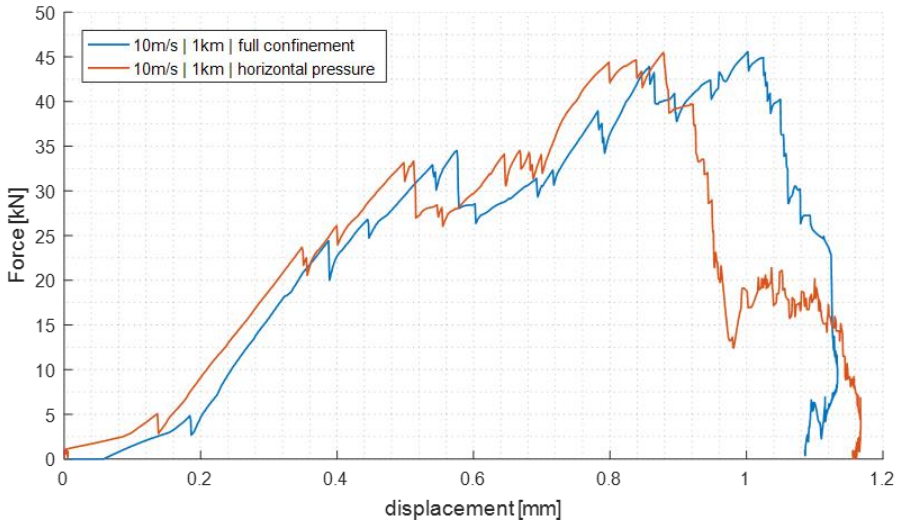

Figure 114. The distribution of the KCC scaled damage parameter of percussive drilling action (10 m/s striking velocity) into a rock cylinder at a depth of 1000 m below the seabed; (a) full confinement, and (b) without vertical pressure (horizontal confinement only).

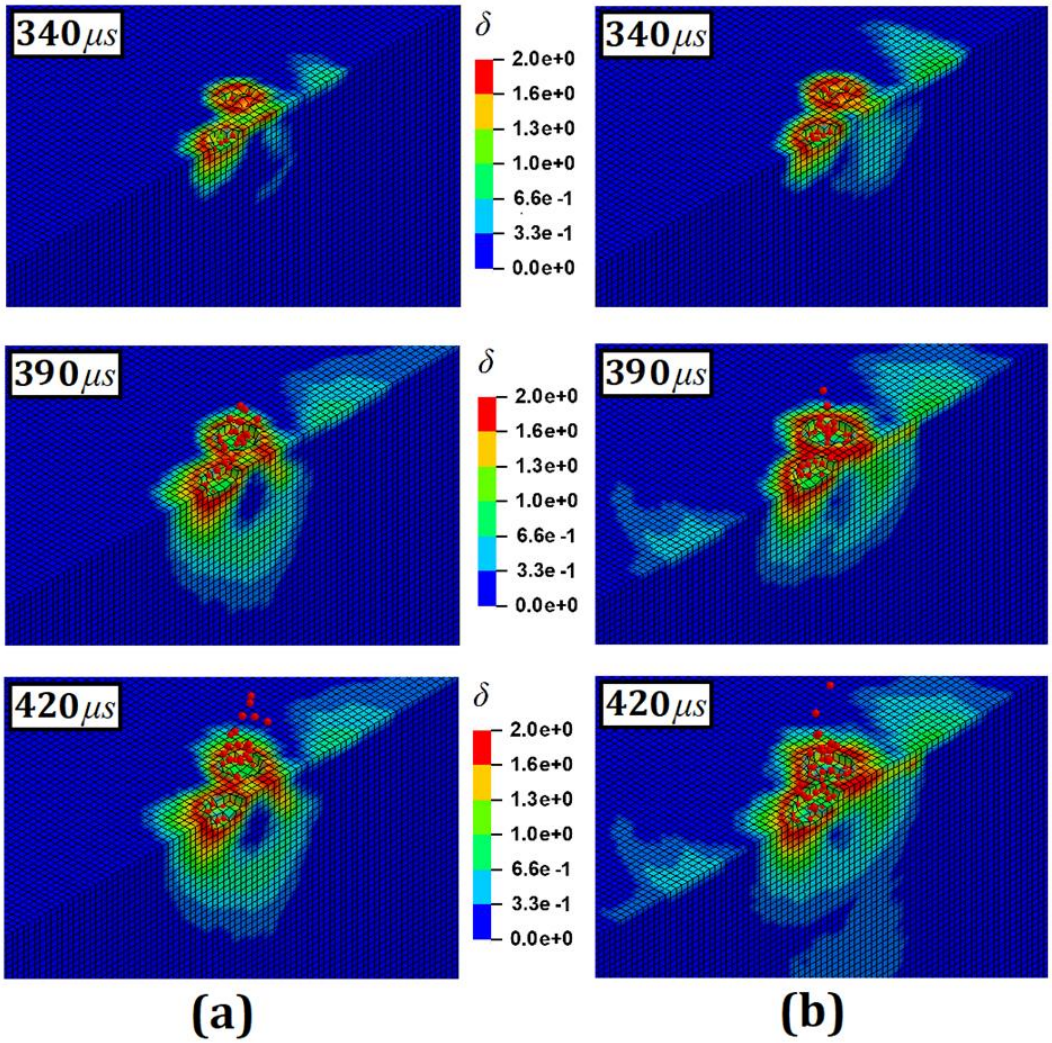

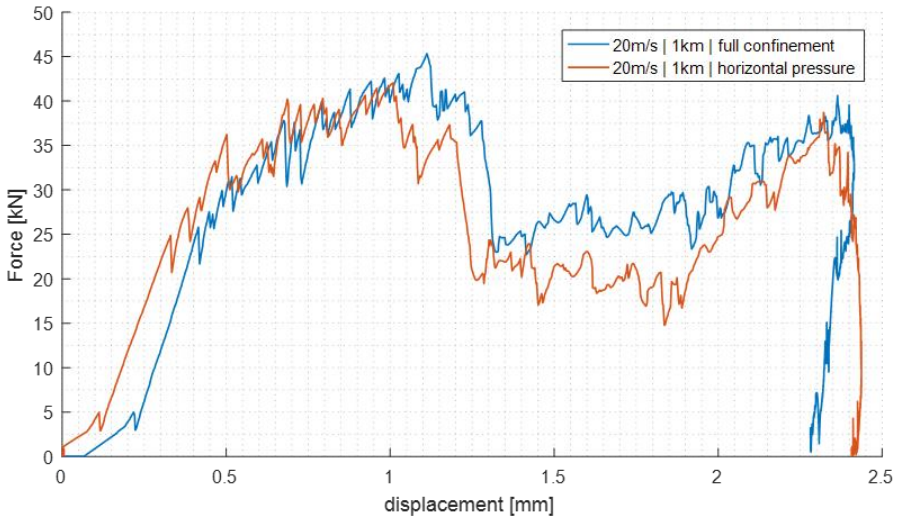

Figure 115. The distribution of the KCC scaled damage parameter of percussive drilling action (20 m/s striking velocity) into a rock cylinder at a depth of 1000 m below the seabed; (a) full confinement, and (b) without vertical pressure (horizontal confinement only).

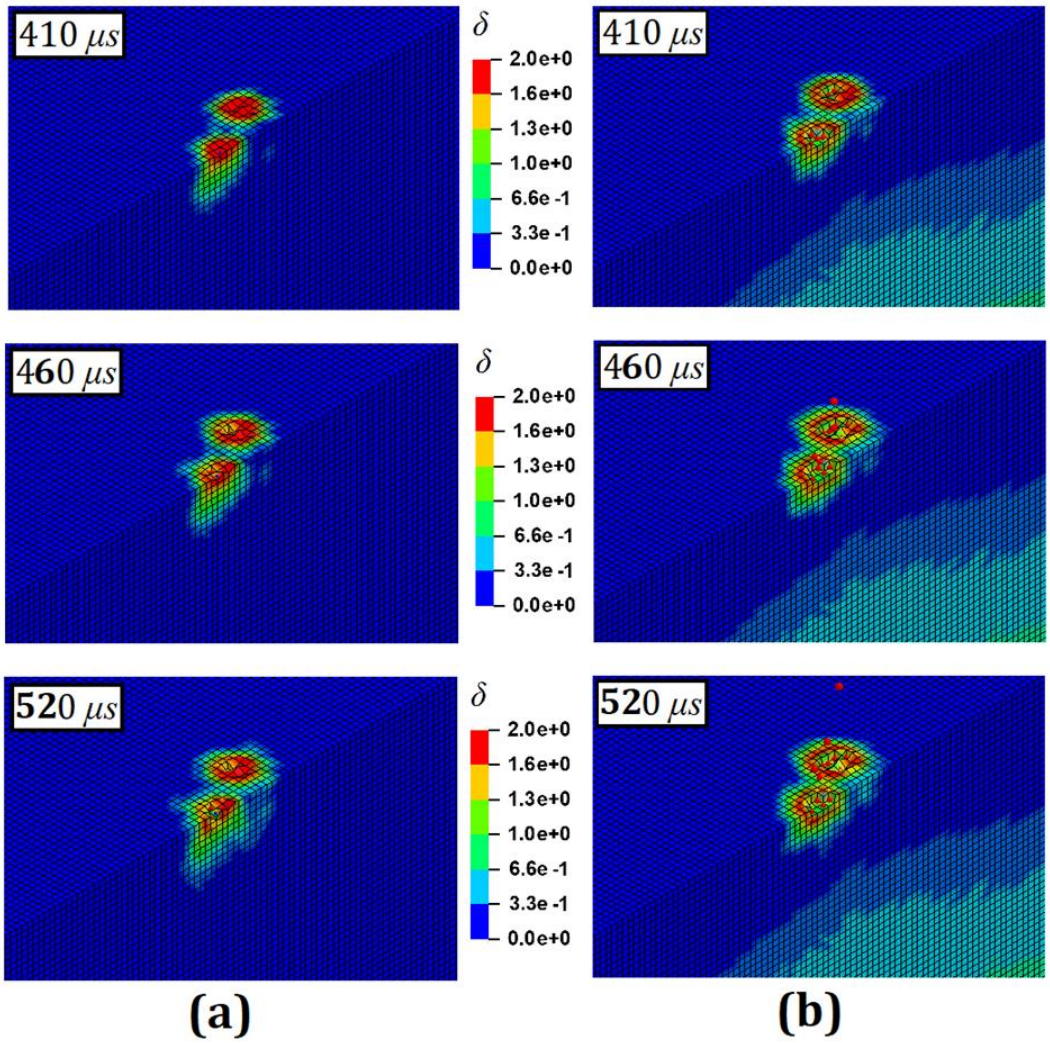

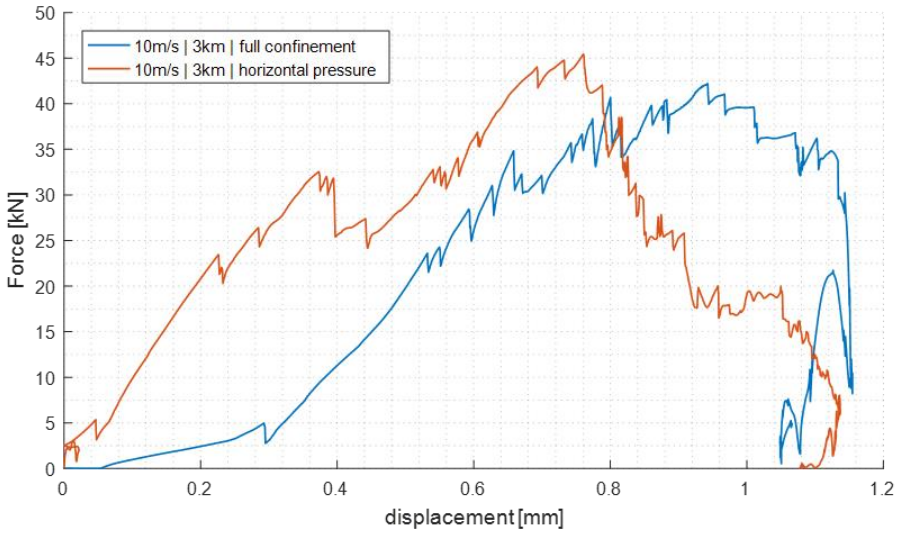

Figure 116. The distribution of the KCC scaled damage parameter of percussive drilling action (10 m/s striking velocity) into a rock cylinder at a depth of 3000 m below the seabed; (a) full confinement, and (b) without vertical pressure (horizontal confinement only).

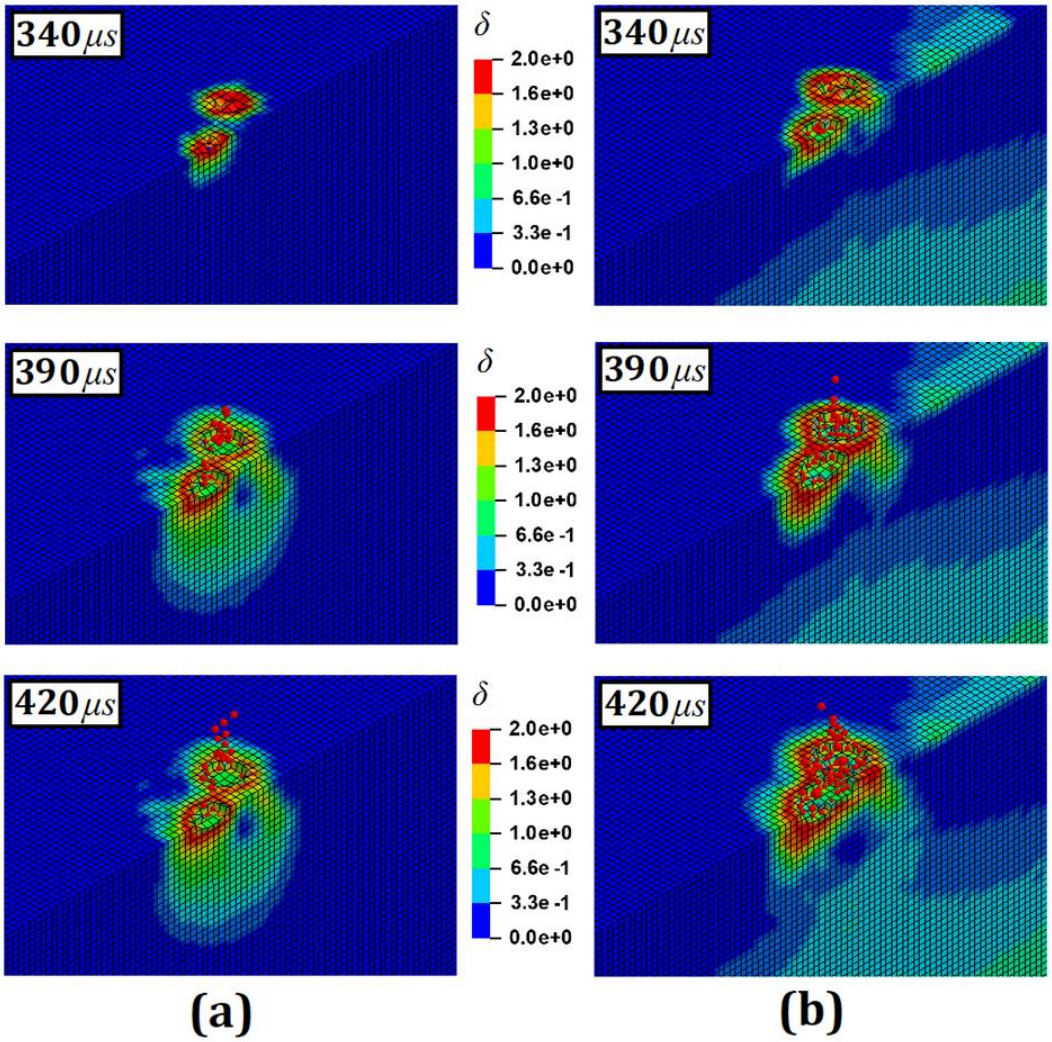

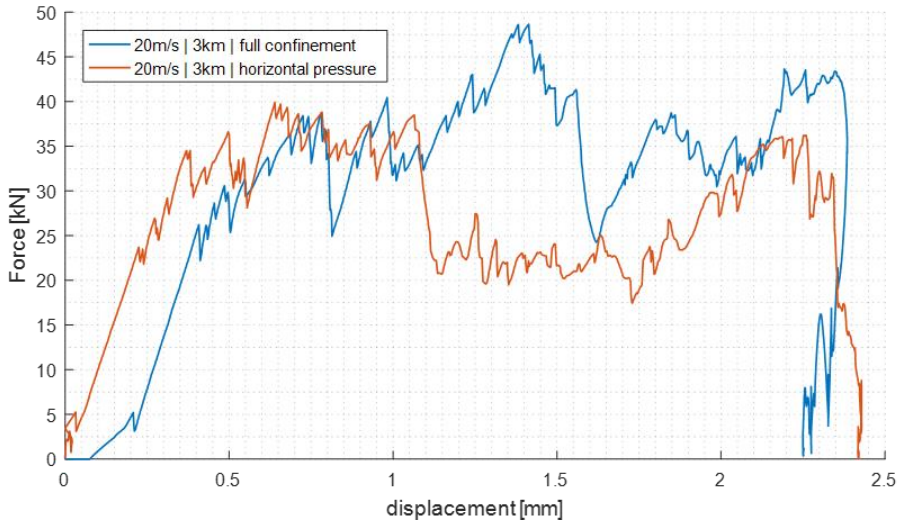

Figure 117. The distribution of the KCC scaled damage parameter of percussive drilling action (20 m/s striking velocity) into a rock cylinder at a depth of 3000 m below the seabed; (a) full confinement, and (b) without vertical pressure (horizontal confinement only).

The critical zones of the numerical results are indicated in Figure 114, Figure 115, Figure 116 and Figure 117 for better observation of the damage zone induced by the drill-bit buttons in terms of the KCC scaled damage parameter. The numerical results illustrated in the column (a) of all these figures correspond to a representative unit of rock which is located at a certain depth below the seabed. Hence, both the vertical and horizontal in-situ stresses are imposed to these unit, while the numerical simulations expressed in the column (b) are just confined by applying the horizontal pressures. The reason behind this assumption is to investigate what happens if it will be possible to somehow avoid the vertical pressure at the button of a borehole. As it was investigated in the previous section, the coalescence of the side cracks and the lateral chipping is observed to be significantly more effective in case of neglecting the effect of vertical pressure. The same observations can be concluded here by comparing all the results indicated in the column (a) of Figure 114, Figure 115, Figure 116 and Figure 117, with the corresponding ones in the column (b).

The craters observed at the striker velocity of 20m/s are significantly wider in comparison to the corresponding ones at the striker velocity of 10 m/s, which is in accordance to the experimental results reported in (Saksala et al., 2014). The interaction between the buttons of the drill bit have resulted in the subsurface lateral crack at the 20 m/s striking velocity. Eventually, this interaction combines the tensile damage zones of the individual buttons, hence, the material between the buttons is removed by the impact. This phenomenon can be observed also by the presence of the converted SPH particles who demonstrate the material removal through crashing failure mode of the rock beneath the triple buttons. It means that by this striking velocity, the percussive drilling action is able to provide enough energy for the rock breakage. Most of the energy available in dynamic indentation goes to the crushing of the rock by shear just below the buttons, while only few percent are consumed to the spall crack formation (chipping), which is the most important material removal mechanism. However, this phenomenon is not observed in the simulations related to the striker velocity of 10m/s.

The other conclusion of these numerical simulations can be derived by considering the penetration depth of the results. Although the reaction forces between the drill bit and the rock are almost the same in all the simulations, the penetration depth is significantly varying by changing the impact velocities. The ultimate penetration depth at the striking velocity of 20 m/s is predicted to be almost double than the one with 10 m/s. Finally, it should be noted that percussive drilling action is less effective in case of dealing with a representative unit at a lower depth (i.e. 3000-m below seabed). This

issue can be justified by the highest amount of confining pressure at lower depth, that requires more effort to overcome the pressure-sensitive failure strength of the material.

Part VI

Conclusions

Chapter 17

Summary and Conclusions

An innovative simulation method of the tool-rock penetration process was implemented in this PhD thesis. The numerical method was based on the coupled FEM-SPH approach where the severely distorted finite elements were converted to SPH particles representing crushed rock. As the constitutive description of the rock material, the capability of an advanced material mode, called KCC material model, was critically discussed.

Several experimental tests were performed in this thesis, mainly based on the protocols of the ASTM standard, in order to investigate the mechanical response of rock materials experimentally. One of these tests, which is called unconfined compression test, used to be performed on the base of standard protocols, i.e. ASTM. This conventional test presents a drawback, mainly due to the radial shearing forces that are generated at the contact interface after applying the compressive load. These undesired radial forces are appeared due to the different elastic properties of the steel of the testing machine platen and the rock specimen. Another arrangement has been found in literature (Mogi specimen) to design the specimen in order to reduce these drawbacks. The experimental and numerical analyses presented in this project demonstrated that the Mogi's suggested method, which is not tough and effortful to be prepared, lead to measure the UCS parameter more precisely. The experimental tests revealed that the variability of the results obtained by Mogi's configuration are much lower than the ones of conventional configuration. The assessments performed on this PhD research project based on numerical simulations justified this issue when the existence of stress concentration was considered at the rock-steel (of compressive platen) interface of conventional configuration.

A procedure proposed in this thesis for calibrating the KCC material model specifically for Pietra-Serena sandstone, however it can also be used for other quasi-brittle materials. This calibration procedure was mainly based on a couple numerical-experimental approach aimed to overcome the main drawback of the KCC material model. The input parameters were investigated and classified into five distinct categories; tensile strength, failure (fixed) strength surfaces, tabular damage function, equation-of-state, damage parameters and strain rate enhancement. The quasi-static Brazilian

disk test was used to measure the ultimate principal tensile strength. The triaxial compression test, with three levels of confining pressure, was carried out to determine the other groups. The yield, the ultimate and the residual strengths measured via the experimental tests were used to determine the a_i-parameters, which are the KCC input parameters to describe the fixed-strength surfaces. Since the KCC material model decouples the deviatoric and volumetric responses, the experimental data of the isotropic stage (of triaxial compression test) can be potentially be used to define the equation of state for a given material. However, due to the absence of an appropriate laboratory device to measure the radial displacement, the equation of state dedicated to the material under investigation in this study was determined analytically, based on the experimental data of the axial displacement.

A modification to the tabular damage function was suggested based on the experimental data of the triaxial compression test in the deviatoric stage. Exploiting the availability of the numerical models, a sensitivity analyses was performed to determine the b_i-parameters, which are the damage parameters of the KCC material model. Finally, the proposed formulation by (Malvar and Crawford, 1998) is used to determine the effect of strain rate enhancement. The diagram of DIF-strain rate, which serves the role of updating the failure surfaces, was calibrated based on the experimental results of dynamic Brazilian disk test.

Therefore, a material model specifically calibrated with the required full set of input data was developed for Pietra-Serena sandstone. The fully calibrated material model was implemented to replicate the experimental tests (verification). The numerical results for both the triaxial compression and the Brazilian tests significantly agreed with the experimental test results. The fully calibrated material model was then further validated by replicating a Flexural (four-point bending) test, which includes both the compressive and tensile stresses, and dynamic Brazilian disk test. The critical comparison between the numerical and the experimental test results demonstrated the capability of the calibrated material model. Therefore, the procedure proposed in this PhD thesis presents a potential new framework for the numerical assessment of quasi-brittle materials.

This numerical approach was then applied in the simulation of the punch penetration test on Pietra-Serena sandstone. Moreover, experimental PPT tests were performed in order to validate the numerical results. Three different numerical techniques for dealing with fully damaged finite elements were applied in order to replicate the PPT test: (a) constant stress (reduced integration) FEM with erosion of heavily distorted elements, (b) fully integrated FEM with erosion of heavily distorted

elements, and (c) reduced integration with coupled FEM-SPH. The numerical results with method (a) exhibited an excessively too soft response. The full integration with erosion method (method b) performed significantly better; however, more severe fluctuations were attested in the force-penetration curve caused by the element erosion events. The reduced integration with a conversion to SPH particles (method c) resulted in a slightly too stiff response compared to the experiments due the continued ability of the SPH particles to bear compressive stresses. However, the major fracture types, excluding lateral spalling, observed in the experiments were also attested in the numerical simulations. Therefore, it can be concluded that the FEM-SPH method, in conjunction with KCC material model, can be considered the most realistic method among the tested methods.

Finally, the proposed numerical method was employed in an attempt to investigate the practical issues in designing offshore deep hole drilling of real projects in the field of oil and gas industries. A drilling problem at extreme conditions was studied by penetrating a double conical tool into a reservoir rock below the seabed. A substantial decrease in the damaged zones beneath the tools as well as a prevention of the lateral chipping between the tools were predicted under the confined stresses expectable at 3 km of depth. Moreover, the simulations demonstrated the importance of the correct spacing of the tools. It was also found that if the vertical pressure at the borehole bottom can be relieved, the drilling at great depths becomes substantially more efficient. Finally, the percussive rock drilling at a certain depth below the seabed is investigated numerically with focus on the effects of impact velocity, depth of drilling and effect of in-situ pressures. Based on the simulation results, it can be concluded that the present numerical method has some predictive capabilities, hence, it can serve as a tool in the research and development pertinent to petroleum engineering.

The following recommendations can be suggested to expand research on the percussive rock drilling topic. First of all, some limitations regarding the FEM-coupled to-SPH method, as well as the KCC material model have been dealt within this research work, i.e. applying pressure on the converted SPH particles after erosion of distorted finite elements, or the size effect. Hence, developing of scientific codes in this regard could be in interest of both scientific and industrial applications. Second, the proposed numerical method was calibrated (and validated) for a specific sandstone, while the method is expected to be valid also for other type of rock materials. Therefore, to facilitate the generalization of the proposed numerical technique, it is desirable to perform other simulations by using a wide range of rock types. Third, the numerical

method can be extended for simulating higher order impact velocities to show the capability of the model in this range.

Finally, the numerical studies presented in the *part V*, which focus on practical issues in designing offshore deep hole drilling of real projects, are not validated by experimental results. There are mainly two problems investigated numerically in this chapter: the double button-bit penetration and the percussive rock drilling, both at a certain depth below the seabed. In fact, the author didn't have access and/or information about any experimental testing procedure (if there is any) that make it possible to apply confining pressures and indentation in the same time. Therefore, conducting a set of rock mechanics laboratory experiments to validate these numerical studies have a significant influence to evaluate the capability of the proposed numerical method.

Acknowledgements

Firstly, I would like to express my sincere gratitude to my supervisors Prof. Marco Giglio and Prof. Andrea Manes for the continuous support of my Ph.D study and related research, for their patience, motivation, and immense knowledge. Their guidance helped me in all the time of research and writing of this thesis. I could not have imagined having better advisors and mentors for my PhD study.

I had a chance to spend three months at the department of Civil Engineering, Tampere University of Technology (TUT), Finland, as a visiting PhD student in 2018. I would like to express my sincere gratitude to Prof. Timo Saksala, my supervisor during my visit at TUT, for his invaluable help in the issues related to percussive drilling and improving my coding skill.

Besides my advisors, I would like to thank my PhD tutor Prof. Nora Lecis, and my external reviewers Prof. Di Prisco and Prof. Calvetti for her insightful comments and encouragement, and the questions which incented me to widen my research from various perspectives.

My sincere thanks also go to Dr. Marco Caruso, Eng. Luca Signorelli, Dr. Ahmad Mardoukhi, and Prof. Mikko Hokka, who gave access to the laboratory and research facilities and collaborated in the experimental results obtained within this thesis. Without they precious support it would not be possible to conduct this research.

Special thanks go to my colleagues, Dr. Mehdi Aminyavari and Dr. Behzad Najafi who inspired and incented me to strive towards my goal and have been always a great support to me. Also, I thank my colleagues in the mechanical department of Politecnico di Milano. In particular, I am grateful to Dr. Massimo Fossati and Dr. Stefano Cardamone for the time and energy they devoted on my PhD research work.

The greatest proportion of my gratitude, however, goes to my family. Words cannot express how grateful I am to my mother, father and brother for all of the sacrifices that you've made on my behalf and for all the support during the years of research. Your prayer for me was what sustained me thus far. At the end I would like express appreciation to my beloved wife Dr. Sadaf Moaveninejad who was always my support in the moments when there was no one to answer my queries.

Bibliography

Åkesson, U., Hansson, J. and Stigh, J., 2004. Characterisation of microcracks in the Bohus granite, western Sweden, caused by uniaxial cyclic loading. Eng Geol, 72(1-2): 131-142.

Anemangely, M., Ramezanzadeh, A., Tokhmechi, B., Molaghab, A. and Mohammadian, A., 2018. Development of a new rock drillability index for oil and gas reservoir rocks using punch penetration test. Journal of Petroleum Science and Engineering, 166: 131-145.

Anghileri, M., Castelletti, L.-M.L., Francesconi, E., Milanese, A. and Pittofrati, M., 2011. Rigid body water impact–experimental tests and numerical simulations using the SPH method. Int J Impact Eng, 38(4): 141-151.

ASTM, 1998. Test Method for Flexural Strength of Dimension Stone, C 880-98. ASTM International, West Conshohocken, PA.

ASTM, 2004. Standard Test Method for Compressive Strength and Elastic Moduli of Intact Rock Core Specimens under Varying States of Stress and Temperatures, D 7012-04. ASTM International, West Conshohocken, PA.

Attaway, S., Heinstein, M. and Swegle, J., 1994. Coupling of smooth particle hydrodynamics with the finite element method. Nuclear engineering and design, 150(2-3): 199-205.

Bai, M., Meng, F., Elsworth, D., Abousleiman, Y. and Roegiers, J.C., 1999. Numerical modelling of coupled flow and deformation in fractured rock specimens. International journal for numerical and analytical methods in geomechanics, 23(2): 141-160.

Bar-Cohen, Y. and Zacny, K., 2009. Drilling in extreme environments: penetration and sampling on earth and other planets. John Wiley & Sons.

Basu, A., Celestino, T.B. and Bortolucci, A.A., 2009. Evaluation of rock mechanical behaviors under uniaxial compression with reference to assessed weathering grades. Rock Mech Rock Eng, 42(1): 73-93.

Basu, A., Mishra, D. and Roychowdhury, K., 2013. Rock failure modes under uniaxial compression, Brazilian, and point load tests. Bulletin of Engineering Geology and the environment, 72(3-4): 457-475.

Bažant, Z.P. and Kazemi, M.T., 1990. Size effect in fracture of ceramics and its use to determine fracture energy and effective process zone length. Journal of the American Ceramic Society, 73(7): 1841-1853.

béton, C.e.-i.d. and précontrainte, F.i.d.l., 1991. CEB-FIP model code 1990: final draft. CEB.

Bieniawski, Z.T., 1984. Rock Mechanics Design in Mining and Tunneling. Rock Mechanics Design in Mining and Tunneling.

Binici, B., 2005. An analytical model for stress–strain behavior of confined concrete. Engineering structures, 27(7): 1040-1051.

Biolzi, L., Cattaneo, S. and Rosati, G., 2001. Flexural/tensile strength ratio in rock-like materials. Rock Mech Rock Eng, 34(3): 217-233.

Biolzi, L. and Labuz, J., 1993. Global instability and bifurcation in beams composed of rock-like materials. International journal of solids and structures, 30(3): 359-370.

Borrvall, T., 2009. A heuristic attempt to reduce transverse shear locking in fully integrated hexahedra with poor aspect ratio, 7th European LSDYNA Conference, May, pp. 14-15.

Bottazzi, F., 2015. Campi di Agosta e Dosso degli Angeli: studio di subsidenza (Management Summary), ENI S.p.A. Development, Operations & Technology.

Brace, W.F., Paulding, B.W. and Scholz, C., 1966. Dilatancy in the fracture of crystalline rocks. J. Geophys. Res., 71(16): 3939-3953.

Brady, B.H. and Brown, E.T., 2013. Rock mechanics: for underground mining. Springer Science & Business Media.

Brannon, R.M. and Leelavanichkul, S., 2009. Survey of four damage models for concrete. Sandia Laboratories, Albuquerque. Sandia Report No. SAND, 5544.

Bresciani, L., Manes, A., Romano, T., Iavarone, P. and Giglio, M., 2016. Numerical modelling to reproduce fragmentation of a tungsten heavy alloy projectile impacting a ceramic tile: Adaptive solid mesh to the SPH technique and the cohesive law. Int J Impact Eng, 87: 3-13.

Busetti, S., Mish, K. and Reches, Z.e., 2012. Damage and plastic deformation of reservoir rocks: Part 1. Damage fracturing. AAPG bulletin, 96(9): 1687-1709.

Camacho, G.T. and Ortiz, M., 1996. Computational modelling of impact damage in brittle materials. International Journal of solids and structures, 33(20-22): 2899-2938.

Cattaneo, S. and Rosati, G., 1999. Effect of different boundary conditions in direct tensile tests: experimental results. Magazine of Concrete Research, 51(5): 365-374.

Ceryan, N., Okkan, U. and Kesimal, A., 2013. Prediction of unconfined compressive strength of carbonate rocks using artificial neural networks. Environ Earth Sci, 68(3): 807-819.

Chen, L.H. and Labuz, J.F., 2006. Indentation of rock by wedge-shaped tools. Int J Rock Mech Min Sci, 43(7): 1023-1033.

Chen, S.H. and Egger, P., 1999. Three dimensional elasto-viscoplastic finite element analysis of reinforced rock masses and its application. International Journal for Numerical and Analytical Methods in Geomechanics, 23(1): 61-78.

Cheon, D., Park, E. and Takahashi, M., 2016. The relationship between pore structure and permeability under confining pressure. Rock Mechanics and Rock Engineering: From the Past to the Future: 107.

Christensen, N. and Wang, H., 1985. The influence of pore pressure and confining pressure on dynamic elastic properties of Berea sandstone. Geophysics, 50(2): 207-213.

Cividini, A. et al., 1992. An apparatus for cyclic tests on cylindrical concrete specimens. Materials and Structures, 25(8): 490.

Coli, M., Livi, E. and Tanini, C., 2002. Pietra Serena in Fiesole. Part I: A historic stone resource in need of cultural and cognitive recovery. J. of Min. Sci.(3).

Coli, M., Livi, E. and Tanini, C., 2003. Pietra Serena in Fiesole. Part II: Geological setting and quarrying. J. of Min. Sci., 39(1).

Coli, M., Livi, E. and Tanini, C., 2006. Pietra Serena mining in Fiesole. Part III: Structural-mechanical characterization and mining. J Min Sci, 42(1): 74-84.

Copur, C., 2003. A set of indices based on indentation tests for assessment of rock cutting performance and rock properties. Journal of The Southern African Institute of Mining and Metallurgy, 103(9): 589-599.

Copur, H., 2001. Theoretical and experimental studies of rock cutting with drag bits toward the development of a performance prediction model for roadheaders.

Cornelissen, H., Hordijk, D. and Reinhardt, H., 1986. Experimental determination of crack softening characteristics of normalweight and lightweight concrete. HERON, 31 (2), 1986.

Coulomb, C.A., 1773. Essai sur une application des règles de maximis et minimis à quelques problèmes de statique relatifs à l'architecture. Mem. Div. Sav. Acad.: 7.

Cunningham, R. and Eenink, J., 1959. Laboratory study of effect of overburden, formation and mud column pressures on drilling rate of permeable formations.

Dai, F., Huang, S., Xia, K. and Tan, Z., 2010. Some fundamental issues in dynamic compression and tension tests of rocks using split Hopkinson pressure bar. Rock Mech Rock Eng, 43(6): 657-666.

Denoual, C. and Hild, F., 2000. A damage model for the dynamic fragmentation of brittle solids. Computer methods in applied mechanics and engineering, 183(3-4): 247-258.

Dollinger, G.L., Handewith, H.J. and Breeds, C.D., 1998. Use of the punch test for estimating TBM performance. Tunnelling and Underground Space Technology, 13(4): 403-408.

Fossum, A. and Brannon, R., 2004. Unified compaction/dilation, strain-rate sensitive, constitutive model for rock mechanics structural analysis applications, Gulf Rocks 2004, the 6th North America Rock Mechanics Symposium (NARMS). American Rock Mechanics Association.

Fowell, R.J., 1993. The mechanics of rock cutting. Comprehensive rock engineering, 4: 155-176.

Goodman, R.E., 1989. Introduction to rock mechanics, 2. Wiley New York.

Hallquist, J.O., 2014. LS-DYNA® Keyword User's Manual: Volumes I, II, and III LSDYNA R7. 1. Livermore Software Technology Corporation, Livermore (LSTC), Livermore, California, 1265.

Hamilton, W.B., 1979. Tectonics of the Indonesian region. US Govt. Print. Off.

Han, G., Bruno, M. and Dusseault, M.B., 2005. Dynamically modelling rock failure in percussion drilling, Alaska Rocks 2005, The 40th US Symposium on Rock Mechanics (USRMS). American Rock Mechanics Association.

Handewith, H., 1970. PREDICTING ECONOMIC SUCCESS OF CONTINUOUS TUNNELING IN HARD ROCK. Canadian Mining and Metallurgical Bulletin, 63(697): 595-+.

Hart, D.J. and Wang, H.F., 1995. Laboratory measurements of a complete set of poroelastic moduli for Berea sandstone and Indiana limestone. Journal of Geophysical Research: Solid Earth, 100(B9): 17741-17751.

Heiniö, M., 1999. Rock excavation handbook for civil engineering. Sandvik, Tamrock.

Hoek, E. and Brown, E.T., 1997. Practical estimates of rock mass strength. Int J Rock Mech Min Sci, 34(8): 1165-1186.

Hokka, M., 2008. Effects of strain rate and temperature on the mechanical behavior of advanced high strength steels. Tampere University of Technology.

Hu, Y. and Randolph, M., 1998. A practical numerical approach for large deformation problems in soil. International Journal for Numerical and Analytical Methods in Geomechanics, 22(5): 327-350.

Huang, X. and Karihaloo, B., 1993. MICROMECHANICAL MODELLING OF THE TENSILE BEHAVIOUR OF QUASI-BRITTLE MATERIALS, Advances in Engineering Plasticity and its Applications. Elsevier, pp. 267-272.

Hudson, J.A. and Harrison, J.P., 2000. Engineering rock mechanics: an introduction to the principles. Elsevier.

Jaeger, J.C. and Cook, N.G.W., 1979. Fundam Rock Mech.

Jaeger, J.C., Cook, N.G.W. and Zimmerman, R.W., 2007. Fundam Rock Mech.

Jeong, H.-Y., Cho, J.-W., Jeon, S. and Rostami, J., 2016. Performance assessment of hard rock TBM and rock boreability using punch penetration test. Rock Mech Rock Eng, 49(4): 1517-1532.

Jiang, H. and Zhao, J., 2015. Calibration of the continuous surface cap model for concrete. Finite Elements Anal Des, 97: 1-19.

Jianhong, Y., Wu, F. and Sun, J., 2009. Estimation of the tensile elastic modulus using Brazilian disc by applying diametrically opposed concentrated loads. Int J Rock Mech Min Sci, 46(3): 568-576.

Jing, L. and Hudson, J., 2002. Numerical methods in rock mechanics. Int J Rock Mech Min Sci, 39(4): 409-427.

Johnson, G.R., 1994. Linking of Lagrangian particle methods to standard finite element methods for high velocity impact computations. Nuclear Engineering and Design, 150(2-3): 265-274.

Johnson, G.R., Stryk, R.A., Beissel, S.R. and Holmquist, T.J., 2002. An algorithm to automatically convert distorted finite elements into meshless particles during dynamic deformation. Int J Impact Eng, 27(10): 997-1013.

Johnson, G.R., Stryk, R.A. and Dodd, J.G., 1986. Dynamic Lagrangian computations for solids, with variable nodal connectivity for severe distortions. International journal for numerical methods in engineering, 23(3): 509-522.

Kahraman, S., 2001. Evaluation of simple methods for assessing the uniaxial compressive strength of rock. Int J Rock Mech Min Sci, 38(7): 981-994.

Kahraman, S., Fener, M. and Kozman, E., 2012. Predicting the compressive and tensile strength of rocks from indentation hardness index. Journal of the Southern African Institute of Mining and Metallurgy, 112(5): 331-339.

Kalyan, B., Murthy, C.S. and Choudhary, R., 2015. Rock indentation indices as criteria in rock excavation technology–A critical review. Procedia Earth and Planetary Science, 11: 149-158.

Khodja, M., Canselier, J.P., Khodja-Saber, M. and Cohaut, N., 2010. Drilling fluid technology: performances and environmental considerations. INTECH Open Access Publisher.

Kong, X., Fang, Q., Li, Q., Wu, H. and Crawford, J.E., 2017. Modified K&C model for cratering and scabbing of concrete slabs under projectile impact. Int J Impact Eng.

Labuz, J. and Biolzi, L., 1991. Class I vs class II stability: a demonstration of size effect, International Journal of Rock Mechanics and Mining Sciences & Geomechanics Abstracts. Elsevier, pp. 199-205.

Labuz, J., Shah, S. and Dowding, C., 1985. Experimental analysis of crack propagation in granite, International Journal of Rock Mechanics and Mining Sciences & Geomechanics Abstracts. Elsevier, pp. 85-98.

Lacy, W.C. and Lacy, J.C., 1992. History of mining. HARTMAN, HL SME Min Eng Handb: 5-23.

Laws, V., 1981. Derivation of the tensile stress-strain curve from bending data. Journal of Materials Science, 16(5): 1299-1304.

Li, D. and Wong, L.N.Y., 2013. The Brazilian disc test for rock mechanics applications: review and new insights. Rock Mech Rock Eng, 46(2): 269-287.

Li, L., Lee, P.K.K., Tsui, Y., Tham, L.G. and Tang, C.A., 2003. Failure process of granite. Int J Geomech, 3(1): 84-98.

Limido, J., Espinosa, C., Salaün, M. and Lacome, J.-L., 2007. SPH method applied to high speed cutting modelling. International journal of mechanical sciences, 49(7): 898-908.

Liu, H., 2004. Numerical modelling of the rock fragmentation process by mechanical tools, Luleå tekniska universitet.

Liu, H., Kou, S. and Lindqvist, P.-A., 2008. Numerical studies on bit-rock fragmentation mechanisms. Int J Geomech, 8(1): 45-67.

Liu, H., Kou, S., Lindqvist, P.-A. and Tang, C., 2002. Numerical simulation of the rock fragmentation process induced by indenters. Int J Rock Mech Min Sci, 39(4): 491-505.

Liu, M. and Liu, G., 2010. Smoothed particle hydrodynamics (SPH): an overview and recent developments. Archives of computational methods in engineering, 17(1): 25-76.

Lubliner, J., Oliver, J., Oller, S. and Onate, E., 1989. A plastic-damage model for concrete. International Journal of solids and structures, 25(3): 299-326.

Malvar, L., Crawford, J. and Morill, K., 2000a. K&C Concrete material model release III: automated generation of material model input, Karagozian & Case, 2000TR-99-24-B1.

Malvar, L., Crawford, J., Wesevich, J. and Simons, D., 1996. A new concrete material model for DYNA3D-Release II: shear dilation and directional rate enhancements. A Report to Defense Nuclear Agency under Contract No. DNA001-91-C-0059.

Malvar, L.J. and Crawford, J.E., 1998. Dynamic increase factors for concrete, DTIC Document.

Malvar, L.J., Crawford, J.E. and Morrill, K.B., 2000b. K&C concrete material model release III-automated generation of material model input.

Malvar, L.J., Crawford, J.E., Wesevich, J.W. and Simons, D., 1994. A new concrete material model for DYNA3D. A New Concrete Material Model for DYNA3D.

Malvar, L.J., Crawford, J.E., Wesevich, J.W. and Simons, D., 1997. A plasticity concrete material model for DYNA3D. Int J Impact Eng, 19(9-10): 847-873.

Manual, A.S.U.s., 2009. Dassault Systemes Simulia Corp. Providence, RI.

Mardalizad, A., Caruso, M., Manes, A. and Giglio, M., 2018a. Numerical assessment of an advanced constitutive model for a quasi-brittle material. International Journal for Numerical and Analytical Methods in Geomechanics [under review].

Mardalizad, A., Manes, A. and Giglio, M., 2016. AN INVESTIGATION IN CONSTITUTIVE MODELS FOR DAMAGE SIMULATION OF ROCK MATERIAL, AIAS – ASSOCIAZIONE ITALIANA PER L'ANALISI DELLE SOLLECITAZIONI, UNIVERSITÀ DEGLI STUDI DI TRIESTE, ITALY.

Mardalizad, A., Manes, A. and Giglio, M., 2017a. INVESTIGATING THE TENSILE FRACTURE BEHAVIOR OF A MIDDLE STRENGTH ROCK: EXPERIMENTAL TESTS AND NUMERICAL MODELS, 14th International Conference on Fracture (ICF14), Rhodes, Greece.

Mardalizad, A., Manes, A. and Giglio, M., 2017b. The numerical modelling of a middle strength rock material under Flexural test by Finite Element method-coupled to-SPH. Procedia Structural Integrity, 3: 395-401.

Mardalizad, A., Scazzosi, R., Manes, A. and Giglio, M., 2017c. Four-point bending test on a middle strength rock: numerical and experimental investigations. Frattura ed Integrità Strutturale(41): 504.

Mardalizad, A., Scazzosi, R., Manes, A. and Giglio, M., 2018b. Testing and numerical simulation of a medium strength rock material under unconfined compression loading. Journal of Rock Mechanics and Geotechnical Engineering, 10(2): 197-211.

Markovich, N., Kochavi, E. and Ben-Dor, G., 2011. An improved calibration of the concrete damage model. Finite Elements Anal Des, 47(11): 1280-1290.

Martin, C.D., 1993. The strength of massive Lac du Bonnet granite around underground openings.

Mayville, R. and Finnie, I., 1982. Uniaxial stress-strain curves from a bending test. Experimental Mechanics, 22(6): 197-201.

Meda, A., 2003. Tensile behaviour in natural building stone: Serena sandstone. Materials and Structures, 36(8): 553-559.

Menéndez, B., Zhu, W. and Wong, T.-F., 1996. Micromechanics of brittle faulting and cataclastic flow in Berea sandstone. Journal of Structural Geology, 18(1): 1-16.

Menetrey, P. and Willam, K., 1995. Triaxial failure criterion for concrete and its generalization. ACI structural Journal, 92(3): 311-318.

Mishnaevsky, L., 1995. Physical mechanisms of hard rock fragmentation under mechanical loading: a review, International Journal of Rock Mechanics and Mining Sciences and Geomechanics Abstracts. Oxford; New York: Pergamon Press, 1974-c1996., pp. 763.

Mogi, K., 1966. Some precise measurements of fracture strength of rocks under uniform compressive stress. Rock Mech. Eng. Geol, 4(1): 41-55.

Mogi, K., 2007. Experimental rock mechanics, 3. CRC Press.

Monaghan, J.J., 1988. An introduction to SPH. Computer Physics Communications, 48(1): 89-96.

Monaghan, J.J., 1992. Smoothed particle hydrodynamics. Annual review of astronomy and astrophysics, 30(1): 543-574.

Murray, Y.D., Abu-Odeh, A.Y. and Bligh, R.P., 2007. Evaluation of LS-DYNA concrete material model 159.

Olleak, A.A. and El-Hofy, H.A., 2015. SPH Modelling of Cutting Forces while Turning of Ti6Al4V Alloy.

Pepper, J.F., 1954. Geology of the Bedford Shale and Berea Sandstone in the Appalachian Basin: A Study of the Stratigraphy, Sedimentation and Paleogeography of Rocks of Bedford and Berea Age in Ohio and Adjacent States, 259. US Government Printing Office.

Price, N., 1964. A study of the time-strain behaviour of coal-measure rocks, International Journal of Rock Mechanics and Mining Sciences & Geomechanics Abstracts. Elsevier, pp. 277-303.

Ramezanzadeh, A., Rostami, J. and Tadic, D., 2008. Impact of Rock Mass Characteristics on Hard Rock Tunnel Boring Machine Performance, 13th Australian Tunnelling Conference, Melbourne, Australia, pp. 213-220.

Rossmanith, H., Knasmillner, R., Daehnke, A. and Mishnaevsky, L., 1996. Wave propagation, damage evolution, and dynamic fracture extension. Part I. Percussion drilling. Materials Science, 32(3): 350-358.

Rots, J.G. and De Borst, R., 1987. Analysis of mixed-mode fracture in concrete. J Eng Mech, 113(11): 1739-1758.

Saksala, T., 2006. Kiven särkymisen numeerinen mallinnus iskumaisessa kuormituksessa. In: von Hertzen, R. & Halme, T.(ed.). Proceedings of the IX Finnish Mechanics Days, 13-14.6. 2006, Lappeenranta. Lappeenrannan teknillinen yliopisto. Konetekniikan osasto. Raportti.

Saksala, T., 2008. Damage-plastic model for numerical simulation of rock fracture in dynamic loading, In: Papadrakakis, M. et al.(eds.). Sixth International Conference on Engineering Computational Technology, Athens, Greece, 2-5 September 2008.

Saksala, T., 2010a. Damage–viscoplastic consistency model with a parabolic cap for rocks with brittle and ductile behavior under low-velocity impact loading. International Journal for Numerical and Analytical Methods in Geomechanics, 34(13): 1362-1386.

Saksala, T., 2010b. Numerical modelling of rock fracture in percussive drilling, PhD Thesis, Tampere University of Technology, Finland.

Saksala, T., Gomon, D., Hokka, M. and Kuokkala, V.-T., 2014. Numerical and experimental study of percussive drilling with a triple-button bit on Kuru granite. Int J Impact Eng, 72: 56-66.

Salagame, R.R. and Belegundu, A.D., 1994. Distortion, degeneracy and rezoning in finite elements — A survey. Sadhana, 19(2): 311-335.

Santarelli, F.J. and Brown, E.T., 1989. Failure of three sedimentary rocks in triaxial and hollow cylinder compression tests. Int J Rock Mech Min Sci, 26(5): 401-413.

SCAZZOSI, R. and MAIOLANI, F., 2015-2016. Experimental and numerical characterization of mechanical behaviour of sandstone, Politecnico di Milano, 2015-2016.

Sivakugan, N., Das, B., Lovisa, J. and Patra, C., 2014. Determination of c and φ of rocks from indirect tensile strength and uniaxial compression tests. International Journal of Geotechnical Engineering, 8(1): 59-65.

Standard, A., 2008. Standard test method for splitting tensile strength of intact rock core specimens. D.

Szwedzicki, T., 2007. A hypothesis on modes of failure of rock samples tested in uniaxial compression. Rock Mech Rock Eng, 40(1): 97-104.

Tan, X., Kou, S. and Lindqvist, P.-A., 1998. Application of the DDM and fracture mechanics model on the simulation of rock breakage by mechanical tools. Eng Geol, 49(3-4): 277-284.

Tan, X., Lindqvist, P.A. and Kou, S., 1997. Application of a splitting fracture model to the simulation of rock indentation subsurface fractures. International journal for numerical and analytical methods in geomechanics, 21(1): 1-13.

Thuro, K. and Schormair, N., 2008. Fracture propagation in anisotropic rock during drilling and cutting. Geomechanik und Tunnelbau: Geomechanik und Tunnelbau, 1(1): 8-17.

Willam, K. and Warnke, E., 1975. Constitutive model for the triaxial behavior of concrete, Proceedings, international association for bridge and structural engineering. ISMES, Bergamo, Italy, pp. 1-30.

Winnicki, A., Pearce, C. and Bićanić, N., 2001. Viscoplastic Hoffman consistency model for concrete. Computers & Structures, 79(1): 7-19.

Wu, J., Li, L., Du, X. and Liu, X., 2017. Numerical study on the asphalt concrete structure for blast and impact load using the Karagozian and case concrete model. Applied Sciences, 7(2): 202.

Wu, X. and Gorham, D., 1997. Stress equilibrium in the split Hopkinson pressure bar test. Le Journal de Physique IV, 7(C3): C3-91-C3-96.

Wu, Y. and Crawford, J.E., 2015. Numerical Modeling of Concrete Using a Partially Associative Plasticity Model. J Eng Mech, 141(12): 04015051.

Xu, J. and Wang, J., 2014. Interaction methods for the SPH parts (multiphase flows, solid bodies) in LS-DYNA, 13th international LS-DYNA users conference, Detroit, MI, pp. 8-10.

Yagiz, S., 2009. Assessment of brittleness using rock strength and density with punch penetration test. Tunnelling and Underground Space Technology, 24(1): 66-74.

Yagiz, S. and Rostami, J., 2012. Indentation test for the measurement of rock brittleness, 46th US Rock Mechanics/Geomechanics Symposium. American Rock Mechanics Association.

Zang, A. and Stephansson, O., 2009. Stress field of the Earth's crust. Springer Science & Business Media.

Zou, D., 2017. Theory and Technology of Rock Excavation for Civil Engineering. Springer.

Appendix A: Dynamic Brazilian disk test

- Test 1 – 10 m/s

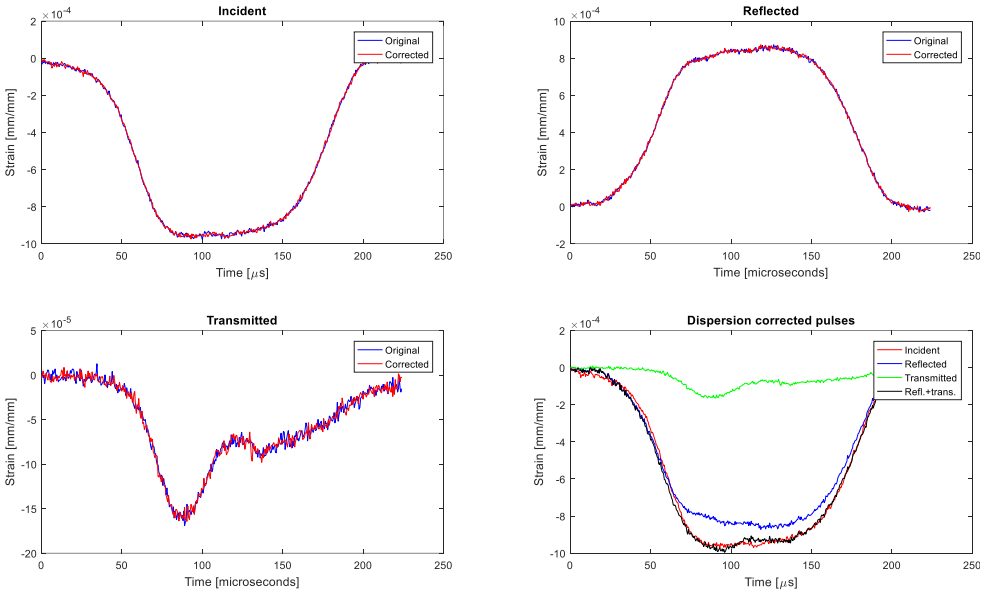

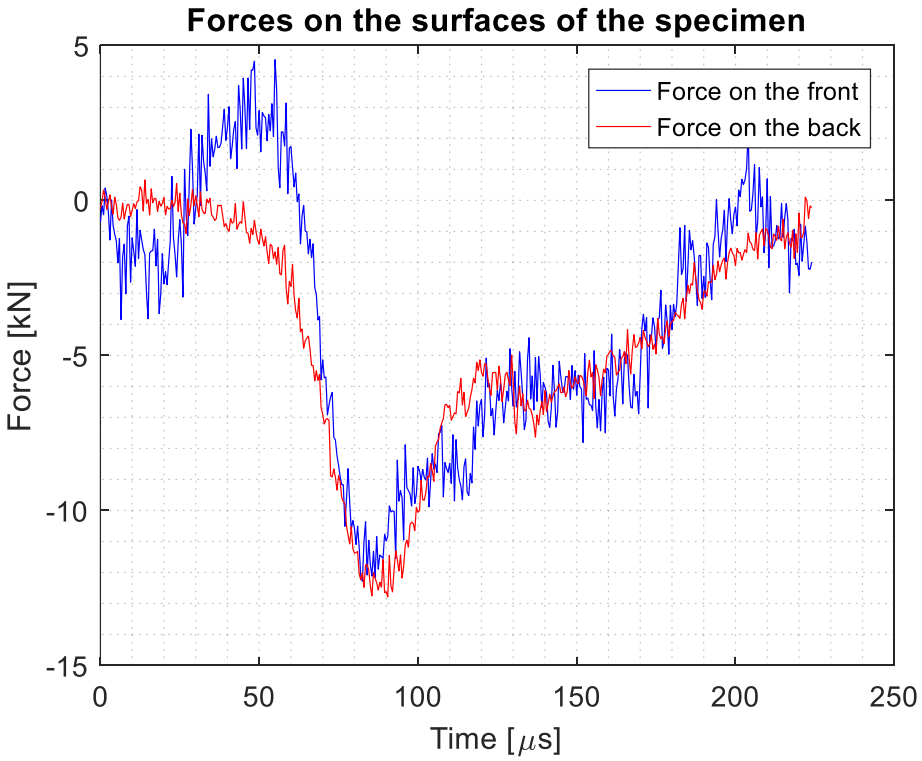

- Test 2 – 10 m/s

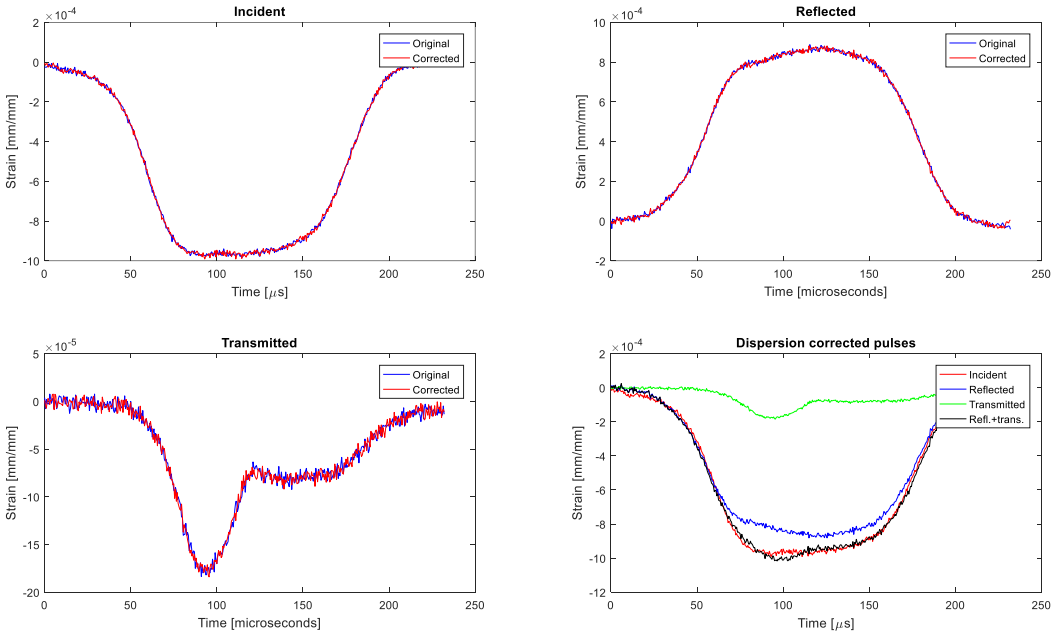
Incident
Original
Corrected
Strain [mm/mm]
Time [μs]
Reflected
Original
Corrected
Strain [mm/mm]
Time [microseconds]
Transmitted
Original
Corrected
Strain [mm/mm]
Time [microseconds]
Dispersion corrected pulses
Incident
Reflected
Transmitted
Refl.+trans.
Strain [mm/mm]
Time [μs]

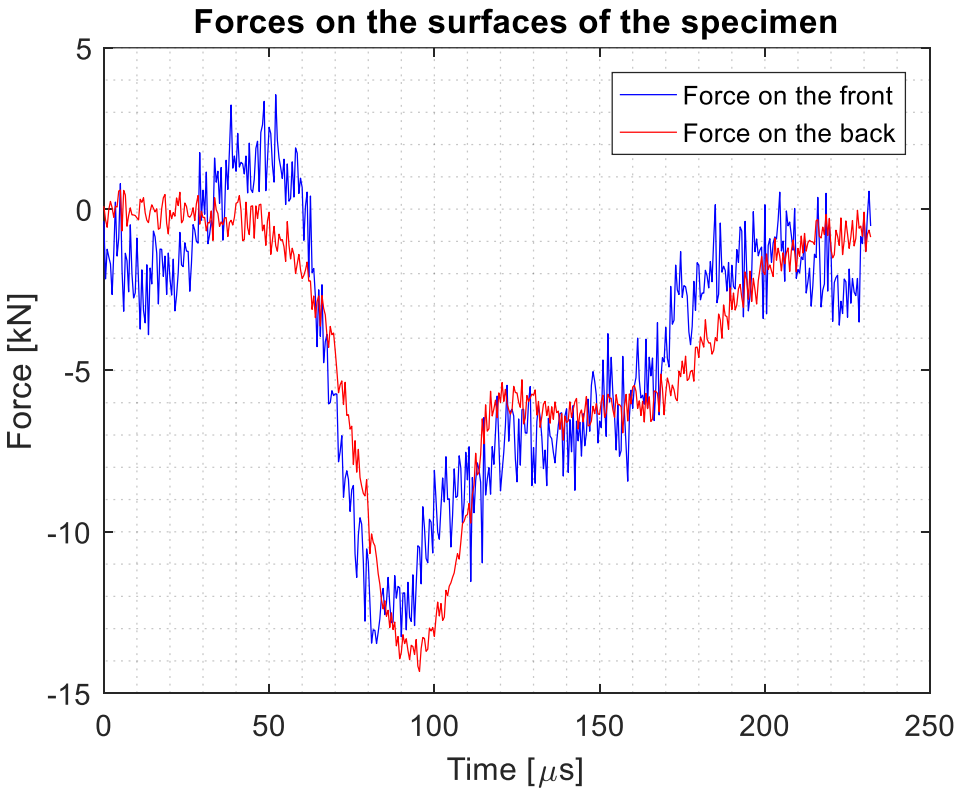
Forces on the surfaces of the specimen
Force on the front
Force on the back
Force [kN]
Time [μs]

- Test 3 – 10 m/s

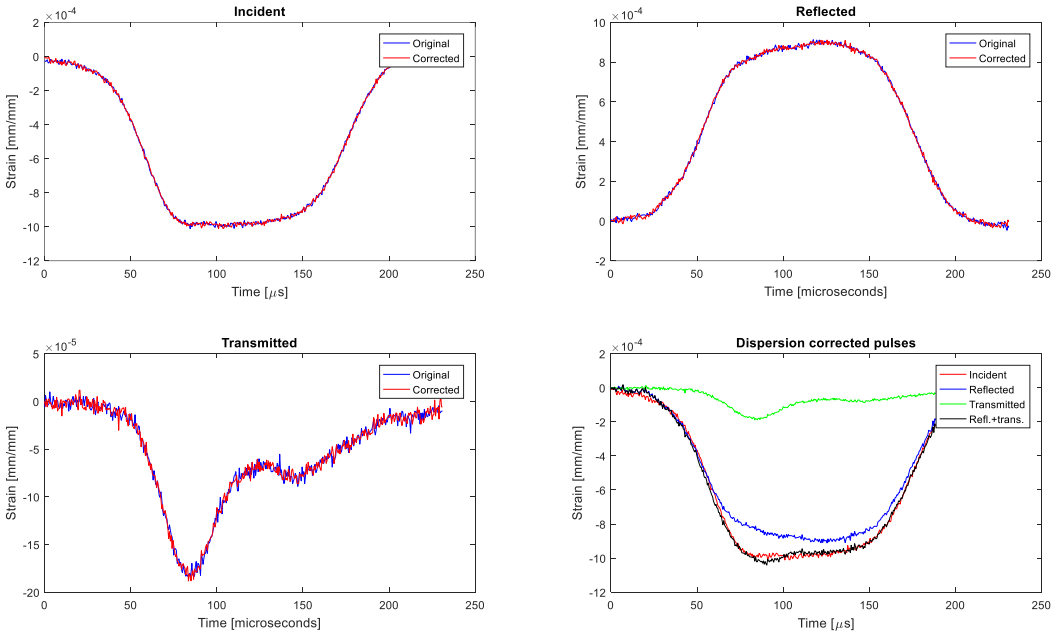
Incident
Original
Corrected
Strain [mm/mm]
Time [μs]
Reflected
Original
Corrected
Strain [mm/mm]
Time [microseconds]
Transmitted
Original
Corrected
Strain [mm/mm]
Time [microseconds]
Dispersion corrected pulses
Incident
Reflected
Transmitted
Refl.+trans.
Strain [mm/mm]
Time [μs]

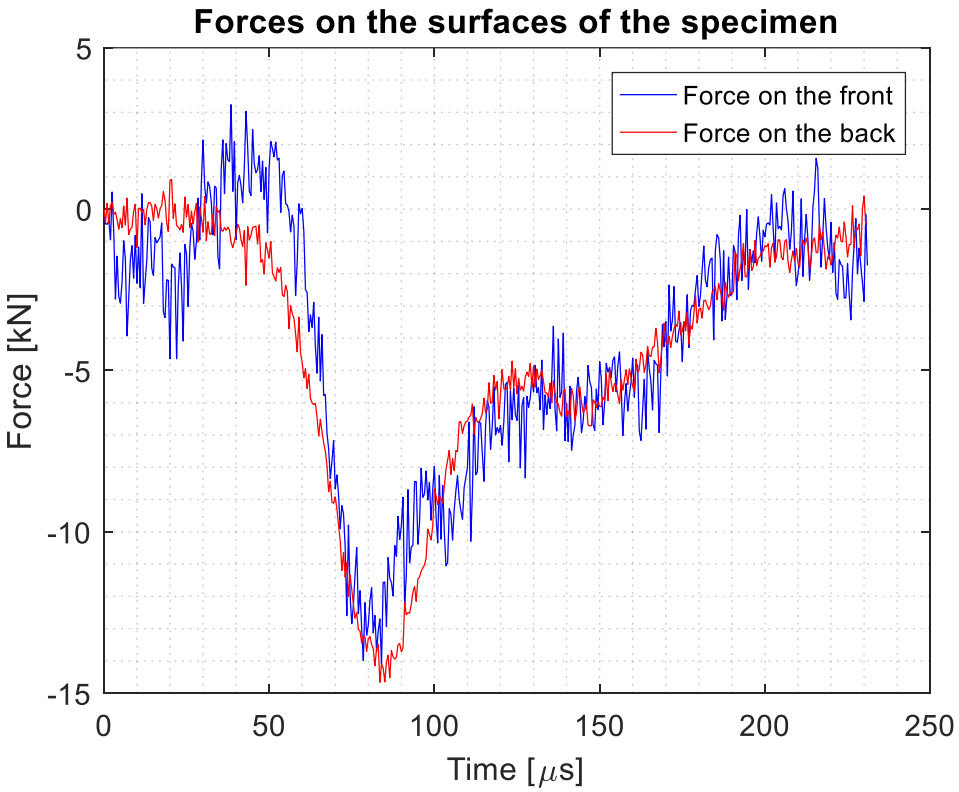
Forces on the surfaces of the specimen
Force on the front
Force on the back
Force [kN]
Time [μs]

- Test 4 – 10 m/s

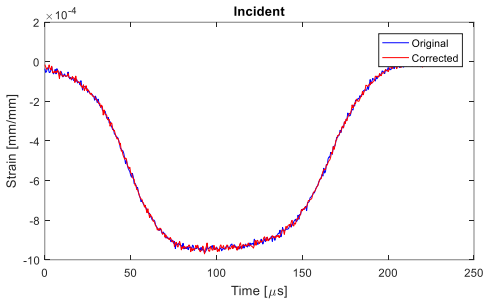
Incident
Original
Corrected
Strain [mm/mm]
Time [μs]

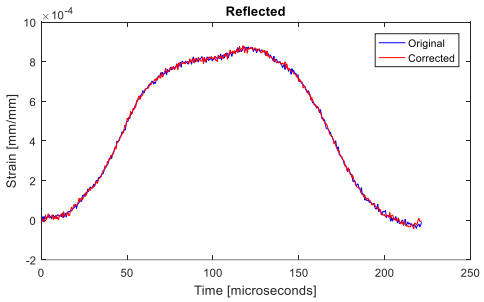
Reflected
Original
Corrected
Strain [mm/mm]
Time [microseconds]

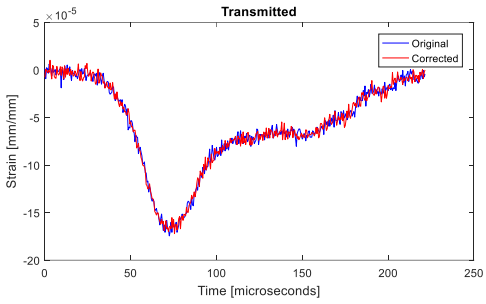
Transmitted
Original
Corrected
Strain [mm/mm]
Time [microseconds]

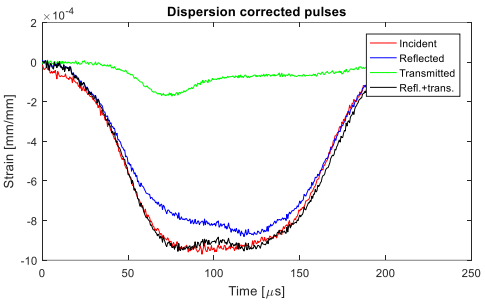
Dispersion corrected pulses
Incident
Reflected
Transmitted
Refl.+trans.
Strain [mm/mm]
Time [μs]

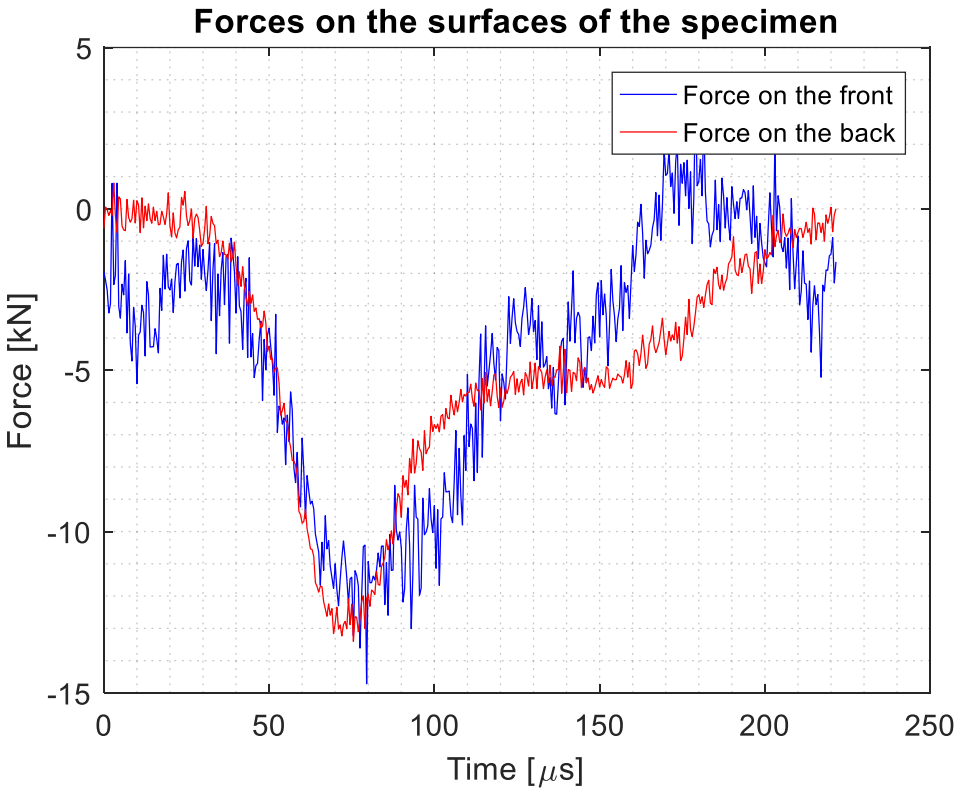
Forces on the surfaces of the specimen
Force on the front
Force on the back
Force [kN]
Time [μs]

- Test 5 – 10 m/s

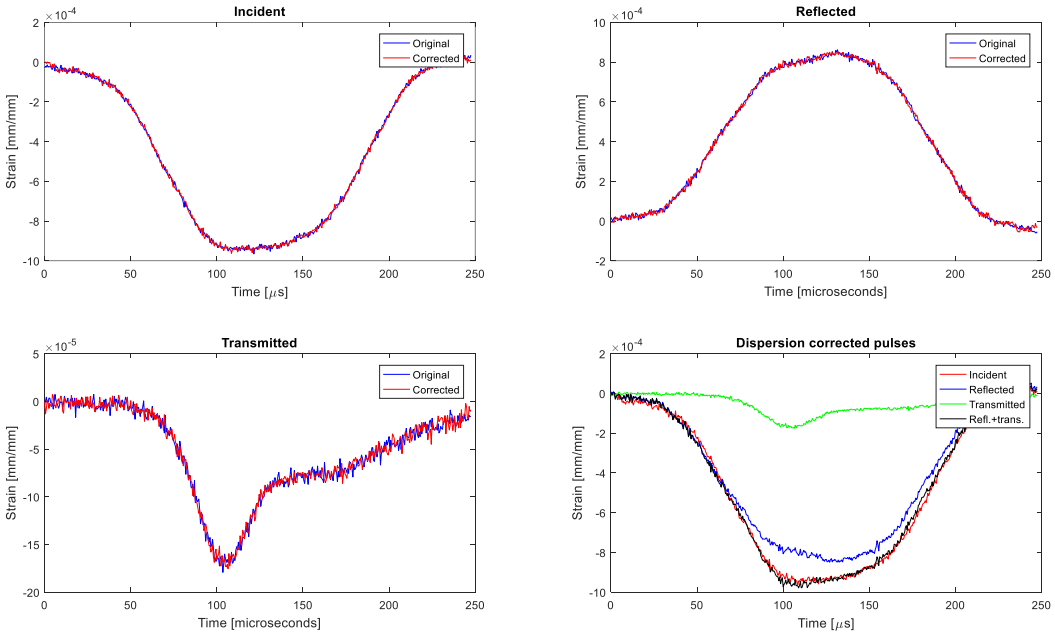
Incident
Original
Corrected
Strain [mm/mm]
Time [μs]
Reflected
Original
Corrected
Strain [mm/mm]
Time [microseconds]
Transmitted
Original
Corrected
Strain [mm/mm]
Time [microseconds]
Dispersion corrected pulses
Incident
Reflected
Transmitted
Refl.+trans.
Strain [mm/mm]
Time [μs]

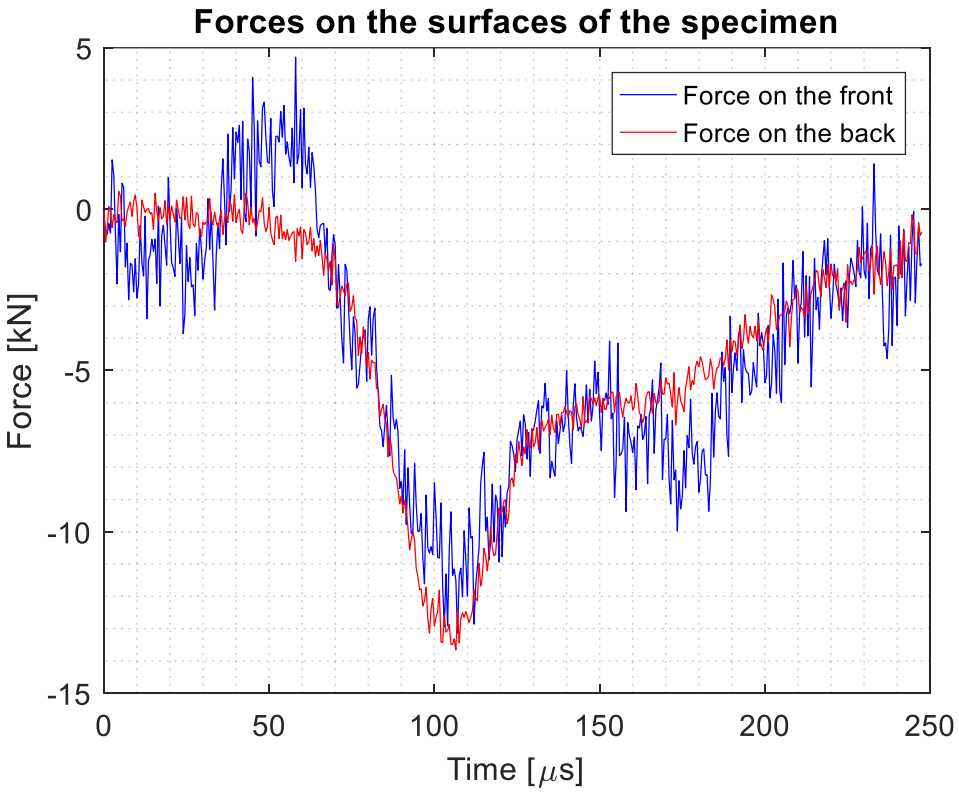
Forces on the surfaces of the specimen
Force on the front
Force on the back
Force [kN]
Time [μs]

- Test 1 – 15 m/s

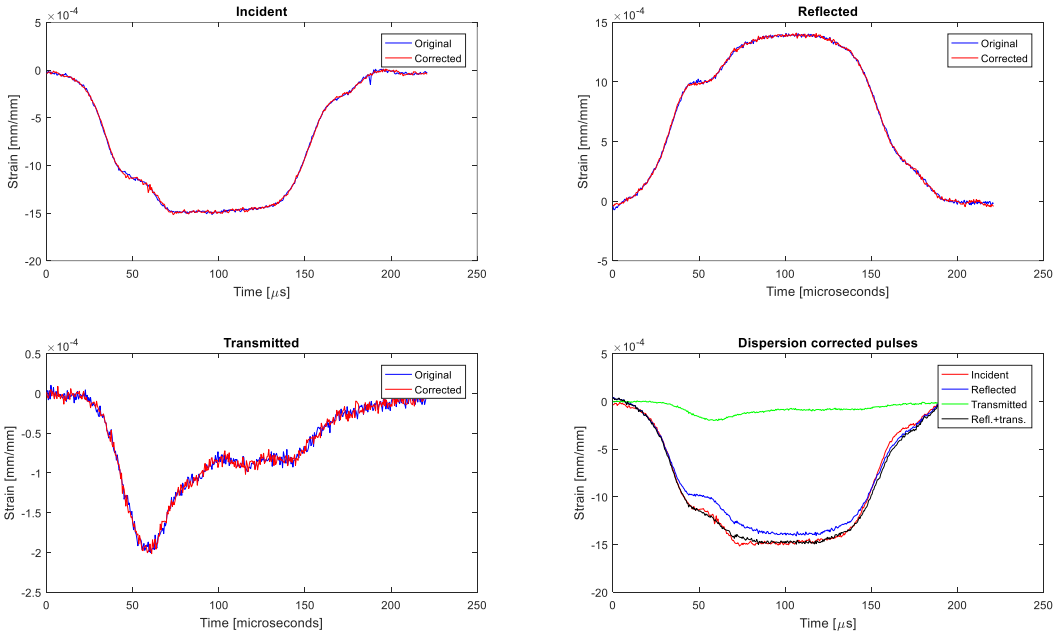
Incident
Original
Corrected
Strain [mm/mm]
Time [μs]
Reflected
Original
Corrected
Strain [mm/mm]
Time [microseconds]
Transmitted
Original
Corrected
Strain [mm/mm]
Time [microseconds]
Dispersion corrected pulses
Incident
Reflected
Transmitted
Refl.+trans.
Strain [mm/mm]
Time [μs]

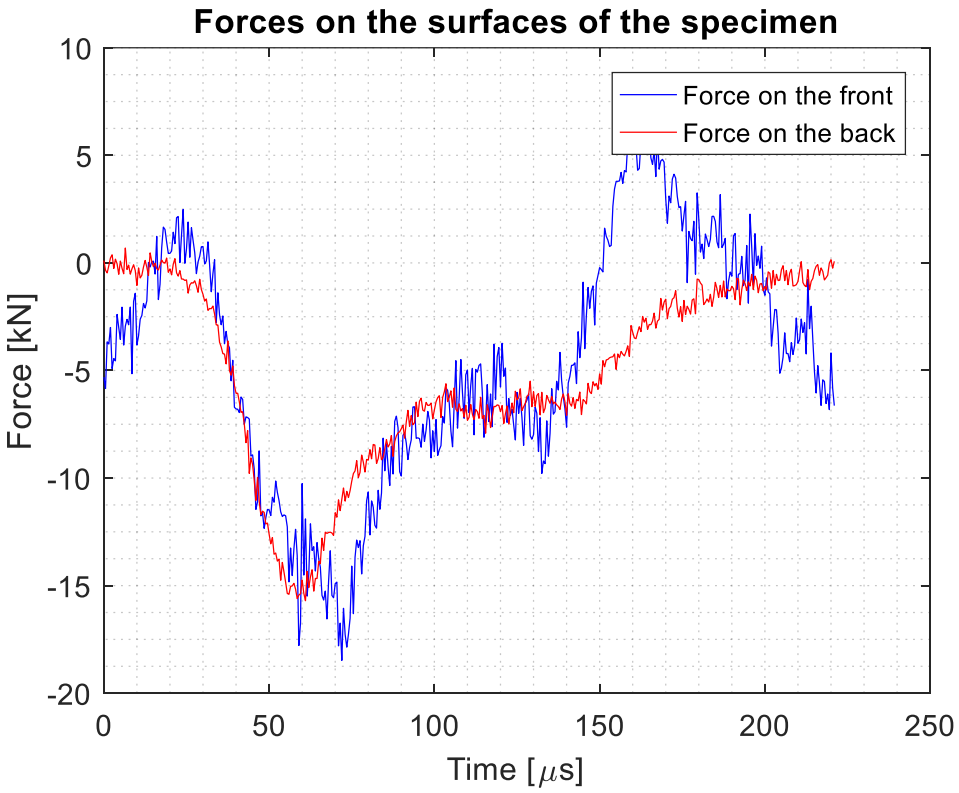
Forces on the surfaces of the specimen
Force on the front
Force on the back
Force [kN]
Time [μs]

- Test 2 – 15 m/s

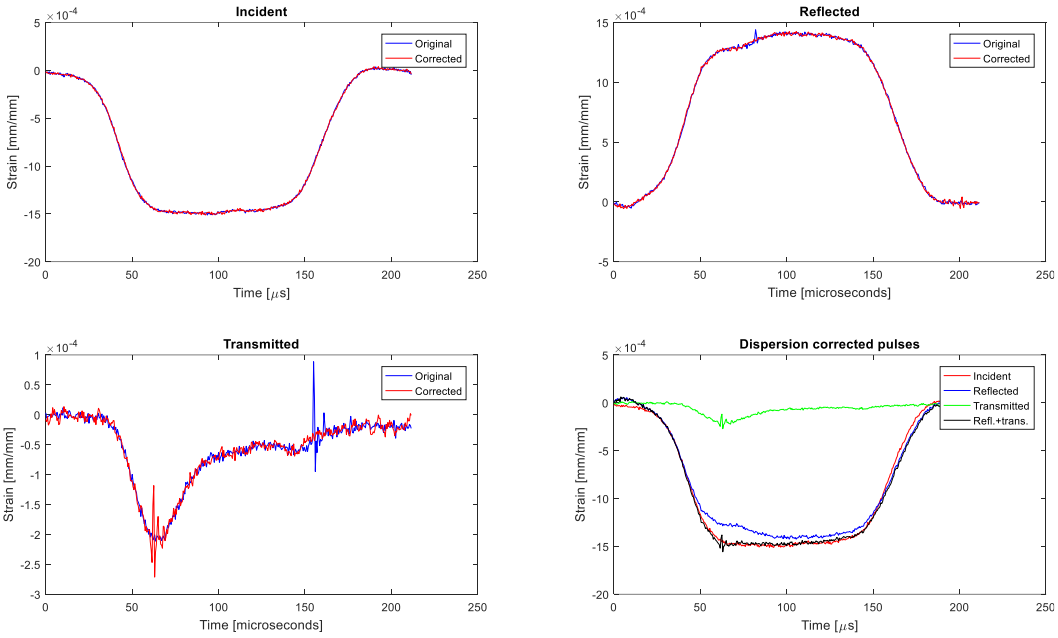
Incident
Reflected
Transmitted
Dispersion corrected pulses
Original
Corrected
Incident
Reflected
Transmitted
Refl.+trans.
Strain [mm/mm]
Time [μs]
Time [microseconds]

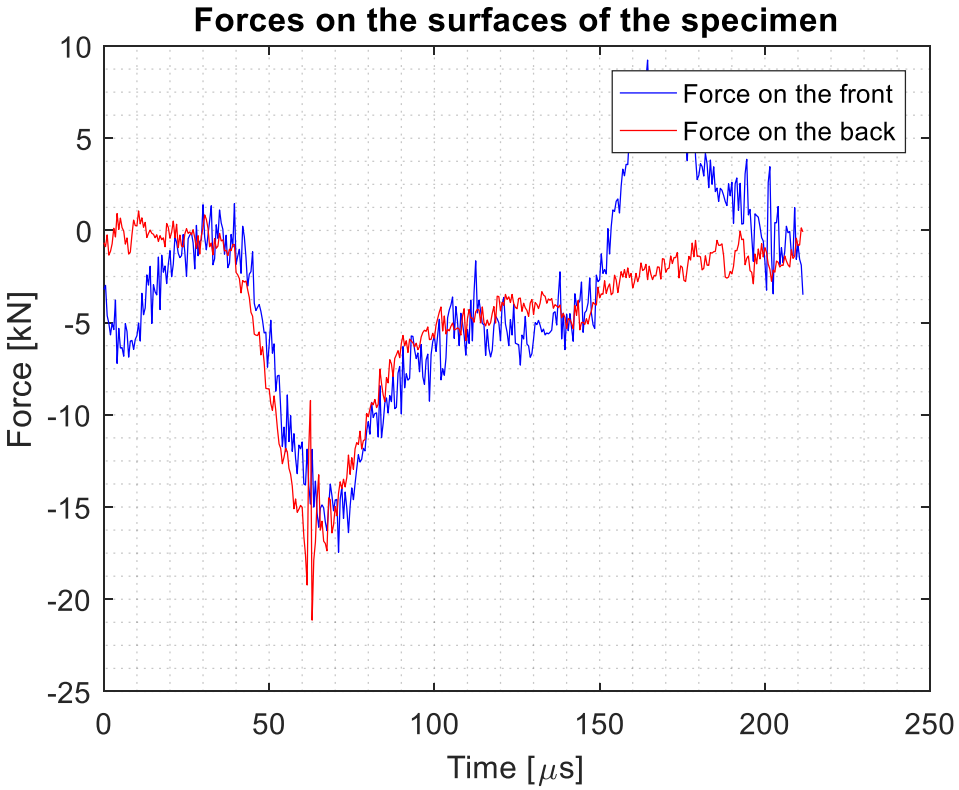
Forces on the surfaces of the specimen
Force on the front
Force on the back
Force [kN]
Time [μs]

- Test 3 – 15 m/s

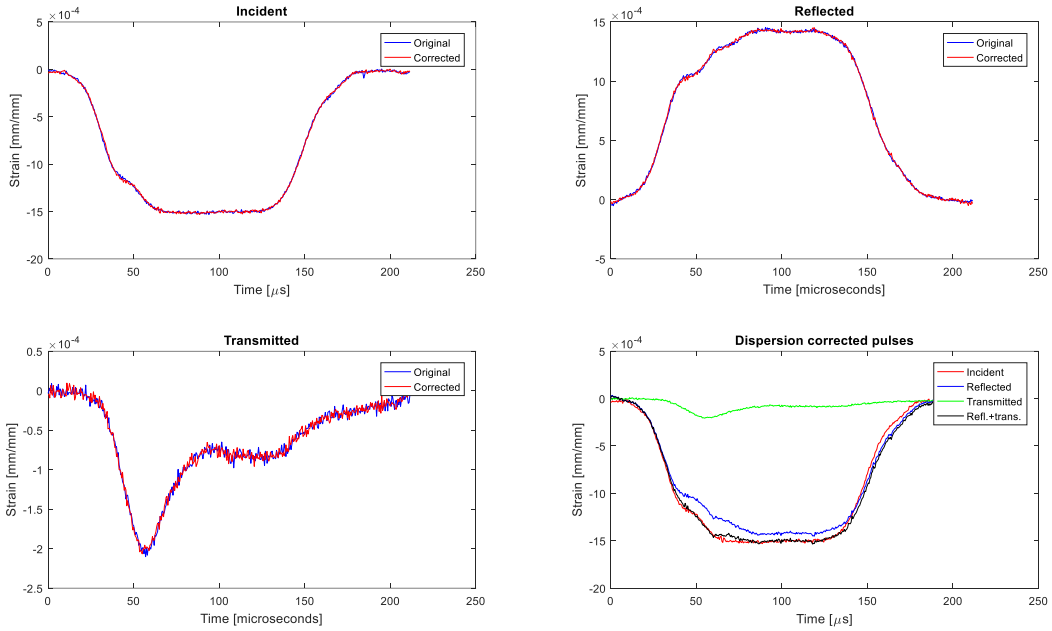
Incident
Original
Corrected
Strain [mm/mm]
Time [μs]
Reflected
Original
Corrected
Strain [mm/mm]
Time [microseconds]
Transmitted
Original
Corrected
Strain [mm/mm]
Time [microseconds]
Dispersion corrected pulses
Incident
Reflected
Transmitted
Refl.+trans.
Strain [mm/mm]
Time [μs]

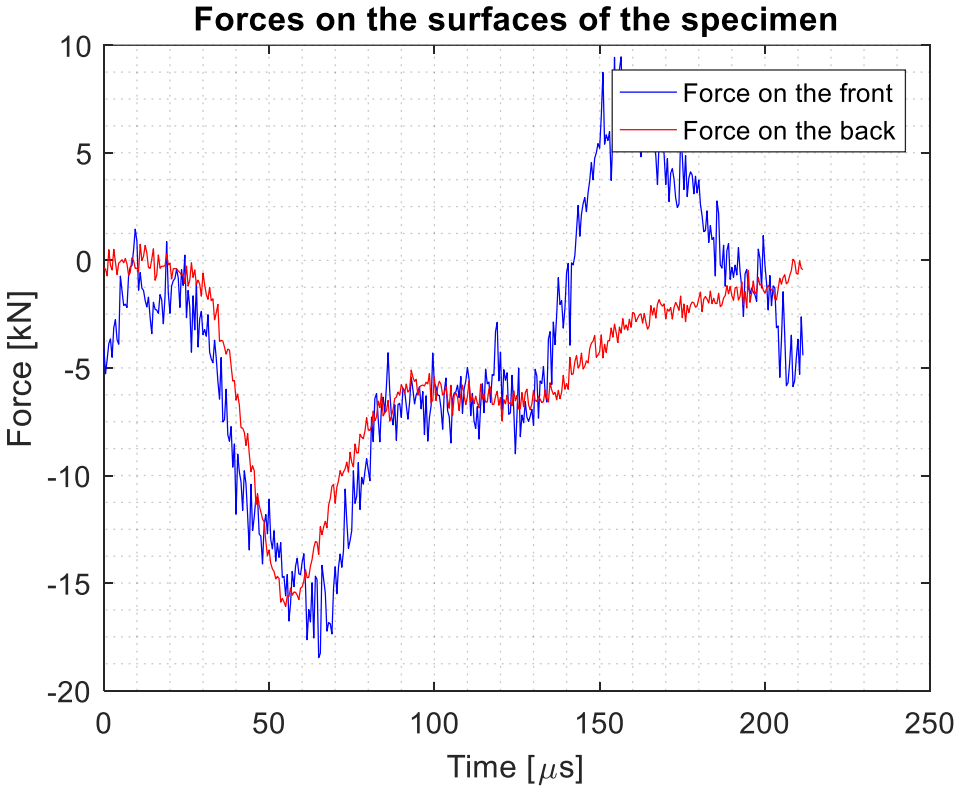
Forces on the surfaces of the specimen
Force on the front
Force on the back
Force [kN]
Time [μs]

- Test 4 – 15 m/s

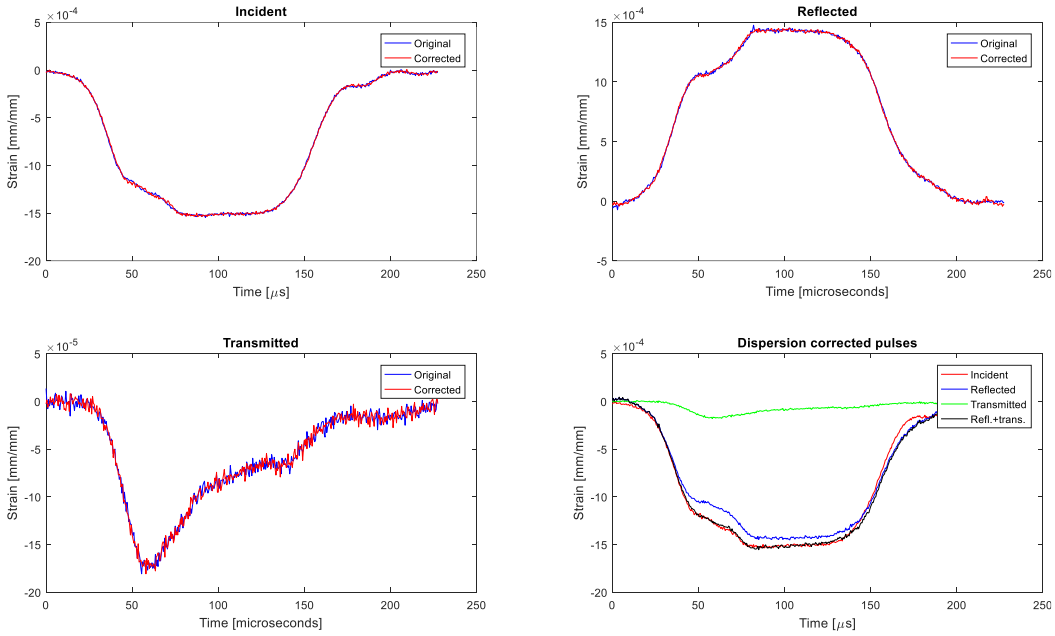
Incident
Original
Corrected
Strain [mm/mm]
Time [μs]
Reflected
Original
Corrected
Strain [mm/mm]
Time [microseconds]
Transmitted
Original
Corrected
Strain [mm/mm]
Time [microseconds]
Dispersion corrected pulses
Incident
Reflected
Transmitted
Refl.+trans.
Strain [mm/mm]
Time [μs]

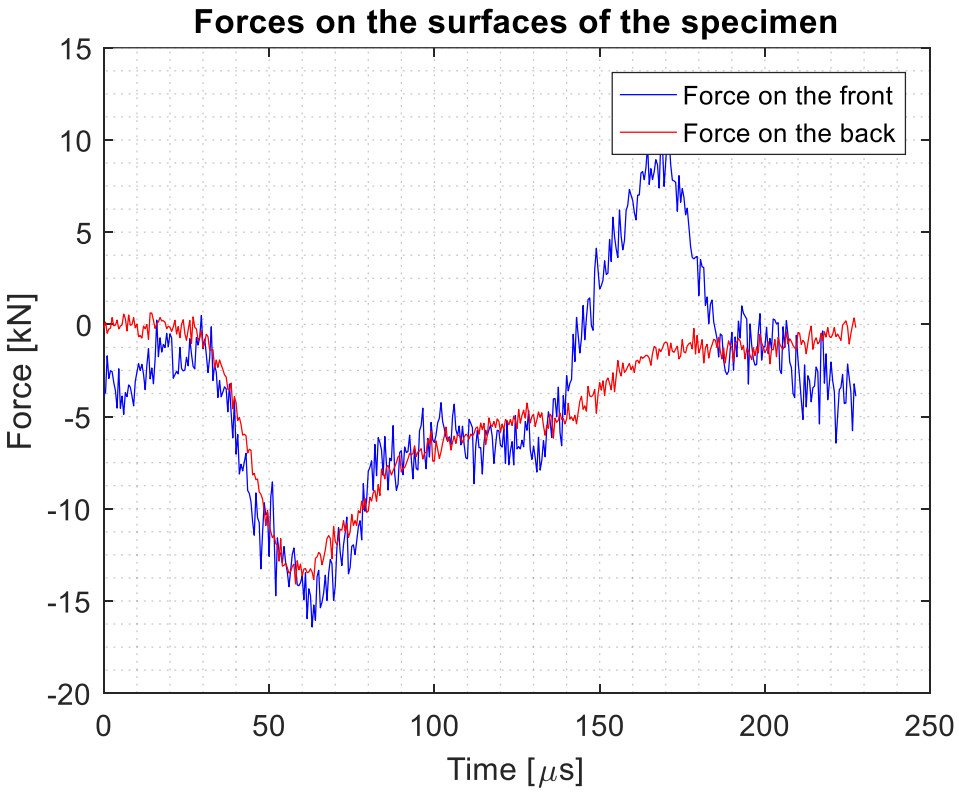
Forces on the surfaces of the specimen
Force on the front
Force on the back
Force [kN]
Time [μs]

- Test 5 – 15 m/s

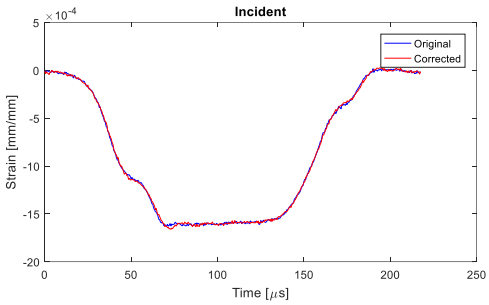
Incident
Original
Corrected
Strain [mm/mm]
Time [μs]

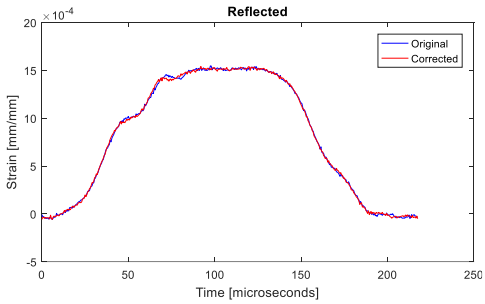
Reflected
Original
Corrected
Strain [mm/mm]
Time [microseconds]

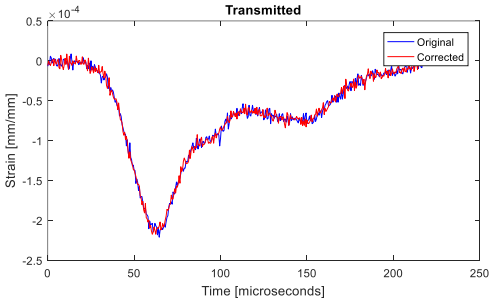
Transmitted
Original
Corrected
Strain [mm/mm]
Time [microseconds]

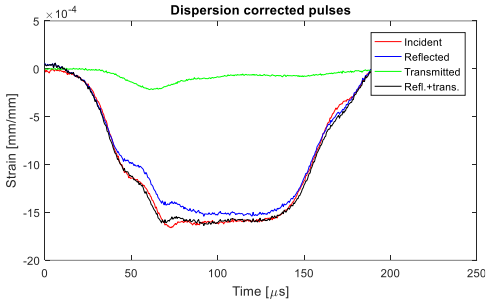
Dispersion corrected pulses
Incident
Reflected
Transmitted
Refl.+trans.
Strain [mm/mm]
Time [μs]

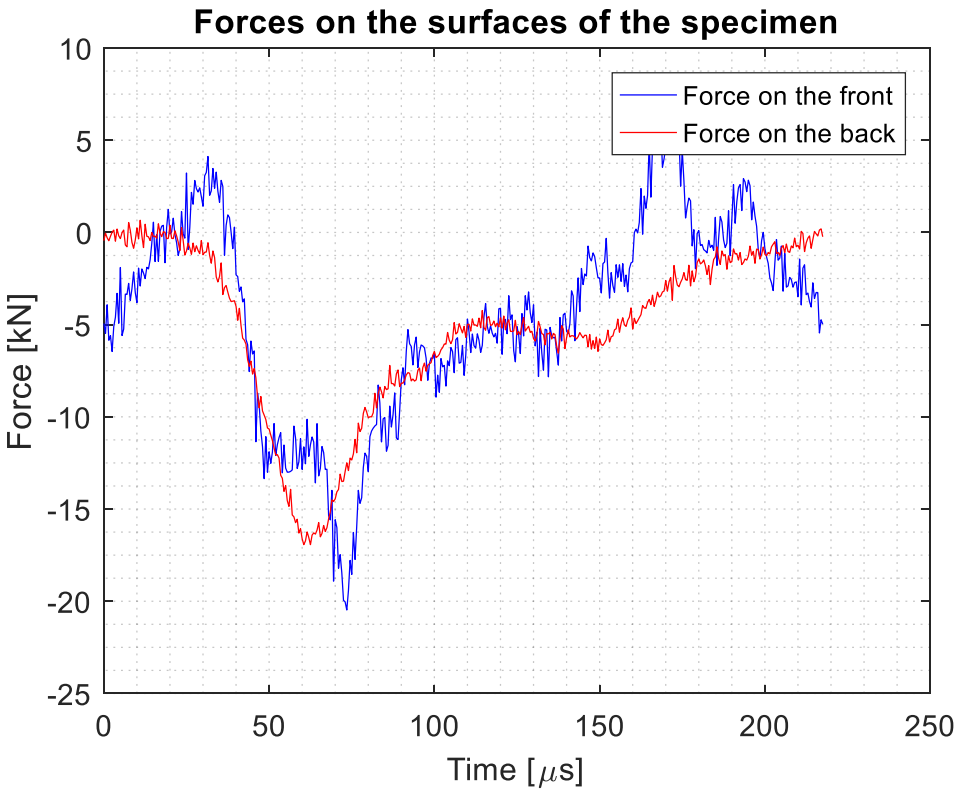
Forces on the surfaces of the specimen
Force on the front
Force on the back
Force [kN]
Time [μs]

- Test 1 – 20 m/s

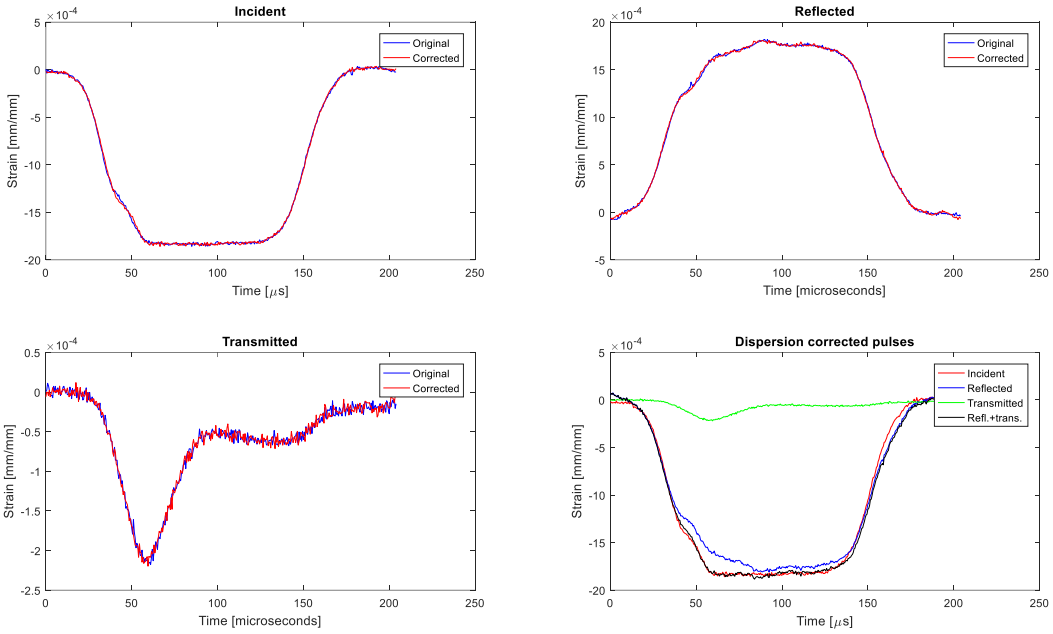
Incident
Original
Corrected
Strain [mm/mm]
Time [μs]
Reflected
Original
Corrected
Strain [mm/mm]
Time [microseconds]
Transmitted
Original
Corrected
Strain [mm/mm]
Time [microseconds]
Dispersion corrected pulses
Incident
Reflected
Transmitted
Refl.+trans.
Strain [mm/mm]
Time [μs]

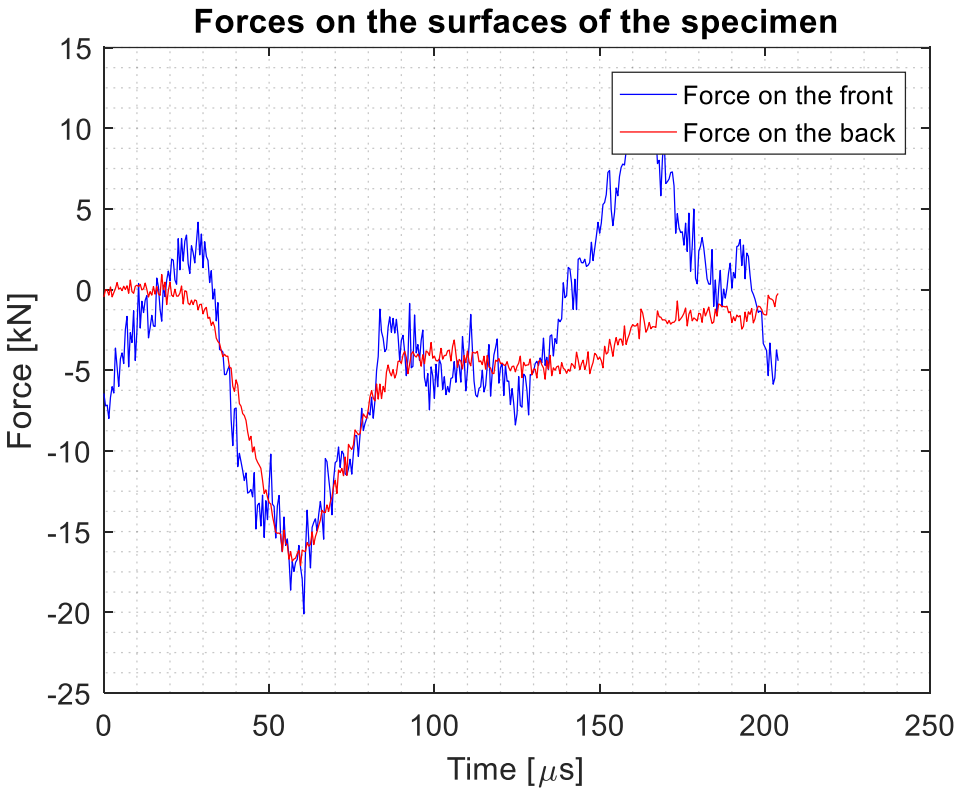
Forces on the surfaces of the specimen
Force on the front
Force on the back
Force [kN]
Time [μs]

- Test 2 – 20 m/s

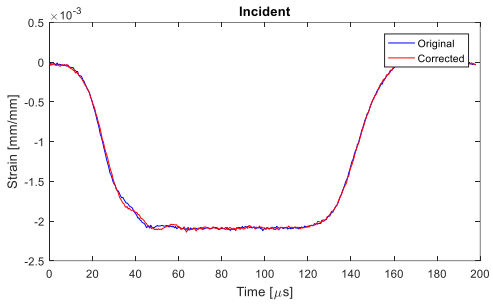
Incident
Original
Corrected
Strain [mm/mm]
Time [μs]

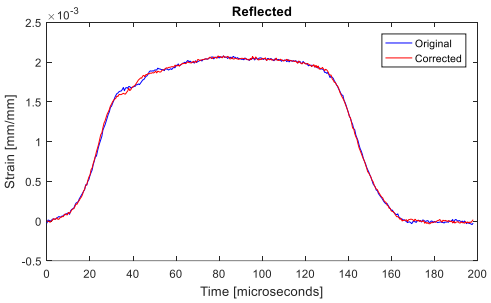
Reflected
Original
Corrected
Strain [mm/mm]
Time [microseconds]

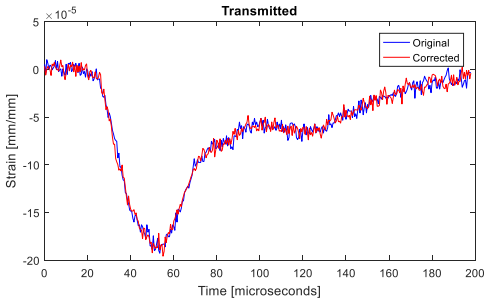
Transmitted
Original
Corrected
Strain [mm/mm]
Time [microseconds]

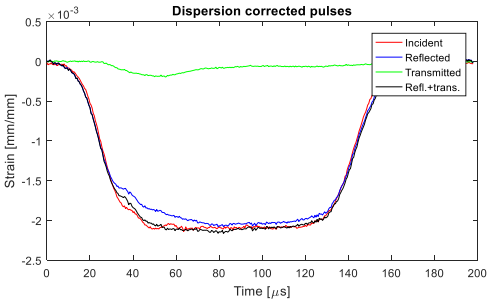
Dispersion corrected pulses
Incident
Reflected
Transmitted
Refl.+trans.
Strain [mm/mm]
Time [μs]

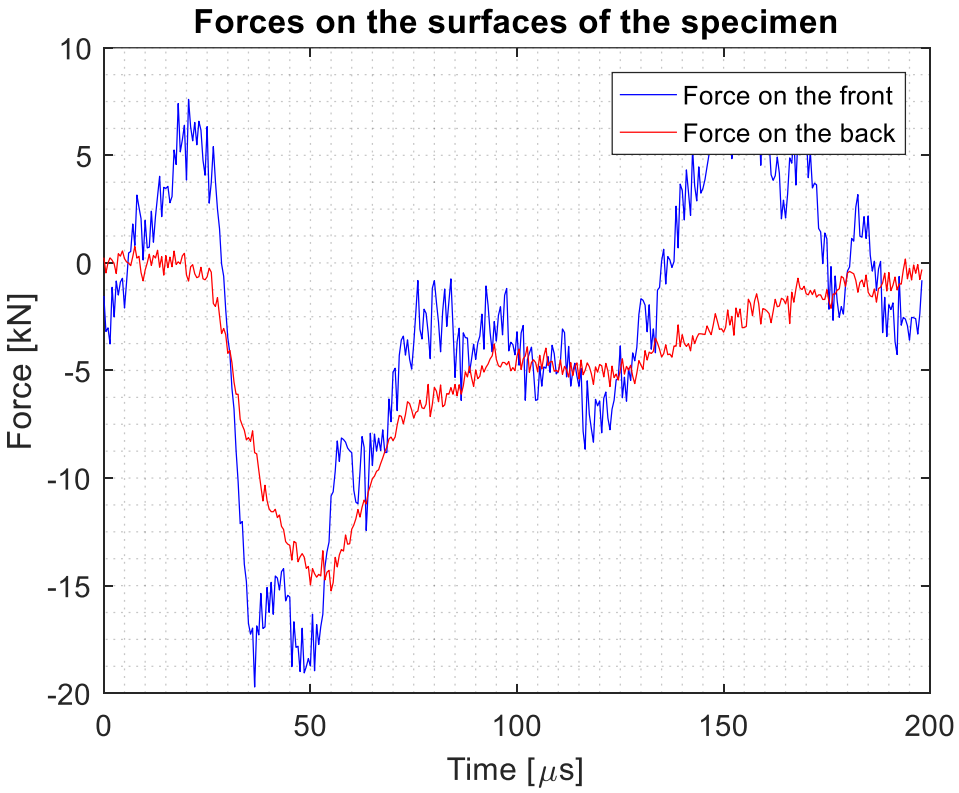
Forces on the surfaces of the specimen
Force on the front
Force on the back
Force [kN]
Time [μs]

- Test 3 – 20 m/s

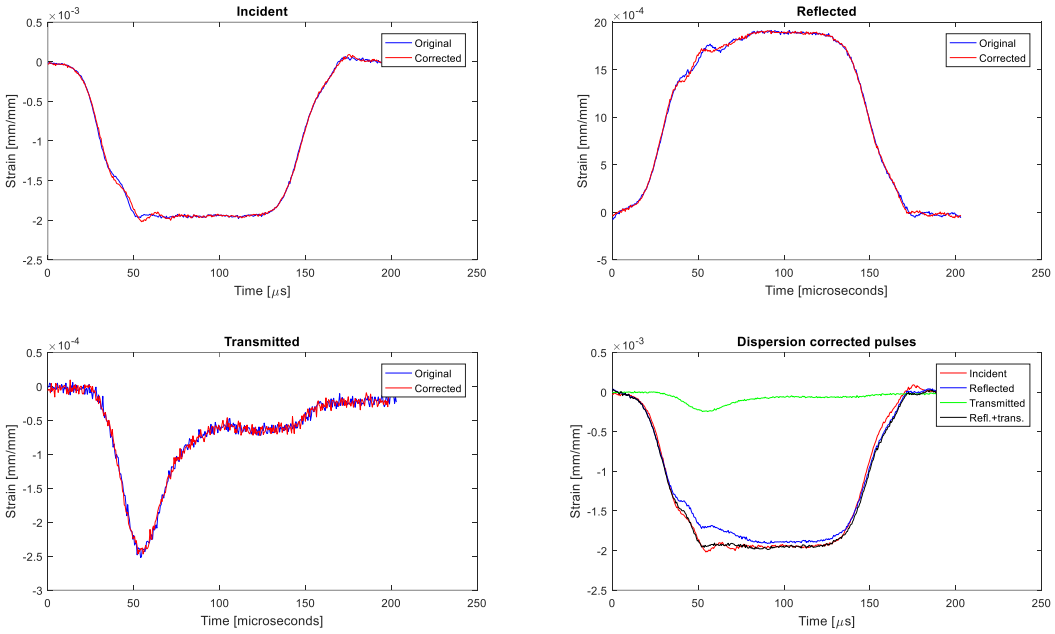
Incident
Original
Corrected
Strain [mm/mm]
Time [μs]
Reflected
Original
Corrected
Strain [mm/mm]
Time [microseconds]
Transmitted
Original
Corrected
Strain [mm/mm]
Time [microseconds]
Dispersion corrected pulses
Incident
Reflected
Transmitted
Refl.+trans.
Strain [mm/mm]
Time [μs]

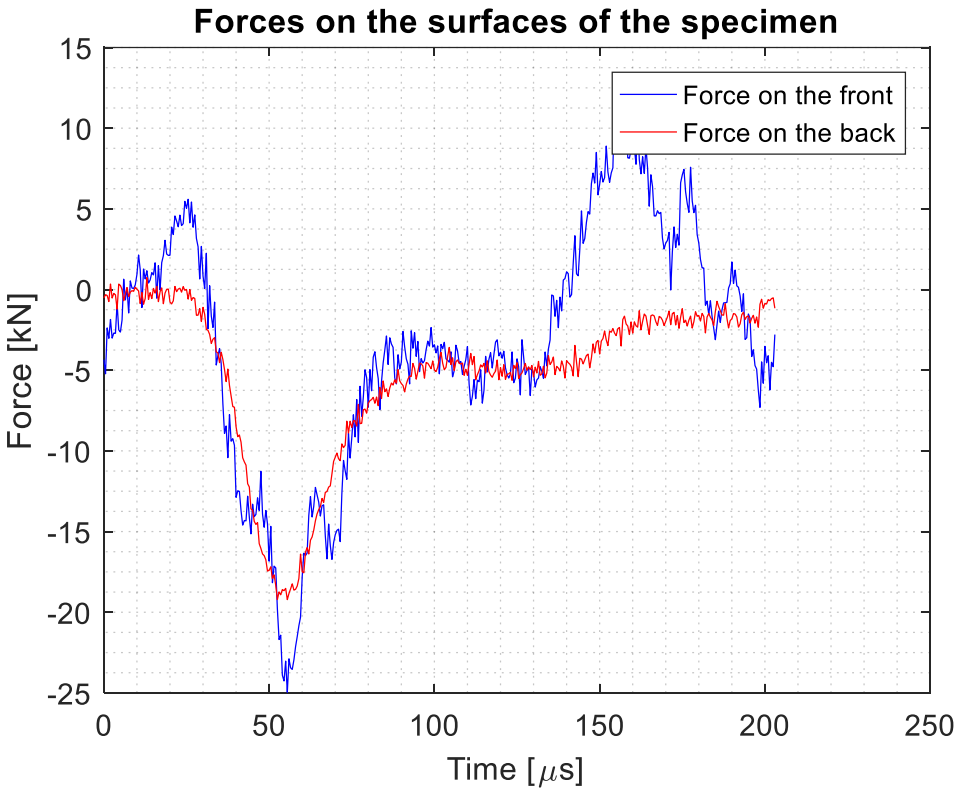
Forces on the surfaces of the specimen
Force on the front
Force on the back
Force [kN]
Time [μs]

- Test 4 – 20 m/s

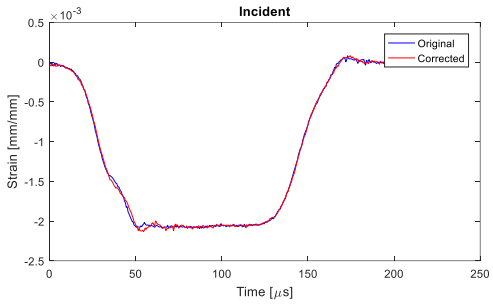
Incident
Original
Corrected
Strain [mm/mm]
Time [μs]

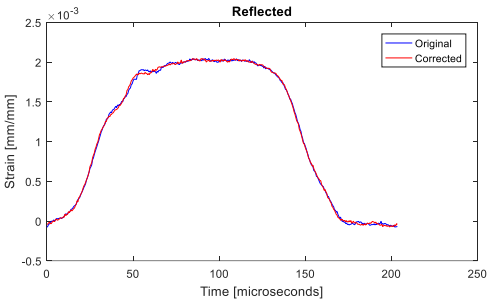
Reflected
Original
Corrected
Strain [mm/mm]
Time [microseconds]

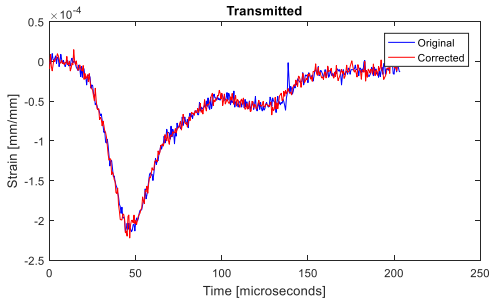
Transmitted
Original
Corrected
Strain [mm/mm]
Time [microseconds]

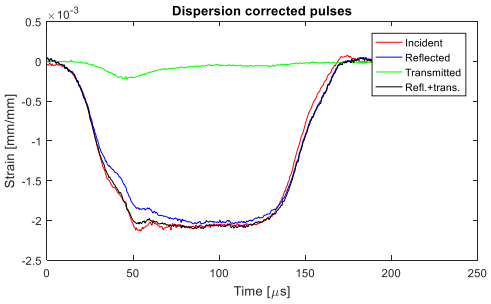
Dispersion corrected pulses
Incident
Reflected
Transmitted
Refl.+trans.
Strain [mm/mm]
Time [μs]

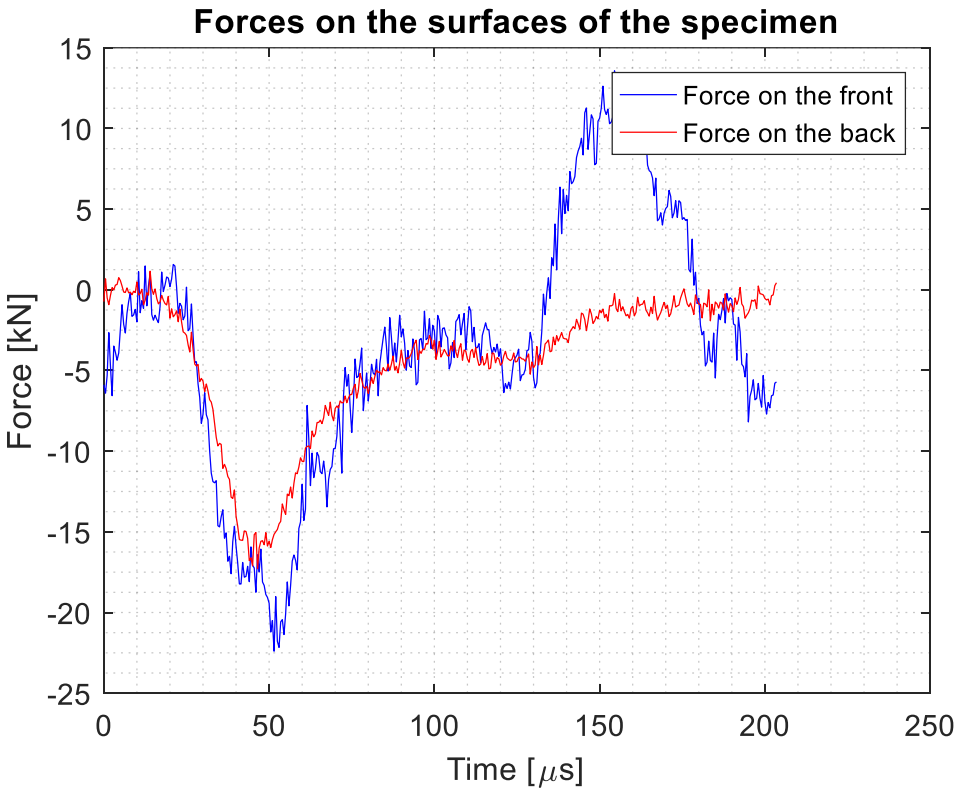
Forces on the surfaces of the specimen
Force on the front
Force on the back
Force [kN]
Time [μs]

- Test 5 – 20 m/s

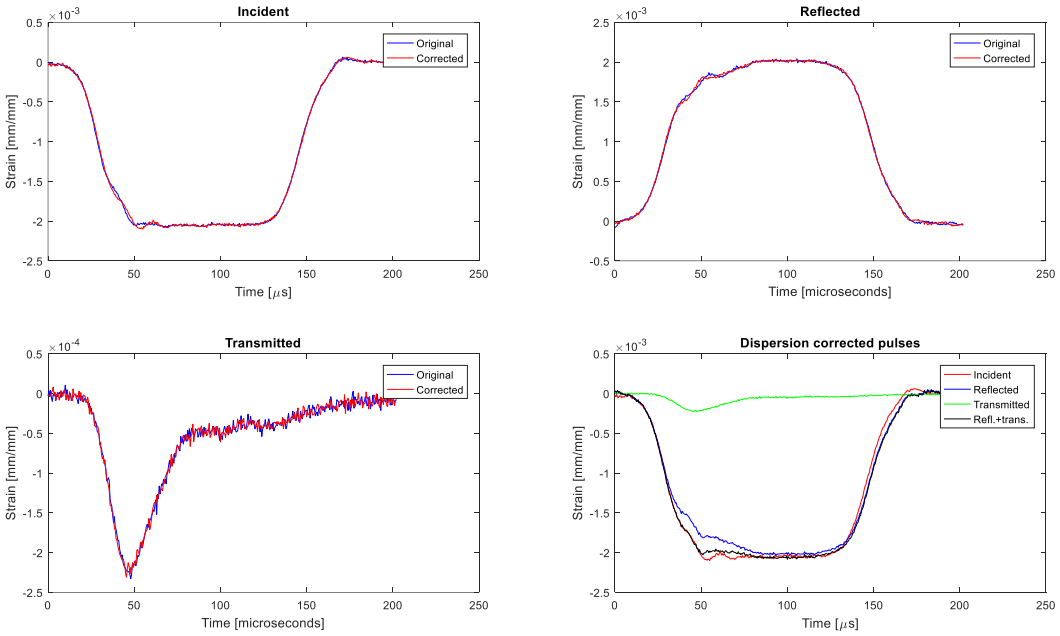
Incident
Reflected
Transmitted
Dispersion corrected pulses
Original
Corrected
Incident
Reflected
Transmitted
Refl.+trans.
Strain [mm/mm]
Time [μs]
Time [microseconds]

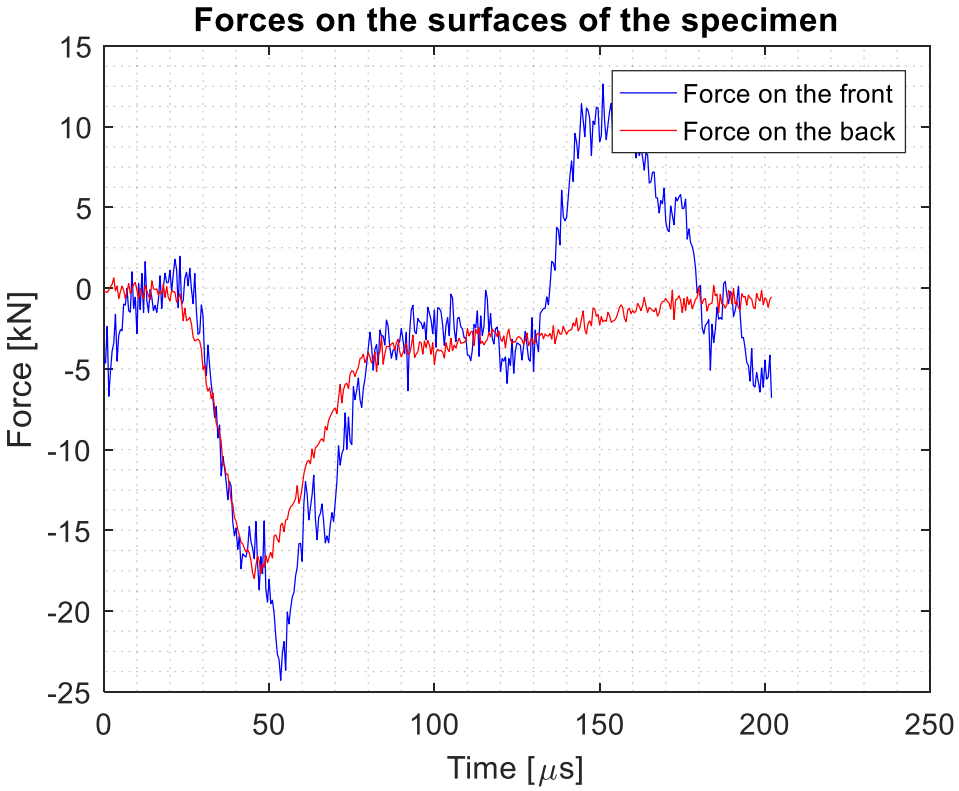
Forces on the surfaces of the specimen
Force on the front
Force on the back
Force [kN]
Time [μs]